Hydrogel based smart bandage for chronic wound healing

Jingwen Yu

Department of Biomedical Engineering
University of Glasgow

This dissertation is submitted for the degree of
Doctor of Philosophy

College of Science and Engineering
Advanced Bioengineering (AB)

Oct 2024

Acknowledgements

Firstly, I would like to give a massive thank you to my supervisors, Professor Jonathan Cooper, Professor Julien Reboud, and Dr. Bernhard Schmidt. Jon, we met during the challenge period, but we have now successfully gotten through it. Thank you for your guidance, generous encouragement, and always believing in me. It's been a lucky experience to do my PhD project in our AB group. Julien, you have always been supportive of every experiment I wanted to try, and your generous encouragement has helped me to be more confident about my work. Bernhard, thanks for always being patient and considerate of my confusion. With your help, I got the chance to become a more multidisciplinary researcher. I am so grateful to you three for all the support you have given me over the years, which has helped me grow into a better researcher.

I would specifically like to give a thank you to our Dr. Andrew Glide, who gave me so much help in all kinds of aspects of my PhD project. Andrew, thank you for always helping me with your kindness and profound knowledge. I am eternally grateful for your support and for showing me the magic world of microscopy and chemistry.

To all the past and present members of the AB group who have helped me a lot, thank you, Fan, Bo, Maha, Narina, Sitang, Tao, Tom, Xin and Xiaobo. Particularly, I would like to thank Pawel for always being nice and patient and helping me with the bacteria work. Olivia, thank you for joining our AB group and encouraging me in my every frustrated and unconfident moment.

To my best friends, Jiaxing, Yana and Zhuoer, you have always been around for everything and every moment; we accompany and support each other on both dark and brightening days, and this four-year life has been sparkling with happiness because of you; I will forever be grateful to have you all in my life.

Lastly, I would like to thank my lovely family—mum, dad, and grandma. I am so lucky to have been born into such a family full of laughter, happiness, and humour. I am who I am because they will always be there for me.

Life is a big maze made up of endless choices, may you walk towards yourself among these countless choices.

This PhD journey is going to arrive at the station, see you next time in our new life.

Declaration

I hereby declare that except where specific reference is made to the work of others, the contents of this dissertation are original and have not been submitted in whole or in part for consideration for any other degree or qualification in this, or any other university. This dissertation is my own work and contains nothing which is the outcome of work done in collaboration with others, except as specified in the text and Acknowledgements. This dissertation contains fewer than 40,000 words including appendices, bibliography, footnotes, tables and equations and has fewer than 100 figures.

Jingwen Yu
Oct 2024

Abstract

Wound healing is one of the most complex natural processes[1]; it requires the spatial and temporal synchronisation of different types of cells with distinct roles in the overlapping stages of haemostasis, inflammation, re-epithelialisation and remodelling. Most acute wounds can undergo regular self-healing and recover to intact tissue in a few weeks. Dysregulated wound repair events will lead to delayed healing and develop into chronic wounds, which tend to stall in the inflammation phase even for several months. Thus, timely and effective wound management during the healing process is of great significance for defencing bacterial infection and improving tissue healing. Skin wound repair requires the coordination of various host cells, which are also mediated by occupied microorganisms in the wound ecosystem. Therefore, appropriate management of bacterial contamination without disturbing the supportive host cells is crucial for chronic wound site treatment; very few works have been done in this field.

In this work, we have developed a visible light polymerised hydrogel with a semiconductor material doping, graphitic carbon nitride (g-C_3N_4) material, which acts as both initiator and reinforcer in the hydrogel polymerisation system. This work aims to provide an effective hydrogel system that can be used as a chronic wound healing bandage with desirable properties of wound site management patches[2], such as good biocompatibility, better conformity, and suitable water vapour exchange. The successful development of such a new hydrogel can be significant in point-of-care devices. Quantitative reactive oxygen species (ROS) can be formed from our visible light-activated hydrogel system in a controllable manner; it can effectively inactive different bacterial strains. In alignment with the urgent demand for a solution to antimicrobial resistance (AMR)[3], our photocatalytic-generated ROS can realise bacterial killing without drug inducement. In particular, g-C_3N_4 hydrogel system can selectively kill bacteria over mammalian cells in the co-existed environment; this work provides insights into the novel chronic wound management method that can stop the bacterial infection and restore the host cell environment through the homeostasis regulation using strictly controlled redox biological process[4]. In parallel, this system can also destroy the compact biofilm to break the being seriously hindered healing process. The results of this thesis suggested that our developed g-C_3N_4 hydrogel system can be used as a promising

chronic wound healing bandage material; it can effectively break the biofilm covering for wound healing sequences initiation and improving the healing process by ROS participation, realising bacterial infection elimination but also shaping the host immune response to against future invasions by signalling pathways transduction.

In all, our g-C_3N_4 hydrogel platform provides a promising concept that ROS released from the photocatalyst-doped hydrogel can successfully be used for complex chronic wound environment regulation, and visible light irradiation also gives an opportunity for wearable device development.

Table of contents

List of figures

List of tables

Abbreviations

Acronyms / Abbreviations

$^{\cdot}OH$ Hydroxyl radicals

H_2O_2 Hydrogen peroxide

$O_2^{\cdot}$ Superoxide anion

AAm Acrylamide

ADA American Diabetes Association

AHL Acyl homoserine lactone

AMR Antimicrobial resistance

APS Ammonium perfulfate

ATP Adenosine triphosphate

BHI Brain Heart Infusion

CBB Coomassie Brilliant Blue

CB Conduction band

CFU Colonies forming units

COB Chip-on-board

DAMPs Damage-associated molecular patterns

DCCT Diabetes Control and Complications Trial

DFT Density Functional Theory

DFUs Diabetic foot ulcers

DMA N,N-dimethyl acrylamide

DM Diabetes Mellitus

DMEM Dulbecco's Modified Eagle Medium

DMSO Dimethyl sulfoxide

ECM Extracellular matrix

ECs Endothelial cells

eDNA Extracellular DNA

EPS Extracellular polymeric substance

ER Endoplasmic reticulum

ESCs Embryonic stem cells

ETCs Electron transport chains

FBS Fetal Bovine Serum

FFAs Free fatty acids

FPG Fasting plasma glucose

FTSG Full-thickness skin graft

g-C_3N_4 Graphitic carbon nitride

GLUT1 Glucose transporter type 1

GLUT4 Glucose transporter type 4

HCs Hematopoietic cells

HF Heart failure

HFpEF heart failure with preserved ejection fraction

HFrEF heart failure with reduced ejection fraction

HPF 3'-(p-hydroxyphenyl) fluorescein

HUVECs Human umbilical vein endothelial cells

IDF International Diabetes Federation

IL-1β Interleukin-1β

IPTG Isopropyl-beta-D-thiogalactopyranoside

LB Luria-Bertani

MBA N, N'-methylene-bis-acrylamide

MMPs matrix metalloproteinases

MSCs Mesenchymal stem cells

NADPH Nicotinamide adenine dinucleotide phosphate

NBT Nitrobule tetrazolium

NETs Neutrophil extracellular traps

NGSP National Glycohemoglobin Standardization Program

NHE Normal hydrogen electrode

NOXs NADPH oxidases

NPN N-phenyl-1-naphthylamine

ONPG *o*-nitrophenol-β-Dgalactoside

PAMPs Pathogen-associated molecular patterns

PDT Photodynamic therapy

Pen/Strep Penicillin Streptomycin

PGH Placental growth hormone

PG Plasma glucose

Phox NOXs of phagocytes

PI Propidium iodide

PPARα peroxisome proliferator-activated receptorsα

PPARγ peroxisome proliferator-activated receptorsγ

PTT Photothermal therapy

QS Quorum sensing

RET Reverse electron transport

RFP Red fluorescent protein

ROS Reactive Oxygen Species

SOD Superoxide dismutase

SR Survival ratio

STSG Split-thickness skin graft

T1DM Type 1 diabetes mellitus

T2DM Type 2 diabetes mellitus

TEMED N, N, N', N'-tetramethylethylenediamine

TNF-α Tumor necrosis factor-α

UK the United Kingdom

UV Ultraviolet

VB Valence band

VEGF Vascular endothelial growth factor

WHO World Health Organization

WIfI Wound, Ischemia, Foot Infection

Chapter 1

Introduction

1.1 Diabetes mellitus (DM) disease and related chronic wounds

1.1.1 Diabetes mellitus (DM) disease

Diabetes mellitus (DM) is a common, constantly, and potentially fatal medical condition that has increased in prevalence over the past decades. According to the World Health Organization (WHO) report, no longer a disease in predominantly developed countries, people with diabetes are steadily increasing all over the world, especially markedly in middle-income countries, contributing to the major public health challenge.

As a chronic long-term disease, diabetes requires continued medical monitoring, timely intervention, and high self-management of patients. The number of adults who live with diabetes has increased from 108 million in 1980 to 422 million in 2014 in the world[16, 17], and this number is predicted to increase to 693 million by 2045, accounting for 6% to 7% of the global population[18, 19].

In 2012, diabetes caused about 1.5 million deaths, and another 2.2 million deaths were due to unstable blood glucose levels (**Figure 1.1**), which usually leads to the risk of abnormal macrovascular, such as coronary heart disease, stroke, peripheral arterial disease, and microvascular conditions, such as diabetic kidney disease, retinopathy, and peripheral neuropathy. Of these 3.7 million deaths, 43% of them occur before the age of 70 years old; in developing countries, death caused by high blood glucose occurs earlier than the age of 70. In recent years, diabetes caused complications that turned into a more complex situation[5].

In 2019, diabetes was estimated to be the eighth leading cause of death and disability combined in the world; nearly 460 million people of all countries, ages and genders live with

this disease. Diabetes brings a substantial economic burden both to the public health system and individual families, and the International Diabetes Federation (IDF) investigated shows that 537 million people worldwide with diabetes in 2021, resulting in $966 billion in health expenditures globally; this number could increase to over $1054 billion by 2054[20]. In the UK, 4.9 million people now live with diabetes, which is equivalent to one in 14 people[21]. During the period March 2020 to January 2021, there was an excess of 2696 deaths caused by diabetes, showing an increase of 24 7% compared to the average number of five years before the pandemic[22, 23].

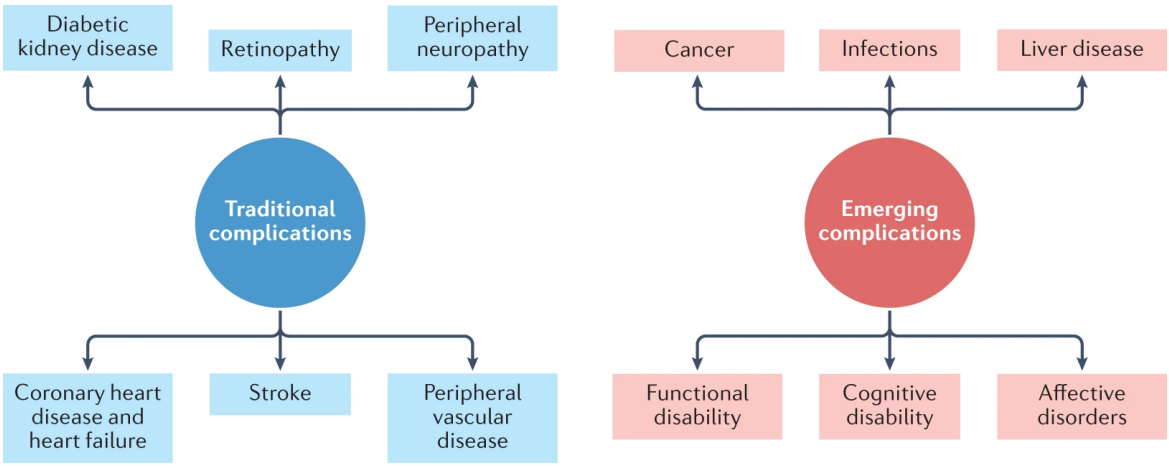

Fig. 1.1 Evolution of diabetes induced complications from (left panel) traditional complications including vascular diseases to recent emerging complications (right panel) including more complex infectious diseases. (Figure adapted from reference[5]).

Diabetes is a group of metabolic diseases characterized by an elevated blood glucose concentration in the body over an extended period. Hyperglycaemia is caused by defects in insulin function, including insulin secretion, contact with tissue cells, receptor synthesis, and insulin action within cells. Diabetes is classified according to different etiologies; the most recent classification criteria were issued by the WHO in 2019[24, 25]. Type I diabetes is usually defined as the result of cellular-mediated autoimmune dysfunction of pancreatic β

cells, leading to absolute deficiency of endogenous insulin[24, 26]. People with type I diabetes can survive with exogenous insulin supplements, but are susceptible to diabetic ketoacidosis. This group represents 5%-10% of all cases of diabetes. Genetic predisposition and possible virus attack from type I diabetes have no strong relationship with individual lifestyle.

The relative insulin deficit characterises type II diabetes due to pancreatic β cell malfunction[27]; the number of type II diabetes could be over 90% of the total population with diabetes. These patients have a very gradual progression of insulin insufficiency, which means that they may remain asymptomatic for many years; 50% of them are undetectable before being affected by the disease. People with type II diabetes can manage their blood glucose levels with lifestyle changes. However, many of them eventually require insulin due to chronic exhaustion of β cell function.

Gestational diabetes (type III) occurs when a woman is pregnant[28]; placental growth hormone (PGH) and some other pro-inflammatory cytokines, like tumour necrosis factor-alpha (TNF-α), were produced by the placenta; this spontaneous hyperglycaemia developed due to the impaired insulin intolerance during pregnancy, these condition does not appear in all pregnant women and the related syndrome would largely subside after the delivery of a child. The diabetes diagnosis criteria recommended by the American Diabetes Association (ADA) in 2021 and approved by the WHO[29] the International Diabetes Federation (IDF) are shown below:

1. Fasting plasma glucose (FPG) $\geq$ 126 mg/dL (7.0 mmol/L) - Fasting is defined as no claoric intake for at least 8h

2. 2h plasma glucose (PG) $\geq$ 126 mg/dL (11.1 mmol/L) during oral glucose tolerance test (OGTT) - The test should be performed, recommeded by WHO, using a glucose load containg the equivalent of 75g anhydrous glucose dissolved in water

3. $HbA_1c \geq 6.5\%$ (48 mmol/mol) - The test should be performed in a laboratory using a method that is NGSP-certified and standardized to the DCCT assay. (NGSP: National Glycohemoglobin Standardization Program; DCCT: Diabetes Control and Complications Trial)

4. A random plasma glucose $\geq$ 200 mg/dL (11.1 mmol/L) - A person with classic symptoms of hyperglycaemia or hyperglycaemic crisis.

Fasting glucose and HbA1c are both used to diagnose diabetes, but they measure different aspects of blood sugar regulation, fasting blood sugar measures the blood sugar level after an overnight fast (at least 8 hours without eating), while the HbA1c (Glycated Hemoglobin) the average blood sugar levels over the past 2–3 months, based on glucose

attaching to haemoglobin in red blood cells. Thus, the HbA1c measurement is more suitable for long-term assessment but the fasting glucose is more reliable in reflecting the single-time status of blood sugar.

1.1.2 Diabetic foot ulcers (DFUs)

Most malignancy results do not come from diabetes mellitus itself but from other severe complications, which could be classified into microvascular diseases or macrovascular diseases in origin. Diabetic foot ulcers (DFUs) are one of the devastating chronic complications of diabetes[30]; the specific pathophysiological factor could be attributed to the impairment of the peripheral vascular during the very early stage, then combined diabetic sensory, motor and autonomic neuropathy dysfunction, resulting in foot deformity, skin pressure increasing with walking.

In the UK, diabetic foot ulcers have become a significant health burden, contributing to the main reason for hospitalisation among people with diabetes, and it has been considered the single most common reason for morbidity and mortality[31]. Every 2% - 3% of diabetes patients are thought to live with an active foot ulcer within a lifetime; the risk of developing diabetic foot ulcers is as high as 25%[32]. 20% of people with diabetic foot ulcers will possibly go through lower extremity amputation[33], which is mainly caused by the infection and progressive gangrene; 50% of diabetic foot ulcers become infected eventually.

As we mentioned, the development of diabetic foot ulcers is a complicated progressed consequence[34], which is caused by the co-existing of peripheral sensory neuropathy, peripheral motor neuropathy, autonomic neuropathy and peripheral artery abnormalities[35]. In diabetic foot ulcer patients, the impaired peripheral motor fibres will result in a partial loss of sensory and motor function, then muscle atrophy, further leading to foot deformities, such as hammer-toe and ankle deformity. The damaged sensorimotor neurones alter sensation, temperature, and local pressure, further affecting weight bearing and pain proprioception. Autonomic system dysfunction leads to the impairment of the sweat gland, so the viscoelasticity of the skin changes; it becomes drier and eliminates its functionality as a barrier to prevent microorganism invasion, and the risk of dermal infection and callus formation is increased as well (**Figure 1.2**).

Persistent hyperglycaemia[36–38] and unstable glucose metabolism lead to endothelial damage, hyperlipidemia, and elevated platelet viscosity and activity, all of which increase the possibility of atherosclerosis development. The peripheral artery occlusive disease will also induce long-term skin perfusion reduction, and then the ischemic ulcer or severe gangrene will develop. The integrity of the skin is damaged due to inadequate perfusion, which then facilitates the invasion of tissue infection. The infections that happen in diabetic foot ulcers

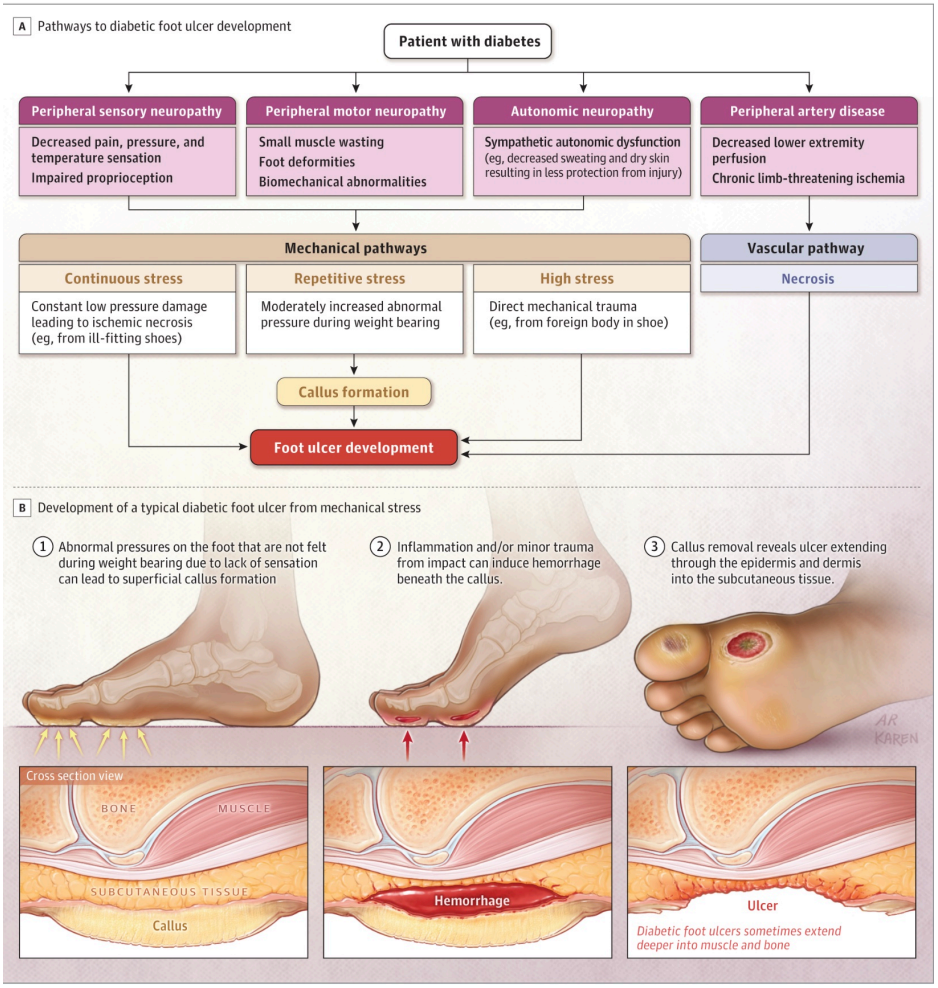

Fig. 1.2 Pathways to Diabetic Foot Ulceration. Part A. Diabetic foot ulcers developed from impaired mechanical sensing and vascular conditions; Part B. Explanations and schematic figures along the diabetic foot ulcers development process in the perspective of mechanical stress changes. (Figure adapted from reference[6]).

could differ from uncomplicated cellulitis to life-threatening necrotising fasciitis, even sepsis. 30% - 40% of diabetic foot ulcer cases might be infected with several bacteria[39–43], and the amputation risk increases when the diabetic foot infection involves resistant bacterial strains, especially methicillin-resistant *Staphylococcus. aureus*.

Evaluation of diabetic foot ulcers usually needs a comprehensive examination of the ulcer site and foot status. According to the assessment guidelines recommended by the National Institute of Clinical Excellent[44, 45], in the annual test of diabetic foot ulcer patients, they should have:

1. Neurological test of wounded foot for four different sites.

2. Foot shape check, including prominent metatarsal heads/claw toes, hallux valgus, muscle atrophy or Charcot's foot.

3. Dermatological test for callus formation, erythema and sweating conditions.

4. Lower-extremity vascular condition, especially on foot pulses and ankle-brachial index.

For an appropriate intervention for diabetic foot ulcers, a reliable descriptive classification system could be helpful for the outcome prediction. The Wagner and University of Texas (UT) classifications are two standard classification systems used worldwide[46]. Wagner Ulcer classification system is usually used to evaluate the duration of hospital stay of the patient, which is based on the depth and penetration of the wound, the presence or absence of osteomyelitis or gangrene, the extent of tissue necrosis on the wound site, shown below:

1. Grade 1: superficial diabetic ulcer.

2. Grade 2: Ulcer deprivation involving ligament, tendon, joint capsule or fascia shows no local swelling or osteomyelitis.

3. Grade 3: Deeper ulcer with abscess or osteomyelitis.

4. Grade 4: Severe gangrene on the foot.

The UT classification is based only on the depth and penetration of the wound site, but it also considers the presence or absence of infection and ischemia. When taking all involved factors together, The Wound, Ischemia, and Foot Infection (WIfI) classification system was developed and validated to evaluate the risk of amputation for patients with diabetic foot ulcers more accurately[47, 48]. It assists clinicians and patients in identifying the severe extent of diabetic foot ulcers in individuals and deciding on further interventions of multidisciplinary clinical care. Usually, a higher score from the WIfI system leads to a lower amputation risk and morbidity.

In general, people with active diabetic foot ulcers heal after appropriate therapy[49, 50], such as controlling glycaemia more carefully, debridement through different methods, off-loading of local pressure, negative pressure wound therapy, treating the infection using pharmacological methods, or even re-vascularisation. The need for amputation would also be changed.

The other efficient method for curing diabetic foot ulcer wounds is wound dressings, with or without modification. Dressings usually provide external protection for the open wound and act as a barrier, which is the previously intact skin. They also maintain a moist environment and manage the exudate from the diabetic foot ulcer wound site.

1.1.3 Diabetic heart failure (HF)

To date, heart failure has been described as 'heart failure with preserved ejection fraction' (HFpEF) heart failure with preserved ejection fraction or 'heart failure with reduced ejection fraction' (HFrEF), which is characterised by the left ventricular function[51–53]. As a global epidemic, heart failure shortens longevity and impairs the life quality of patients severely. 10%-15% of the general population have diabetes mellitus worldwide, and the data from recent studies show that 44% of patients hospitalised for HF have diabetes mellitus. Approximately 40 million adults worldwide are affected by HF[54].

Diabetes could induce significant changes in the myocardium in both structural and functional ways (**Figure 1.3**), which increases the risk of heart failure largely. For years, several studies have discovered a dramatically increased incidence of heart failure (HF) in patients with diabetes, which is hardly explained by traditional risk factors, such as obesity, hypertension, dyslipidaemia, age, region, lifestyle, coronary artery disease and severe valvular disease. People who live with diabetes mellitus show over twice the chance of developing heart failure; usually, the outcomes are mortality or hospitalisation for heart failure. According to the Framingham Heart Study, diabetes mellitus increases the risk of HF independently, which is up to 2-fold in males and 5-fold in females compared with the same-age parallel subjects. Patients with diabetes show a higher risk of developing heart failure due to the abnormal cardiac metabolic process involving glucose and free fatty acids (FFAs)[55–57].

In diabetes mellitus, patients live with compromised glucose metabolism, which usually leads to dysfunctions starting from unstable blood glucose levels, then causes structural and functional abnormalities of the heart, ending in cardiac system breakdown eventually. Cardiac dysfunction in diabetic patients is caused by several different mechanisms comprehensively and synergistically; the characterised feature of cardiac metabolism is its flexibility, which means that the heart can switch among different substrates to meet its energetic demands with different sufficient nutrients at a specific moment. Under normal conditions, energy generation of the heart primarily relies on fatty acid as its primary source, which accounts for 60% to 90%[58], with a significant contribution from glucose oxidation around 10% to 40%, production of ketone bodies, lactate and amino acids is relatively low, their contribution to myocardial function is considered less than 10%[59–61]. While the glucose is taken up via insulin-dependent glucose transporter type 1 (GLUT1) and glucose transporter type 4 (GLU4), the ATP is generated in mitochondria through phosphorylation oxidation after glycolysis[62–64].

In type 1 diabetes mellitus (T1DM), the glucose transport across the sarcolemmal membrane to the myocardium at a slow rate, leading to a reduction of the myocardial

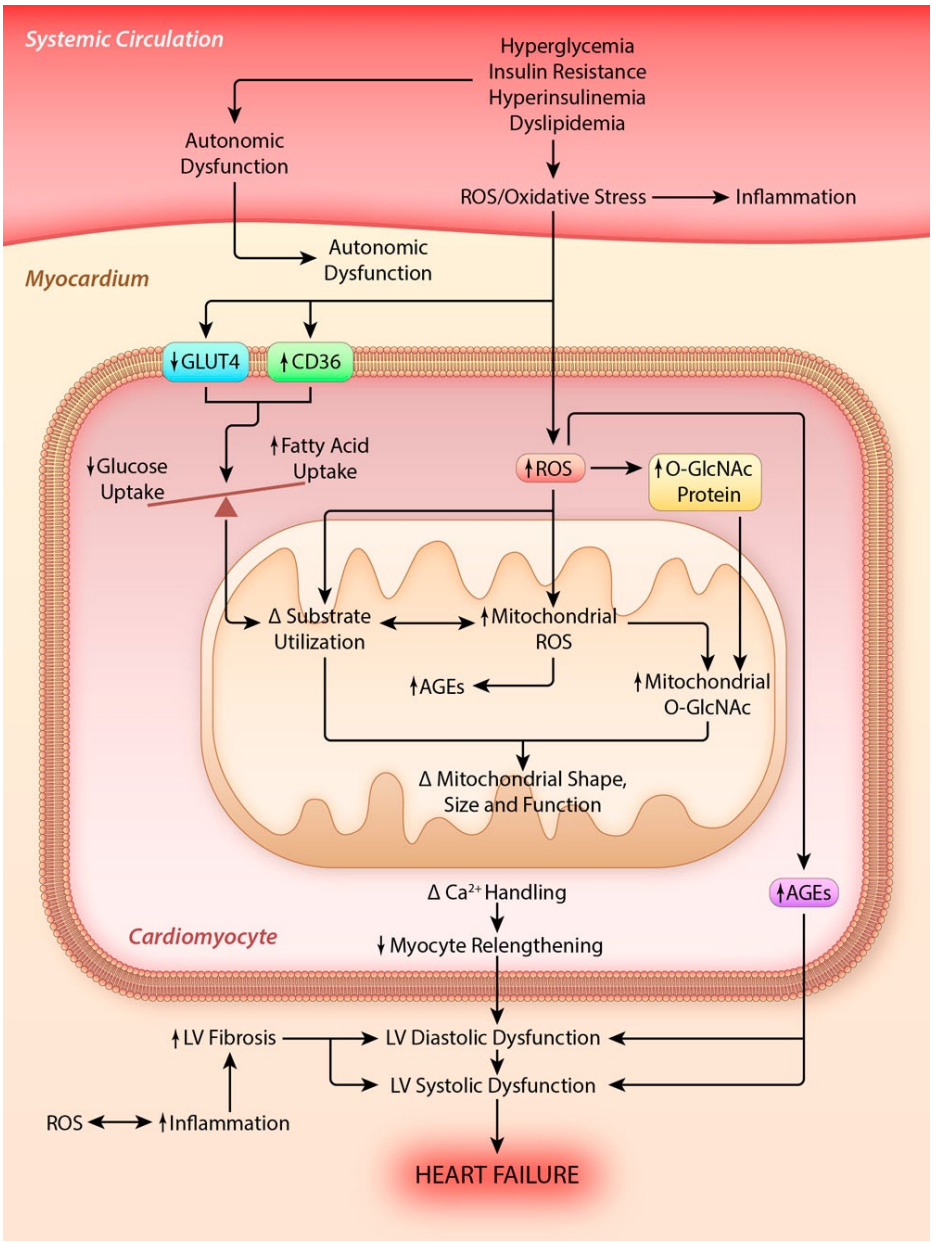

Fig. 1.3 **Mechanisms for Cardiac phenotype of diabetes mellitus development.** The potential contributing mechanisms, including microenvironmental oxidative stress (OS), inflammation, impaired calcium ions (Ca^{2+}) fluxing, cascaded alterations in internal metabolic process, insulin signaling, gene regulation, dysfunction of mitochondria and endoplasmic reticulum (ER), as well as cardiac cell death. AGE, advanced glycation end product; CD36, cluster differentiation 36; GLUT4, glucose transporter 4; LV, left ventricle; and ROS, reactive oxygen species. (Figure adapted from reference[7]).

concentration of glucose transporter type 1 (GLUT1) and glucose transporter type 4 (GLU4), reducing the glycolysis and glucose oxidation[65–68]. The heart in T1DM patients relies

more on fatty acid oxidation as glucose metabolism is impaired. Increased blood glucose and ketone body production also require more effort. Continuous generation of higher energy supply is critical for maintaining heart function. As the increased utilisation of FFA becomes the primary source of energy generation in the heart, the β-oxidation of fatty acid is much less efficient than glycolysis oxidation; this long-term insufficiency leads to decreased energy reservation and cardiac efficiency, exacerbating cardiac dysfunction more[56, 69]. Thus, diabetic heart failure is commonly characterised by diminished high-energy phosphate production (ATP) generation in the heart.

However, in type 2 diabetes mellitus (T2DM), the metabolic substrate switch mechanism is still unclear now because there is not enough evidence to prove the activation of peroxisome proliferator-activated receptors (PPAR) α and γ, which is considered as the trigger of the metabolic substrate switch[70–72]. Another possible explanation of the fatty acid involved in glycolysis suppression could be the hyperacetylation of one of its essential enzymes.

Imaging studies on diabetic heart failure show that the left ventricular concentric remodelling could be one of the characterisations of diabetic myocardium, which is the consequence of damaged myocardial energetics and decreased systolic strain. The increased extracellular volume caused by collagen deposition and fibrosis in the myocardium could be an indicator of mortality and heart failure in patients with diabetes as well. Mounting research has found a strong association between microvascular damage and cardiomyocyte stiffness caused by advanced glycation end-product deposition.

Energetic metabolic changes in the myocardium are the critical factors for cardiac dysfunction in diabetes. Heart failure severely affects cardiac metabolism and leads to a shift of cardiac substrate utilisation from fatty acids towards glucose oxidation, which is opposite to the conditions in diabetes. This change happens because glucose oxidation is more oxygen-efficient than fatty acid oxidation[73].

Before considering the specific interventions for patients with diabetic heart failure, the decision is usually made according to the particular situations in individuals. Generally, it goes into two groups: 1) the treatment for heart failure therapy in patients with diabetes and 2) diabetes treatment in patients with heart failure. When diabetes and diabetic heart failure co-exist, heart failure always shows a much poorer prognosis than diabetes mellitus. It is always better to make heart failure a priority.

1.2 Cellular events in the acute and chronic wound healing process

The skin is the largest organ in our body, covering all the tissues to prevent injury from external harms[74], such as intense ultraviolet radiation, mechanical damage, high and low-temperature exposure, and bacterial infection[75, 76].

Our intact skin is the primary physical barrier; the outer epidermis is an impermeable layer that can defend against harsh conditions. The dermis comprises the extracellular matrix (ECM), vascular system, and mechanoreceptors responsible for strength, nutrients, and immunity supplements[77]. Adipose tissue is under the dermis for energy preservation and is a source of growth factors transported to the dermis. Thus, our skin also works as an immunity barrier against possible pathogenic attacks.

The skin is exposed to various external and internal pressures, making it susceptible to injuries and damage. Once the integrity of the skin architecture, a mucosal surface, deep tissue, and even bone is lost due to any external damage, this results in cell damage and the formation of wounds. A wound is defined as the disturbance of the standard anatomic structure and function[78, 79].

1.2.1 Acute wound healing

Wound healing is a complicated biological process involving various cell types sequentially (**Figure 1.4**). Once damage occurs to tissue, organ, or body, multiple relative pathways are activated and all these cells, factors, and mediators interact with each other in an extremely sophisticated cascade of cellular events. Generally, the wound healing process[80–82] goes through the following stages: hemostasis, inflammation, angiogenesis, growth phase, re-epithelialization, tissue maturation, and remodeling phase; they proceed sequentially and overlap.

In the haemostasis stage[83, 84], all events usually happen on a macro- and micro-vascular level; the whole haemostasis process is tightly controlled by the balance among coagulation, endothelial cells, thrombocytes and fibrinolysis. Once the wound is formed, the first response is that the blood vessels on the wound site are contracted immediately, and then the platelet is activated to form a fibrin clot to stop bleeding. When entering the secondary hemostasis stage, the coagulation cascade is activated to reinforce the platelet plug by fibrin mesh and form a thrombus, which acts as the scaffold for upcoming inflammatory cells, such as neutrophils, monocytes, macrophages and other adaptive immune cells, to promote the healing process goes into the next phase.

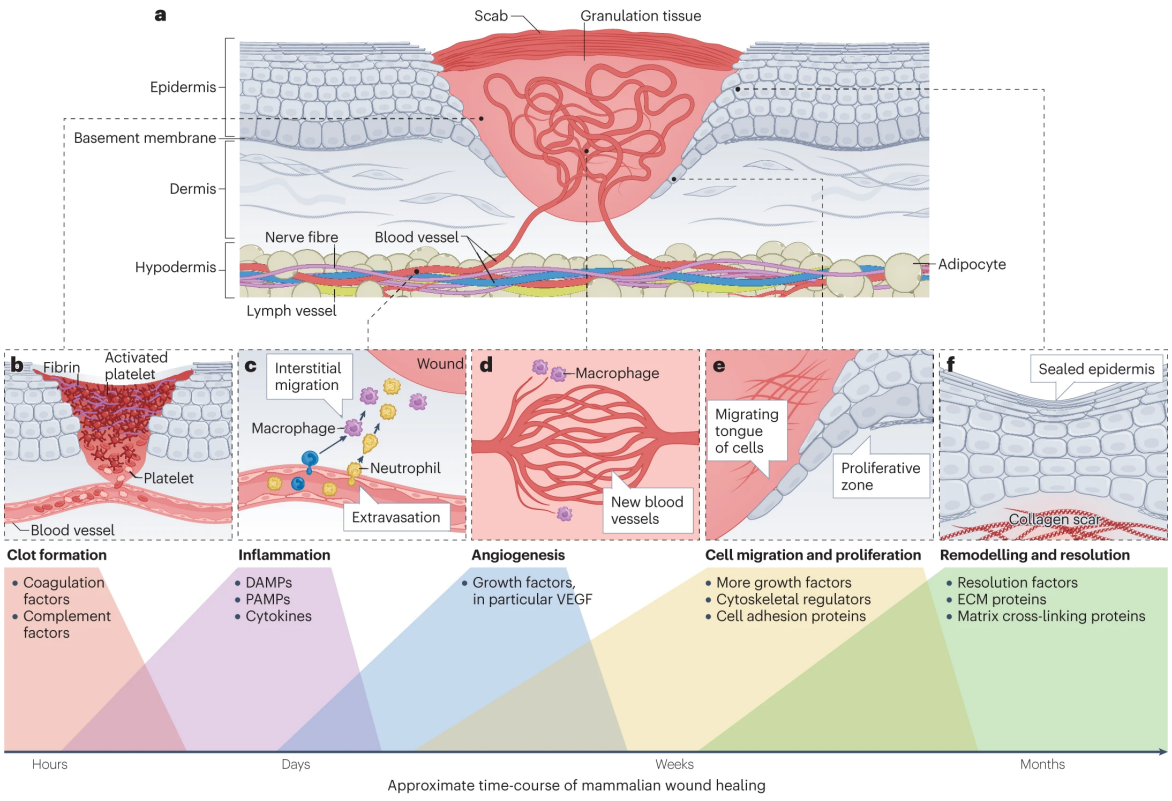

Fig. 1.4 **Process of wound healing.** **(a)** Schematic of wounded skin structure and functional part involved in the healing phase. **(b)** coagulation phase, the platelet helps stop bleeding once the tissue gets injured. **(c)** Inflammation phase, after then the wound inflammatory response, the inflammatory cells, including neutrophils, and macrophages are recruited. **(d)** Angiogenesis phase, granulation forms to refill the missing connective tissue to further support the wound angiogenesis, fibroblast cell migration and new collagen matrix deposition. **(e)** Cell migration and proliferation phase, once the granulation tissue is reformed, the re-epithelialization will be initiated by epidermal cell migration to reconstruct the intactness of the skin barrier. **(f)** Remodelling phase, finally the open wound heals as the wound edges merge, however different wounds remodel to different extents, usually with scar tissue left. Abbreviations: DAMPs, damage-associated molecular patterns; ECM, extracellular matrix; PAMPs, pathogen-associated molecular patterns; VEGF, vascular endothelial growth factor. (Figure adapted from reference[8].)

Inflammation is the primary nonspecific immune response against external harmful signals[1], such as microorganism infection, damage to the biological tissue and invasion of any other toxic substances. Injury-induced signals trigger the inflammation response, characterised by swelling, pain, tissue redness and cellular dysfunction. As the tissue gets injured immediately, a significant increase of intracellular calcium ions (Ca^{2+}) forms a calcium wave[85, 86]. These increased Ca^{2+} leads to the modifications of several transcriptional

pathways, besides the other cellular responses and damage signals, including reactive oxygen species (ROS), damage-associated molecular patterns (DAMPs), pathogen-associated molecular patterns (PAMPs) from bacterial components, lipid mediators, related cytokines and chemokines activate the transcriptional-independent pathways to attract the inflammatory cells as well.

The inflammatory phase could be divided into early and late inflammatory phases. The early inflammatory phase is initiated from the late coagulation stage; neutrophils are the first responders; they destroy the infectious threats by releasing reactive oxygen species (ROS), proteolytic enzymes, and neutrophil extracellular traps (NETs). In the late inflammatory phase[87, 88], various cytokines and breakdown products recruit more phagocytotic cells at the wound site; the attracted macrophages then start the phagocytosis process to clear the pathogens and toxic substances. During this time, macrophages also show a phenotype conversion from M1-macrophage (pro-inflammatory macrophage) to the alternatively activated macrophage (M2-macrophage); the M2-macrophages mainly participate in the angiogenesis process to generate new blood vessels for promoting proliferation and re-epithelialisation process.

Once the initial immune response is completed, that is the signal of the inflammatory phase ends, and the healing process proceeds into tissue re-epithelialisation. The re-epithelialisation is the main stage for lost tissue repair and refilling so that the open wound can be reclosed and the biological tissue functions through the combination of processes of angiogenesis, fibroblast proliferation, re-epithelialisation, neovascularisation and immunomodulation. In this stage, the granulation tissue, extracellular matrix (ECM) and collagen are formed by activated fibroblasts and endothelial cells[89]; the fibroblast then synthesises new ECM, secret cytokines and growth factors to regulate the immunomodulation in the healing process. Granulation tissue[77] is eventually replaced by new connective tissue, and the fibroblast cells are presented in the connective tissue to maintain the integrity and plasticity of the structure. The microvascular endothelial cells (ECs) are mainly responsible for forming new blood cells, activated by the signals secreted from the adjacent cells. The angiogenesis process is initiated when the ECs sense the proangiogenic activation signals secreted from the adjacent cells[90, 91]. The ECs migrate within the fibrin/fibronectin-rich clot, and the activated ECs are devoted to establishing and strengthening the interaction with the perivascular cells. ECs usually exhibit heterogeneity during angiogenesis when acting as tip and stalk cells. This heterogeneity is regulated by Notch pathways triggered by the mediators secreted by the proliferation of keratinocytes, subcutaneous adipose stromal cells and macrophages in the wound environment. During the angiogenesis process[92, 93], the ECs present as the tip cells sense VEGF and many other signalling molecules to extend their

filopodia, which is used for control and organise the formation of new capillaries; the stalk ECs commonly follow the tip cells to support the integrity of the vascular system. Pericytes and circulating progenitor cells[94, 95] play critical roles in the stage of neovascularisation during the wound healing process. The pericyte cells are embedded in the basement membrane of the vascular system, playing an essential role in maintaining the stabilisation of the microvasculature system and defence against bacterial invasion by forming the vascular barrier. The pericytes show multipotent generation capacity[96, 97]; they promote wound healing by interacting with ECs and hematopoietic cells (HCs) and depositing ECM on the wounded site. The hematopoietic stem cells and endothelial progenitor cells bind to the endothelial cells at the hypoxia/ischemic tissue site to form new blood vessels to accelerate wound healing. It is necessary for maintaining nutrient delivery and oxygen homeostasis[77]; cellular proliferation and tissue regeneration could happen. Circulating progenitor cells contribute to neovascularisation during wound healing. First, the injured tissue releases the chemokines, which cause the bone marrow-derived progenitor cells to enter circulation. Then, these circulating progenitor cells are attracted by the increased chemokine gradients and bind to the hypoxia or ischemic tissue of the wound site[98, 99]. After this, these progenitor cells embed into the sprouting endothelium, where the stem cells and progenitor cells differentiate into endothelial cells. Fibroblast cells are the most commonly present in the connective tissue of every organ[100]; they mainly contribute to ECM deposition and remodelling. There is strong evidence to reveal the heterogeneity among fibroblasts derived from different tissues. This heterogeneity allows fibroblasts to differentiate into various phenotypes of subpopulations that participate in different stages of wound healing, including ECM deposition and re-organisation, growth factors and chemokines secretion and immunomodulation[101, 102]. Fibroblast heterogeneity shows positional differences. Data shows that the initial dermal repair is due to the lower lineage fibroblasts that express myofibroblast markers like α-smooth muscle actin (α-SMA), and these cells synthesise a large amount of ECM for scarring formation. In addition to positional and origin-specific differences, fibroblasts also change because their activation status, like some fibroblasts in the wound healing process, needs more contractile phenotype by expressing β- and γ-cytoplasmic actin and α-SMA to convert into contractile myofibroblasts.

Wound contraction is one of the significant parts of wound healing[103, 104], which encloses the open wound area and helps accelerate the re-epithelialisation process. During this process, the generated collagen fibrils are arranged perpendicularly to the wound edge, so the mechanical strength of the tissue is increased significantly. This stiffness change in the wound environment promotes the fibroblast cells that migrate into the wound centre to convert into myofibroblasts with α-SMA expression. The myofibroblast cells are one of the

transitional cells, contributing to the ECM deposition and showing similar characteristics of contractile smooth muscle. These cells are formed when normal fibroblasts generate bundles of microfilament, and the primary source of myofibroblast cells is usually the normal fibroblast within the uninjured dermis. One of the mechanisms of myofibroblasts that help with wound contraction is that they attach to the polymerised fibronectin via their integrins and pull the fibres towards the wound centre[105]. The apoptosis process clears the myofibroblasts when the injured tissue is finally restored.

Open wound closure is commonly considered the end of wound healing, but the remodelling process can continue for several months or even a year. The tissue remodelling includes neovasculature regression[106–108], ECM deposition, and scar tissue replacing previous granulation tissue. In this process, collagen I synthesis and collagen III lysis happen coincidently, and collagen III is gradually replaced by the more robust collagen I, resulting in ECM reconstruction[77]. Once the healing process is complete, myofibroblasts usually undergo apoptosis. If the cells within granulation tissue fail to go through apoptosis after tissue remodelling, hypertrophic scars form. These processes are how acute wounds heal; they usually follow these orderly and timely reparative processes that bring a sustained reconstruction of cellular function and tissue integrity.

1.2.2 Chronic wound healing

Chronic wounds occur when one of the normal healing processes is disrupted once or several times in the phases of haemostasis, inflammation, proliferation, and remodelling, indicating that the chronic wound does not follow the timely healing cascades.

They are usually stuck in the inflammation phase and then challenging to transfer into the proliferation phase. The high mitogenic activity usually happens in acute wounds is significantly decreased in chronic wounds. The local tissue hypoxia, repetitive trauma and severe bacterial invasion, combined with the impaired cellular and internal host responses to the external stimuli, cause a harmful cycle that hinders the healing process moving towards the proliferative phase of healing. In chronic wounds, multifactorial applied stimuli create an unfriendly microenvironment where the sophisticated balance between pro-inflammatory cytokines and anti-inflammatory cytokines is disturbed. All these complex factors together stop the injury from healing within the expected time[109–111].

The reason for the non-healing process present in the chronic wound is complicated and multifaced (**Figure 1.5**). Firstly, several abnormal events happen in different cells, involving chronic healing. Excessive neutrophil infiltration[112, 113] is a crucial event that impairs the normal cycle of inflammation and is usually considered a biological marker of chronic wounds. Overloaded neutrophils in the microenvironment generate many reactive oxygen

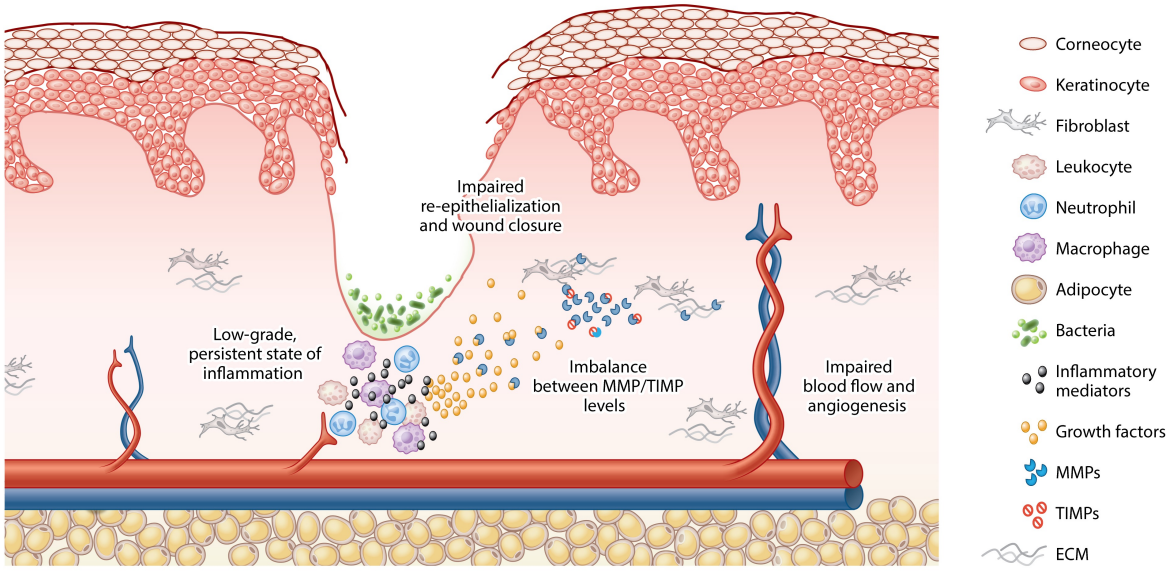

Fig. 1.5 **The microenvironment of chronic wounds.** The innate inflammatory response is insufficient to defend against the invaded infectious factors; An imbalanced level of inflammatory/proinflammatory factors leads to a persistent inflammation stage; Then the angiogenesis, collage matrix deposition and re-epithelialization process are hindered as well, resulting in the non-healing chronic wound. Abbreviations: ECM, extracellular matrix; MMP, matrix metalloproteinase; TIMP, tissue inhibitor of MMP. (Figure adapted from reference[9].)

species (ROS), which could directly damage the ECM and cell integrity and even promote cell senescence. These neutrophils also release several proteases[114] such as elastase and matrix metalloproteinases (MMPs)[115]; elastase usually degrades essential growth factors, while collagenase could degrade and inactive the component of ECM; on the other hand, both neutrophils and activated macrophages produce various pro-inflammatory cytokines, such as interleukin-1β (IL-1β) and tumour necrosis factor-α (TNF-α), which further increase the MMP production but decrease the production of their inhibitor, this imbalance accelerates ECM degradation, prevents cell migration, reduces fibroblast proliferation and collagen synthesis. Wound fluid is one of the characterisations of a non-healing chronic wound; it is also rich in several pro-inflammatory cytokines, like IL-1β and TNF-α. The byproducts that come from ECM degradation will further promote inflammation, and this forms a self-feeding circle. The typical healing cascade can be initiated when the debridement or cleaning breaks this sustainable deleterious cycle. In addition, growth factors secreted in acute wounds usually help with the healing process proceeding; they are also significantly decreased in the chronic wound environment.

Chronic non-healing wounds also result from several coexistent components[116, 117], such as ageing-caused systemic alteration, repeated injury in local tissue and microorganism

colonisation; these signals prolong inflammation status and delay the normal healing process. During the process, reduced angiogenesis is also an important factor causing the impaired proliferation and migration of endothelium progenitor cells, keratinocytes and fibroblasts, diminishing the re-epithelialisation process. Finally, biofilm structure formation at the injured wound site is another critical feature for chronic wounds[118, 119]. Compact biofilm is highly resistant to antibiotic interventions and perpetuates the persistence of non-healing wounds.

1.2.3 Biofilm in chronic wound

Biofilm is usually defined as the congregation of microorganisms attached to the substratum surface and enclosed in the extracellular polymeric substance (EPS)[120], a significant characterisation of the biofilm. Not a single bacterial infection, the biofilm is a complex microbial ecosystem constituted by several bacteria and fungi. Several factors regulate biofilm formation[121, 122], including type of bacteria, bacterial surface expression, hydrodynamics, cell-cell interactions, cell-host interactions, and oxygen and nutrient supplements. The biofilm formation process is commonly categorised into three main stages: surface attachment, maturation, and final dispersal and detachment (**Figure 1.6**).

The first stage of the attachment is reversible attachment; the extracellular DNA (eDNA) initiates the microbe to generate the matrix, which is finally replaced by the complex protein and polysaccharide structure. In this stage, the planktonic bacteria will first come into contact with the possible surface where they can attach; this attachment could be reversible or irreversible. The reversible attachment is usually loose and fragile, which could be destroyed easily. When bacteria attach to the abiotic surface, this is mediated mainly by some physiochemical interactions, such as electrostatic, van der Waals force and hydrophobic interaction. However, the attachment between bacteria and biotic surfaces (including aortic walls, heart valves and chronic open wound tissue) mainly relies on specific ligand-receptor interactions. Studies show that most bacterial surfaces present a negative charge due to the bacterial envelope and cellular wall components; this might generate a repulsive electrostatic force in the simple physical contact process, but the unique organelles in bacteria, such as flagella or pili would act as an additional propeller or hooks to help with the attachment. The irreversible attachment tends to be permanent and develops into biofilm. Colonised bacteria usually promote this process by secreting adhesins to bind to the substratum, and the attachment is gradually transferred from the weak irreversible attachment to the solid irreversible attachment. After this boarding, the whole process will proceed into the maturation of the cells in the matrix.

Maturation is the second stage of biofilm formation. In this stage, the attached bacterial aggregation will proliferate firstly, producing the sticky extracellular polymeric substance

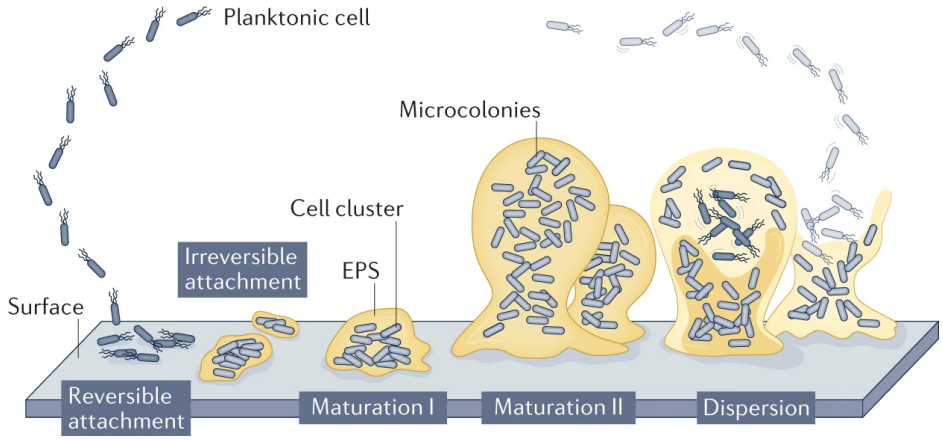

Fig. 1.6 **Schematic explanation of five-step biofilm formation. Reversible attachment:** planktic bacterial cells attach to the surface via their flagellum; **Irreversible attachment:** then this attachment transits into irreversible status as the flagella reversal rates are reduced, biofilm matrix components are released and attached bacteria present drug tolerance as well. **Maturation I:** A cell cluster with the thickness of several cells is formed and embedded into the existing biofilm matrix. **Maturation II:** The maturation stage is then fully finished with microcolonies formation. **Dispersion:** The external environment can trigger the biofilm to degrade, some bacterial cells detach from the formed biofilm, returning to the planktic cells and re-attach on a new surface, continuing the biofilm cycle. (Figure adapted from reference[10].)

(EPS), which is highly hydrated, with more than 90% of water and exopolysaccharide polymer, proteins, lipids, nucleic acids and nutrients; this monolayer protects the embedded bacteria from cleaning and damaging. The bacterial cells within the structure then form the micro-colonies; when the thickness of the biofilm is around 10 - 25μm[123], the base of the biofilm turns to be anaerobic; this is a signal of biofilm maturation. After this, the bacterial cells in this micro-colony begin the specific cell-to-cell communication called the quorum sensing (QS) mechanism[124]. Several events, such as bacterial cell density, genetic expression change, biofilm colonisation, and antimicrobial resistance, are regulated by this quorum sensing mechanism. Quorum sensing can generally be divided into two types. One is intraspecies signalling, and in this situation, gram-negative bacteria usually use acyl homoserine lactone (AHL) for communication[125]. Furthermore, the gram-positive bacteria use a peptide-based signalling system to communicate intraspecies. Another is interspecies signalling[126], which happens to gram-positive and gram-negative bacteria with the *luxS* gene.

This cell-to-cell communication makes the irreversible attachment stronger. The bacterial cell division rate remains low, but they become resistant to detergent clearing. Meanwhile,

the bacterial cells mature and construct a three-dimensional biofilm structure to recruit more planktonic cells and assemble them into the architecture. The recruiting process makes the thicker biofilm structure much more challenging to be disrupted by the surface tension change or detergent application; external mechanical stress is needed now.

Complex EPS structure acts as the protective layer, and biofilm maturation is supplemented by rapid cell division and development. The protection of the EPS structure causes the involution of a more complicated biofilm architecture with the generation of channels and holes. Moreover, the new structure promotes the redistribution of bacteria around the attached substratum. The most critical event of maturation is the generation of an absolutely different protein profile[127], which is absent in their planktonic counterparts. This novel protein profile supports the biofilm as highly resistant to the applied shear force and antibiotics in high concentrations.

In the final stage, some mature cells detach from the biofilms and float as planktonic cells to form a new biofilm in a new environment. Most of the bacteria are dispersed passively as the result of external shear force, but they also periodically actively disperse[128, 129]. Generally, this detachment and disperse phenomenon is a complex and dynamic process regulated by multiple genetic factors and signalling mechanisms. Destroying biofilm structure is important for promoting the effective treatment of non-healing chronic wounds. However, there is yet to be a reliable point-of-care diagnosis method for detecting biofilm at a very early stage. For the future development of chronic wound healing, timely monitoring of biofilm formation should be included to assist with further interventions.

1.2.4 Therapeutic strategies for chronic wound healing

From the clinical perspective, chronic wound management focuses on the shield of the open wound site. One specific wound management system is called 'TIME'[130]; it has been usually used as a standard guide for chronic wound management, including four different parts as follows: 'T' for tissue, evaluation and debridement of the inactivated biological tissue is critical for the wound bed preparation and the very first step for tissue repair. It could be realised through low-frequency ultrasound implementation, surgical process and enzymatic reagents. 'I' for infection; in this step, some antibiotics are used to prevent infection and biofilm formation after appropriately clearing the wound site. 'M' for moisture balance, exudate is one of the essential components of the wound site; it is a reliable reflection of wound bed physiology. Wound moisture equilibrium is necessary for wound management; too much exudate causes surrounding skin damage, but less wound exudate is not beneficial for wound healing involving cellular activities. 'E' for epithelial, wound edge contraction during the wound healing process to reduce the exposed open wound area is a significant

signal for practical wound treatment evaluation. The steps in the TIME system are standard processes to manage wound healing sequentially and timely.

In the past few years, many novel therapy methods have been developed with a better understanding of the physiological details of chronic non-healing wounds; they can be generally divided into dressing-free methods and wound-dressing therapies.

Dressing-free therapeutic methods usually rely on drug delivery, like antibiotics, to achieve therapeutic effects[131–133]. Systemic administration has several disadvantages, such as the systemically administrated antibiotics hardly breaking down the biofilm structure at the wound site to initiate the healing process. Furthermore, the overall systemic administration shows lower accuracy on specific target binding, leading to adverse effects due to the overall circulating process.

Because of the low effectiveness and potential adverse effects of systemic administration, local therapeutic methods are now the most accepted intervention for cutaneous chronic wound healing. In this case, drugs and several growth factors are used as the administration reagents for the localised treatment. To improve the drawbacks of the short half-life time of some delivered growth factors, more delivery systems, like encapsulation techniques using micro- or nanocarriers and nanoparticle modifications, are investigated to get a better therapeutic result and a longer active period.

Another widely accepted therapeutic method for open chronic wounds is skin grafting[134, 135], which helps to reconstruct different kinds of skin defects and is considered the gold standard for the care of most injuries, especially thermal-caused trauma. When the grafted skin contains the whole epidermis and part of the dermis, that is called a split-thickness skin graft (STSG). They are usually used for injury with large open areas and do not need a well-established vascular system to survive. Still, they suffer from tissue contraction during the healing process. Another graft constituted by the epidermis and the whole dermis is called full-thickness skin graft (FTSG); they require a better vascular system condition in the grafted zone but contract less during the healing process, so they are the better choice for the exposed areas of the body. Skin grafts can come from the same patient, called autografts, from dead or alive patients, that is, allografts, or from other animals that are xenografts. All these skin grafts are restricted by limitations to some extent, such as high cost and inevitable host immune rejection.

The conception of wound dressing therapy[136–139] has become mainstream due to the fast development of material science; they can be classified into different categories according to different characterisations. In the beginning, conventional wound dressings focus on the bleeding stopping; they promote the healing process in a passive method; the main characterisations of the conventional patches are protecting the open wound site from

external stress, keeping the moisture condition of the wound site, manage the exudate in a suitable level, and preventing infection.

However, in recent years, the wound dressing design has evolved due to the new theory that a moist environment is beneficial for wound healing processing[140, 141]. So, the most used materials for chronic wound dressing turn into absorbent materials, such as hydrocolloids and hydrogel; both are effective for maintaining a high moisture wound environment because of their strong absorb capability, but they tend to create a hypoxia environment and excessively moisture condition increase the risk of infection potentially. Other common dressing materials are foam and film[139, 142–144]; they are generally easy to manipulate and permeable to gas exchange, especially the foam, which can easily fit with wound shape and be left there for up to seven days.

Considering that the wound healing process is a complicated and well-organised process with several different cellular events happening simultaneously, the healing extent mainly depends on many factors, like wound status, health conditions of the patient, selected dressing and therapeutic methods used. The single functional passive wound dressing cannot meet all demands to manage and intervene in the wound healing process in a timely response way. Thus, drugs, antibiotics and several growth factors are combined with different polymeric wound dressings to accelerate the healing. Moreover, an ideal wound care device is expected to have these significant features: 1) keep a suitable moisture and clean environment, 2) prevent the open wound from secondary mechanical or bacterial infection, 3) show good gas exchange capability to keep the wound site fresh, 4) deliver practical therapeutic components to promote the healing process in both spatial and temporal manner, which means the simple assembled wound dressing still faces with a significant demand on improving the diagnosis, continuing monitoring and a timely feedback to reveal the specific process, giving the suitable intervention decision making. The next-stage smart bandage[145–148] for chronic wound healing is expected to integrate the multi-zone sensing function, on-demanded therapeutic function, signal reading and transmission in a single platform to realise a close-looped multifunctional health care process (**Figure 1.7**).

Generally, in this specific field, some critical points still need to be taken into consideration and improved: 1) Suitable substrate materials[149], as the chronic wound is presented as the damaged skin structure, so the wound dressing is used as a temporary skin to cover the wound and provide protection to against the external infections. Among all previously mentioned materials, hydrogels have gradually become the most competitive candidates because they usually show good performance on biocompatibility, hydrophilicity and intrinsic three-dimensional network structure much closer to the original extracellular matrix (ECM); all these features make them get the attention of researchers. 2) Microenvironment management

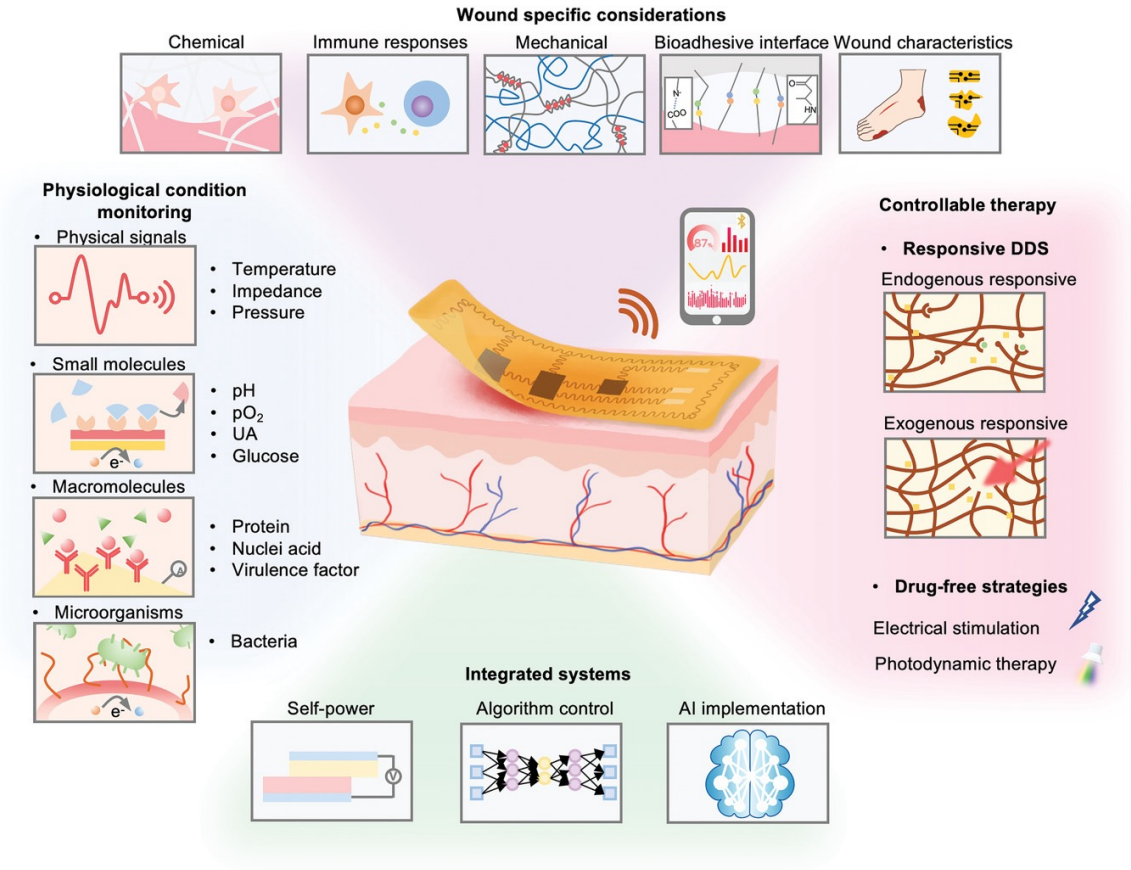

Fig. 1.7 Schematic illustration of wearable bioelectronics design for wound biosensing and on-demand therapy administration, including specific wound conditions, necessary vital/physiochemical signal monitor, controllable therapeutic methods and predictive modulates integration. (Figure adapted from reference[11].)

with the multiplexed sensing[150, 151] part: previously, wound dressing covered the wound site for protection and allowed the healing process to proceed in the 'black box'. As the healing process is dynamic and complex, the information from every specific healing status is vital for next-step decision-making. Moreover, chronic wounds show different statuses compared with normal tissue, such as the pH being naturally acidic in intact skin, with a value between 4.0 – 6.0, and the tissue underlying skin showing a more neutral pH value of 7.4. When injured tissue is infectious, the pH value could elevate to 10[152]. Temperature change and oxygen concentration at the wound site could also reflect the wound status to help heal. Apart from these physical indicators, many growth factors and cytokines secreted during the immune response also matter when evaluating the healing stage. 3) Therapeutic approach: Proper and timely drug delivery to the wound site is critical to accelerating healing. However, the old passive delivery methods are incapable of adjusting the release scheme

automatically. So, the actively responsive therapeutic methods are expected to be integrated into the platform to meet the requirements of precise treatment of different stages and avoid the potential drug resistance caused by overdose. 4) Closed-loop[153] health care system: guided by the breaking-through development of the algorithm and network, a closed-loop system is possible for the integrated wound healing bandage. Under this scheme, four indispensable components are included: a) the multiplexed biosensor module works for the signal collection, b) well-trained algorithms for input signal analysis and transduction, c) an on-demanded[154] therapeutic system to initiate the suitable intervention, d) wireless communication for data collection and transmission. All these features, combined with the progressing fabrication techniques, give a chance to achieve an ideal remote, personalised and precise wound care.

1.3 Graphitic carbon nitride (g-C_3N_4) material

High demands for energy lead to large consumption of fossil fuels; these traditional energy sources are not environmentally friendly, thus further causing environmental damage, global warming and climate change. In this situation, solar energy conversion provides a green and promising solution because of the possibility of being sustainable, clean, and having unlimited characterisations. In addition to the abundant solar light as the driving force, photocatalysis requires an effective semiconductor to proceed with the catalytic reactions[155–157].

Graphitic carbon nitride (g-C_3N_4) material has attracted much attention due to its tunable optoelectrical properties and metal-free semiconductor[158]. Bulk g-C_3N_4 is analogous to graphene in the layer-by-layer structure, which is attached to weak Van der Waals force and easily exfoliated by external forces. g-C_3N_4 material is easily prepared by several nitrogen-containing precursors such as melamine, dicyandiamide, cyanamide, urea, thiourea and ammonium thiocyanate through thermal polymerisation. The molecular structure of g-C_3N_4 mainly consists of two different units[159–161], tri-*s*-triazine (C_6N_7) or *s*-triazine (C_3N_3) rings connected via tertiary amines (**Figure 1.8**). From the energy theory perspective, tri-*s*-triazine is considered the most stable structure under ambient conditions. Unlike graphene, graphitic carbon nitride contains carbon and nitrogen, which are sp^2 hybridised, forming an π-conjugation graphitic plane. Studies prove that prepared g-C_3N_4 shows a 3D configuration with misalignment of tri-*s*-triazine-based layers; this misalignment helps eliminate the π-electrons induced repulsive forces in adjacent layers.

Graphitic carbon nitride materials also show excellent electric properties due to their π-conjugated delocalised system formed by the hybridisation of carbon and nitrogen. As a typical n-type semiconductor, g-C_3N_4 material could also be explained through the band gap

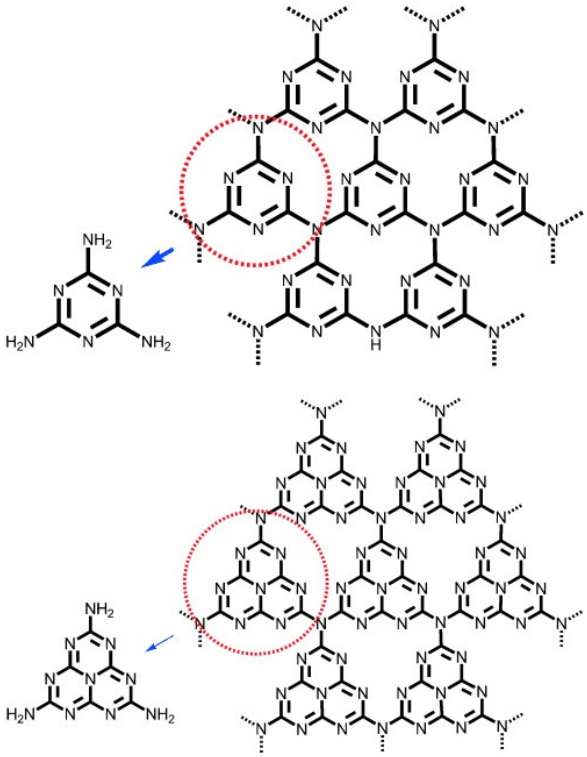

Fig. 1.8 Building blocks of g-C_3N_4: *s*-Triazine (top) and tri-*s*-triazine (bottom). (Figure adapted from reference[12].)

theory[158]; the bandgap is usually defined as the void region between the top of the filled valence band (VB) and the bottom of the vacant conduction band (CB), according to the calculation from Density Functional Theory (DFT), the bandgap of g-C_3N_4 is about 2.7eV, with the edge of the conduction band and valence band lying at -1.0V and +1.6V (vs. NHE) respectively, which enables light absorption of g-C_3N_4 up to 450nm to 480nm, located in visible light region in the spectrum.

All these factors allow g-C_3N_4 to be photosensitive, which means that the photo-induced electron-hole pairs[162, 163] could initiate the oxidation and reduction reactions with the reactants from the surrounding environment. The photo-excited electron-hole pairs generation process or the basic photocatalytic process of g-C_3N_4 material could be generally described as following steps: At the beginning, a photon with energy equal to or even more significant than the energy of the bandgap is absorbed, this action results in the excitation of an electron from the valence band to the conduction band, leaving behind an empty state which is present as a positive hole. Once they are separated spatially, the specific charge carriers under the excited states migrate to the g-C_3N_4 surface, initiating the redox reactions for the photocatalytic conversion of attached reactant molecules. The activated reactive sites could be either on the g-C_3N_4 surface where the photoexcitation occurs immediately or across another

semiconductor's or its cocatalyst's interface. However, g-C_3N_4 material could be chemically stimulated only when the photo-induced electron-hole pairs are consumed efficiently before recombination occurs within almost nanoseconds. Noticeably, only the successfully migrated charge carriers meet with acceptor molecules, which leads to the reduction and oxidation process. Alternatively, they could also get back to the de-excited status through several recombination processes, including surface recombination, which occurs on the particle surface, and volume recombination, which occurs on the way of migration.

The recombination process always hinders the photocatalytic efficiency; when this happens, the excited electrons fall back to the valence band, dissipating the extra energy through the formation of heat instead of reacting with molecules near the g-C_3N_4 surface. Thus, several requirements are critical for an effective photocatalyst: 1) light absorption in a wide range: They should have a suitable bandage to absorb light in a broader spectrum and an intrinsic high absorption coefficient to converse the energy from absorbed incident light. 2) Efficient charge carrier generation and separation: The material is capable of generating enough electron-hole pairs efficiently once the light is absorbed, relying on its high quantum efficiency (QE), then minimizing the recombination of photogenerated electron-hole pairs and getting efficient charge carrier transfer and migration, which requires the high conductivity of materials. 3) Chemical stability: The material should remain stable under irradiation without severe degradation and resist oxidation or other chemical reactions that may occur during the photocatalytic process.

Thus, different methods are used to modify or improve the performance of g-C_3N_4 to get a better photocatalytic property. Exfoliation is one of the standard methods; In this way, the low force of Van der Waals is broken between every single layer, and then the layer-by-layer attached structure (three-dimensional) of bulk g-C_3N_4 material would be transformed into two-dimensional, such as nanosheet even quantum dots, this helps the g-C_3N_4 materials get a large surface area and give more chance for reactions to occur. The shortened diffusion path length essentially decreases the recombination rate, which improves the electronic properties of g-C_3N_4.

The g-C_3N_4 materials provide a promising solution to meet the sustainability requirements as a metal-free semiconductor, but it still has some drawbacks, such as structural disorder and poor dispersibility. Thus, some strategies were explored to combine carbon nitride material with polymers to generate a g-C_3N_4/polymer combination (**Figure 1.9**). The formation of the hydrogel can broaden the applications of g-C_3N_4 material or introduce new properties. At the same time, the incorporated g-C_3N_4 material can also modify the chemical and mechanical properties of the formed polymer. In general, the present investigation of g-C_3N_4/polymer cooperation mainly through four methods: 1) g-C_3N_4

acts as the photo-initiator in the polymerisation system, 2) polymer-modified g-C_3N_4 to improve the dispersibility, 3) g-C_3N_4/polymer hybrid materials prepared via physical bonding and 4) g-C_3N_4 based hydrogels. The related g-C_3N_4/polymer hybrids research is still in an early phase, and most of the research about g-C_3N_4 materials is mainly focusing on biosensing[164, 165], photocatalysis[166], and photovoltaics[167] areas. Some preliminary biomedical studies[168, 169] involving drug delivery and bioimaging are entirely based on two-dimensional g-C_3N_4 materials and are always limited by complicated modification techniques. The research of g-C_3N_4 materials in biomedicine is still in its infancy; more efforts for exploration could be put into it.

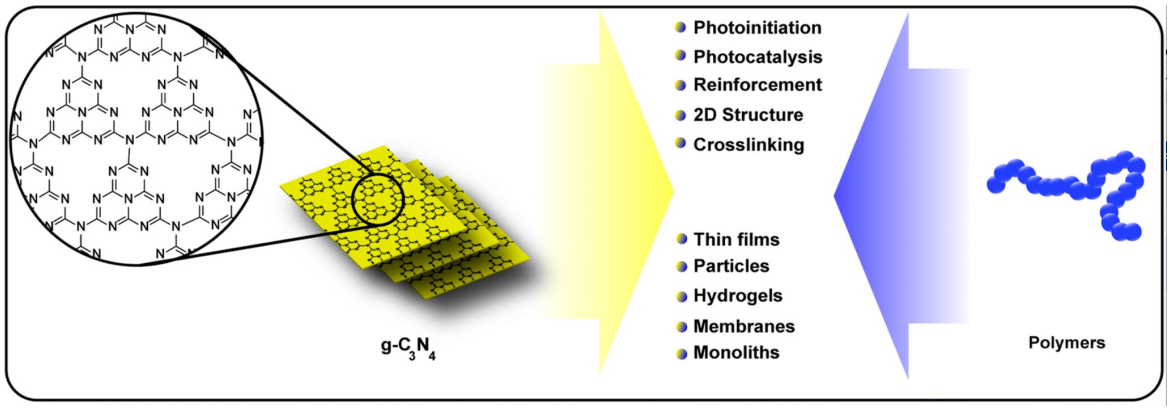

Fig. 1.9 Structure of g-C_3N_4 and polymers (top) functions of g-C_3N_4 in g-C_3N_4/polymer combination and (bottom) possible morphologies of g-C_3N_4/polymer. (Figure adapted from reference[13].)

1.4 Reactive oxygen species (ROS) and redox medicine

1.4.1 What are reactive oxygen species (ROS)?

Free radical or radical species are specific species that could exist independently with one or more unpaired electrons in their outer orbit. Their unpaired electron could be generated by the loss or gain of a single electron from another non-radical species; the free radicals are easily generated when a covalent bond is broken by homolytic fission. They are highly reactive due to their unpaired electron and can trigger chain reactions with contacted molecules to generate more byproducts of radicals or non-radicals (**Figure 1.10**).

Reactive species is a broader term, a relative conception, including free and non-free reactive radicals. They are a large family that includes reactive nitrogen, sulfur, carbon, selenium, electrophile and halogen species; all of them can undergo redox reactions and

induce oxidative effects[170] on different biological macromolecules, participating in redox signalling and biological processes.

Reactive oxygen species (ROS)[171] could be considered a subset of reactive species; they come explicitly from O_2, which shows much higher activity than O_2. ROS includes oxygen-centred free radicals and some non-radical derivatives from O_2. Hence, all oxygen radicals are ROS, but not all ROS are radical species.

Based on our work, we will mainly focus on specific ROS, including superoxide anion, hydrogen peroxide, hydroxyl radical (**Figure 1.10**), and singlet oxygen molecules. Superoxide anion and hydroxyl radicals belong to free radicals with only one single electron, while hydrogen peroxide and singlet oxygen molecules are non-radical ROS with two paired electrons.

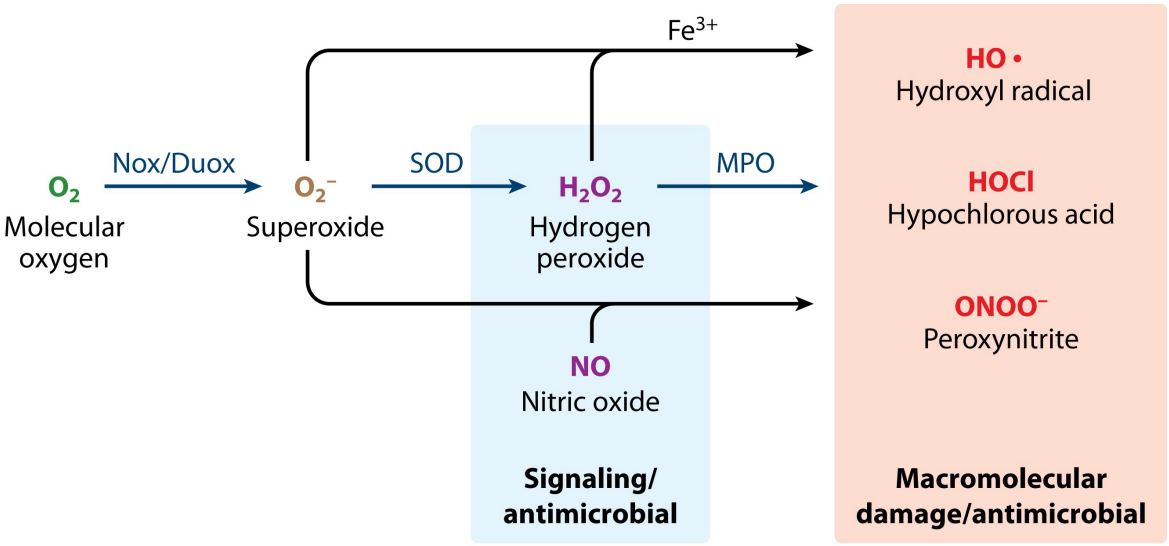

Fig. 1.10 **Mechanism of reactive oxygen species (ROS) generation.** Superoxide anion ($O^{\cdot -}$) can be generated from both NADPH oxidase (Nox) and dual oxidase (Duox) enzymes. Hydrogen peroxide (H_2O_2) will follow formed from two molecules of superoxide anion via a dismutation reaction, which can be accelerated by the superoxide dismutase (SOD) enzyme. Then, the hydroxyl radicals ($\cdot OH$) can be formed once the H_2O_2 encounter iron-sulfur cluster or transition ions through the metal-catalysed reaction. While other reactive species, such as hypochlorous acid (HOCl), Nitric oxide (NO) and peroxynitrite ($ONOO^-$) will also formed as by-products. The colour indicates the relative activity of corresponding molecules: green, unreactive; brown, low reactivity; purple, moderate reactivity; red, high reactivity and damage with no specificity). Abbreviations: myeloperoxidase (MPO). (Figure adapted from reference[14].)

Superoxide anion ($O^{\cdot -}$) is formed by one-electron reduction of O_2 through electron transport chains (ETCs), which usually happens in mitochondria, endoplasmic reticulum

and plasma membrane, and sometimes it is also formed by enzymes[172]. Its negative sign indicates that it is an anion. Superoxide anion is the first product of various metabolic processes[173]. Due to its high reactivity, it exists at deficient concentrations, but cells usually keep a low superoxide anion concentration to prevent oxidative damage. Its cell concentration is commonly between nanomolar to micromolar, depending on the specific cell type; generally, it is between 1-10 nM under normal physiological conditions[174]. One of the significant consumptions of superoxide anion is dismutation with another superoxide anion to generate O_2 and H_2O_2 spontaneously. Superoxide dismutase (SOD) is the involved enzyme that usually accelerates this process.

Hydrogen peroxide (H_2O_2) acts as a pleiotropic oxidant signalling agent[175] in physiological processes. It is a two-electron oxidant, showing relatively stable properties compared to other ROS, except when encountering specific protein Cys proteins, which participate in selective and specific signalling[176].

Hydroxyl radical ($\cdot OH$) is the most reactive biological oxidant with an unpaired electron; it is the reduction product from H_2O_2 involving metal-catalysed Fenton chemistry with free iron. Hydroxyl radicals exist for an extremely short time, and the unpaired electron renders it highly reactive and oxidises all biomolecules at a diffusion-controlled rate; it is the main reason for lipid peroxidation. Different from other ROS species mentioned above, singlet oxygen is an electronically excited species of O_2 generated by energy transfer from ultraviolet or visible light with a suitable sensitiser. It also shows a high level of reactivity and is easy to react with unsaturated organic molecules, such as lipids and some amino acids[177].

Sources of reactive oxygen species

Chemically, the formation of ROS species relies on UV irradiation or other electron reduction processes of oxygen initiated by transition metals or reducing radicals. The biological sources of ROS could be endogenous or exogenous.

In the endogenous approaches[178–180], phagocyte NADPH oxidases were the first identified enzyme system that generates ROS primarily, not just as the byproducts. This ROS generation system in mammalian cells was the NOXs of phagocytes (Phox), mainly including neutrophils and macrophages, which initiates the respiratory burst. This oxidase will only be activated by exposure to microorganisms or inflammatory mediators, generating ROS without mitochondria involved.

NOX1 is the first homologue of gp91phox (NOX2)[181–183], discovered in 1999. This enzyme came from a colon epithelial cell complementary DNA library. NOX1 generates a low amount of ROS when expressed in cells, but once it co-expresses with a novel regulatory subunit, a large amount of ROS will be produced. NOX1, NOX3 and NOX4 are almost the

same as gp91phox (NOX2) in size and structure; they all have significant electron transfer centres that could deliver the electron from NADPH to molecule oxygen to produce superoxide. NOX5 have an amino-terminal calmodulin-like domain on the base of the gp91phox structure, which contains four extra calcium binding sites.

The specific process of ROS generated from NADPH starts from activating NADPH oxidase; NOX is a typical transmembrane enzyme consisting of catalytic and regulatory subunits. It is usually activated by the stimulations from growth factors, cytokines and stress signals. During activation, the cytosolic regulatory subunits combine with the membrane-bound catalytic subunits. After this, the NADPH will bind to the catalytic subunit of the assembled NOX complex, donating two electrons to convert NADPH to $NADP^+$ and release one single proton. The transferred electrons reduce molecular oxygen into superoxide anion, as the primary product of NADPH involved enzymatic pathway. Besides this, it is well established that the mitochondria[183] are another significant source of cellular ROS. The generation of ROS in mitochondria occurs primarily within the oxidative phosphorylation process in the electron transport chain (ETC). The production of ROS that occurs in ETC is caused by premature leakage of electrons, which do not follow the typical transfer sequence but directly leak out of the ETC and interact with molecular oxygen to generate superoxide, which is further dismutase into hydrogen peroxide (**Figure 1.11**).

The mitochondrial electron transport chain of mammalian cells (ETC) consists of complexes I-IV, ubiquinone electron transporter, and cytochrome *c*. Complex I has two identified superoxide anion generation sites, site I_F (FMN site) and site I_Q (CoQ binding site); with the forward transfer of two electrons from NADH, the ubiquinone (CoQ) is fully reduced into ubiquinol (QH_2), the leaked electron during this process reacts with oxygen to generate superoxide anion. Another mechanism of superoxide anion generation in Complex I relies on reverse electron transport (RET). When the Q pool is highly reduced, and the local O_2 tension is high, the energy is high enough to drive electron transport against the redox potential gradient of ETC and the electrons are forced back from ubiquinol to complex I. Complex II generated ROS at site II_F, related to succinate dehydrogenase. However, the ROS generated from site II_F under normal conditions is negligible. Complex III is another ROS-dominating generator within ETC, specifically at the site of QH_2 oxidation. Two electrons were carried by QH_2 when it binds to complex III; then they are transferred in the order of QH_2 to the Rieske Fe-S cluster and then to cytochrome *c*. One stays on the Q cycle to form a transient formation of semiquinone radical, which further reacts with oxygen to generate a superoxide anion. ROS generated by complex III and other related enzymes are usually released into the mitochondria matrix and the intermembrane side.

In addition to NOX, ETC, ROS is also generated by other enzymes in subcellular local-

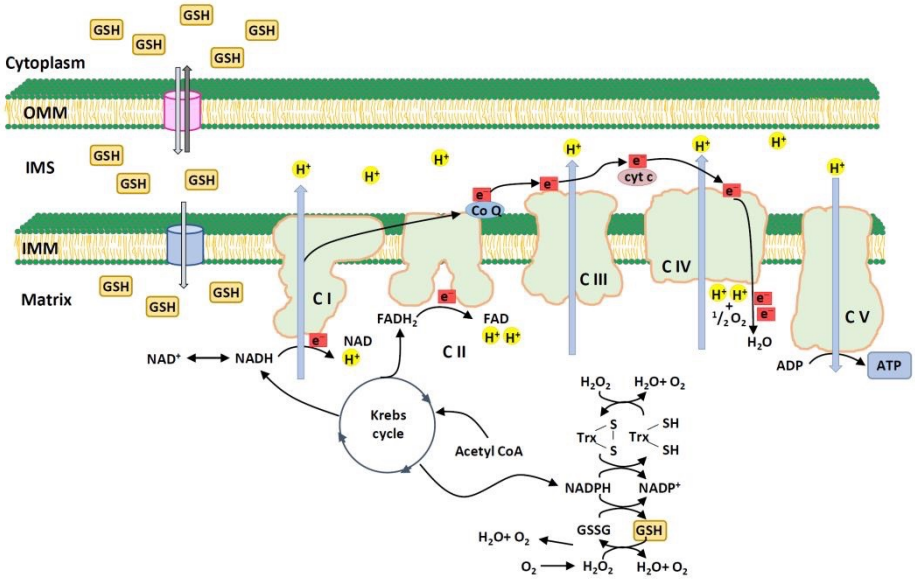

Fig. 1.11 Reactive oxygen species (ROS) from mitochondrial oxidative phosphorylation process, which occurs in the electron transport chain (ETC) located in the inner mitochondrial membrane. This process includes protein complexes I, II, III, IV, and V and two electron carriers – CoQ and cyt *c*. Electrons from NADH are transferred to CoQ by complex I. Complex II transfers the electrons from succinate to CoQ, and complex III transfers all electrons from CoQ to cyt *c*, then complex IV continues to transfer the electrons from cyt *c* to molecular oxygen and reduces it into water. Complex V (ATP synthase) is responsible for ATP production, it uses the energy generated from complex I – IV to drive the phosphorylation of ADP to ATP. Abbreviations: CoQ, coenzyme Q; cyt *c*, cytochrome complex; NADH, reduced form of nicotinamide adenine dinucleotide; ADP, adenosine adenosine diphosphate; ATP, adenosine triphosphate; OMM, outer mitochondrial membrane; IMS, inner mitochondrial space; IMM, inner mitochondrial membrane; GSH, glutathione; FAD, flavin adenine dinucleotide; NADPH, reduced form of nicotinamide adenine dinucleotide phosphate. (Figure adapted from reference[15].)

izations, such as the endoplasmic reticulum (ER) and peroxisomes or by several superoxide dismutase enzymes (SOD1-SOD3).

1.4.2 Reactive oxygen species (ROS) functions in wound healing process

In recent years, increasing studies have revealed that ROS acts as critical second messengers[184–186] involved in many different intracellular events, such as oxidative mechanisms, essential in immune system function, especially wound healing. They act as critical signal mediators and become involved in many complicated processes.

The wound healing process usually involves a sophisticated combination of reconstruc-

tion and degradation processes with various cellular events. ROS could mediate them to seal tissue and fight bacterial infection sequentially. Many immune cells and proteins react during wound healing in the initiated immune reaction and inflammation phase. ROS can act as signaling molecules and host defense mediators such as these secreted proteins, such as cytokines and growth factors. A basic level of ROS within the wound is beneficial for the healing process, especially the migration and proliferation of keratinocytes, which is promoted by the low level of H_2O_2 through the activation of the MAPK/ERK pathway[187, 188]. Fibroblasts, which play an essential role in wound healing by their proliferation and secreting collagens to promote matrix deposition, are also affected by ROS. Studies show that ROS could mediate the phenotype of fibroblast differentiation in myofibroblast by influencing p38 and JNK signaling cascades[189, 190].

Although overdosed ROS can cause irreversible tissue damage and long-term inflammation, maintaining a baseline ROS level is critical to rapid and efficient tissue repair. Thus, the optimal balance of ROS level and application period is crucial in wound healing management to synergistically regulate the antibacterial effect and tissue remodeling.

1.4.3 Research gap and challenges

Chronic wounds, including diabetic foot ulcers (DFUs) and pressure ulcers (PUs) are difficult to heal due to the external infections caused by alterations in the microenvironment, resulting in imbalanced anti-inflammatory / pro-inflammatory cytokine secretion and persistent inflammation stage. Furthermore, microorganism infection will also affect several cellular events, such as cell migration, proliferation, and angiogenesis, all of which hinder tissue remodeling and open wound closure.

In recent years, reactive oxygen species (ROS) involved in noninvasive bacterial inactivation and microenvironment reconstruction have become promising solutions for chronic wound environment management[191]. Combined with the development of hydrogel bandages, ROS-generating materials have attracted more attention because of their ability to kill bacteria through oxidative stress, regulate the healing process by modulating the balance of the anti-inflammatory and pro-inflammatory environment and promoting tissue remodeling. However, despite this remarkable progress, several key research gaps remain:

- Selectively kill bacteria without damaging surrounding healthy mammalian cells;
- Precisely controlled ROS generation and dosage optimization;
- Better understanding of specific ROS functions in the wound healing process;
- Biocompatible ROS-generating method exploration;

- Development of wearable devices with advanced therapeutic methods;
- Clinical translation from laboratory to real-world application

ROS-generating material shows a bright future for chronic wound management, but the challenges mentioned above still need to be solved. Based on these demands, the work presented in this thesis is aimed at addressing these research gaps and helping to accelerate the development of a next-generation comprehensive chronic wound management platform that acts ROS as both an antibiotic and a signaling factor.

1.5 Aims of this project

Aim 1: To develop the visible light photo-crosslinked hydrogel with graphitic carbon nitride (g-C_3N_4) material and characterize the essential properties.

Aim 2: To evaluate the formation of reactive oxygen species and their related interactions with cells.

Aim 3: To explore the selectively kill property in a cocultured group of bacteria and mammalian cells and identify possible damage targets.

In this work, g-C_3N_4 hydrogel as a chronic wound healing bandage material was evaluated from its intrinsic properties to its effects on encountered bacteria and mammalian cells systematically as shown in **Figure 1.12**.

The background investigation in **Chapter 1** gives a comprehensive understanding of diabetes mellitus-induced chronic wounds and their threat to both the public healthcare system and individuals, mechanisms of non-healing chronic wounds and roles of ROS in the wound healing process, revealing the existing challenges that need to be addressed, demonstrating the necessary of this research work.

In **Chapter 2**, experimental materials used in this work are described in detail, and all involved reagents and equipment are listed as well.

In **Chapter 3**, the polymerisation process of g-C_3N_4 hydrogel is explained, and the basic physiochemical and biocompatible properties of prepared g-C_3N_4 hydrogels are explored. In detail, a batch of g-C_3N_4 hydrogel including 0.1%, 0.2%, 0.4%, 0.6%, 0.8% and 1.0% of g-C_3N_4 material are prepared, the optical properties of g-C_3N_4 dispersion are confirmed to support the free-radical based polymerisation mechanism. The water retention capability and swelling ratio of g-C_3N_4 hydrogels are studied to verify the hydrogel performance as a wound bandage material. Finally, biocompatibility is demonstrated in different methods to prove its safety as a biomedicine material.

In **Chapter 4**, reactive oxygen species (ROS) generation from all prepared g-C_3N_4

hydrogel is quantified and the interactions between hydroxyl radical and bacteria/mammalian cell groups are investigated. Specifically, g-C_3N_4 hydrogel-generated ROS, including superoxide anion, hydrogen peroxide and hydroxyl radical, is quantified using the calibration curve obtained from chemical reactions. After this, the highly active species hydroxyl radical is selected as the target to figure out the viability change of bacteria and mammalian cell groups along the variations of intracellular hydroxyl radical concentration in different time scales.

In **Chapter 5**, ROS-induced selective killing of bacteria over mammalian cells is evaluated in an RFP-expressed E. coli/fibroblast cells cocultured model, biofilm eradication and essential mammalian cell functions after treatment are also evaluated in detail. Additionally, the possible interpretation of selectively killing is explored through the measurements of ROS attack targets in bacteria and mammalian cells.

Overall, this thesis proves the ability of g-C_3N_4 hydrogel to work as a chronic wound management material completely and comprehensively. The possible improvements and future work is then discussed in **Chapter 6**.

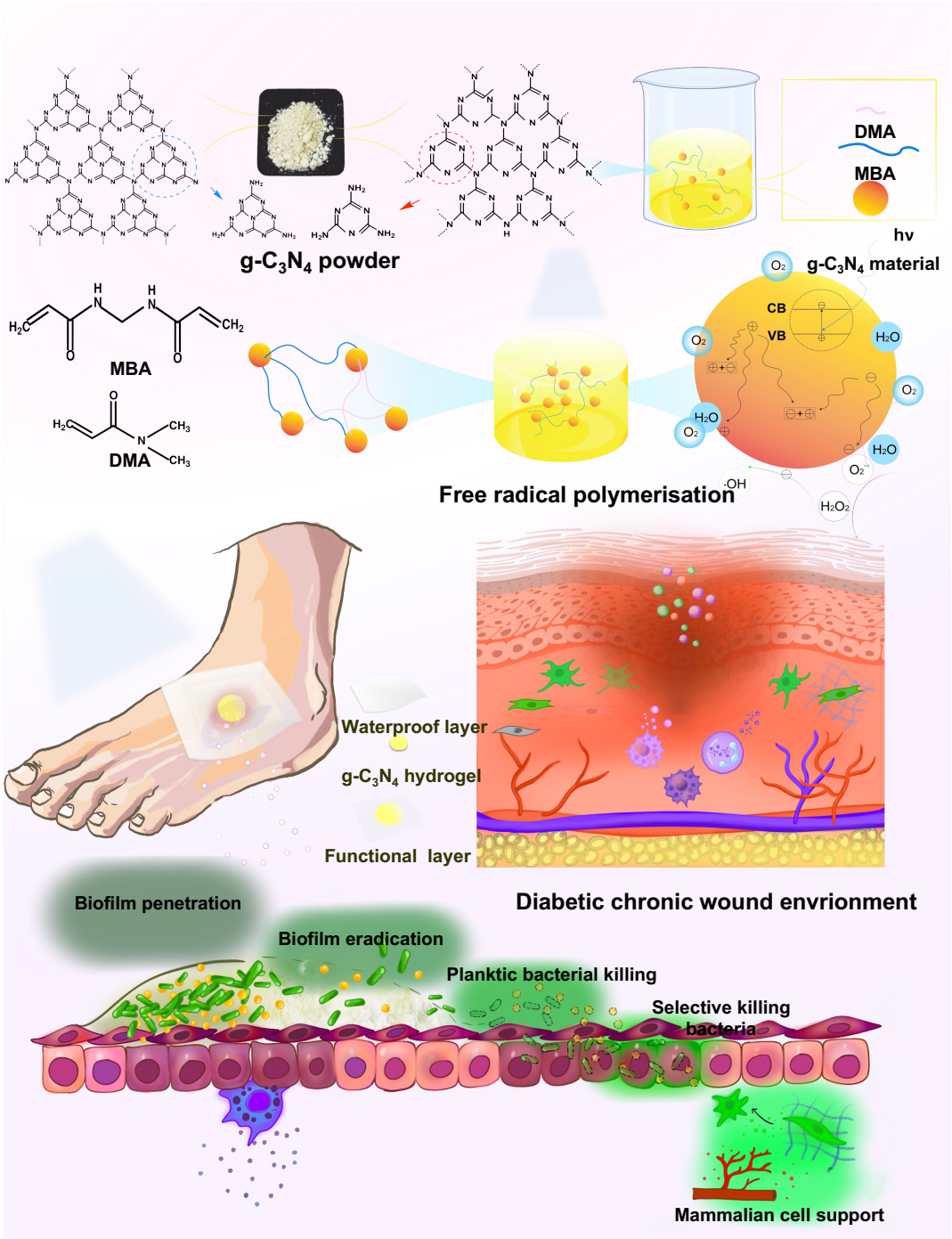

Fig. 1.12 Schematic of project. Abbreviations: DMA, *N,N*-dimethylacrylamide; MBA, *N, N'*-methylene-bis-acrylamide; g-C_3N_4, graphitic carbon nitride.

Chapter 2

Materials and Methods

2.1 Reagents and equipements list

Table 2.1 Experimental material list

Product	**Catalogue**	**Company**
Acrylamide	A3553	Sigma-Merck
N,N'-Methylene bisacrylamide (MBA)	146072	Sigma-Merck
Viability/cytotoxicity assay for bacteria	L7012	ThermoFisher
N,N-Dimethylacrylamide	274135	Sigma-Merck
Melamine	M2659	Merck
Cyanuric acid	8203580250	Merck
Xanthine	X7375	Sigma-Merck
Nitro Blue Tetrazolium	N5514-25TAB	Sigma-Merck
Iron(II) chloride-$FeCl_2$	372870	Sigma-Merck
Amplex™ Red Hydrogen Peroxide/Peroxidase Assay Kit	A22188	ThermoFisher
Coomassie Brilliant blue G 250	1.15444	Sigma-Merck
50% Hydrogen peroxide solution	516813	Sigma-Merck
LB Agar, powder	22700025	ThermoFisher
LB Broth Base	12780052	ThermoFisher
Brain Heart Infusion Broth	53286	Sigma-Merck
Brain Heart Infusion Agar	70138	Sigma-Merck
DAPI, FluoroPure™ grade	D21490	ThermoFisher
Rhodamine Phalloidin	R415	ThermoFisher
LIVE/DEAD™ Viability/Cytotoxicity Kit	L3224	ThermoFisher
2',7'-Dichlorofluorescin diacetate	D6883	Sigma-Merck
Xanthine Oxidase	X1875	Sigma-Merck

Table 2.2 Experimental material list-2

Product	Catalogue	Company
N-Lauroylsarcosine	61739	Sigma-Merck
Ammonium persulfate	A3678	Sigma-Merck
N,N,N',N'-Tetramethyl ethylenediamine	1.10732	Sigma-Merck
HPF	H36004	Thermofisher
N-Phenyl-1-naphthylamine	104043	Sigma-Merck
Polymyxin B sulfate salt	P4932	Sigma-Merck
ONPG	34055	Thermofisher
Anti-rabbit IgG (H+L) F(ab')2 Fragment	4412	Cell signalling technology
Phospho-Histone H2A.X (Ser139) (20E3) Rabbit mAb	9718	Cell signalling technology
Normal Goat Serum	5425	Cell signalling technology
CellMask™ Green Actin Tracking Stain	A57243	Thermofisher
NucRed™ Live 647 ReadyProbes™ Reagent	R37106	Thermofisher
HUVECs Basal Medium (formerly Medium 200)	M200500	Thermofisher
Large Vessel Endothelial Supplement (LVES)	A1460801	Thermofisher
Matrigel® Basement Membrane Matrix	356234	Corning

Table 2.3 Experimental equipment list

Product	Catalogue	Company
50 W COB Light Emitter	1DGL-JC-50W-CW	Amazon/CHANZON Store
Chanzon LED Driver 1500mA	B01N25KCGI	Amazon
Hammond RL6585BK Project Enclosure GPABS 175x125x100mm		
General Purpose Black	31-1513	Hammond
Heatsink with fan	158-540	RS Components
32 V power supply	124-4713	RS Components
12 V power supply	815-3124	RS Components
Fisherbrand™ Sterile Syringes	15859152	Fisher Scientific

2.2 Experimental methods

2.2.1 Agarose gel preparation

To obtain the 1% agar gel, acting as the blank control gel in the whole test, 0.1 g of ultrapure agarose powder (ThermoFisher) was dissolved in 10 mL deionised water. The solution was heated in the microwave, using higher mediate power. The solution status was

checked every 30 seconds, and the heating stopped immediately when the solution went boiling. Dissolved agar solution was transferred into 3 mL syringes as soon as possible. Leave the syringes at room temperature, waiting for their gelation. The agar gel was kept in deionised water and changed daily to keep it fresh and moist.

2.2.2 N, N-dimethylacrylamide (DMA) hydrogel preparation

Here the polymerisation system includes comonomers N, N-dimethyl acrylamide (DMA, Sigma, 0.962 g/mL) / N, N'-methylene-bis-acrylamide (MBA, Sigma, 0.008 g/mL), the redox couples are ammonium persulfate (APS, Sigma, 5.175 mg/mL) and N, N, N', N'-tetramethylethylenediamine (TEMED, Sigma, 0.78 g/mL). All the compositions were generally mixed and gelated at room temperature.

2.2.3 g-C_3N_4 precursor preparation

The g-C_3N_4 precursor can be prepared by the thermal condensation process using a lot of abundant and low-cost rich organic precursors, such as melamine, cyanamide, dicyandiamide and urea. Here, the precursors we used were prepared a modified literature procedure[192]. Melamine (5.0 g, 39.7 mmol) and cyanuric acid (5.0 g, 38.8 mmol) were mixed in 200 mL of deionized water, and then, the mixture was shaken overnight. Afterward, the precipitate was filtered and freeze-dried. The white solid was placed into a tube furnace and heated in nitrogen atmosphere to 550 °C for 4 h, with a heating rate of 2.3 °C /min . After cooling to ambient temperature, CN (1.9 g, 19%) was collected as a yellow powder.

2.2.4 g-C_3N_4 hydrogel preparation

For the g-C_3N_4 hydrogel formation, 0.06 g prepared g-C_3N_4 precursor powder was briefly added to 9.2 g distilled water and ultrasonic used 70% power for 30 minutes with ice bath protection to obtain a well-dispersed mixture. After this, 0.8 g N, N-dimethyl acrylamide (DMA) and 0.06 g N, N'-methylene-bis-acrylamide (MBA) were added in, mixing for 1 min; the mixture was then transferred into a tightly sealed container. Continuous N_2 was bubbled for 20 minutes. Here the continuous N_2 introduced into the polymerisation was aimed to remove the dissolved oxygen molecules as much as possible, protecting the generated electron-hole to activate the DMA radical, initiating the poly(DMA) chain grow and increase the polymerisation efficiency. After the N_2 flush, solutions were quickly transferred into a sealed polymerisation container and placed between the face-to-face LED (50 W) light sources to initiate the polymerisation process. Obtained g-C_3N_4 hydrogels were

immersed in deionised water for purification, changing the water daily for one week, until have no exfoliations dropped from hydrogels. For future experimental requirements, six concentrations of g-C_3N_4 hydrogels were prepared here: 0.1%, 0.2%, 0.4%, 0.6%, 0.8% and 1.0%.

2.2.5 Bacterial culture

E. coli - DH 5α

E. coli - DH 5α was cultured in LB Broth Base (Thermofisher) medium. For medium preparation, 20 g LB Broth Base powder was dissolved in 1 L distilled water; after it was dissolved, the medium was sterilised in an autoclave at 120 °C for 1 hour.

First, to recover the frozen *E. coli - DH 5α* bacteria from glycerol stock, the frozen bacteria from -80 °C was scrapped using a sterile loop without thawing the rest of the glycerol, then the picked bacteria was streaked on the prepared LB agar plate and incubated in the incubator at 37 °C overnight in an inverted position. The next day, from each of the streaked LB agar plates with the rehydrated strains, three separate *E. coli - DH 5α* colonies were picked by sterile loop and inoculated into three tubes of prepared LB Broth liquid medium by submerging the picked colonies in the sterile medium and the bacteria was dissolved by moving the loop up and down. These tubes were incubated in the incubator at 37 °C for 12 hours. Then, the prepared *E. coli - DH 5α* bacterial solutions were kept in a 4 °C fridge for future use.

Staphylococcus. epidermidis

S. epidermidis was cultured in Brain Heart Infusion (BHI) Broth Base (Millipore) medium. For medium preparation, 37 g BHI Broth powder was dissolved in 1 L distilled water and then sterilised by autoclaving at 121 °C for 15 minutes. First, to recover the frozen *S. epidermidis* bacteria from glycerol stock, the frozen bacteria from -80 °C was scrapped using a sterile loop without thawing the rest of the glycerol stock, then the picked bacteria was streaked on the prepared Brain Heart Infusion (BHI, Millipore) agar plate and incubated in the incubator at 37 °C overnight in an inverted position. The next day, from each of the streaked BHI agar plates with the rehydrated strains, three separate *S. epidermidis* colonies were picked by sterile loop and inoculated into three tubes of prepared BHI Broth liquid medium by submerging the picked colonies in the sterile medium. The bacteria were dissolved by moving the loop up and down. These tubes were incubated in the incubator at 37 °C for 12 hours. The prepared *S. epidermidis* bacterial solutions were collected and kept in a 4 °C fridge for future use.

Red fluorescent protein (RFP)-expressed *E. coli - DH 5α*

A glycerol stock of *pexp5*-plasmid transfected *E. coli - DH 5α* was kept at -80 °C freezer and inoculated into 5 mL of LB base liquid medium with 5 μL ampicillin solution (Sigma, 100 mg/mL), then this inoculated bacterial solution was cultured in an incubator at 37 °C, 200 rpm overnight. The collected bacterial solution was diluted into 1:100 in another 5 mL fresh LB base liquid medium with 5 μL ampicillin solution (Sigma, 100 mg/mL); continue culture another 4 hours in the incubator at 37 °C, 200 rpm, after this, 5 μL isopropyl-betaD-thiogalactopyranoside (IPTG, 1 M) was added in, culturing another 3 hours in the same condition. The prepared RFP-expressed *E. coli - DH 5α* bacterial solutions were collected and kept at 4 °C for future use.

2.2.6 Mammalian cell culture

hTERT Fibroblast cell culture

The hTERT fibroblast cells were used in this work; after obtaining the cryopreserved vial of hTERT fibroblast cells, the cells were thawed and recovered, then cultured and expanded to get stock. The cell culture medium was prepared with Dulbecco's Modified Eagle Medium (DMEM) in high glucose (4.5 g/L), with glutamine, phenol red, sodium bicarbonate, without sodium pyruvate and HEPES (ThermoFisher), then 10% Fetal Bovine Serum (FBS, ThermoFisher), 1% Penicillin Streptomycin (Pen/Strep, Gibco) were added to prepare completed medium. Following the standard cell culture, the fibroblast cells were cultured in a T-75 plastic cell culture flask in a humidified incubator at 37 °C, 5% CO_2 atmosphere.

HUVECs cell culture

The Human umbilical vein endothelial cells (HUVECs) were used in this work; the delivered cryopreserved vial of HUVECs was thawed in a water bath as quickly as possible; the cryopreservation solution was diluted with cell culture medium and then centrifuged and discarded. The cells were cultured and expanded to create a stock for subsequent experiments. Following the standard protocols for HUVECs culture, here the cell culture medium is Human Large Vessel Endothelial Cell Basal Medium (ThermoFisher) supplied with Large Vessel Endothelial Supplement (ThermoFisher); the cells were cultured in the plastic cell culture flask in a humidified incubator at 37 °C, 5% CO_2 atmosphere.

2.2.7 LED light source conditions

LED light assembly

LED light assembly g-C_3N_4 based hydrogel is polymerised through the free-radical polymerisation system; when the doped g-C_3N_4 material is worked as the initiator in this polymerisation system, then the wavelength of irradiation light source should match with the absorption wavelength. Here, the maximum absorption wavelength of g-C_3N_4 precursor powder was around 450 nm to 480 nm. As shown in **Figure 2.1**, the irradiation light source was assembled with chip-on-board (COB) light emitter components diode 50 W bulb and fan used as the cooling part. The polymerisation light system was two of these 50 W LED light sources placed face-to-face; the distance of the two LEDs was 20 cm to keep the distance between the light sources and the sample 10 cm.

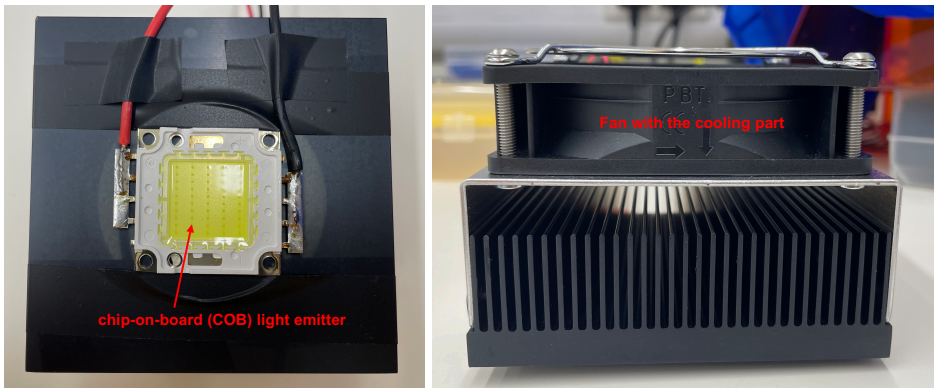

Fig. 2.1 Picture of LED light set-up used for experiments in lab.

The power density of LED light

As the energy of LED light usually decreases gradually along the direction perpendicular to the cross-section, the power density was measured using a power meter with the thermal power sensor detection head (Thorlabs, S425C). The specific power density of the LED light source was measured from 1 to 10 cm.

Temperature control of light source

This LED system is designed for the bacterial and mammalian cell test in the next step; thus, the temperature generated from the whole system is an essential factor to be considered. For the measurement, 2 mL of deionised water and DMEM cell culture medium were added to a multi-well plate. LED light was placed at a 10 cm distance, the same as the conditions

for the further cell experiment. The temperature variation was continuously monitored by the thermos-couple meter (PicLog) for 60 minutes.

2.2.8 Physicochemical properties of g-C_3N_4 hydrogel

Water retention capability of g-C_3N_4 hydrogel

Water content and water retention capability of all prepared hydrogel, including 0.2% agar gel, DMA hydrogel and g-C_3N_4 hydrogels with different content of g-C_3N_4 precursor (0.1%, 0.2%, 0.4%, 0.6%, 0.8% and 1.0%), was evaluated by leaving the water immersed cylinder-shaped hydrogels (diameter = 10 mm, thickness = 2 mm) to the environment with the 47% relative humidity (RH) and temperature at 21 °C. Then, their weight was recorded at every interest time point (0, 1, 2, 3, 4, 5, 6, 7, 8, 9, 10, 11, 12 and 25 hours) using an electronic scale, the water content of all hydrogels at a specific time is calculated using **Equation (2.1)** and the water retention rate of all tested hydrogels at every time is calculated using **Equation (2.2)**:

$$\text{Water content} = \frac{W_t - W_0}{W_t} \times 100\% \tag{2.1}$$

$$\text{Water retention rate} = \frac{W_t - W_0}{W_s - W_0} \times 100\% \tag{2.2}$$

Where W_0 is the weight of dried hydrogel disc.
W_t is the weight of hydrogel at every timepoints.
W_s is weight of swollen hydrogels.

Swelling capability of g-C_3N_4 hydrogel

To measure the swelling ratio of g-C_3N_4 hydrogels, all prepared hydrogels were cut into hydrogel discs (10 mm in diameter and 2 mm in thickness) and exposed to the open area with 47% relative humidity and 21 °C to get dried hydrogel. All of them were immersed in 5 mL of deionised water for 24 hours to get the equilibrium status; the deionised water was removed, all hydrogels were wiped gently with a tissue roll to remove extra attached water, and their weight was measured again using an electronic scale, the swelling ratio is

then calculated by **Equation (2.3)**:

$$\text{Swelling ratio}(g/g) = \frac{W_s - W_0}{W_0} \times 100\% \tag{2.3}$$

Where W_0 is the mass of dried hydrogel.
W_s is the mass of swelling equilibrium hydrogel.

2.2.9 Spectroscopic properties of g-C_3N_4 hydrogel

Absorbance wavelength of g-C_3N_4 dispersion

UV-Vis diffuse reflectance spectra were obtained using a UV-Vis spectrometer (Biochrom Ultraspec 9000) using the g-C_3N_4 dispersion and deionised water as the reference. The absorption of the g-C_3N_4 solution from 300-800 nm was measured in a 1 nm step.

The photothermal effect of g-C_3N_4 hydrogel

1 mL of deionised water and 0.4% g-C_3N_4 dispersion was added to the multi-well plate and irradiated using visible LED light (centre wavelength is 460 nm) at a 10 cm distance. During the irradiation period, the temperature change of deionised water and 0.4% g-C_3N_4 solution was continuously measured using a thermocouple meter (PicLog) every 1 minute for 60 minutes.

2.2.10 Intrinsic antibacterial properties of g-C_3N_4 hydrogel

S. epidermidis (ATCC 12228) and *E. coli - DH 5α* (ATCC 8739) were used to evaluate the intrinsic antibacterial properties of all g-C_3N_4 hydrogel; bacterial culture is described previously.

Bacterial growth curve measurement

For the continuous growth curve measurement, freezing bacterial strain was inoculated into 5 mL of fresh bacterial culture medium, Brain Heart Infusion (BHI) base for *S. epidermidis* and LB broth base for *E. coli – DH 5α*, 1 of the tested cylinder-shaped hydrogels with 10 mm in diameter and 2 mm in thickness was put into the bacterial culture medium as well. They were together cultured in the shaking incubator under 37 °C, 200 rpm, for 100 hours. The optical density of all bacterial solutions was measured using a UV-Vis spectrometer ((Biochrom Ultraspec 9000) at 600 nm at every specific time point; here are 0, 1, 2, 3, 4, 5, 10, 15, 20, 25, 50, 75 and 100 hours, every data was measured for three times.

Colonies forming units (CFU) counting

For assessment of colonies forming units (CFU), the exponential liquid culture of *S. epidermidis* and *E. coli – DH 5α* (OD_{600} = 0.8) from the samples mentioned above was diluted into 1:1000 with fresh bacterial culture medium; they were spreading on the BHI agar plate, and LB agar plate respectively, a bacterial solution without hydrogel immersed in was used as the negative control. After 20 hours of incubation under 37 °C, 5% CO_2 atmosphere, grown colonies were counted, and the survival ratio (SR) was calculated according to **Equation (2.4)**:

$$\text{Survival ratio}(\%) = \frac{CFU_t}{CFU_0} \times 100\% \tag{2.4}$$

Where CFU_t is the CFU number from specific tested hydrogel immersed bacterial solution. CFU_0 is the CFU number of bacterial cultured in the original bacterial culture medium.

Fluorescence imaging of Live /Dead bacteria

The bacterial live/dead viability direct contact with all hydrogels was further confirmed with fluorescence imaging. The frozen bacterial strain was inoculated into the liquid medium culture in the shaking incubator at 37 °C, 200 rpm overnight; all the bacterial solutions were collected at exponential phase and diluted into OD_{600} = 0.1. Prepared bacterial solutions were seeded into a 24-well plate and cultured in the incubator under 37 °C, 5% CO_2 environment for 4 hours to get the attachment. Then, the tested hydrogels were placed on top of the attached bacterial single layer, and all samples were put back into the incubator for another 24-hour culture. After this, tested hydrogels were removed, and bacteria were stained using LIVE/DEAD™ BacLight™ Bacterial Viability Kits according to the manufacturer's protocol. The Live / Dead stained cells were imaged immediately using a Zeiss inverted fluorescence microscope (Zeiss, Axvio Z1) with a 40× objective lens; the FITC filter was used to capture the live cell signals from green fluorescence and the TRITC filter for the red fluorescence, of dead cell signals. Random places were imaged for one sample to show the viability of bacteria after treatment.

2.2.11 Cytocompatibility of g-C_3N_4 hydrogel

The cytocompatibility test of g-C_3N_4 hydrogels was implemented in two schemes: 1) conditional medium culture and 2) direct contacts.

In the first scenario, the general idea was to prepare a conditional cell culture medium by immersing hydrogels in the fresh medium for various time points and then investigate the

medium for its influence on the cultured cells. Generally, at time zero, three circular g-C_3N_4 hydrogels were placed in a 25 mL complete cell culture medium (DMEM with 10% Fetal Bovine Serum, 1% penicillin/streptomycin and 1% L-glutamine).

They were placed in a 37 °C, 5% CO_2 environment. At every time point of interest, here is 24 hours and 48 hours, hydrogels were removed from the medium, filtered with 0.2 μm cellulose filter, then frozen in the freezer. After all test time points, a conditional medium was prepared, and the medium was thawed and used to culture the cell line for the following assays described below. Thus, the potentially harmful substances released from the g-C_3N_4 hydrogels are assessed in this cumulative pattern.

Indirect cytocompatibility - *PrestoBlue* test of fibroblast cells

PrestoBlue assay was used for measuring conditional medium cultured cell viability; the active ingredient is resazurin, a non-toxic, cell-permeable compound that is blue and originally non-fluorescent. Once entering the live cells, resazurin will be reduced to resorufin by the intracellular reducing environment, changing into red with high fluorescence. Viable cells continuously convert resazurin to resorufin, leading to an apparent medium colour change and fluorescence enhancement; therefore, cell viability could be measured by the change in absorbance wavelength or fluorescence intensity.

Briefly, for this indirect viability measurement of fibroblast cells, fibroblast cells were seeded in a 96-well plate in different concentrations of 0.1, 0.2, 0.4, 0.8, 1.6 and 3.2×10^4 cells per well in 100 μL of fresh complete medium for overnight to get attached cells. Then, the previous medium was discarded, and continuously, the cells were with the prepared conditional medium (24-hour conditional medium and 48-hour conditional medium) for another 24 hours. After this, the conditional medium was removed, and cells were incubated with the *Prestoblue* reagent and fresh medium in the ratio of 1:9 (10 μL of *PrestoBlue* reagent and 90 μL of fresh medium). Then, the samples were incubated in the incubator prevent from light irradiation for 30 minutes; results of viability were measured by fluorescence intensity, excitation wavelength of 560 nm and emission wavelength of 590 nm, or the absorbance of reagent at 570 nm, using BIOTEK microplate reader. The absorbance and fluorescence intensity of the sample without cells with 100 μL of *PrestoBlue* reagent were extracted from each sample to remove the background signal. The control group was treated with the fresh medium all the time. The cell viability was then calculated by the following **Equation (2.5)**:

$$Viability(\%) = \frac{A_t}{A_0} \times 100\% \tag{2.5}$$

where A_t is the absorbance of tested samples at 570nm.
A_0 is the absorbance of control samples at 570 nm.

Direct cytocompatibility – Live / Dead imaging of fibroblast cells covered by g-C_3N_4 hydrogel

After direct contact with all hydrogels, the fibroblast cell viability test was performed below. First, test cells were seeded in 24-well plate in 4×10^4 cells/mL per well cultured overnight to get attached to the cell layer; afterwards, all hydrogels were directly put on the top of the cell layer, co-incubating under 37 °C, 5% CO_2 atmosphere for interested time points. After this, test hydrogels were removed gently, and cells were washed with warm DPBS 3 times, then stained using LIVE/DEAD™ Viability/Cytotoxicity Kit for mammalian cells, following the protocol from manufacture, 0.5 μL of Calcein-AM stock solution and 1 μL of ethidium homodimer-1 was added into 1 mL of complete cell culture medium (DMEM, with 10% Fetal Bovine Serum, 1% Penicillin/Streptomycin and 1% Lgluamine). 200 μL of prepared Live/Dead work solution was added into samples and kept at room temperature for 30 minutes; then the dye solution was removed and washed with DPBS three times, and another 200 μL of fresh DPBS was added to cover the samples before imaging. Stained fibroblast cells were imaged immediately using a Zeiss inverted fluorescence microscope (Zeiss, Axvio Z1) with a 10× objective lens; FITC filter was used for the live cell signals from green fluorescence and TRITC filter for the red fluorescence of dead cell signals. Random places were imaged for one sample to show the general view of fibroblast cell viability after covering by the test hydrogels. Obtained images were analysed using Image J software.

2.2.12 Evaluation of mammalian cell functions after covered by g-C_3N_4 hydrogels

Migration of fibroblast cell

The migration behaviour of the hydrogel-covered fibroblast cells was tested using an *in vitro* wound healing assay. Briefly, the 80% confluency fibroblast cells were suspended in the complete cell culture medium (DMEM, with 10% Fetal Bovine Serum, 1% Penicillin/Streptomycin and 1% L-glutamine) at 3×10^5 cells/mL, and 70 μL cell solution was pipetted into each chamber of the cell culture insert (Ibidi, United Kingdom), the cell culture insert with cell solution inside was put back into cell culture incubator for overnight co-incubating. After this, the cell culture inserts were removed, a cell-free gap was formed, each sample was washed with warm DPBS three times, tested hydrogels were put in and covered

on the whole cell attached area, co-incubating in cell culture incubator was implemented for another 24 hours. After this, all tested hydrogels were removed, and cells were washed with warm DPBS and changed with a fresh, complete cell culture medium. After 12 hours, 24 hours and 48 hours of continuous culture, cells were stained with 2 μM Calcein-AM solution, cell migration status was observed using a fluorescence microscope with a 5$\times$ objective lens under the FITC channel, and images were analysed using Image J software.

Morphology of fibroblast cell

First, 80% confluence fibroblast cells were prepared into cell suspension in 4×10^6 cells/mL and seeded into a 24-well plate in 1 mL. Samples were cultured in the cell culture incubator (37 °C, 5% CO_2 atmosphere) for well attached. All tested hydrogels were put on top of the attached cell layer and co-incubated for another 24 hours in the incubator. After this, tested hydrogels were removed, and the cells were stained with Rhodamine-Phalloidin (Thermofisher) for the cell skeleton and DAPI (Sigma) for the cell nucleus. The previous cell culture medium was removed, and cells were washed with DPBS three times. Then, the samples were fixed using 3.7% methanol–free formaldehyde solution for 15 minutes at room temperature; after this, the samples were permeabilised in 0.1% Triton X-100 in PBS for 15 minutes, then 1% Bovine Serum Albumin (BSA Protein, Sigma) solution was added in to avoid non-specific background staining. After removing the BSA solution, diluted fluorescent Phalloidin (1:400) was added to cover the sample area and incubated at room temperature for 60 minutes. Rhodamine Phalloidin solution was removed, and samples were washed with DPBS three times; DAPI solution in 0.1 μg/mL was added and incubated for another 5 minutes to stain the cell nucleus. When staining processes were finished, samples were washed with fresh DPBS to reduce the background signal and immersed with another 500 μL of DPBS, imaging with a fluorescence microscope using a 20$\times$ objective lens, TRITC channel for a signal from cell skeleton and DAPI channel for a signal from the cell nucleus.

Tube formation of HUVECs

Another critical function of supportive mammalian cells is angiogenesis, which accelerates the wound healing process. Here, the angiogenic performance of Human Umbilical Vein Endothelial Cells (HUVECs) after being covered by all tested hydrogels was evaluated. Briefly, 100 μL of Matrigel (Corning, USA) in a fridge (4 °C) was pipetted into the 24-well plate to coat the bottom layer, followed by solidification at 37 °C for 1 hour. Then, 4×10^4 cells/cm^2 HUVECs suspensions were seeded onto the Matrigel-coated 24-well plate and tested hydrogels were added. Plates were then put back into a cell culture incubator.

After 6 hours, the HUVECs were stained with Calcein-AM solution for 30 minutes, and the capillary-like structures were observed using fluorescence microscopy (Zeiss, Germany) with a 5× objective lens. Generated branches and nodes were quantified by Image J software with six randomly selected fields.

2.2.13 Evaluation of bacterial and fibroblast cells adhesion on g-C_3N_4 hydrogel

The distance between bacteria / mammalian cells and our tested hydrogels is important for biocompatible performance and reactive oxygen species (ROS) interaction efficiency. Here, the adhesion and spreading of bacteria and fibroblast cells on prepared g-C_3N_4 hydrogels were evaluated through fluorescence imaging, respectively. For *E. coli - DH 5α*, the bacterial strain was inoculated into the liquid Luria-Bertani (LB) medium and cultured for 16 hours; the bacterial solution was collected and diluted into a ready sample solution with OD_{600} = 0.5. The fibroblast cells were cultured till 80% confluency and prepared into sample solutions at a density of 1×10^6 cells/mL. Then, all the tested hydrogels were placed into a 48-well plate, and the prepared bacterial and fibroblast cell solutions were added in; plates with samples were put back into a cell culture incubator for 24 hours co-incubating. After this, all bacterial / fibroblast cell solutions were removed and tested hydrogels were stained using Calcein-AM solution at room temperature for 30 minutes. Stained hydrogels with bacteria/fibroblast cells were observed using upright fluorescence microscopy (Zeiss, AxioObserver) with a 40× and 5× objective lens, respectively. All obtained images were quantified with Image J software.

2.2.14 Measurement of Reactive oxygen species (ROS) generated from g-C_3N_4 hydrogels

Reactive oxygen species (ROS) are the active molecules used in this project, so here, the specific hydroxyl radical (·OH), superoxide anion ($O_2^{\cdot}$) and hydrogen peroxide (H_2O_2), generated from prepared g-C_3N_4 hydrogels was measured quantitatively.

Measurement of hydroxyl radical (·OH)

Calibration of Hydroxyl radical (·OH) using chemical reaction

Hydroxyl radical (·OH) in calibration was implemented in three steps: (1) calibration of ferrous ions (Fe^{2+}) in 1-10 μM; (2) hydroxyl radical concentration confirms using Fenton

reaction; (3) hydroxyl radical concentration measurement using Coomassie Brilliant Blue (CBB) solution.

(1) Concentration of ferrous ions was confirmed using the 1,10-phenanthroline solution as the indicator; in addition to its ferrous ion (Fe^{2+}) form, iron also can exist in a ferric ion (Fe^{3+}) form. The complex formed by 1,10-phenanthroline and Fe^{2+}, ferrous tris (1,10-phenanthroline) iron (II) or $[Fe(phen)^3]^{2+}$, is a bright orange colour, showing apparent absorption at 520 nm. To keep the Fe^{2+} stable, hydroxylamine hydrochloride solution is added to reduce any Fe^{3+} in the solution to Fe^{2+} before adding the phenanthroline to form the complex.

(2) Fe^{3+} formed after the Fenton reaction is confirmed using the same colourimetric method; consumed Fe^{2+} could be calculated from the decreased absorption value.

(3) Generated hydroxyl radical could be measured by the Coomassie Brilliant Blue (CBB) degradation using the BIOTEK microplate reader at 588 nm.

For ferrous ion (Fe^{2+}) calibration, Iron (II) chloride tetrahydrate was used to prepare the ferrous ions solution from 1 to 10 μM; every 25 mL of ferrous ions solution was mixed with another 1 mL of 10% hydroxylamine hydrochloride solution, to keep the solution in reducing environment (**Equation 2.6**). After this, 2 mL of 0.12% o-Phenanthroline solution was added as the colourimetric indicator (**Equation 2.7**). The absorption at 510 nm of ferrous ions solution from 1 to 10 μM was measured using a BIOTEK microplate reader; every test was repeated three times.

$$2Fe^{3+} + 2NH_3OH^+ \rightarrow 2Fe^{2+} + N_2 + 2H_2O + 4H^+ \tag{2.6}$$

$$Fe^{2+} + 3\text{phen} \rightarrow [Fe(phen)^3]^{2+} \tag{2.7}$$

After this, ferrous ion solution and hydrogen peroxide solution were mixed in a ratio of 1:1.5 molar concentration to undergo the Fenton reaction (**Equation 2.8**); mixed reactants were placed at room temperature for 30 minutes to react completely, 0.12% *o*-Phenanthroline solution was added in and residual Fe^{2+} was evaluated using a microplate reader at 510 nm. The Fenton reaction generated a hydroxyl radical concentration similar to consumed ferrous ions. Then, another total same Fenton reaction (Fe^{2+} from 1 – 10 μM, Fe^{2+}:H_2O_2 = 1:1.5 in molar concentration) was reacted with 10 μM Coomassie Brilliant Blue (CBB) solution, absorption degradation at 588 nm, which is caused by hydroxyl radical oxidation,

ΔA (**Equation 2.9**) was measured to calculate the standard curve.

$$Fe^{2+} + H_2O_2 \rightarrow Fe^{3+} + {}^{\cdot}OH + OH^{-} \tag{2.8}$$

$$\Delta A = A_0 - A_t \tag{2.9}$$

A_0 is the original absorption of CBB solution at 588 nm.
A_t is the absorption of CBB solution at 588 nm after degrading by hydroxyl radical from Fenton reaction.

Quantification of *g-C_3N_4 hydrogel generated hydroxyl radical ($^{\cdot}OH$) generated from g-C_3N_4 hydrogels*

Hydroxyl radical generated from g-C_3N_4 hydrogels after light irradiation was measured in two different schemes: (1) continuous mode: continuous irradiation for 30, 60, 90, 120, 150 and 180 minutes; (2) ON-OFF-ON mode: irradiation for 30 minutes, turn off the light for 30 minutes, irradiating for another 30 minutes.

For the specific method to measure hydroxyl radicals from g-C_3N_4 hydrogels after irradiation, 10 μM of Coomassie Brilliant Blue (CBB) solution was also used as the indicator. Agar gel and DMA hydrogel were used as the control groups in all tested hydrogels. All tested hydrogel discs (10 mm in diameter and 2 mm in thickness) were immersed in 10 μM CBB solution; the samples were irradiated by our assembled LED light source from the top side at a 10 cm distance for interested time points. Absorption of CBB solution before and after irradiation was measured at 510 nm using a BIOTEK microplate reader, absorption change was calculated, and the specific hydroxyl radical concentration from every tested group was calculated using the calibration curve obtained before.

Measurement of superoxide anion ($O_2^{\cdot -}$)

Calibration of Superoxide anion ($O_2^{\cdot -}$)

Superoxide anion ($O_2^{\cdot -}$) calibration was performed using the enzymatic reaction of xanthine (X7375, Sigma) and xanthine oxidase (X4500, Sigma) as **Equation 2.10**. Generally, the xanthine was dissolved in 1 M NaOH to prepare a series of solutions in 15.63 μM, 31.25 μM, 62.5 μM, 125 μM and 250 μM; the corresponding superoxide anion was generated using xanthine oxidase, 1 mg/mL of Nitrobule tetrazolium (NBT) solution was used as the indicator, formed superoxide anion was then measured through the absorbance change at 560

nm.

$$\text{Xanthine} + \text{H}_2\text{O} + 2\,\text{O}_2 \xrightarrow{\text{Xanthine oxidase}} \text{Urine} + 2\,\text{O}_2^{\cdot -} + 2\,\text{H}^+ \tag{2.10}$$

Quantification of g-C_3N_4 hydrogel generated superoxide anion ($O_2^{\cdot -}$) generated from g-C_3N_4 hydrogels

Superoxide anion ($O_2^{\cdot -}$) generated from g-C_3N_4 hydrogels after light irradiation was measured in two different schemes: (1) continuous mode: continuous irradiation for 30, 60, 90, 120, 150 and 180 minutes; (2) ON-OFF-ON mode: irradiation for 30 minutes, turn off the light for 30 minutes, irradiating for another 30 minutes.

For the specific method to measure hydroxyl radicals from g-C_3N_4 hydrogels after irradiation, 1 mg/mL of Nitrobule tetrazolium (NBT) solution was used as the indicator. Agar gel and DMA hydrogel were used as the control groups in all tested hydrogels. All tested hydrogel discs (10 mm in diameter and 2 mm in thickness) were immersed in 1 mg/mL of NBT solution; the samples were irradiated by our assembled LED light source from the top side at a 10 cm distance for interested time points. After this, all tested hydrogels were immersed in the dimethyl sulfoxide (DMSO) solution overnight to release the formed formazan due to superoxide anion generation; the whole process needed to protect from light irradiation. After this, the absorption of released formazan in DMSO solution and pure DMSO solution was measured at 560 nm using a BIOTEK microplate reader, absorption change was calculated, and the specific superoxide anion concentration from every tested group was calculated using the calibration curve obtained before.

Measurement of hydrogen peroxide (H_2O_2)

Calibration of hydrogen peroxide (H_2O_2)

Hydrogen peroxide (H_2O_2) calibration was finished with a 30% H_2O_2 solution and the commercialised Amplex Red kit (**Equation 2.11**). Diluted H_2O_2 solutions in the 1 – 10 μM range were reacted with the Amplex Red work solution in 1:1 stoichiometry to produce the red-fluorescent oxidation product. The fluorescence signal of the reacted products reflected the H_2O_2 concentration.

$$\text{Amplex Red} + \text{H}_2\text{O}_2 \xrightarrow{\text{HRP}} \text{Resorufin} + \text{H}_2\text{O} \tag{2.11}$$

Quantification of hydrogen peroxide (H_2O_2) generated from g-C_3N_4 hydrogels

Hydrogen peroxide (H_2O_2) generated from g-C_3N_4 hydrogels after light irradiation was measured in two different schemes: (1) continuous mode: continuous irradiation for 30, 60, 90, 120, 150 and 180 minutes; (2) ON-OFF-ON mode: irradiation for 30 minutes, turn off the light for 30 minutes, irradiating for another 30 minutes.

For the specific method to measure hydrogen peroxide from g-C_3N_4 hydrogels after irradiation, the commercialised assay kit Amplex Red was used as the indicator. Agar gel and DMA hydrogel were used as the control groups in all tested groups. All tested hydrogel discs (10 mm in diameter and 2 mm in thickness) were immersed in 1 mL of deionised water; the samples were irradiated by our assembled LED light source from the top side at a 10 cm distance for interested time points. Deionised water in tested samples was immediately transferred into a 96-well plate and mixed with prepared Amplex Red work solution in a 1:1 stoichiometry to produce the red-fluorescent oxidation product, resorufin, which has excitation and emission wavelength around 571 nm and 585 nm. The fluorescence intensity caused by (H_2O_2) was measured using a BIOTEK microplate reader, and the specific (H_2O_2) concentration from every tested group was calculated through the calibration curve obtained before.

2.2.15 Bacterial cell number counting

All bacterial killing tests in the next step need to keep the same bacterial cell number in 1 $\times 10^8$ cells per sample. Thus, the relationship between the optical density of bacterial solution at 600 nm and specific cell number was evaluated in detail first. Briefly, *S. epidermidis* and *E. Coli – DH 5α* strain was inoculated and cultured in the liquid bacterial culture medium, continuous culturing for 16 hours at 37 °C, 200 rpm. After this, the bacterial solutions were collected and adjusted OD_{600} into 0.1, 0.2, 0.3, 0.4, 0.5, 0.6, 0.7, 0.8, 0.9 and 1.0. All these bacterial solutions were then spread onto prepared LB agar plates (for *E. Coli – DH 5α*) and BHI agar plates (for *S. epidermidis*), and then all agar plates were cultured in a cell culture incubator for 18 hours. Formed colonies form units (CFU) on every agar plate were counted, and the calibration curve was calculated. Every data was repeated three times.

2.2.16 Live / Dead calibration curve of bacteria and fibroblast cells

Live / Dead calibration curve for bacteria

30 ml cultures of either *S. epidermidis* and *E. coli – DH 5α* were grown in 30 mL until the late log phase in a liquid medium. 25 mL of cultured bacterial solution was centrifuged at

5000 rpm for 15 minutes. The supernatant was removed, and the cell pellet was resuspended in another 2 mL of 0.85% NaCl solution. 1 mL of this suspension was added into two falcon tubes containing either 20 mL of 0.85% NaCl (for live bacteria) or 20 ml of 70% isopropyl alcohol (for killed bacteria). Both samples were incubated at room temperature for 1 hour, mixing every 15 minutes. After incubation, both samples were pelleted by centrifugation at 5000 rpm for 15 minutes; then, the cell pellet was resuspended in two tubes of 10 mL 0.85% NaCl solution separately. Then, the samples were centrifuged again and resuspended in another two fresh 10 mL 0.85% NaCl solution separately. Standard sample solutions were prepared as follows (**Table 2.1**):

Table 2.4 Standard Live / Dead sample

Live percent	0%	10%	20%	30%	40%	50%	60%	70%	80%	90%	100%
Live sample	0	10	20	30	40	50	60	70	80	90	100
Dead sample	100	90	80	70	60	50	40	30	20	10	0

After this, all prepared standard Live / Dead samples were stained using commercialised LIVE/DEAD BacLight Bacterial Viability Kits, with 3.34 mM SYTO-9 solution for live bacteria and 20 mM Propidium iodide solution for dead bacteria. Briefly, 1.5 μL of SYTO-9 solution (3.34 mM) and 1.5 μL of Propidium iodide solution (20 mM) were mixed evenly for 1 mL of suspension bacterial sample, dye solution and standard bacterial solution were mixed thoroughly and then incubated at room temperature in the dark for 15 minutes. After staining, all standard bacterial solution samples were centrifuged at 14500 rpm for 5 minutes and resuspended in fresh DPBS solution; this step was repeated three times to wash the background signal in the sample solution. The fluorescence signal of all these standard samples was measured using a BIOTEK microplate reader; a fluorescence channel of 495 ± 15 nm was used for the SYTO-9 signal, and a fluorescence channel of 535 ± 15 nm was used for the PI signal; every data was repeated three times.

2.2.17 Antibacterial effects of ROS generated from different g-C_3N_4 hydrogels

g-C_3N_4 hydrogels were prepared with different g-C_3N_4 concentrations, including 0.1%, 0.2%, 0.4%, 0.6%, 0.8% and 1.0%. For the aim of selecting one best-performance g-C_3N_4 hydrogel, g-C_3N_4 hydrogels in all concentrations were used to interact with bacteria (*S. epidermidis* and *E. coli – DH 5α*) for 10 minutes and 60 minutes, live dead signal of bacteria were measured to evaluate the killing efficiency caused by g-C_3N_4 hydrogels. First, bacteria

(*S. epidermidis* and *E. coli – DH 5α*) were cultured following the previously mentioned method, and the bacterial cell number was adjusted into 1×10^8 cells per sample, according to the bacterial cell number counting curve in 2.3.16. 1×10^8 bacterial cells were resuspended in 1 mL of DPBS, and one g-C_3N_4 hydrogel disc (10 mm in diameter and 2 mm in thickness) was immersed in the bacterial solution; an LED light source was used to irradiate the sample from the top side at 10 cm distance, after 10 minutes and 60 minutes, all immersed g-C_3N_4 hydrogel discs were removed. Bacterial solutions were collected and centrifuged at 14500 rpm for 5 minutes; the cell pellet was resuspended in fresh DPBS and stained with commercialised LIVE/DEAD BacLight Bacterial Viability Kits, SYTO-9 for live signal and propidium iodide for dead signal, the fluorescence signal of all tested samples was measured using BIOTEK microplate reader, fluorescence channel of 495 ± 15 nm was used for SYTO-9 signal, Fluorescence channel of 535 ± 15 nm was used for PI signal, every data was repeated for six times.

The same test was also implemented on red fluorescent protein–expressed *E. coli – DH 5α* (RFP-*E. coli*), the same as before, RFP-*E. coli* was adjusted into 1×10^8 cells per sample, suspended in 1 mL of DPBS, and then tested hydrogels were immersed in these prepared bacterial samples, irradiating under an LED light source, at a 10 cm distance. After an interesting period, bacterial suspensions were collected and centrifuged at 14500 rpm for 5 minutes; the bacterial cell pellet was resuspended in fresh DPBS. The fluorescence intensity of red fluorescent protein from samples was measured using a BIOTEK microplate reader; 532 nm wavelength was used for excitation, and 588 nm wavelength was used for emission. Every data was repeated four times.

2.2.18 Fibroblast cells damage induced by ROS generated from different g-C_3N_4 hydrogels

To further test the influence of g-C_3N_4 hydrogel on fibroblast cells, fibroblast cells were cultured until 80% confluency and detached using trypsin-EDTA (0.25%). Then, the cell suspension was prepared in 1×10^6 cells per sample in DPBS. Fibroblast cell suspension and tested hydrogels were added to a 24-well plate. Samples were irradiated using LED light at a 10 cm distance for 10 and 60 minutes separately. After treatment, tested hydrogels were discarded, and fibroblast cells were collected, centrifuged at 14500 rpm for 5 minutes, and cell pellets were resuspended in another 1 mL of fresh DPBS. Collected fibroblast cell samples were stained using LIVE/DEAD®Viability/Cytotoxicity Kit for mammalian cells (L7012, Thermofisher), 2 μL of the supplied 2 mM EtdD-1 stock solution and 5 μL of the supplied 4 mM Calcein-AM stock solution was added into 1 mL of collected sample, cells

were then incubated at room temperature for 30 - 45 minutes, washed using fresh DPBS for three times. Fluorescence signals were measured using a BIOTEK microplate reader; the live signal was measured using 495 nm excitation wavelength and 515 nm emission wavelength, and the dead signal was measured using 535 nm excitation wavelength and 617 nm emission wavelength. Every data was repeated six times.

2.2.19 Quantification of intracellular hydroxyl radical concentration using HPF probe

To quantify the intracellular hydroxyl radical signal, which should be the main attack species responsible for bacterial killing, 3'-(p-hydroxyphenyl) fluorescein (HPF) (H36004, ThermoFisher) was used as the intracellular hydroxyl radical probe (20 μM), it can work in both extracellular and intracellular.

First, a new calibration curve was obtained using this HPF probe and a 1, 2, 3, 4, 5, 6, 7, 8, 9, and 10 μ M hydroxyl radical formed from the Fenton reaction described above. The generated hydroxyl radical was measured using an HPF probe, and the fluorescence intensity was measured using a BIOTEK microplate reader. The 495 nm channel is the excitation wavelength and the 515 nm channel is the emission wavelength.

After this, the fluorescence intensity of the hydroxyl radical in bacteria and fibroblast cells after treatment with 0.4% g-C_3N_4 hydrogel and light system was also collected using the BIOTEK microplate reader, then calculated through the calibration curve obtained to obtain the intracellular hydroxyl radical concentration.

In this work, the Live/Dead signal and intracellular hydroxyl radical concentration were compared in parallel, but the fluorescence channel overlapped, thus duplicated experimental samples were set and treated under the same conditions, and the Live/Dead staining and intracellular hydroxyl radical labeling were implemented, respectively.

2.2.20 Antibacterial effects of ROS from 0.4% g-C_3N_4 hydrogel and visible light system

For the specific killing pattern caused by 0.4% g-C_3N_4 hydrogel, selected as the best-performance hydrogel, the killing pattern for bacteria and mammalian cells and the specific relationship with ROS from g-C_3N_4 hydrogels were investigated in detail. In the bacterial killing part, same as the work mentioned in 2.3.18, all bacterial solutions were prepared into the samples with 1×10^8 cells per sample in 1 mL of DPBS, 0.4% g-C_3N_4 hydrogel discs in 10 mm diameter and 2 mm thickness were put into the bacterial solution to create an even

and random interaction possibility with 0.4% g-C_3N_4 hydrogel formed ROS. Samples were added to a 24-well plate and irradiated using LED light from the top side at a 10 cm distance; treated bacterial solutions were collected after irradiating for 1, 2, 4, 6, 8, 10, 30, 60, 120, and 180 minutes, washed using fresh DPBS for three times. Then, all samples were stained with the commercialised LIVE/DEAD BacLight Bacterial Viability Kits (L7012, ThermoFisher), SYTO-9 for live signal and propidium iodide for dead signal, fluorescence signal of all tested samples were measured using BIOTEK microplate reader, fluorescence channel of 495 ± 15 nm (excitation), was used for SYTO-9 signal, and fluorescence channel of 535 ± 15 nm (excitation), 595 ± 15 nm (emission) was used for PI signal, every data was repeated for three times.

2.2.21 Measurement of intracellular hydroxyl radical concentration in bacteria after treatment with 0.4% g-C_3N_4 hydrogel and visible light system

Meanwhile, intracellular hydroxyl radical diffused from 0.4% g-C_3N_4 hydrogel was also measured. Bacterial suspensions were prepared with 1×10^8 cells per sample in 1 mL of DPBS, and HPF stock solution was added in to make 20 μM final concentration. All bacterial solutions were incubated for 60 minutes at 37 °C, then washed with fresh DPBS three times to remove the unloaded probe. All probe-loaded samples were directly contacted with 0.4% g-C_3N_4 hydrogel discs and irradiated using an LED light source from 10 cm away for 1, 2, 4, 6, 8, 10, 30, 60, 120, and 180 minutes. Bacteria solution after treatment was collected and washed with DPBS as quickly as possible to remove the extra signal in a solvent. Intracellular hydroxyl radical concentration after 0.4% g-C_3N_4 hydrogel treatment was measured using a BIOTEK microplate reader, using 495 nm as the excitation wavelength and 515 nm as the emission wavelength. Every data was repeated three times. Specific hydroxyl radical concentration in bacterial cells was calculated through the calibration curve obtained in 2.2.19.

2.2.22 Fibroblast cells damage induced by the ROS from 0.4% g-C_3N_4 hydrogel and visible light system

Sample preparation is same as 2.3.19; 1×10^6 cell suspension was prepared as samples and added into a 24-well plate, one 0.4% g-C_3N_4 hydrogel disc with 10 mm diameter and 2 mm thickness was put into every sample, LED light was used at 10 cm distance from the top side (hydrogel side), for 1, 2, 4, 6, 8, 10, 30, 60, 120, and 180 minutes. After treatment,

hydrogel discs were discarded, and fibroblast cells were collected and washed with fresh DPBS three times. Fibroblast cells were stained using LIVE/DEAD®Viability/Cytotoxicity Kit for mammalian cells (L7012, Thermofisher), 2 μL of the supplied 2 mM EtdD-1 stock solution and 5 μL of the supplied 4 mM Calcein-AM stock solution was added into 1 mL of collected sample, cells were then incubated at room temperature for 30 - 45 minutes, washed using fresh DPBS for three times. Fluorescence signals were measured using a BIOTEK microplate reader; the live signal was measured using 495 nm excitation wavelength and 515 nm emission wavelength, and the dead signal was measured using 535 nm excitation wavelength and 617 nm emission wavelength. Every data was repeated three times.

2.2.23 Measurement of intracellular hydroxyl radical in fibroblast cells after treatment with 0.4% g-C_3N_4 hydrogel and visible light system

For the intracellular hydroxyl radical in fibroblast cells after 0.4% g-C_3N_4 hydrogel treatment, the HPF probe was mixed with 1×10^6 fibroblast cell suspension in 1 ml of DPBS, confirming the final concentration of HPF is 20 μM. All samples were incubated in the cell culture incubator at 37 °C, 5% CO_2 atmosphere for 60 minutes; after this, cell suspensions with HPF were washed three times to remove excess probes. Fibroblast cells with an HPF probe were contacted with 0.4% g-C_3N_4 hydrogel discs, irradiating for 1, 2, 4, 6, 8, 10, 30, 60, 120, and 180 minutes. The fibroblast cells were collected and quickly washed with DPBS, and the fluorescence signal of intracellular hydroxyl radical was using a BIOTEK microplate reader; fluorescence excitation and emission are 495 nm and 515 nm as emission wavelength. Every data was repeated three times. Hydroxyl radical diffused from immersed 0.4% g-C_3N_4 hydrogel disc into fibroblast cells was calculated using the equation obtained in 2.3.20.

2.2.24 Co-culture of bacteria and mammalian cell

This work constructed a bacteria and mammalian cell co-cultured model to explore the initiatively selective killing property of g-C_3N_4 hydrogel.

A red fluorescent protein expressed – *E. coli – DH 5*α was accepted as the bacteria component, and the hTERT fibroblast cell was the mammalian cell in this model. Briefly, hTERT fibroblast cells were cultured with high glucose Dulbecco's Modified Eagle Medium (DMEM) supplemented with 10% fetal bovine serum (FBS), 1% L-glutamine and 1% antibodies, grown in the cell culture incubator at 37 °C in 5% CO_2 with suitable humidity. hTERT fibroblast cells were passaged at 80% confluency with 0.25% trypsin-EDTA and

prepared into 1 x 10^6 cells suspension in 1 mL fresh cell culture medium. The 24-well plates were pretreated with 0.01% poly-L-lysine (P4707, Sigma) for one hour in a cell culture incubator and rinsed three times with fresh DPBS before seeding. Prepared hTERT fibroblast cells sample with 1×10^6 cells in 1 mL were seeded into tissue culture treated 24-well plate, culturing in cell culture incubator overnight to get attached. *pexp5-mCherry E. coli* were grown for 16 hours from a single colony under the previously described bacterial culture conditions, and 100 μg/mL ampicillin sodium salt (J63807.06, Thermo Fisher) was added to maintain the plasmid. Previous DMEM medium was removed from the hTERT fibroblast cell cultures, 1×10^8 bacterial cells and 100 μg/mL ampicillin sodium salt in 1 ml of DMEM was added. Plates with samples were put back into a cell culture incubator with 5% CO_2 at 37 °C for interested periods.

2.2.25 Evaluation of RFP-expressed bacteria accumulation in the co-cultured group

hTERT fibroblast cell and RFP-expressed *E. coli* were cultured as 2.3.25; the co-group was cultured for 2, 4, 6, 8, 12 and 24 hours. The previous cell culture medium was removed, and intracellular F-actin was stained using CellMaskTM Actin Tracking Stains (A57243, ThermoFisher); briefly, the stock solution was diluted into 1× in the cell culture medium. A prepared work solution was applied to samples to cover the fibroblast cells adhering fully to the bottom. Plates with samples were incubated for 30 minutes at 37 °C and 5% CO_2 atmosphere. A nuclear stain (NucRed, R37106, Thermo Fisher) was added at 1× concentration, and another was incubated for another 30 minutes in the incubator. All stain solutions were removed, and samples were rinsed with DPBS three times at 37 °C. Fluorescence images were collected using a Zeiss inverted fluorescence microscope (Zeiss, Axvio Z1) with a 40× objective lens; FITC filter was used for the F-actin signals from green fluorescence, *Cy5* filter for the deep red fluorescence of nucleus signals and TRITC filter for the fluorescence signal from red fluorescent protein. Random places were imaged for every sample to display the general view of the RFP-expressed *E. coli* accumulation tendency in the co-cultured group; every sample was set triplicated. Statistic colocalisation analysis was performed using Image J software.

2.2.26 Measurement of fibroblast cell viability in the co-cultured group

The live status of the hTERT fibroblast cell was also evaluated in the same condition to establish a robust co-culture model and exclude the misleading that might be caused by bacterial invasion. hTERT fibroblast cell and RFP-expressed *E. coli* were cultured as

2.3.25; the co-group was cultured for 2, 4, 6, 8, 12 and 24 hours. Cell culture medium was discarded, 2 μM of Calcein-AM solution and 4 μM EthD-1 solution (L7012, ThermoFisher) were mixed and added to cover all cells attached on the bottom entirely. Plates with all samples were incubated for 30 minutes at room temperature; after staining, Calcein-AM solution was removed, and samples were washed with DPBS three times to suppress the background signal. Fluorescence images were collected using a Zeiss inverted fluorescence microscope (Zeiss, Axvio Z1) with a 10$\times$ objective lens; the FITC filter was used for the live signal of fibroblast cells, and the TRITC filter was for the fluorescence signal from red fluorescent protein and dead cells. Random places were imaged for every sample to display the general live dead status of fibroblast cells in these co-cultured groups; every sample was set triplicated. Live dead signals and red fluorescent protein signals were extracted using Image J software.

2.2.27 Evaluation of Selectively killing effects of ROS generated from 0.4% g-C_3N_4 hydrogel and visible light system in the co-cultured group

To quantitatively assess the selective killing due to the ROS from 0.4% g-C_3N_4 hydrogel, *pexp5-mCherry E. coli* were grown for 16 hours from a single colony under the previously described bacterial culture conditions, and 100 μg/mL ampicillin sodium salt (J63807.06, ThermoFisher) was added to maintain the plasmid. Collected bacteria were prepared into samples with 1×10^8 cells per sample in 0.5 mL of DPBS with 100 μg/mL of ampicillin sodium salt. 80% confluency hTERT fibroblast cells were suspended in 0.5 mL of DMEM with 1 x 10^6 cells. These bacterial samples and hTERT fibroblast cell samples were mixed. One 0.4% g-C_3N_4 hydrogel disc and 1 mL of bacteria–mammalian cell co-group were added into 24-well plate, irradiating with LED light source at 10 cm distance for 1, 2, 4, 6, 8, 10, 30, 60, 120, and 180 minutes, cells were collected and washed with fresh DPBS for three times, fibroblast cells were stained with LIVE/DEAD® Viability/Cytotoxicity Kit for mammalian cells (L7012, Thermofisher) according to manufacturer's protocol. After staining, all samples were washed with fresh DPBS three times to remove the extra dye and the viability of fibroblast cells and RFP-*E. coli* in the co-group was evaluated using a BIOTEK microplate reader, a live signal of fibroblast cells was measured using 495/515 nm as excitation and emission wavelength, a dead signal of fibroblast cells was measured using 535/617 nm as excitation and emission wavelength, live percent of RFP-*E. coli* was confirmed by the red fluorescent protein signal after treatment. Fluorescence images were collected after 10 minutes and 60 minutes of irradiation; the FITC filter was used for the live

signal of fibroblast cells, and the TRITC filter was used to collect both the dead signal of fibroblast cells and the red fluorescent protein signal for live RFP-*E. coli*. Every sample was set triplicated, and analysis was implemented using Image J software.

2.2.28 Measurement of intracellular hydroxyl radical in co-cultured group after treatment with 0.4% g-C_3N_4 hydrogel and visible light system

The intracellular hydroxyl radical concentration change is also investigated using the previously mentioned HPF probe. *pexp5-mCherry E. coli* were grown for 16 hours from a single colony under the previously described bacterial culture conditions, and 100 μg/mL ampicillin sodium salt (J63807.06, Thermo Fisher) was added to maintain the plasmid. Collected bacteria were prepared into samples with 1×10^8 cells per sample in 0.5 mL of DPBS with 100 μg/mL of ampicillin sodium salt. 80% confluency hTERT fibroblast cells were suspended in 0.5 mL of DMEM with 1×10^6 cells. These bacteria and hTERT fibroblast cell samples were mixed to obtain a co-group sample. Different from live dead signal collecting, here, 20 μM of HPF probe was loaded into co-group through incubating for 60 minutes at 37 °C, 5% CO_2, then samples were washed with fresh DPBS three times to remove the unloaded HPF probe. Every 1 mL of co-group sample and one 0.4% g-C_3N_4 hydrogel disc was added into a 24-well plate; LED light irradiated the samples from the top side for 1, 2, 4, 6, 8, 10, 30, 60, 120, and 180 minutes. Cells were collected and washed with DPBS as quickly as possible. Intracellular hydroxyl radicals were measured using a BIOTEK microplate reader with 495 nm and 515 nm as the excitation and emission wavelengths separately. Everyone was set triplicated; fluorescence images were collected using a Zeiss inverted fluorescence microscope (Zeiss, Axvio Z1) with 20× objective lens, FITC filter was used for the hydroxyl radical signal of co-group, TRITC filter for the fluorescence signal from red fluorescent protein. Random places were imaged for every sample to display the hydroxyl radical distribution in the co-cultured groups after treating with 0.4% g-C_3N_4 hydrogel disc; every sample was set triplicated. Hydroxyl radical and red fluorescent protein signals were extracted using Image J software, and all data were analysed using Prism software.

2.2.29 Biofilm eradication

Crystal violet stain of biofilm

S. epidermidis and *E. coli – DH 5α* were grown for 16 hours from a carefully picked single colony under the previously described bacterial culture conditions. Bacterial solution

was collected, and bacterial cell number was adjusted into 1×10^8 cells per sample using a liquid bacterial culture medium. 500 μL of the prepared bacterial solution was added to a 48-well plate. Plates were cultured in the bacterial cell culture incubator for 24 hours at 37 °C. After incubation, the liquid medium was removed gently, preventing destroying the formed biofilm. Tested 0.4% g-C_3N_4 hydrogel discs with 10 mm diameter and 2 mm thickness were put on top of the formed biofilm, and DPBS was carefully added to keep the environment moist. LED light was applied to the hydrogel-covered samples from 10 cm away; irradiating periods were 10, 30, 60, 120 and 180 minutes. The control group have no treatment. After this, hydrogels were removed carefully; samples were rinsed with DPBS gently three times, and plates were placed in the fume hood to dry the residual biofilm. 500 μL of 0.1% (v/v) crystal violet (C0775, Sigma) solution was added and reacted for 5 minutes.

Crystal violet solution was discarded, and sample wells were washed with 0.85% NaCl solution to remove unbonded crystal violet dye. Samples were dried in a fume hood again, and 500 μL of 30% acetic acid (695092, Sigma) was added to release the crystal violet for 30 minutes at 37 °C. Absorption at 590 nm was measured using a BIOTEK microplate reader. Every sample was repeated three times, and the data was analysed using Prism software.

Confocal laser scanning microscope imaging of biofilm

Confocal laser scanning was applied to evaluate the eradication caused by 0.4% g-C_3N_4 hydrogel-generated ROS. Mature biofilm was obtained by adding the bacterial suspension (1×10^8 cells/mL in liquid medium) to a tissue culture-treated 48-well plate, cultured for 24 hours at 37 °C. The liquid medium was removed, and 0.4% g-C_3N_4 hydrogel disc was added; samples were treated using an LED light source for 180 minutes. Control groups include a) blank control, no treatment; b) hydrogel control, 0.4% g-C_3N_4 hydrogel was covered on the biofilm but had no LED light irradiation; c) light control, only LED light was applied, having no 0.4% g-C_3N_4 hydrogel covering on biofilm sample.

After treatment, residual biofilm was washed with DPBS gently and stained with commercialised LIVE / DEAD BacLight Bacterial Viability Kits, using 1.5 μL of SYTO-9 solution (3.34 mM) and 1.5 μL of Propidium iodide solution (20 mM) was mixed in 1 mL of DPBS solution, biofilm was stained with the ready dye solution at room temperature in the dark for 15 minutes. Bacteria in biofilm after treatment were observed using confocal laser scanning microscopy (Zeiss, LSM510) with 10$\times$ objective lenses, 1024 $\times$ 1024 pixels, scanning thickness of 35 μm, layered by every 0.5 – 1.0 μm, whole scanned area of 850 μm $\times$ 800 μm. Every sample was repeated three times, and the obtained image data was analysed using Image J software.

2.2.30 Evaluation of mammalian cell functions after treatment of 0.4% g-C_3N_4 hydrogel and visible light system

To obtain robust results of selectively killing caused by the ROS from g-C_3N_4 hydrogel, the functions of mammalian cells were checked under the same treatment conditions.

Fibroblast cell migration

In the fibroblast cell migration test, 80% confluency fibroblast cells were suspended in the complete cell culture medium (DMEM, with 10% Fetal Bovine Serum, 1% penicillin/streptomycin and 1% L-glutamine) at 3×10^5 cells/mL, and 70 μL cell solution was pipetted into each chamber of the cell culture insert (Ibidi, United Kingdom), the cell culture insert with cell solution inside was put back into cell culture incubator for overnight co-incubating. After this, the cell culture inserts were removed, a cell-free gap was formed, and each sample was washed with warm DPBS three times; for the treatment groups, 0.4% g-C_3N_4 hydrogel disc with 10 mm diameter and 2 mm thickness was added in to fully cover the attached cell area with a gap, and irradiated under the LED light for 10, 30 and 60 minutes. Except for the treatment group, the effect of g-C_3N_4 on cell migration performance was explored in detail with three other different treatment conditions: 1) blank control: have no intervention at all; 2) 0.4% g-C_3N_4 conditional medium treated group: conditional medium was prepared as a previously mentioned method, and the formed gap model was cultured with conditional medium for 3 days. After this, all tested hydrogels were removed, and cells were washed with warm DPBS and changed with a fresh, complete cell culture medium. After 12 hours, 24 hours and 48 hours of continuous culture, cells were stained with 2 μM Calcein-AM solution, cell migration status was observed using a fluorescence microscope with a 5$\times$ objective lens under the FITC channel, and images were analysed using Image J and Prism software.

Fibroblast cells morphology

The morphology changes of fibroblast cells after the same treatment as the selectively killing part, 80% confluence fibroblast cells were prepared into cell suspension in 4×10^6 cells/mL, seeded into a 24-well plate in 1 mL. Samples were cultured in the cell culture incubator (37 °C, 5% CO_2 atmosphere) for well attached. 0.4% g-C_3N_4 hydrogel disc (10 mm in diameter and 2 mm in thickness) were added to cover all attached cells, and then 10, 30, and 60 minutes irradiation was applied from the top side at a 10 cm distance. To fully reveal the influence of g-C_3N_4 hydrogel on fibroblast cells, the different extent of test conditions was applied on 1) blank control group, having no treatment; 2) 0.4% conditional

medium treated group: conditional DMEM medium was prepared as 2.3.12 mentioned, the fibroblast cells were treated with this conditional medium for the whole process; 3) 0.4% g-C_3N_4 hydrogel covered group: seeded fibroblast cells were covered with 0.4% g-C_3N_4 hydrogel disc for 24 hours before staining. CellMaskTM Actin Tracking Stains (A57243, ThermoFisher), briefly, the stock solution was diluted into 1× in cell culture medium. A prepared work solution was applied to samples to thoroughly cover the fibroblast cells adhering to the bottom. Plates with samples were incubated for 30 minutes at 37 °C and 5% CO_2 atmosphere. A nuclear stain (NucRed, R37106, ThermoFisher) was added at 1× concentration, and another was incubated for another 30 minutes in the incubator. All stain solutions were removed, and samples were rinsed with DPBS three times at 37 °C. After treatment, all hydrogels were removed, and the cells were stained with CellMask Actin Tracking Stains (A57243, ThermoFisher) cell skeleton and Nuclear stain (NucRed, R37106, ThermoFisher) for cell nucleus. Briefly, the previous cell culture medium was removed, cells were washed with DPBS three times to remove the detached parts, and then these live cell samples were stained with these two different dye solutions in 1× concentration for 30 minutes at 37 °C. After the staining process, dye solutions were discarded. Cells were washed with fresh DPBS to decrease the background signal. Another 500 μL of DPBS was added to the moisture of the samples, which were imaged using a fluorescence microscope using a 20× objective lens, FITC channel for a signal from the cell skeleton and *Cy*5 channel for a signal from the cell nucleus.

HUVEC tube formation

The angiogenesis capability of endothelial cells was also evaluated after the same treatment conditions to confirm the hard harm to mammalian cell function. Same as the previous test sample preparation, 24-well plates were pre-coated using 100 μL of Matrigel (Corning, USA) and incubated at 37 °C for 1 hour to finish the coating process. Then, 4×10^4 cells/cm^2 HUVECs suspensions in 200 μL were seeded on the Matrigel-coated 24-well plate; the 1) blank control group had no treatment; 2) 0.4% conditional medium treated group: conditional DMEM medium was prepared as 2.3.12 mentioned, the HUVECs were resuspended in this conditional medium and seeded on the Matrigel-coated 24-well plate; 3) 0.4% g-C_3N_4 hydrogel covered group: seeded HUVECs were covered with 0.4% g-C_3N_4 hydrogel disc for 1 hours before they were put back the incubator for tube formation. 4) the test group was firstly covered by 0.4% g-C_3N_4 hydrogel disc, then shone with LED light at a 10 cm distance from the top side for 10, 30 and 60 minutes, then the hydrogels were removed, and plates were put back into the incubator for normal tube formation process. After another 6 hours of incubation, all samples were stained with 2 μM Calcein-AM solution for 30

minutes. Formed capillary-like structures were observed using fluorescence microscopy (Zeiss, Germany) with a 5× objective lens. Generated branches and nodes were quantified by Image J and Prism software with six randomly selected fields.

2.2.31 Oxidative stress measurement

Possible oxidative stress caused by the applied light source was evaluated by γH2Ax phosphorylation via acute and chronic exposure to compare the performance of UV light and our LED light.

Briefly, 4×10^4 cells in 1 mL were seeded into a 24-well plate, culturing overnight to get an attached single-cell layer. Then, the samples were treated following the two specific models: 1) acute exposure: fibroblast cells seeded in 24-well plates were irradiated for two 20-minute cycles within 2 hours in a single day. 2) chronic exposure: seeded fibroblast cells in 24-well plates were irradiated for 20 minutes on three consecutive days. After the treatment, cells were fixed using 4% methanol-free formaldehyde solution for 10 minutes at room temperature. A 0.1% Triton X-100 solution was used to permeabilise the sample for 10 minutes. Then, block it with 5% normal goat serum (5425, Life Technologies) for 60 minutes.

After this, γH2Ax antibody (9718, Cell Signalling Technology) was diluted into work concentration to cover all sample areas, incubating at 4 °C overnight. The next day, A fluorochrome-conjugated Alexflour-488 anti-rabbit secondary antibody (4412, Cell Signalling Technology) was added to label the specific antibody; samples were then incubated for another 1 hour at room temperature. Fibroblast cell skeleton and nuclear were stained using Rhodamine phalloidin and DAPI solution. All samples were imaged using a Zeiss inverted fluorescence microscope (Zeiss, Axvio Z1) with 20× and 40× objective lenses; the FITC filter was used for the γH2Ax signal, the TRITC filter for the cell skeleton signal and the DAPI filter was used for the nuclear signal. Random places were imaged for every sample to display phosphorylation of the γH2Ax after irradiation using different light sources under different exposure models; every sample was triplicated. γH2Ax signal from every cell was extracted using Image J software; all data were analysed using Prism software.

2.2.32 Assessment of target sites affected by ROS generated from 0.4% g-C_3N_4 hydrogel

Specific damage sites were explored to obtain more details and explain why these g-C_3N_4 hydrogel-generated ROS could selectively kill bacterial cells over mammalian cells.

Membrane integrity

For the damage of g-C_3N_4 hydrogel generated ROS to the bacterial inner and outer membrane, Gram-positive bacterial strain *S. epidermidis* and Gram-negative bacterial strain *E. coli – DH 5*α were cultured in liquid medium for 16 hours from picked single colony following previously described bacterial culture conditions. Then, the bacterial solutions were collected, and the bacterial cell number was adjusted into OD_{600} = 2.0 using fresh DPBS. The negative control group have no intervention. The light control group was only irradiated using LED light from the top side at a 10 cm distance for 60 minutes. The hydrogel control group added 0.4% g-C_3N_4 hydrogel disc for 60 minutes in the dark. The test group was treated with 0.4% g-C_3N_4 hydrogel and irradiated with LED light for 60 minutes. Outer membrane positive control was treated with Polymyxin B solution (128 μM) for 60 minutes, and inner membrane positive control was treated using 0.1% Triton X -100 for 60 minutes. After treatment, bacterial cells were collected and incubated with 40 μM Propidium iodide (PI) solution or 50 μM N-phenyl-1-naphthylamine (NPN) solution, incubating in the dark for 30 minutes. Then, the fluorescence intensity was measured using a microplate reader (BIOTEK Instrument, synergy H1) (PI: ex/em is 535 nm and 617 nm; NPN: ex/em is 350 nm and 420 nm). Every sample was repeated six times, and the data was analysed using Prism software.

Protein damage

The bacterial internal enzyme activity was measured to evaluate the g-C_3N_4 hydrogel generated ROS to bacteria, bacterial suspension (*S. epidermidis* and *E. coli – DH 5*α) in DPBS (OD_{600} = 2.0) was treated with only LED light irradiation for 60 minutes, or only 0.4% g-C_3N_4 hydrogel was added in and co-incubated in the dark for 60 minutes, or 0.4% g-C_3N_4 hydrogel was added in first then irradiated with LED light source for 60 minutes. After treatments, bacterial solutions were collected and centrifuged, the supernatant was discarded, and bacterial cell pellets were resuspended in DPBS. Then, the bacterial suspensions were physically lysed using an ultrasonic material dispenser (22 kHz) on the ice and then centrifuged at 14500 rpm for 5 minutes. The supernatant containing β-galactosidase was collected to characterise the internal enzyme activity. 50 μL of prepared bacterial supernatant was mixed with 50 μL of 10 mg/mL *o*-nitrophenol-β-Dgalactoside (ONPG) and incubated at 37 °C with shaking for 4 hours. The optical density value was then measured at 420 nm using a microplate reader (BIOTEK Instrument, Synergy HT). Every sample was repeated three times, and the data was analysed using Prism software.

2.2.33 Fluorescence intensity data collect

All the fluorescence intensity data in this work were collected using a BIOTEK microplate reader. Samples were triplicated and repeated, and the final data analysis was completed using Prism 10.

2.2.34 Fluorescence images collect and image analysis

All the images were acquired using the Zeiss AxioObserver Z1 inverted fluorescence microscope, Zeiss AxioObserver Z1 upright fluorescence microscope and Zeiss LSM510 confocal microscope. Obtained data were analysed using Image J software.

Chapter 3

Preparation and Characterisations of Graphitic carbon nitride (g-C_3N_4) hydrogel

3.1 Introduction

Chronic wounds happen because the cells do not follow the original healing process, both spatial and temporal; changes in various cells involved in the different phases of wound healing stage of haemostasis, inflammation, re-epithelialisation and remodelling results in the delay of the biological tissue reconstruction[193]. Different from acute wound healing, often, the chronic wound is stuck in a long-term inflammation stage; high levels of proinflammatory cytokines, proteases and senescent cells exist in the chronic wound environment, and all the dysfunctional ROS levels and stem cell behaviour stop the chronic wound healing through cascade cellular events and damage skin closure.

Diabetic foot ulcers (DFUs) are typical refractory chronic wounds and are mainly caused by diabetic neuropathy, peripheral vascular lesions, foot malformations and trauma; as a significant complication of diabetes mellitus (DM). It is difficult to cure and always leads to an increase of morbidity, mortality or limb amputation of diabetic patients, due to the limited monitoring and untimely intervention.

Many patches have been developed towards different types of chronic wounds. The majority of chronic wound healing patches are dry, passive and cannot meet several specific requirements. Our original intact skin can prevent bacterial infection, manage the substance exchange and resist injuries caused by heat or cold environments. The ideal chronic wound healing bandage is expected to mimic the basic properties of the skin barrier and could be

modified according to specific demands[194]. The bandage needs to manage the exudate fluid on the wound site appropriately to keep a suitable moisture level and provide an oxygen-rich environment to accelerate wound healing. These make hydrogels an ideal candidate for next-stage chronic wound healing bandage development.

Hydrogels are a three-dimensional network of crosslinked polymer chains; they can absorb and keep water or tissue fluid due to their hydrophilicity. This water absorption capability is closely related to the molecular structure of the crosslinking network, and different water content helps hydrogels present various softness to comfort with different biological tissues, combined with their excellent biocompatibility, which makes hydrogels show great potential in biomedical applications. Hydrogels[195] could be polymerised through different crosslink modes, such as physical, chemical and enzymatic. Photo-crosslinked hydrogels have attracted more attention due to their simple and tunable reaction process.

Different kinds of photo-crosslinked hydrogels[196] have been used for drug delivery, cell encapsulation, and regenerative tissue engineering. Various sophisticated modifications meet different demands but also prevent them from clinical translation.

This section introduces a graphitic carbon nitride (g-C_3N_4)-based hydrogel polymerised by photo-crosslinking with free radicals under visible light irradiation. Instead of other photo-polymerised hydrogel systems using UV light, our hydrogel could be prepared under gentle visible light, reducing risks from UV irradiation and possible underlying damages. The visible light responsive property provides an excellent opportunity for our further photo-modulated wearable device towards personalised biomedical therapeutic applications.

As a candidate for wound healing bandage material, the optimal wound healing system is expected to be biocompatible with the open wound site and display no toxicity during the healing process while guaranteeing the provision and maintenance of the environmental moisture and air exchange. Besides, in this study, the significant factors for wound healing are the controllable reactive oxygen species (ROS) generated from g-C_3N_4 hydrogel, so the photo-initiated properties of g-C_3N_4 hydrogel are evaluated first.

3.2 Results

3.2.1 Photo-crosslinked g-C_3N_4 hydrogel preparation

The g-C_3N_4 initiated hydrogel formation, and polymerisation steps were carried out[197, 198], as shown in **Figure 3.1**. Graphitic carbon nitride (g-C_3N_4) material was added to the mixture, acting as both initiator and reinforcer. Free radical-based polymerisation formed this photo-crosslinked hydrogel. When the whole system is exposed to a suitable wavelength

of light, the embedded g-C_3N_4 material will produce free radicals inside and, on its surface, providing a lot of active sites for monomer (DMA) and crosslinker (MBA) to form 3D network structures, finishing the gelation process. Different concentrations of g-C_3N_4 affect the polymerisation time, toughness of hydrogel, and free radical release capability. To systematically investigate the performance of g-C_3N_4 hydrogel, different contents of g-C_3N_4 0.1%, 0.2%, 0.4%, 0.6%, 0.8% and 1.0% were used. In addition, agar gels were prepared to provide essential information about the cellular system with a biocompatible additive, and DMA hydrogel was used as the control group of g-C_3N_4 hydrogel because they were synthesised using the same monomer and crosslinker in the polymerisation system (**Figure 3.1**).

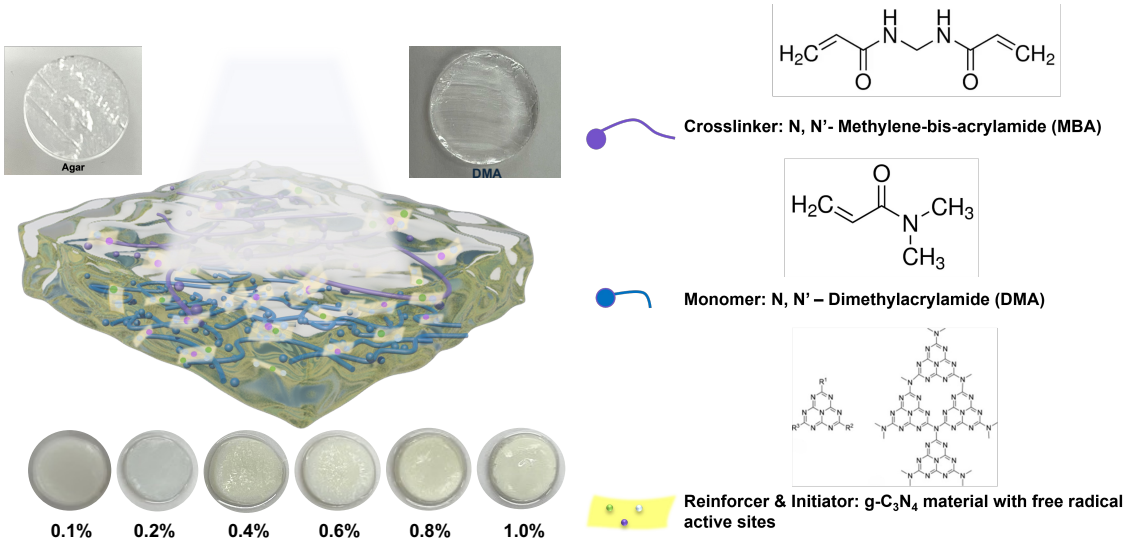

Fig. 3.1 Schematic of g-C_3N_4 hydrogel polymerisation system and pictures of prepared agar gel, DMA hydrogel, 0.1%, 0.2%, 0.4%, 0.6%, 0.8% and 1.0% g-C_3N_4 hydrogels. Polymerisation process: g-C_3N_4 consists of *tri-s*-triazine (C_3N_4) units linked via conjugated C-N bonds in a 2D layered structure. Once the g-C_3N_4 material is activated by induced visible light, C=N will contribute to the electron delocalization, π-electrons in C=N bonds become excited into the conduction band, weakening the bond and a hole (h^+) remains in the valence band. $\cdot OH$ will be generated after the reaction between H_2O and h^+, breaking the C=C π-bond in DMA, forming a C-centered radical ($C^{\cdot}$) on the α-carbon. Then, the DMA radical propagates by attacking the C=C bond of another DMA monomer, leading to a new C-C σ-bond formation, this process repeats, forming poly(DMA) chains. MBA contains two acrylamide ($-CH=CH-CONH_2$) groups, allowing it to covalently crosslink growing poly(DMA) chains. When a growing poly(DMA) radical attacks one of the C=C bonds in MBA, it forms a C-C σ-bond, crosslinking through the $-CH_2-$ bridge of MBA, resulting in a crosslinked 3D hydrogel network.

In this work, LED light with a 460 nm centre wavelength was assembled and applied for both hydrogel polymerisation and experimental implementation. The power density of the LED light source was measured to keep the experimental conditions consistent, and a 10 cm distance was set for the following work.

As shown in **Figure 3.2A**, light power density was decreased as the measure distance changed from 1 cm to 10 cm. The specific value at 10 cm was 48.15 mW/cm^2, which is satisfactory for a biomedical device, compared with existing photo-modulated biomedical devices; the power density of most applied light sources is around 1-5 W/cm^2; our LED light is much lower than this. A temperature change of 2 mL of deionised water within 1-hour irradiation was also measured in **Figure 3.2B**, as the ploymerisation dispersion was also kept between 2 - 3 mL, increase of temperature from room temperature (18 °C) to 25 °C occurs within the first 10-minute irradiation; the maximum temperature is stable at 28 °C until 60 minutes, this proves that this g-C_3N_4 initiated hydrogel could be prepared in a simple condition, making it easier to be prepared and getting more chance to be translated.

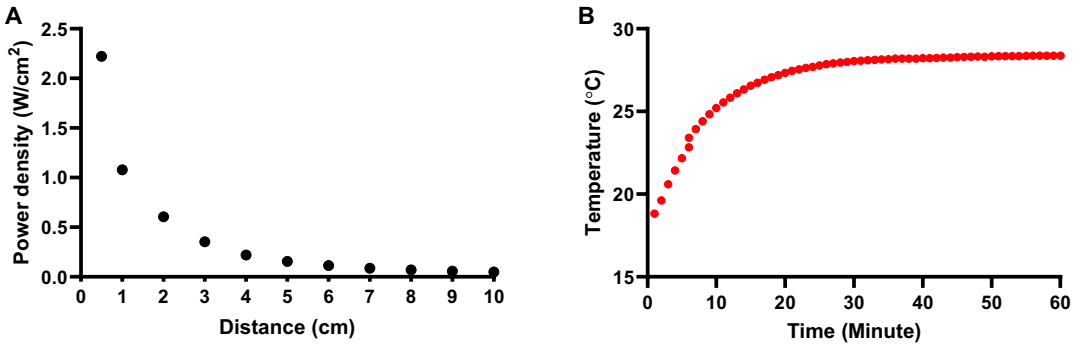

Fig. 3.2 Properties of LED light source (A) Power density of the LED at different distances (1 - 10 cm) (B) Temperature change of 2 ml of deionized water under the LED irradiation for 60 minutes.

3.2.2 Physicochemical properties of g-C_3N_4 hydrogels

The remarkable mechanical properties of g-C_3N_4-initiated hydrogel were studied by previous research[13], such as excellent stretchability and keep toughness and flexibility at the same time. Hydrogel formation with other photoinitiator instead of g-C_3N_4 showed weak properties, while the g-C_3N_4 hydrogel possessed G' up to 8.3 kPa when the g-C_3N_4 material content is 11 wt%[198]. This is because of the specific structure of g-C_3N_4, allowing it to act as a colloidal dopant by forming a secondary network of inorganic structures within the hydrogel, providing extra strength to the formed hydrogel. Moisture is necessary to accelerate

the wound healing process. Moist wound healing means providing and maintaining suitable hydration of the open wound tissue rather than letting the exposed wound site dehydrate and dry out.

Water retention capability

To this consideration, the water retention capability of prepared g-C_3N_4 hydrogels, agar and DMA hydrogel were evaluated. As shown in **Figure 3.3A**, both agar gel DMA hydrogels lose contained water rapidly within the first 6 hours when exposed to the air. Because of their porous structure, water molecules could escape from the matrix easily due to the large pore size. After 6 hours of exposure, almost no water remains in both agar gel and DMA hydrogel, which is not ideal for a wound patch material, as its rapid water loss makes it challenging to keep the open wound site moist.

The g-C_3N_4 hydrogels present a much better water retention capability through 25 hours; in the first 6 hours of exposure, 0.8% and 1.0% g-C_3N_4 hydrogels showed similar water loss tendency as agar gel and DMA hydrogel, which could be attributed to the higher concentration of dopped g-C_3N_4 materials, leading to a higher density of crosslinked matrix, decreasing the capability of water storage. 0.1%, 0.2% and 0.6% g-C_3N_4 hydrogel kept 35% - 40% percent after 6 hours of exposure and 25% - 30% of water remaining after 25 hours test.

0.4% g-C_3N_4 showed a moderate water retention capability, with 20% of the water remaining after the first 6 hours of exposure and only 5% more water evaporating over the next 20 hours. This water vapour is beneficial for the chronic wound healing process, as the controllable water loss rate provides a moisture environment and allows excess wound fluid absorption.

Swelling ratio

Water uptake of g-C_3N_4 hydrogels in different concentrations was evaluated and compared to the agar and DMA hydrogel. The swelling test indicated that all the g-C_3N_4 hydrogels reached equilibrium swelling after being immersed in DPBS for 24 hours. All swelling ratios of tested hydrogels shown in **Figure 3.3B** revealed no significant difference among all g-C_3N_4 hydrogels for different percent of g-C_3N_4 doping. The similar swelling ratio shown in the obtained data is unmistakable evidence that adding this reinforcer (g-C_3N_4) does not affect the water absorption capability of g-C_3N_4. For the detail, 0.1% and 1.0% g-C_3N_4 hydrogels could get back to their initial weight after 24 hours of immersion, and 0.2%, 0.4%, 0.6% and 0.8% g-C_3N_4 hydrogels show around 80% recovery capability.

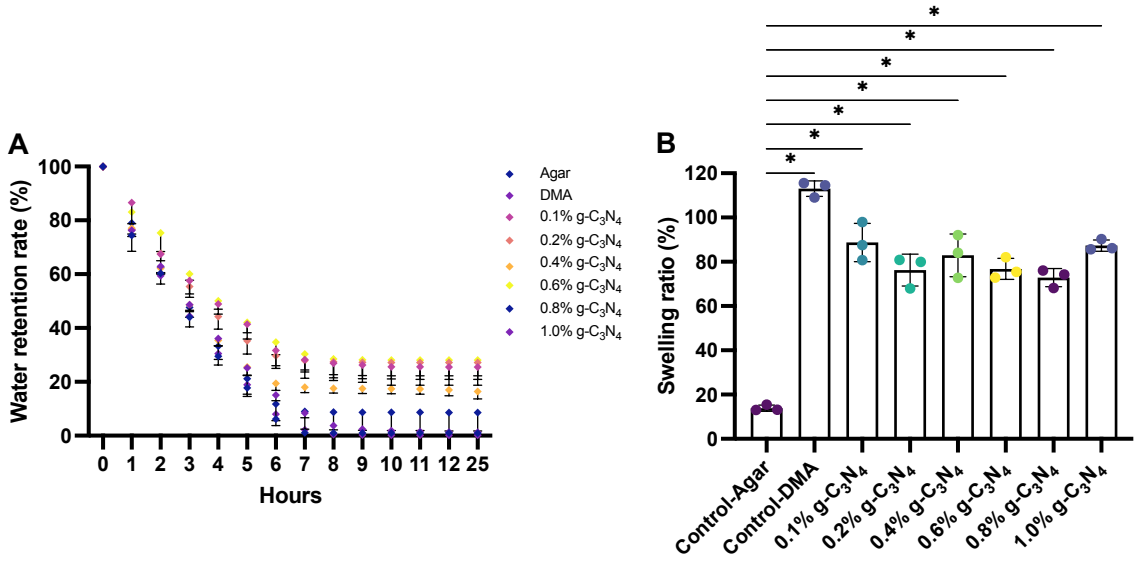

Fig. 3.3 Physiochemical properties of g-C_3N_4 hydrogel (A) Water retention capability and (B) Swelling ratio of agar gel, DMA hydrogel, 0.1%, 0.2%, 0.4%, 0.6%, 0.8% and 1.0% g-C_3N_4 hydrogel. Data are presented as *mean* $\pm$ *SD* (n = 3). Statistical analysis was performed using one-way ANOVA followed by Dunnett's post hoc test. P $\leq$ 0.05 was considered statistically significant (* p $\leq$ 0.05, **p $\leq$ 0.01, *** p $\leq$ 0.001, **** p $\leq$ 0.0001). Statistical analysis was conducted using GraphPad Prism 10.0.

However, a significant difference was seen between agar gel and DMA hydrogel, with a swelling ratio of 15% to 120%, respectively. These results further confirmed that the g-C_3N_4 hydrogel could be an ideal candidate material for a wound patch because it is capable of absorbing fluid on the wound site but will not expand to form extra pressure, which will cause a secondary injury to the chronic wound and then hinder the healing process.

These swelling ratio tests provided evidence for the fully polymerised g-C_3N_4 hydrogel. Hydrogels typically swell in water, but fully cross-linked hydrogels will have limited swelling compared to under-cross-linked ones, the results obtained from our g-C_3N_4 hydrogels in **Figure 3.3B** only presented an 80% swelling ratio, indicating the completed polymerisation.

3.2.3 Spectroscopic properties of g-C_3N_4 hydrogel

This g-C_3N_4 hydrogel is expected to generate reactive oxygen species through the photo-activated catalytic process[199]. Therefore, the spectroscopic properties of prepared g-C_3N_4 hydrogels were investigated to confirm that they satisfied the requirement of photodynamic process initiation.

Absorbance wavelength of g-C_3N_4 dispersion

One of the most critical components of a photodynamic process is the absorption of applied material at a specific wavelength. Here, 0.4% g-C_3N_4 powder was well dispersed in deionised water, and the UV-Vis absorption spectra were measured between 300 nm and 800 nm. **Figure 3.4A** revealed a characteristic peak around 420 nm, corresponding to the presence of g-C_3N_4 in the mixed liquid system[199].

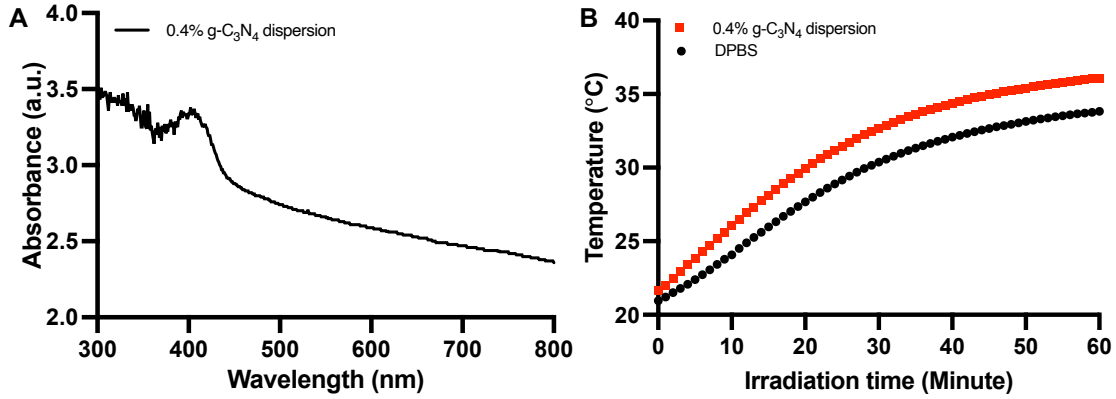

Fig. 3.4 Spectroscopic properties of g-C_3N_4 hydrogels. (A) Absorbance spectra of 0.4% g-C_3N_4 dispersion. (B) Photothermal effect of 0.4% g-C_3N_4 dispersion under 460 nm LED irradiation for 60 minutes

Photothermal properties of g-C_3N_4 hydrogel

The two most common processes activated by induced photoirradiation are the photodynamic process (PDT) and photothermal effect (PTT). To make sure all results in this work are caused by the only reactive oxygen species (ROS) involved process, the temperature change of 1 mL 0.4% g-C_3N_4 solution, which will be polymerised into 0.4% g-C_3N_4 hydrogel, and 1 mL of DPBS solution were continuously measured in 60 minutes of irradiation. Obtained results showed that the temperature of 1 mL DPBS was increased from 21 °C to 33 °C after 60 minutes of irradiation while the final temperature of 0.4% g-C_3N_4 solution at 60 minutes was 36 °C (**Figure 3.4B**), the temperature difference between these two groups were kept within 3 degree , which means that the photothermal conversion efficiency of g-C_3N_4 material is too low to trigger the photothermal effect.

3.2.4 Antibacterial properties of g-C_3N_4 hydrogel

Following the physical and chemical characterisations, the intrinsic biological performances of prepared g-C_3N_4 hydrogels were also assessed to evaluate their biocompatibility. For this purpose, the antibacterial properties of agar gel are as follows: DMA hydrogel and all g-C_3N_4 hydrogels against *S. epidermidis* and *E. coli - DH 5α* were explored through both indirect and direct contact methods, as shown in **Figure 3.5**.

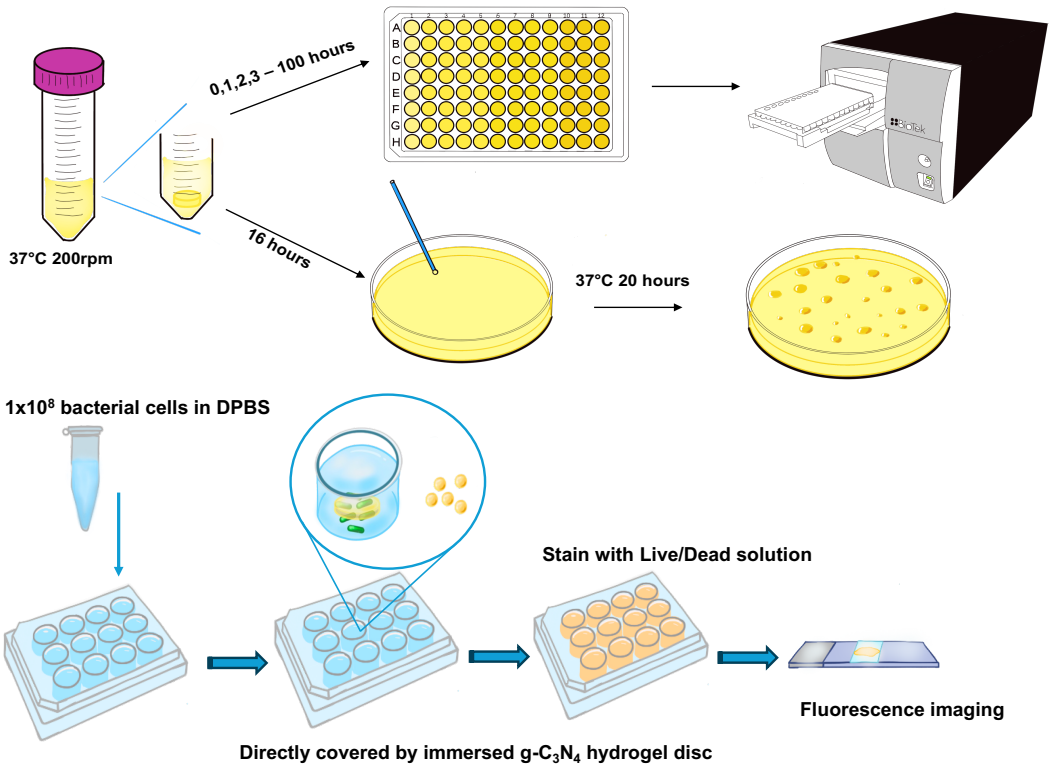

Fig. 3.5 Schematic figure of direct (below) and indirect (top) contact method for antibacterial properties test of g-C_3N_4 hydrogels

In the indirect contact experiments, bacterial growth curves and colonies forming unit (CFU) counting were implemented to prove the antibacterial properties of g-C_3N_4 hydrogels. For *S. epidermids*, agar gel, DMA hydrogel and g-C_3N_4 hydrogels in all concentrations were co-incubated with bacterial strain after they were inoculated into the liquid culture medium, at the specific timepoints, the immersed hydrogels were removed and the bacterial liquid was collected. Turbidity of bacterial solutions was measured at 0, 1, 2, 3, 4, 5, 10, 15, 20, 25, 50, 75 and 100 hours as shown in (**Figure 3.6A**). The 16-hour co-incubated sample was spread onto an agar plate, and formed bacterial colonies below 50% percent compared to no

hydrogel added to the group; 1.0% g-C_3N_4 hydrogel immersed sample showed the highest colonies form units number around 5×10^8 CFU/mL, survival ratio was calculated about 30%.

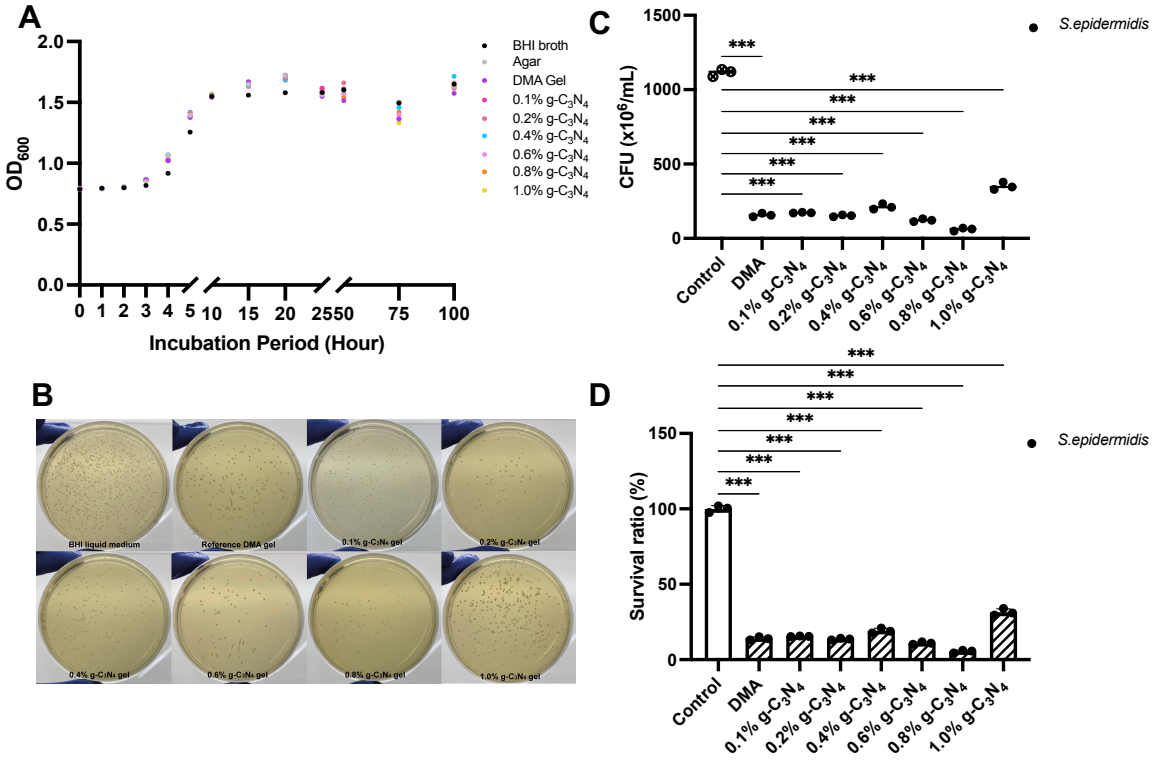

Fig. 3.6 Antibacterial properties against *S. epidermids*. (A) Growth curve of *S. epidermids* after co-incubating with all tested hydrogels for 100 hours. (B) Colonies forming units (CFU) pictures of 16-hours co-incubated *S. epidermids*. (C) Colonies forming units (CFU) number from data B. (D) Survival ratio calculated from data C. Data are presented as $mean \pm SD$ (n = 3). Statistical analysis was performed using one-way ANOVA followed by Dunnett's post hoc test. $P \leq 0.05$ was considered statistically significant (* $p \leq 0.05$, **$p \leq 0.01$, *** $p \leq 0.001$, **** $p \leq 0.0001$). Statistical analysis was conducted using GraphPad Prism 10.0.

E.coli – DH 5α showed the same results as *S. epidermidis*; compared to the control group, the bacterial growth curve through 100 hours presented no noticeable change among all tested groups; CFU numbers counted from the agar plate were located around 5×10^8 CFU/mL; it is 50% of the control group. 1.0% g-C_3N_4 hydrogel treated group showed the highest CFU counting number in this *E.coli – DH 5α* test group as well; one different point is that the survival ratio of 1.0% g-C_3N_4 treated *E.coli – DH 5α* group was around 110%, showing no damage (**Figure 3.7**).

In the direct contact experiments, bacteria were seeded in a multi-well plate to obtain an attached monolayer; all tested hydrogels were directly covered on the top of the bacterial

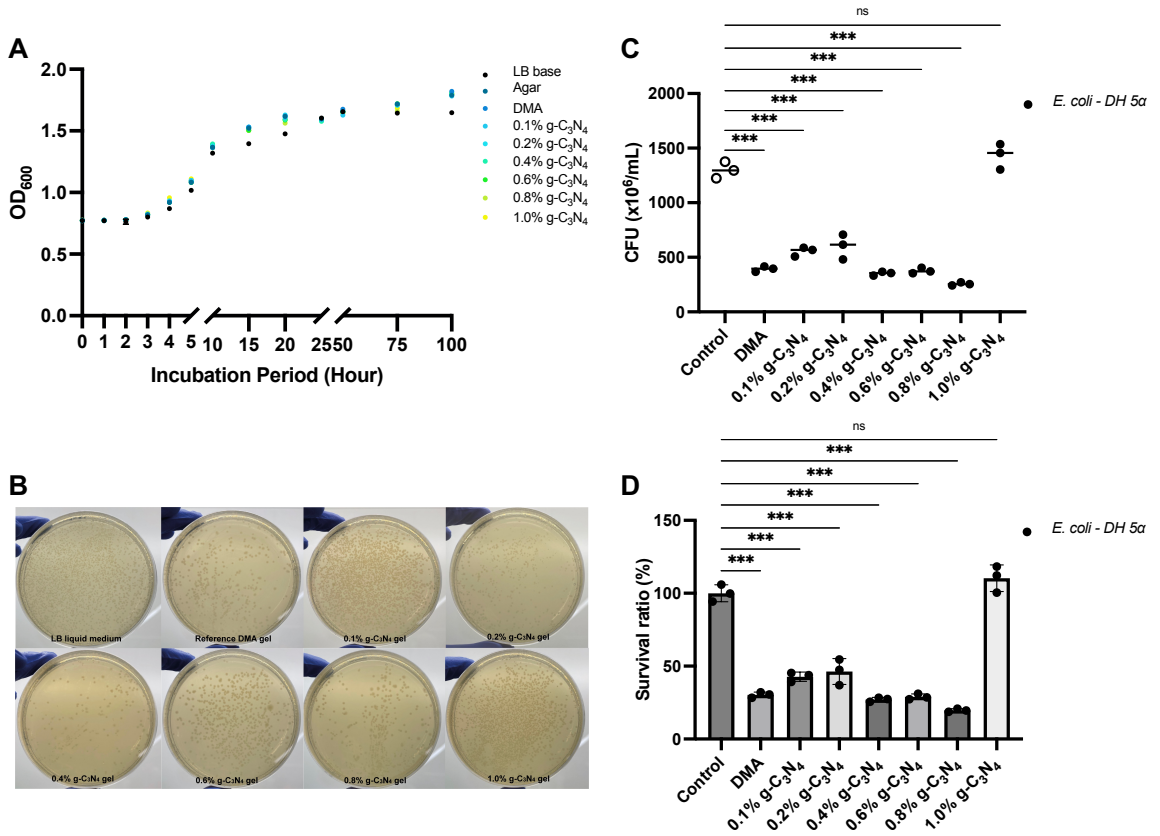

Fig. 3.7 Antibacterial properties against *E.coli – DH 5α* . (A) Growth curve of *E.coli – DH 5α* after co-incubating with all tested hydrogels for 100 hours. (B) Colonies forming units (CFU) pictures of 16-hours co-incubated *E.coli – DH 5α*. (C) Colonies forming units (CFU) number from data B. (D) Survival ratio calculated from data C. Data are presented as $mean \pm SD$ (n = 3). Statistical analysis was performed using one-way ANOVA followed by Dunnett's post hoc test. $P \leq 0.05$ was considered statistically significant (* $p \leq 0.05$, **$p \leq 0.01$, *** $p \leq 0.001$, **** $p \leq 0.0001$). Statistical analysis was conducted using GraphPad Prism 10.0.

monolayer for 24 hours, and then the viability of bacteria was evaluated vis a Live / Dead staining experiment. Experiments were also carried out on the *S. epidermidis* and *E. coli DH 5α* to explore the viability of Gram-positive and Gram-negative cultures. Live /Dead images were quantified using image analysis to calculate the fluorescence signals that came from the Live (green) group and the Dead (red) group (**Figure 3.8, 3.9**). Compared to the blank control group, no obvious bactericidal activity was observed after 24 hours of co-incubation with all tested g-C_3N_4 hydrogel and agar gel. The DMA-covered samples presented 30% and 20% dead groups in *S. epidermidis* and *E. coli – DH 5α*, respectively (**Figure 3.8D, 3.9D**).

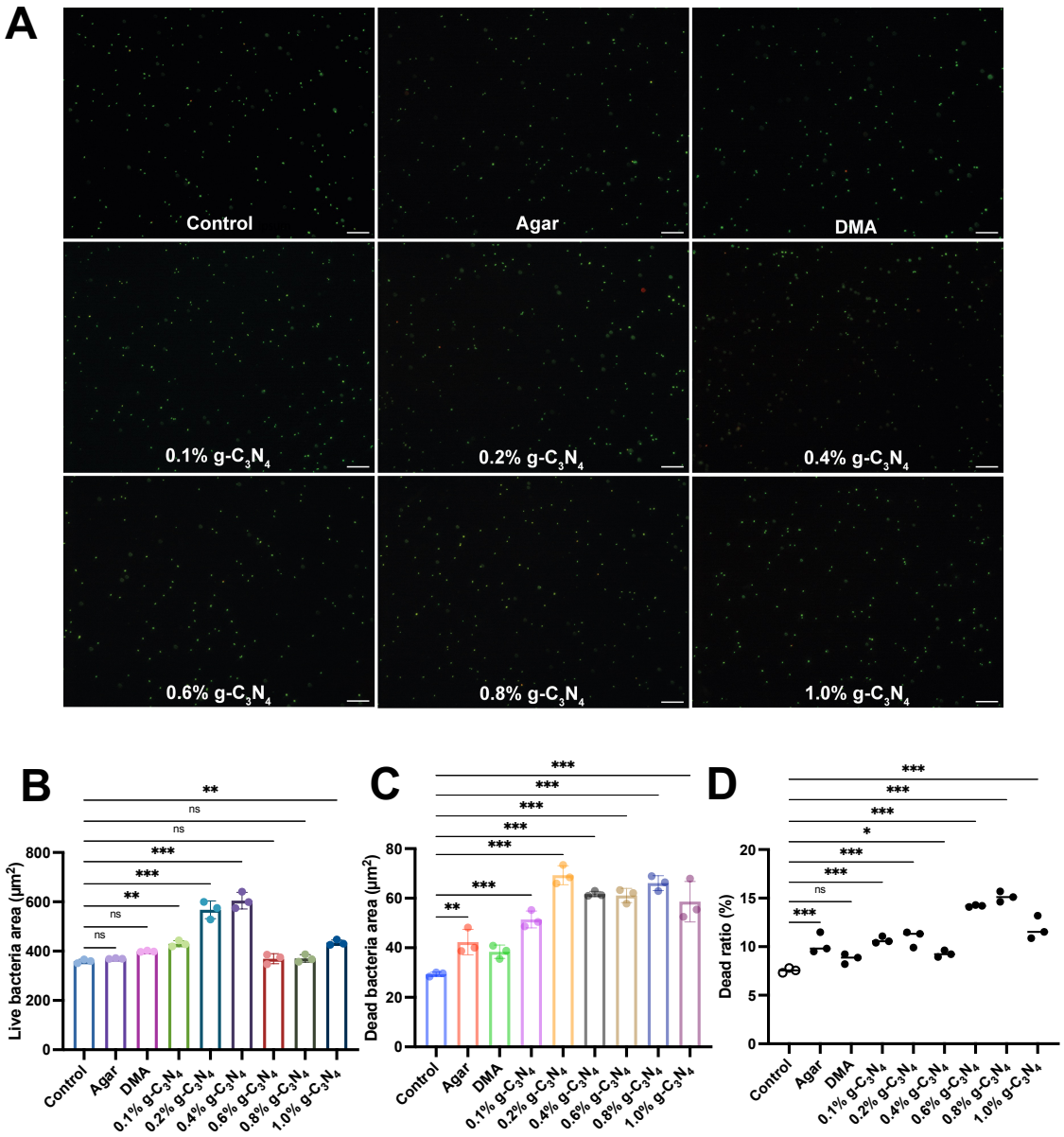

Fig. 3.8 (A) Live / Dead images of 24-hours tested hydrogels covered *S. epidermidis*, the scale bar is 50 μm. (B) Live signal from A. (C) Dead signal from A. (D) Dead ratio calculated from A. Data are presented as $mean \pm SD$ (n = 3). Statistical analysis was performed using one-way ANOVA followed by Dunnett's post hoc test. $P \leq 0.05$ was considered statistically significant (* $p \leq 0.05$, **$p \leq 0.01$, *** $p \leq 0.001$, **** $p \leq 0.0001$). Statistical analysis was conducted using GraphPad Prism 10.0.

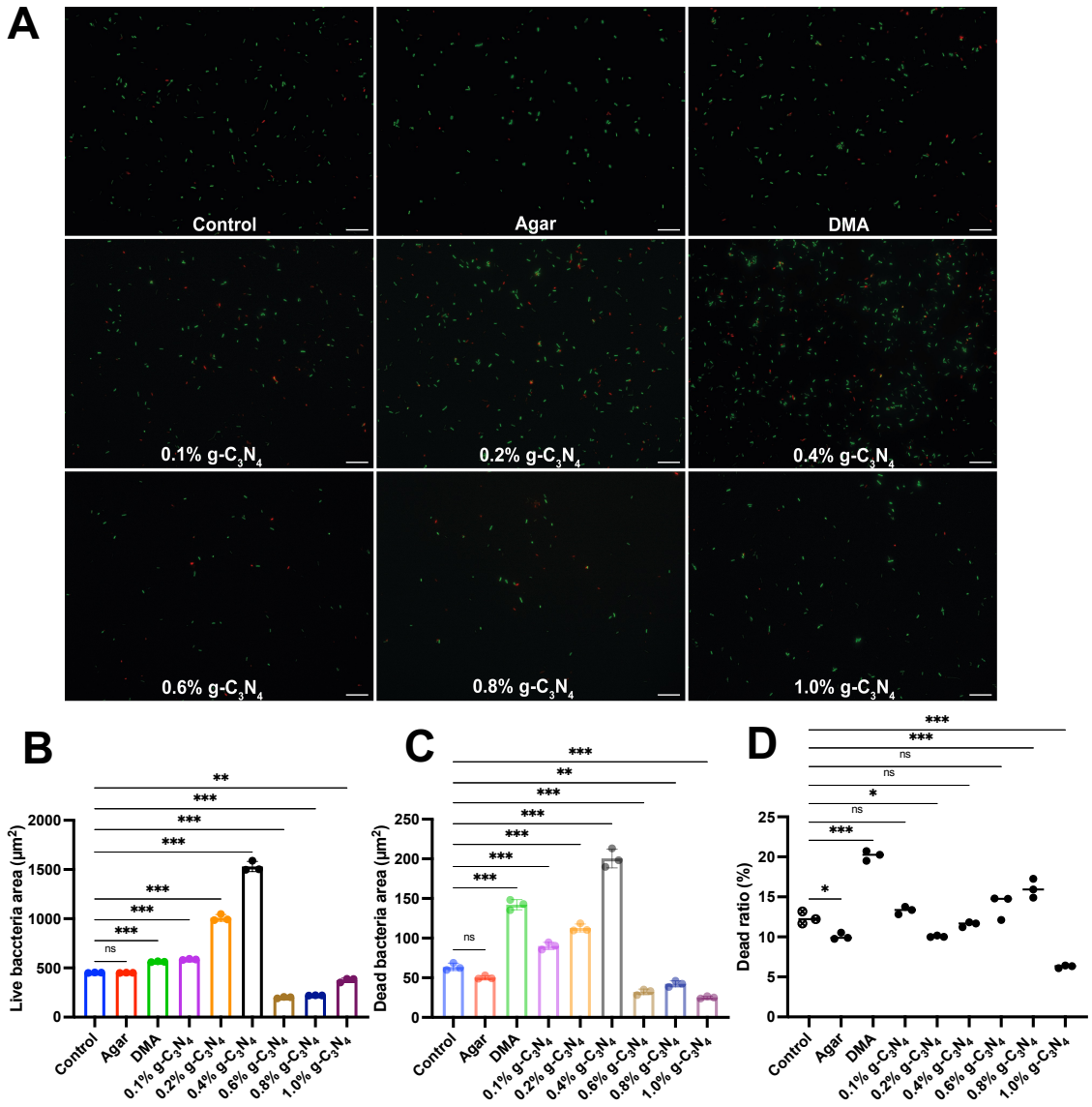

Fig. 3.9 (A) Live / Dead images of 24-hours tested hydrogels covered *E. Coli – DH 5α*, the scale bar is 50 μm. (B) Live signal from A. (C) Dead signal from A. (D) Dead ratio calculated from A. Data are presented as $mean \pm SD$ (n = 3). Statistical analysis was performed using one-way ANOVA followed by Dunnett's post hoc test. $P \leq 0.05$ was considered statistically significant (* $p \leq 0.05$, **$p \leq 0.01$, *** $p \leq 0.001$, **** $p \leq 0.0001$). Statistical analysis was conducted using GraphPad Prism 10.0.)

3.2.5 Mammalian cell function influenced by g-C_3N_4 hydrogels

Successful wound healing requires both the bacterial elimination and the activation of mammalian cells. The specific re-epithelialisation phase in wound healing depends on skin

epithelial cells dragging themselves to cover and form the new wound matrix. Therefore, the health and mobility of these cells are crucial for wound closure.

Morphology change of fibroblast cells covered by g-C_3N_4 hydrogels

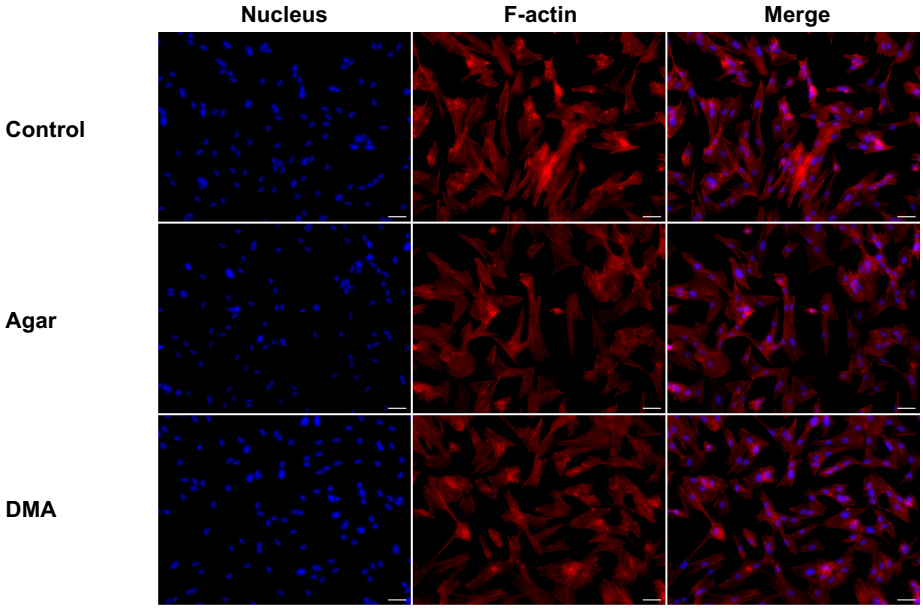

Fig. 3.10 Morphology change of fibroblast cells covered by agar gel and DMA hydrogel, nucleus was stained by DAPI and F-actin was stained with Rhodamine-Phalloidin. The scale bar is 50μm.

First, as the predominant stromal cell in soft connective tissues, the morphology of fibroblast cells covered by g-C_3N_4 hydrogels was observed using F-actin and nucleus staining. Compared to the blank control group, fibroblast cells covered by all tested hydrogel (agar, DMA, 0.1% g-C_3N_4, 0.2% g-C_3N_4, 0.4% g-C_3N_4, 0.6% g-C_3N_4, 0.8% g-C_3N_4 and 1.0% g-C_3N_4) showed similar F-actin and nucleus staining, with stretched fibres, plump spindle shape and centrally placed oval nucleus (**Figure 3.10, 3.11, 3.12**).

Single cell area, aspect ratio, and roundness (**Figure 3.13**) were quantified from the obtained fluorescence images. No statistical difference was discovered between the negative control group and the hydrogel-covered groups, meaning only hydrogel-covering has no observed adverse effect on fibroblast structure.

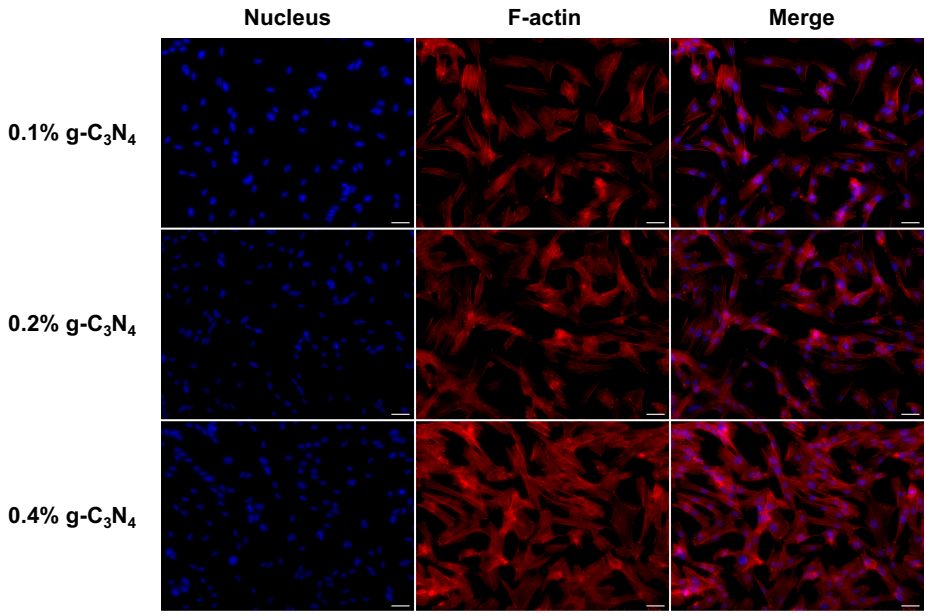

Fig. 3.11 Morphology change of fibroblast cells covered by 0.1%, 0.2% and 0.4% g-C_3N_4 hydrogel, nucleus was stained by DAPI and F-actin was stained with Rhodamine-Phalloidin. The scale bar is 50μm.

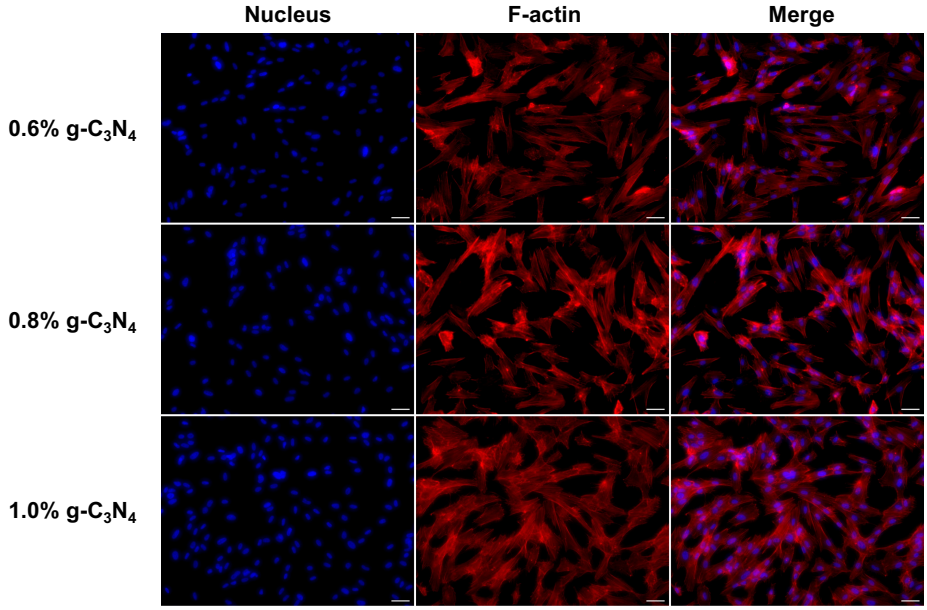

Fig. 3.12 Morphology change of fibroblast cells covered by 0.6%, 0.8% and 1.0% g-C_3N_4 hydrogel, nucleus was stained by DAPI and F-actin was stained with Rhodamine-Phalloidin. The scale bar is 50μm.

Migration of fibroblast cells covered by g-C_3N_4 hydrogels

After this, the migration capability of fibroblast cells under the same condition was also evaluated. A wound healing or scratch assay was used for the *in vitro* migration experimental

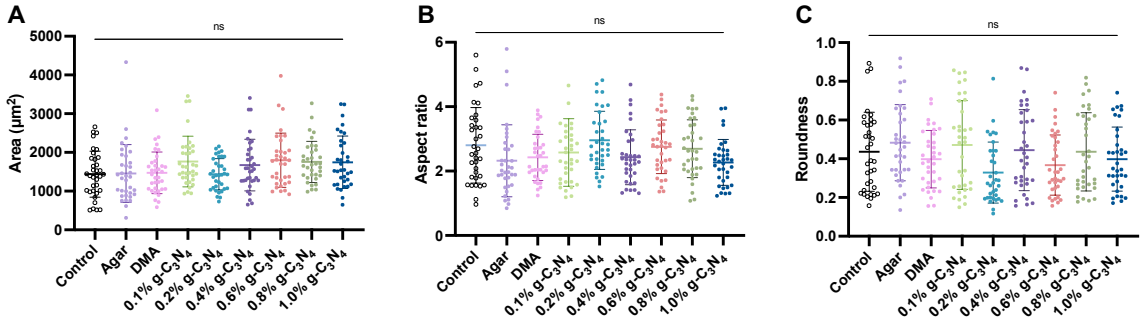

Fig. 3.13 Analysis of fibroblast cells morphology after covered by hydrogels. (A) Single cell area. (B) Aspect ratio of fibroblast cells. (C) Roundness of fibroblast cells. Data are presented as $mean \pm SD$ (n = 35). Statistical analysis was performed using one-way ANOVA followed by Dunnett's post hoc test. $P \leq 0.05$ was considered statistically significant (* $p \leq 0.05$, **$p \leq 0.01$, *** $p \leq 0.001$, **** $p \leq 0.0001$). Statistical analysis was conducted using GraphPad Prism 10.0.

model. The formed gap was covered by hydrogel for 24 hours, and then the cells were cultured with fresh complete DMEM for 12, 24, and 72 hours (**Figure 3.14, 3.15, 3.16**).

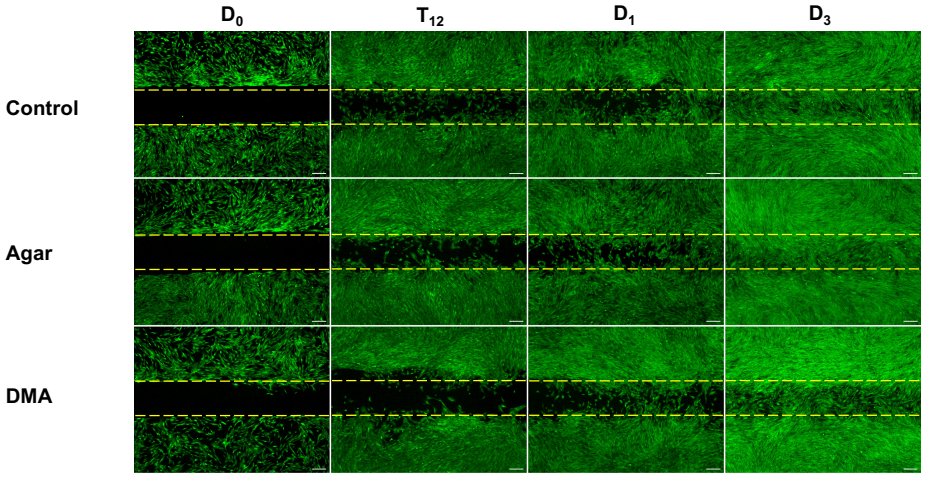

Fig. 3.14 Migration assay of fibroblast cells covered by hydrogels. Control group, agar gel and DMA hydrogel group. D_0 is the gap formed originally; T_{12} is the gap after co-incubating without and with covered hydrogels for 12 hours; D_1 is the gap after co-incubating without and with covered hydrogels for 1 day (24 hours); D_3 is the gap after co-incubating without and with covered hydrogels for 3 days (72 hours). The scale bar is 200μm.

To evaluate the effect of g-C_3N_4 hydrogels on the migration behaviour of fibroblast cells, time-dependent fluorescence images were collected, and the wound closure rate was assessed by the width of the gap. The corresponding scratch closure rate is calculated as

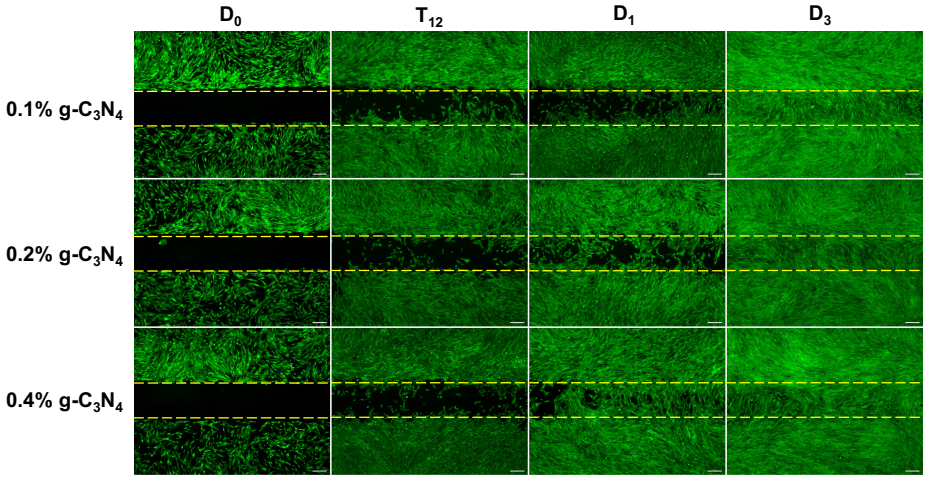

Fig. 3.15 Migration assay of fibroblast cells covered by hydrogels. 0.1% g-C_3N_4 hydrogel, 0.2% g-C_3N_4 hydrogel and 0.4% g-C_3N_4 hydrogel group. D_0 is the gap formed originally; T_{12} is the gap after co-incubating without and with covered hydrogels for 12 hours; D_1 is the gap after co-incubating without and with covered hydrogels for 1 day (24 hours); D_3 is the gap after co-incubating without and with covered hydrogels for 3 days (72 hours). The scale bar is 200μm.

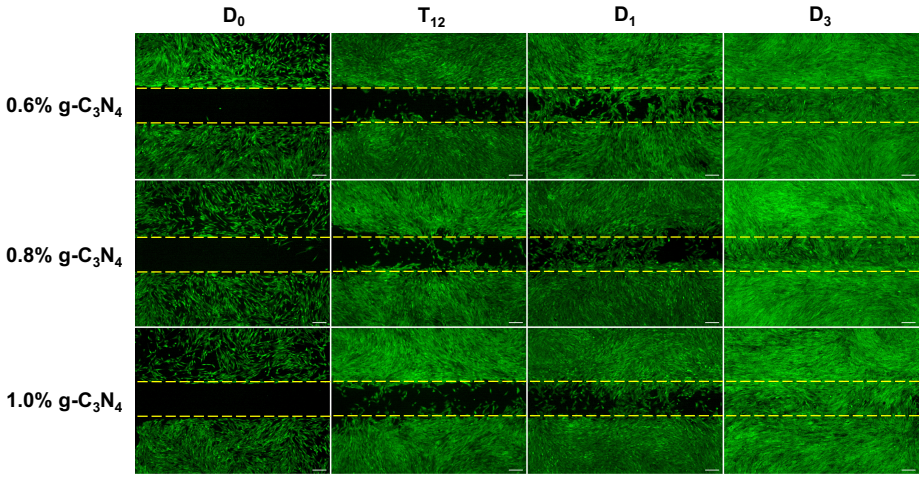

Fig. 3.16 Migration assay of fibroblast cells covered by hydrogels.0.6%, 0.8% and 1.0% g-C_3N_4 hydrogel group. D_0 is the gap formed originally; T_{12} is the gap after co-incubating without and with covered hydrogels for 12 hours; D_1 is the gap after co-incubating without and with covered hydrogels for 1 day (24 hours); D_3 is the gap after co-incubating without and with covered hydrogels for 3 days (72 hours). The scale bar is 200μm.

below:

$$\text{Scratch closure rate}(\%) = \frac{W_0 - W_t}{W_0} \times 100 \tag{3.1}$$

Where W_0 is the width of initial wound.
W_t is the width after treatment of interested period.

After the first 12-hour culture (**Figure 3.17A**), DMA-covered fibroblast cells presented a lower migration and proliferation activity with a 14% closure rate, which the strong oxidative effect of DMA hydrogel might cause. Agar gel and 0.1% g-C_3N_4 hydrogel-covered fibroblast showed 27.9% and 29.7% closure rates, respectively, higher than the negative control group, which showed a 27% closure rate after 12 hours of refreshing. Statistical difference was observed in the rest of the test groups, with around 20% migration capability.

After 24 hours of culture (**Figure 3.17B**), the DMA group still showed a compromised

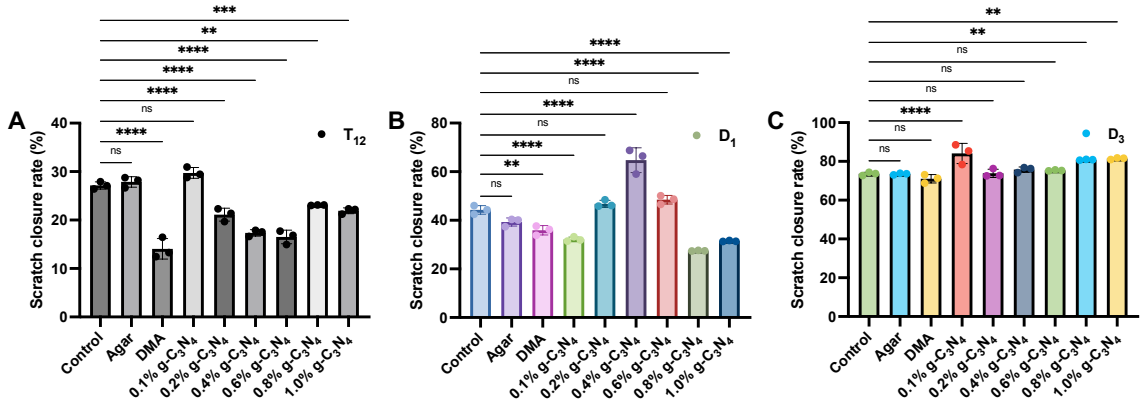

Fig. 3.17 Analysis of fibroblast cell migration covered by agar, DMA and 0.1%, 0.2%, 0.4%, 0.6%, 0.8% and 1.0% g-C_3N_4 hydrogels for 24 hours, then the migration status of scratched fibroblast cells were measured after normal culture for another (a) 12-hours, (b) 1 day and (c) 3 days. Data are presented as $mean \pm SD$ (n = 3). Statistical analysis was performed using one-way ANOVA followed by Dunnett's post hoc test. $P \leq 0.05$ was considered statistically significant (* $p \leq 0.05$, **$p \leq 0.01$, *** $p \leq 0.001$, **** $p \leq 0.0001$). Statistical analysis was conducted using GraphPad Prism 10.0.

closure status, with a 35% closure rate compared to the control group (44%). On the contrary, the 0.4% g-C_3N_4 hydrogel-treated group displayed a significant difference from other groups, with a 64.7% closure rate. Continuously culture to 72 hours (**Figure 3.17C**), all test groups showed a great wound closure performance with around 80% gap covering. According to the obtained data, no apparent impairment in the migration and proliferation behavior of fibroblast cells is observed after they are covered by all hydrogels, giving positive support for their intrinsic cytocompatibility.

3.2.6 Cytocompatibility of g-C_3N_4 hydrogel

As the hydrogel is to interface with an open wound environment, where different types of mammalian cells are presented, cytocompatibility of g-C_3N_4 in all concentrations was evaluated, and DMA hydrogel was the synthetic control hydrogel.

The cytocompatibility test was performed *in vitro* using hTERT fibroblast cells. Two

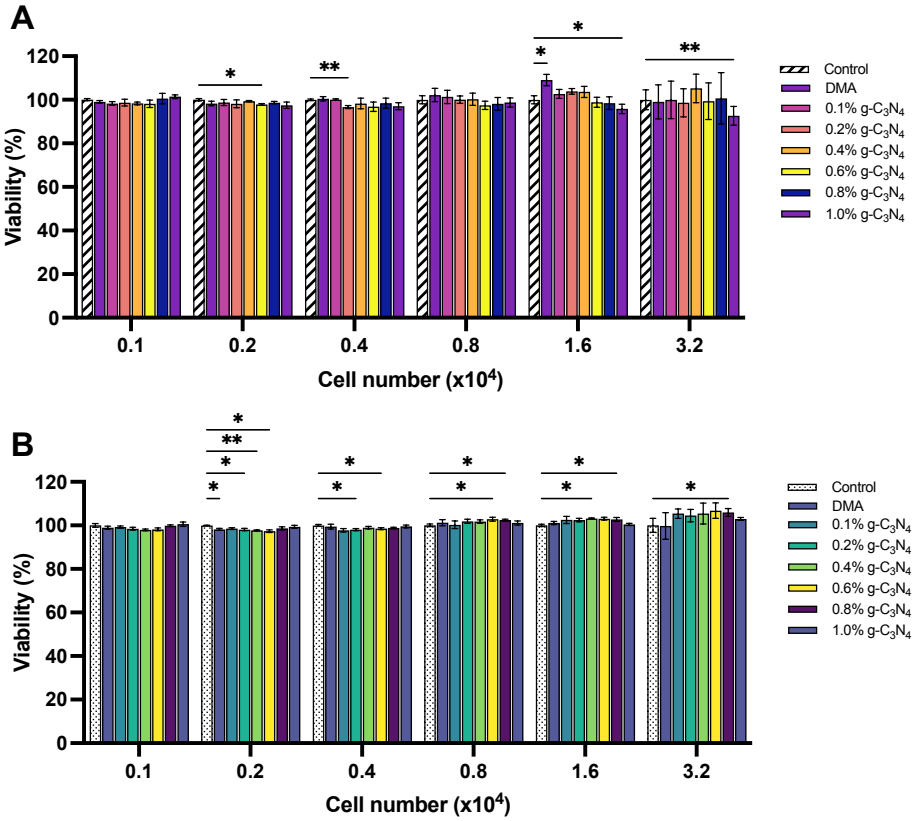

Fig. 3.18 Indirect cytocompatibility of g-C_3N_4 hydrogels. (A) Cytocompatibility using 24-hours conditional medium from g-C_3N_4 in different concentrations. (B) Cytocompatibility using 48-hours conditional medium from g-C_3N_4 in different concentrations. Data are presented as *mean* $\pm$ *SD* (n = 3). Statistical analysis was performed using Two-way ANOVA followed by Turkey's post hoc test. P $\leq$ 0.05 was considered statistically significant (* p $\leq$ 0.05, **p $\leq$ 0.01, *** p $\leq$ 0.001, **** p $\leq$ 0.0001). Statistical analysis was conducted using GraphPad Prism 10.0.

different test schemes were applied here; in the first scheme, conditional cell culture medium was prepared by immersing tested hydrogel disc (10 mm in diameter and 2 mm in thickness) into complete DMEM for 24 hours and 48 hours, different number of fibroblast cells were cultured with the obtained conditional medium to evaluate the damage caused by harmful substances released from g-C_3N_4 hydrogels. *PrestoBlue* assay was carried out to quantify the

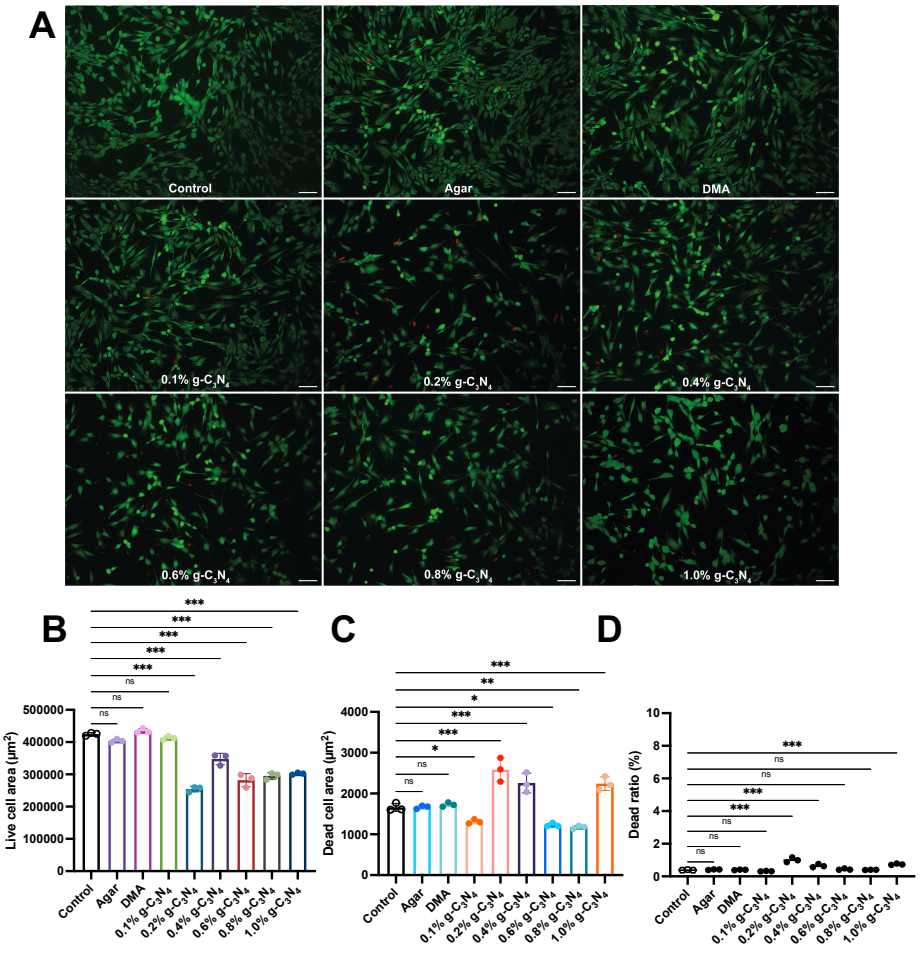

Fig. 3.19 Direct cytocompatibility covered by g-C_3N_4. (A) Live / Dead fluorescence image of fibroblast cells covered by all g-C_3N_4 hydrogels. Scale bar is 100μm. (B) Live cell area from fluorescence images. (C) Dead cell area from fluorescence images. (D) Dead ratio of fibroblast cells from figure A. Data are presented as $mean \pm SD$ (n = 3). Statistical analysis was performed using one-way ANOVA followed by Dunnett's post hoc test. $P \leq 0.05$ was considered statistically significant (* $p \leq 0.05$, **$p \leq 0.01$, *** $p \leq 0.001$, **** $p \leq 0.0001$). Statistical analysis was conducted using GraphPad Prism 10.0.

viability of conditional medium cultured fibroblast cells; 24-hour samples showed excellent viability in all tested hydrogel groups with different cell numbers, and a slight viability decrease was observed in 1.0% g-C_3N_4 conditional medium cultured 1.6×10^4 cells and 3.2×10^4 cells (**Figure 3.18A**), with average viability of 95% and 92%, respectively. No significant viability decline was shown in 48-hour conditional medium test groups (**Figure 3.18B**); these data showed that g-C_3N_4 conditional medium has no impairment on cell live status within all tested periods.

After this, fibroblast cell viability was studied by exposing attached bacterial cell layers

to g-C_3N_4 hydrogel with various g-C_3N_4 material concentrations, 0.1%, 0.2%, 0.4%, 0.6%, 0.8% and 1.0% for 24 hours of co-incubation, all tested hydrogels showed no obvious harm to fibroblast cells live status (**Figure 3.19**).

Live (**Figure 3.19B**) and dead (**Figure 3.19C**) cell number extracted from fluorescence images are varied, because the extracted data is heavily affected by the cell number under the view, thus, normalised dead ratio of every sample was calculated (**Equation 3.2**) to compare the viability among all tested groups to blank control.

$$\text{Dead ratio}(\%) = \frac{\text{Fluorescence intensity}_{\text{Dead}}}{\text{Fluorescence intensity}_{\text{Live}} + \text{Fluorescence intensity}_{\text{Dead}}} \times 100 \qquad (3.2)$$

It was observed that, after 24 hours the nomalised dead ratio of all tested groups was lower than 2% (**Figure 3.19D**), which proves the biocompatibility performance of g-C_3N_4 hydrogel at all concentrations.

3.2.7 Cell attach capability on g-C_3N_4 hydrogel surface

To further optimise the contact method between g-C_3N_4 hydrogel and bacterial/mammalian cells, the attach capability was investigated by seeding the bacteria and fibroblast cells on all g-C_3N_4 hydrogels and co-incubating for 24 hours. The attached bacteria and fibroblast cells were stained with the Live / Dead assay kit for bacteria and mammalian cells. Fluorescence images were collected to reveal the details. The attached E. coli—DH 5α cell number was around 1×10^6 cells per cm^2 (**Figure 3.20B**). 0.2% g-C_3N_4 hydrogel showed the lowest bacterial attach capability. No statistical differences were observed among all g-C_3N_4 hydrogels, showing no obvious effect of doped g-C_3N_4 material. The attachment could be attributed to the small size of the bacteria, making it easier for them to be trapped on the hydrogel surface.

For the fibroblast cells, around 5000 fibroblast cells were counted on the hydrogel surface after co-incubating. Live / Dead staining was carried out on cells attached to the hydrogel surface (**Figure 3.21**). Images collected from samples can only represent the fibroblast cell roughly attach capability because the completely stretched cell area is around 2000 μm^2, and the cross-section area of the tested hydrogel is only 0.785 cm^2.

Obtained images were quantified and compared to the cells seeded on a tissue culture petri dish with 2000 μm^2 area. The fibroblast cells on the hydrogel surface in 1000 μm^2 are much smaller (**Figure 3.22A**); this might be caused by the stiffness and chemical bonds of the hydrogel surface, leading to a different mechano-interaction. The aspect ratio accumulated between 1-2 (**Figure 3.22B**) instead of 2-6, indicating the adhesion of fibroblast cells on g-C_3N_4 hydrogel might partially be embedded into hydrogels, so they tended to have a

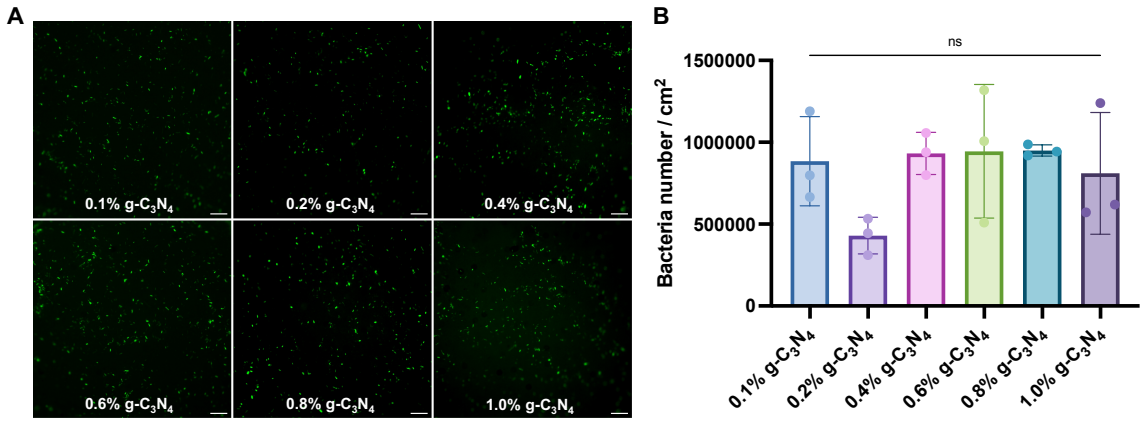

Fig. 3.20 Bacterial attach capability. (A) Fluorescence images of *E. coli - DH 5α* attached on different g-C_3N_4 hydrogel surface. The scale bar is 20 μm. (B) Bacterial cell number counting on g-C_3N_4 hydrogel surface after co-incubating for 24 hours. Data are presented as $mean \pm SD$ (n = 3). Statistical analysis was performed using one-way ANOVA followed by Dunnett's post hoc test. P $\leq$ 0.05 was considered statistically significant (* p $\leq$ 0.05, **p $\leq$ 0.01, *** p $\leq$ 0.001, **** p $\leq$ 0.0001). Statistical analysis was conducted using GraphPad Prism 10.0.

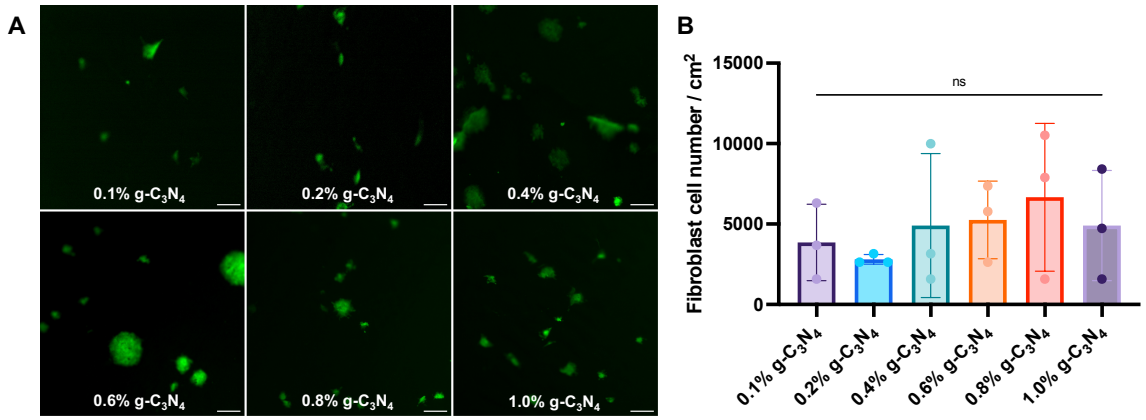

Fig. 3.21 Fibroblast cells attach capability. (A) Fluorescence images of fibroblast cells attached on different g-C_3N_4 hydrogel surface. The scale bar is 50 μm. (B) Fibroblast cell number counting on g-C_3N_4 hydrogel surface after co-incubating for 24 hours. Data are presented as $mean \pm SD$ (n = 3). Statistical analysis was performed using one-way ANOVA followed by Dunnett's post hoc test. P $\leq$ 0.05 was considered statistically significant (* p $\leq$ 0.05, **p $\leq$ 0.01, *** p $\leq$ 0.001, **** p $\leq$ 0.0001). Statistical analysis was conducted using GraphPad Prism 10.0.

spherical morphology (**Figure 3.22C**) and lack actin stress fibres.

No significant difference in fibroblast cell adhesion on g-C_3N_4 hydrogel was observed

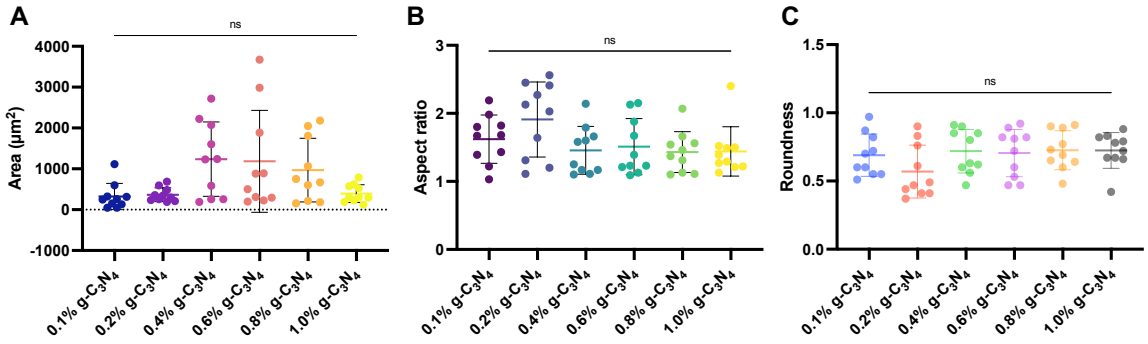

Fig. 3.22 Analysis of fibroblast cells on g-C_3N_4 hydrogel surface. (A) Area of fibroblast cells on g-C_3N_4 hydrogel surface. (B) Aspect ratio of fibroblast cells on g-C_3N_4 hydrogel surface. (C) Roundness of fibroblast cells on g-C_3N_4 hydrogel surface. Data are presented as *mean* $\pm$ *SD* (n = 10). Statistical analysis was performed using one-way ANOVA followed by Dunnett's post hoc test. P $\leq$ 0.05 was considered statistically significant (* p $\leq$ 0.05, **p $\leq$ 0.01, *** p $\leq$ 0.001, **** p $\leq$ 0.0001). Statistical analysis was conducted using GraphPad Prism 10.0.

across all g-C_3N_4 hydrogels; results revealed that fibroblast cells showed lower attach capability than bacteria cells after culturing on the hydrogel.

3.3 Discussion

The first step of this work is to create a light-responsive hydrogel suitable for open chronic wound environments by doping g-C_3N_4 materials into a polymerisation system already developed in our previous study mentioned above.

g-C_3N_4 hydrogel was prepared. It is a photo-crosslinked hydrogel polymerised using graphitic carbon nitride (g-C_3N_4), a metal-free photocatalyst material, as both initiator and reinforcer. It can easily be polymerised using visible light irradiation at room temperature. Spectroscopic characterisations confirmed that the intrinsic semiconductor properties of the added g-C_3N_4 material were retained in this hydrogel form, so the material could be used as the bandage for the nonhealing wound site while further LED light activation process was not impaired.

Water retention capability tests revealed a moderate water vapour in g-C_3N_4 hydrogels; the specific chronic wound site may continuously generate excess wound exudate fluid; when the hydrogel is applied, this water escape helps with the absorbance of wound fluid on the covered wound site, creating a clean and moist environment for improved healing[140, 141]. The examination of swelling capability among all hydrogels suggested that g-C_3N_4 hydrogel showed significant recovery after drying out but no additional swelling; this makes it a great

candidate for chronic wounds. This moderate swelling ratio aids fluid absorption while maintaining its structure and effectiveness, reducing the risk of hydrogel structure breakdown or degradation. Moreover, this appropriate swelling ratio is beneficial for hydrogel adherence and secondary injury to the wound site due to extra pressure from the swollen hydrogel might also be avoided effectively.

Biocompatibility is a significant factor that needs to be evaluated for all biomedical materials. First, the intrinsic antibacterial properties of g-C_3N_4 hydrogels against *S. epidermidis* and *E. Coli – DH 5*α were tested. All assays were performed by examination of the bacterial activity upon direct contact of the bacteria with g-C_3N_4 hydrogels. The growth curve of bacteria showed no difference compared to the negative control groups, but colonies forming units counting decreased obviously in the g-C_3N_4 treated group; one possible explanation could be that the proliferation of bacterial was not impaired, but the viability was affected by the covalent bond and degraded substance from g-C_3N_4 hydrogel.

Further, Live / Dead staining confirmed that direct cover of g-C_3N_4 hydrogel does not introduce damage to bacteria and fibroblast cells, implying its outstanding biocompatibility with no light illumination. Morphology staining and migration of HUVECs excludes that only g-C_3N_4 hydrogel covering leads to no possible adverse effect, such as hypoxia condition[77], to hinder the normal functions of mammalian cells. In this work, active species released from g-C_3N_4 hydrogel after light irradiation is a significant factor for the subsequent work. Thus, the attachment capability of bacteria and fibroblast cells was tested first; compared to bacteria, the attachment capability of fibroblast cells on g-C_3N_4 is much lower, with around 4000 cells per cm^2; this evidence showed that the mammalian cells had no affinity to the g-C_3N_4 hydrogel, the higher number of bacteria attached on hydrogel surface could attribute to its small volume or surface properties, general, these results gave us a clue that the bacteria are capable of staying much closer to the g-C_3N_4 hydrogel, getting more chances to be exposed to the active species from g-C_3N_4 hydrogels.

3.4 Conclusion

In this chapter, a batch of g-C_3N_4 hydrogels, including 0.1%, 0.2%, 0.4%, 0.6%, 0.8% and 1.0% g-C_3N_4 materials contained, were prepared through the free-radical based polymerisation process. The light source was the 460 nm catered visible LED light with 48.15 mW/cm^2 of power density at 10 cm. Before the polymerisation process is initiated, the light-induced temperature variation was monitored using the Piclog thermocouple under 60 minutes of irradiation of 2 mL of deionised water - as the polymerisation solution of g-C_3N_4 hydrogels is also kept between 2 mL to 3 mL, obtained maximum temperature is 28 °C at

60 minutes, which demonstrate this polymerisation proceeded under a moderate condition, different from previous free radical polymerised hydrogels[200, 201] that are initiated under strict conditions, such as UV light irradiation, high-temperature dissolve and long periods of gelation. The water retention capability and swelling ratio of prepared g-C_3N_4 hydrogels were measured using the method described in Chapter 2; hydrogels contained lower g-C_3N_4 materials, including 0.1%, 0.2%, 0.4% and 0.6% g-C_3N_4 materials, showing 40% of water remaining after 6 hours of exposure in room temperature and 25% of water after 25 hours of exposure. But 0.8% and 1.0% g-C_3N_4 hydrogel kept less water with lower than 10%. All prepared g-C_3N_4 hydrogels presented moderate swelling capability after being immersed in deionised water for 24 hours, which is beneficial for the wound site to avoid second-pressure damage.

The UV-Vis spectrometer measured absorption wavelength proves the optical properties of g-C_3N_4 material were kept in the 0.4% g-C_3N_4 dispersion, indicating the extra optical property endowed in the g-C_3N_4-based hydrogel. The temperature measurement of 0.4% g-C_3N_4 dispersion further excludes the potential of the photothermal effect.

The intrinsic antibacterial properties and cytocompatibility of g-C_3N_4 hydrogels were evaluated using the methods adapted from previous work[202]. Antibacterial properties of g-C_3N_4 hydrogels were assessed using optical density measurement and colonies forming units counting method, showing the impaired viability of bacterial cells after co-incubating with immersed g-C_3N_4 hydrogel disc. In the direct contact test, bacterial cells under the cover of g-C_3N_4 hydrogels presented no obvious damage, as the calculated dead ratio of bacteria cells in the test group is statistically higher than the value in the control group. The cytocompatibility of fibroblast cells was also studied using PrestoBlue test and Live/dead staining methods, demonstrating good biocompatibility with a dead ratio of covered fibroblast cells below 2%. Under the simple cover of g-C_3N_4 hydrogels, fibroblast cell morphology and migration performance were measured using fluorescence images, confirming that the hydrogel coverage will not affect the basic functions of cells in the absence of light source irradiation. Attachment tests of bacteria and mammalian cells on the hydrogel surface proved that the bacteria are much easier resident on the g-C_3N_4 hydrogel surface than fibroblast cells under the same test conditions.

In all, in this part, we described the prepared visible light polymerised hydrogel with g-C_3N_4 material doped in. This hydrogel successfully retains the optical properties of two-dimensional g-C_3N_4 materials while forming a well-behaved and biocompatible hydrogel format, which could be used for wound healing bandages. The present work suggests that our g-C_3N_4 hydrogel has excellent potential as a visible LED light-activated biomaterial for wound healing applications.

Chapter 4

Interactions of Reactive Oxygen Species (ROS) Generated by g-C_3N_4 Hydrogels with Bacteria and Mammalian Cells

4.1 Introduction

Reactive oxygen species (ROS) is a generic term for various highly active molecules derived from oxygen; they belong to a large family of reactive species, including reactive nitrogen, sulfur, carbon and so on, undergoing redox (reduction-oxidation) reactions to generate oxidative modifications on biological molecules, participating into downstream redox signalling and biological functions[176]. This collective term of ROS includes not only oxygen radicals with hydroxyl radical ($\cdot OH$) and superoxide anion ($O_2^{\cdot -}$) but also some non-radical derivatives of O_2 such as hydrogen peroxide (H_2O_2). Their activity is also a relative description; hydrogen peroxide (H_2O_2) and superoxide anion ($O_2^{\cdot -}$) existed with moderate activity; they present unreactive with most biomolecules; however, the hydroxyl radical ($\cdot OH$) attacks every molecule within the effective radius.

Down to the specific species, superoxide anion ($O_2^{\cdot -}$) primarily generated by one-electron transfer to O_2 in mitochondrial electron transport chains (ETC), it existed at a very low concentration of about 10^{-11} M[173], much lower than that of H_2O_2 at 10^{-8} M. Comparing to hydroxyl radical, superoxide anion ($O_2^{\cdot -}$) possess weak oxidative and reduces capability as it is a one-electron radical, usually reacts with Fe-S clusters and other transition metal ions to release iron, it also react rapidly with encountered radicals to give secondary products but the primary fate of superoxide anion is fast dismutation with another $O_2^{\cdot -}$ to form O_2 and H_2O_2.

H_2O_2 is a significant redox signalling factor with pleiotropic functions[177]. Intracellular H_2O_2 keeps a low concentration at approximately 1-100 nM; this concentration of H_2O_2 plays a similar role as Ca^{2+} in cells. The steady-state physiological flow of H_2O_2 to specific destinated proteins results in reversible oxidation, affecting protein activity and interactions, thus leading to various cellular functionalisation and evolution, such as cell proliferation, differentiation and angiogenesis. H_2O_2 is mainly produced by mitochondrial electron transport chains, NADPH oxidases combing with superoxide dismutase, and other enzymes.

Hydroxyl radical ($\cdot$OH) is the most reactive ROS, which oxidises the molecules non-specifically at a diffusion-controlled rate. It usually forms through the catalyse of H_2O_2 by metal ions such as Fe^{2+} and Cu^{2+}; thus, the possible oxidative target of $\cdot$OH could roughly be determined by the location of transition metals and hydrogen peroxide due to its short lifetime and highly reactivity. Most oxidative stress in cells is caused by hydroxyl radicals[203], presenting as damaged DNA, oxidised protein, severe lipid peroxidation, and even cell lysis. ROS can be generated by various sources through both endogenous and exogenous processes, and it is well-known that the supraphysiological concentration of ROS could cause irreversible damage. Thus, maintaining redox balance in the cellular environment is essential for normal metabolic processes.

Considering the specific environment of chronic wounds, progenitor cell recruitment, proliferation and growth factor release are impaired, causing compromised cellular functions and persistent inflammation stage[111]. In addition to the affected cellular factors, the open wound site is also a host to various bacteria. These microbes can be deleterious to immunocompromised individuals to prolong the healing process. Some occupying bacteria strains can also be devastating pathogens, which are especially difficult to treat due to their biofilm-forming characterisation, leading to immune evasion and antibiotic resistance. Thus, the applied wound bandages are expected to clear the bacteria in the complex environment of chronic wounds.

In Chapter 3, we developed the light-responsive hydrogel system composed of visible light cross-linkable graphitic carbon nitride (g-C_3N_4) material as a photo-initiator and reinforcer. The g-C_3N_4 hydrogel showed excellent properties as hydrogels for wound healing bandages; great biocompatibility presented no observed harm to directly contacted bacteria and fibroblast, satisfying the biomedical material. In addition, the developed g-C_3N_4 hydrogel also presented characterised optical properties as two-dimensional g-C_3N_4 material. Thus, the release of reactive oxygen species is expected.

Here, we further studied the capability of g-C_3N_4 to produce detectable reactive oxygen species (ROS) with visible light irradiation; generated ROS was measured quantitatively, and the ROS release pattern was monitored in different schemes. After this, the interaction

between g-C_3N_4 hydrogels and bacteria and fibroblast cells were evaluated, and the bacterial killing caused by g-C_3N_4 hydrogel generated ROS was confirmed with Live / Dead assay. We also determined why g-C_3N_4 hydrogel kills bacteria by introducing hydroxyl radicals in bacterial cells.

4.2 Results

4.2.1 Quantification of hydroxyl radical generated by g-C_3N_4 hydrogels

The Fenton reaction (**Equations 4.1 and 4.2**) was accepted to produce the hydroxyl radical in different concentrations to obtain a standard calibration curve to quantify the hydroxyl radical from g-C_3N_4 hydrogel.

$$\text{Primary reaction} : Fe^{2+} + H_2O_2 \rightarrow Fe^{3+} + OH^- + {}^{\cdot}OH \tag{4.1}$$

$$\text{Secondary reaction} : Fe^{3+} + H_2O_2 \rightarrow Fe^{2+} + HO_2\cdot + H^+ \tag{4.2}$$

First, a ferrous ion solution in 1-10 μM concentration was prepared. The *o*-phen was used for the photometric determination of ferrous ion (Fe^{2+}) with a prominent absorption peak at 510 nm (**Figure 4.1A, Equation 4.3**), and a linear calibration curve was obtained between standard ferrous ion solution and absorbance value at 510 nm (**Figure 4.1B**).

$$\textit{o}\text{-pen reaction} : 3\,C_{12}H_8N_2 + Fe^{2+} \rightarrow [Fe(C_{12}H_8N_2)]^{2+} \tag{4.3}$$

The Fenton reaction was initiated with a molar ratio of Fe^{2+} : H_2O_2 in 1:1.5; the concentration of ferric ions in production presented the same molar concentration as the hydroxyl radical (**Figure 4.1C**), which is further confirmed by the degradation of the Coomassie brilliant blue (CBB) solution at 588 nm. Therefore, the standard calibration curve for the hydroxyl radical of 1-10 μ M was calculated using the change in absorbance values (**Figure 4.2**).

To confirm whether the hydroxyl radical will be generated from g-C_3N_4 hydrogel, prepared g-C_3N_4 hydrogel disc with 10 mm in diameter and 2 mm in thickness was immersed in 10 μM CBB solution, 460 nm cantered LED light was applied to the hydrogel immersed CBB solution, after 30, 60, 90, 120, 150 and 180 minutes of irradiation, absorbance of CBB solution was measured, concentration of hydroxyl radical in the solution was calculated according to the obtained calibration curve in **Figure 4.2D**.

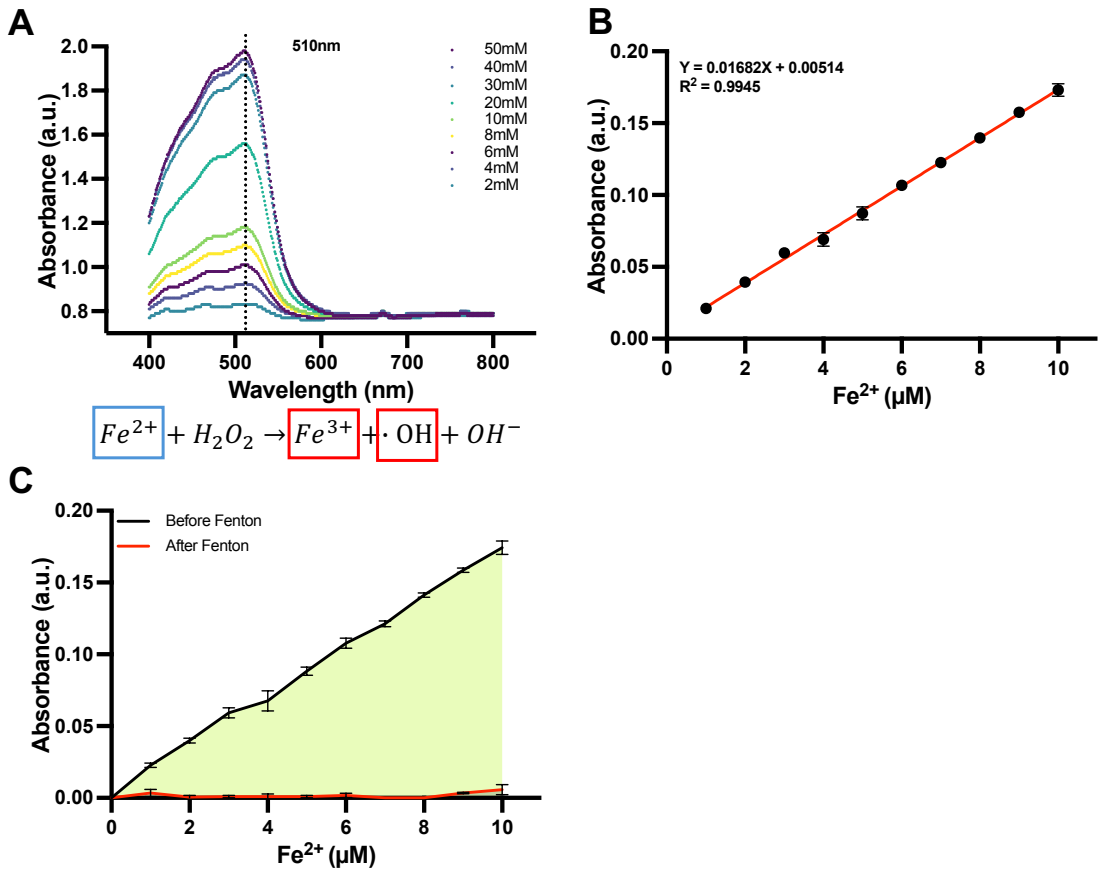

Fig. 4.1 (A) Absorption wavelength of different concentrations Fe^{2+} react with *o*-phen. (B) Standard curve of Fe^{2+} from 1 to 10 μM, using *o*-phen as indicator to measure the absorbance at 510 nm. (C) Measurement of Fe^{2+} consumption before and after Fenton reaction. Data represent mean ± SD from three independent experiments (n = 3).

Hydroxyl radicals from all hydrogels tested are shown in **Figure 4.3**; there is no generation of hydroxyl radicals from agar gel during all irradiation periods. During the same irradiation time, hydroxyl radical production from g-C_3N_4 hydrogels slightly increased as the g-C_3N_4 concentration increased. Within 180 minutes of shining, the generation of the hydroxyl radical from 0.1% and 0.2% g-C_3N_4 hydrogel was between 8 – 23 μM. When the irradiation time was up to 150 minutes, a noticeable jump in hydroxyl radical production occurred at 0.4%, 0.6%, 0.8% and 1.0% hydrogels with 25 - 30 μM of hydroxyl radical, whereas 0.2% g-C_3N_4 hydrogel can only form 17 μM under the same conditions. The maximum hydroxyl radical was 32.6 μM after 180 minutes of irradiation for 1.0% g-C_3N_4 hydrogel.

To further explore whether the hydrogel could release hydroxyl radicals in a sustainable pattern (**Figure 4.3B**), the same measurement was carried out in an ON-OFF-ON cycle

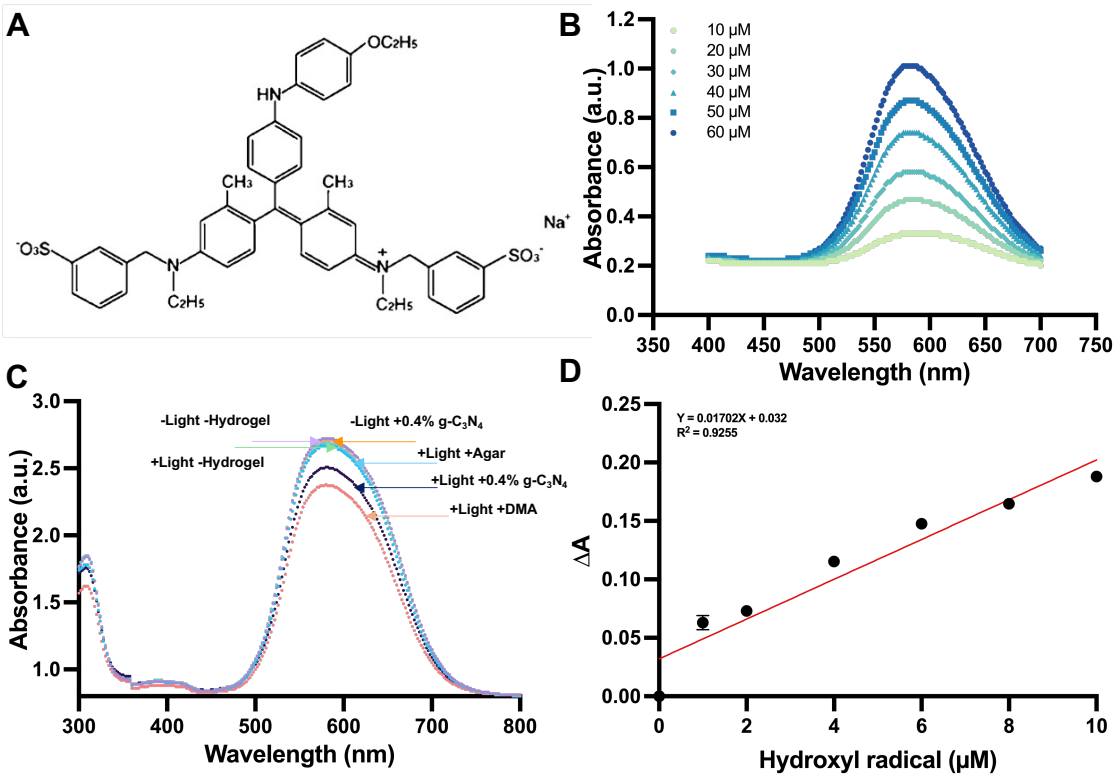

Fig. 4.2 Hydroxyl radical (·OH) calibration. (A) Chemical strucutre of Coomassie Brilliant Blue (CBB). (B) Absorption spectrum between 400 - 700 nm of CBB solution in different concentrations. (C) Absorption spectrum of CBB solution under different treatment conditions. (D) Standard calibration curve of 1 - 10 μM hydroxyl radical from Fention reaction. Linear fitting equation: Y = 0.01702X + 0.032, R^2 = 0.9255. Data represent mean ± SD from three independent experiments (n = 3).

with a duration of 30 minutes for each cycle. The supernatant was collected after the entire process and the released hydroxyl radical was measured using 10 μM CBB solution as an indicator. Compared with the hydroxyl radical from continuous irradiation, the production concentration under the ON-OFF-ON mode showed a slight increase in the concentration of generated hydroxyl radical. A sharp increase in the formation of hydrogen radicals from the DMA hydrogel was observed because in the DMA test group, degradation of the CBB solution was caused by the strong oxidative of DMA hydrogel.

4.2.2 Quantification of superoxide anion generated by g-C_3N_4 hydrogels

For superoxide anion measurement, a specific concentration of superoxide anion was formed by the enzymatic reaction initiated using xanthine and xanthine oxidase, shown in **Equation 4.4**. Nitrobule tetrazolium (NBT) was used as an indicator, as the superoxide anion

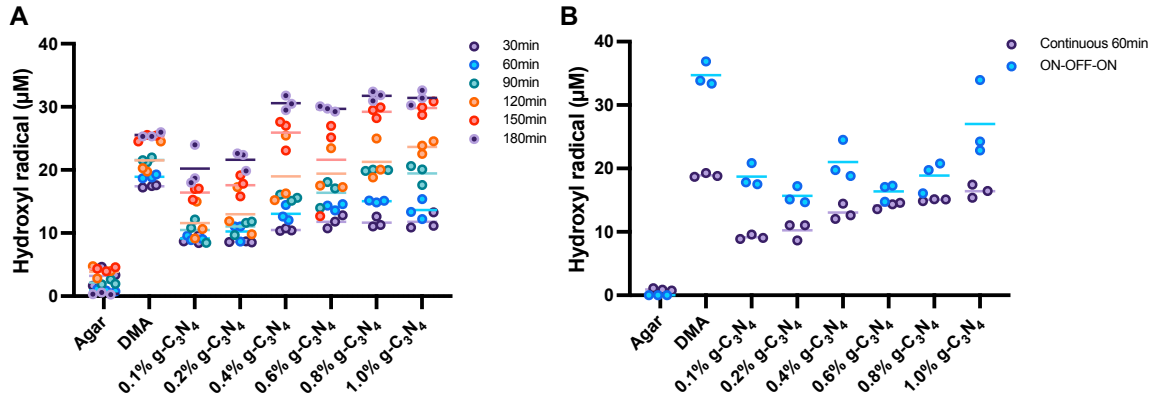

Fig. 4.3 Hydroxyl radical from g-C_3N_4 hydrogel. (A) Hydroxyl radical generated from all hydrogel discs with 10 mm in diameter and 2 mm thickness (Agar, DMA, 0.1%g-C_3N_4, 0.2% g-C_3N_4, 0.4% g-C_3N_4, 0.6% g-C_3N_4, 0.8% g-C_3N_4 and 1.0% g-C_3N_4) under 460 nm centered LED light irradiation for 30, 60, 90, 120, 150 and 180 minutes. (n=3) (B) Hydroxyl radical measurement from all hydrogel discs under continuous 60 minutes of irradiation and ON-OFF-ON mode with a 30 minutes duration for one cycle. Data represent mean ± SD from three independent experiments (n = 3).

generated in the solution would react with the NBT solution to form formazan (**Figure 4.4**), which causes an apparent change in absorption at 560 nm after being released in DMSO solution.

$$\text{Xanthine} + H_2O + 2O_2 \xrightarrow{\text{Xanthine oxidase}} \text{Urine} + 2O_2^{\cdot -} + 2H^+ \tag{4.4}$$

First, the standard calibration curve (**Figure 4.5**) of enzymatically formed superoxide anion in 31.25, 62.5, 125, 250 and 500 μM was confirmed using 1 mg/mL NBT solution. After this, to evaluate the superoxide anion generation from all hydrogels, including agar, DMA and g-C_3N_4, all hydrogel discs were immersed into 1 mg/mL of NBT solution, irradiated by the 460 nm centred LED light for 30, 60, 90, 120, 150 and 180 minutes. As the formed formazan in hydrogels is dissoluble in aqueous, all tested hydrogel discs were then immersed in DMSO overnight to release the formazan. As obtained data shown in **Figure 4.6**, agar gel and DMA hydrogel did not generate superoxide anion at all. No superoxide anion was detected from agar gel and DMA hydrogel, which also proves that the apparent decline in the absorption of CBB solution is due to the strong oxidation of the component in the DMA polymerisation system.

Superoxide anion released from 0.1% and 0.2% g-C_3N_4 hydrogel showed very slight growth from 15 μM to 30 μM (**Figure 4.6A**). When the doped concentration of g-C_3N_4

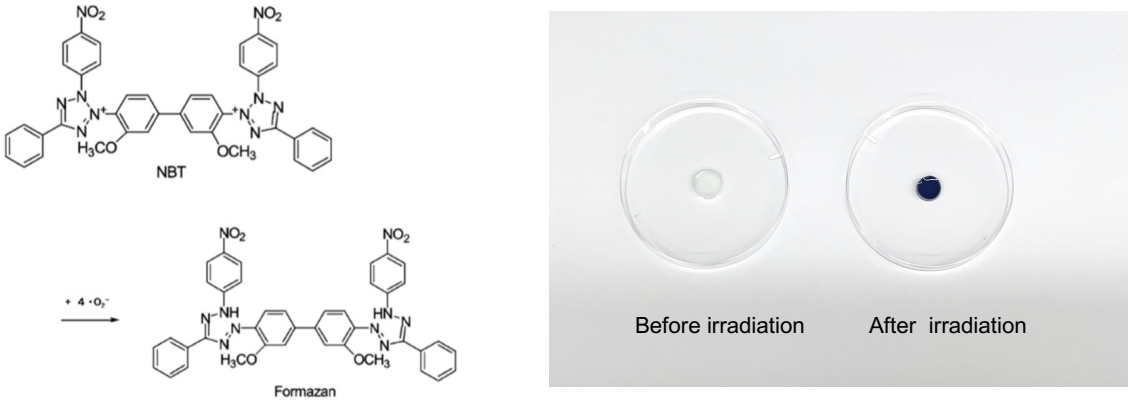

Fig. 4.4 Illustration figure of formazan formation after react with generated superoxidea anion. (A) Chemical reaction between Nitrobule tetrazolium (NBT) and superoxide anion. (B) Picture for display the g-C_3N_4 difference before and after superoxide anion generation.

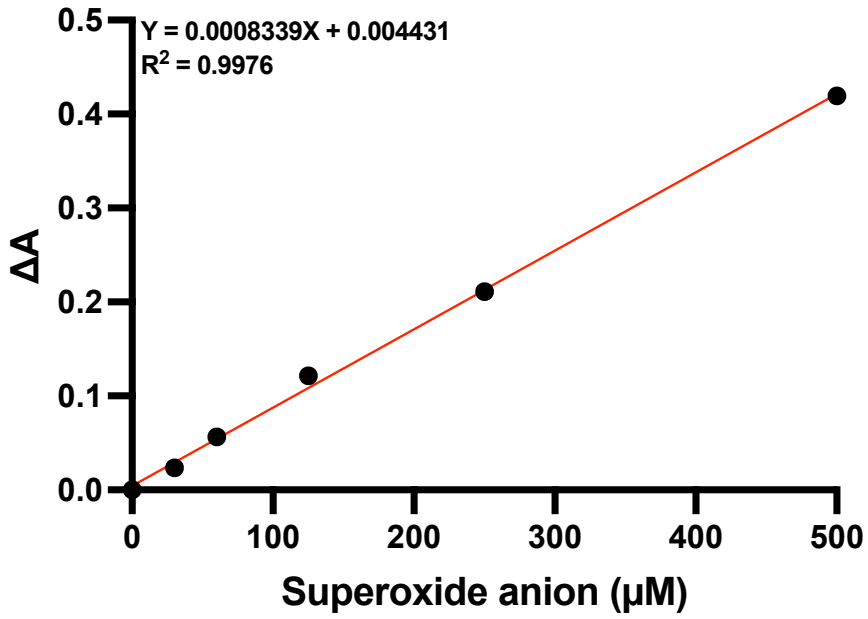

Fig. 4.5 Stanadard curve of superoxide anion from enzymatic xanthine reaction. Linear fitting equation: Y = 0.0008339X + 0.004431, R^2 = 0.9976. Data represent mean ± SD from three independent experiments (n = 3).

material up to 0.4%, 0.6%, 0.8% and 1.0% generated superoxide anion under 30 minutes of irradiation also rose to 30 – 50 μM, after 180 minutes of irradiation, formed superoxide anion concentration were between 57 – 83 μM, much higher than the value from 0.1% and 0.2% g-C_3N_4 hydrogel, which were between 19 – 41 μM. In the ON-OFF-ON mode of irradiation (**Figure 4.6B**), superoxide anion generation also presented a similar tendency as

before, under all different periods of irradiation, measured superoxide anion concentration in the second mode higher than the value from continuous 60 minutes of irradiation, with a 10 μM increment in a lower concentration of g-C_3N_4 hydrogel and 20 μM in a higher concentration of g-C_3N_4 hydrogel.

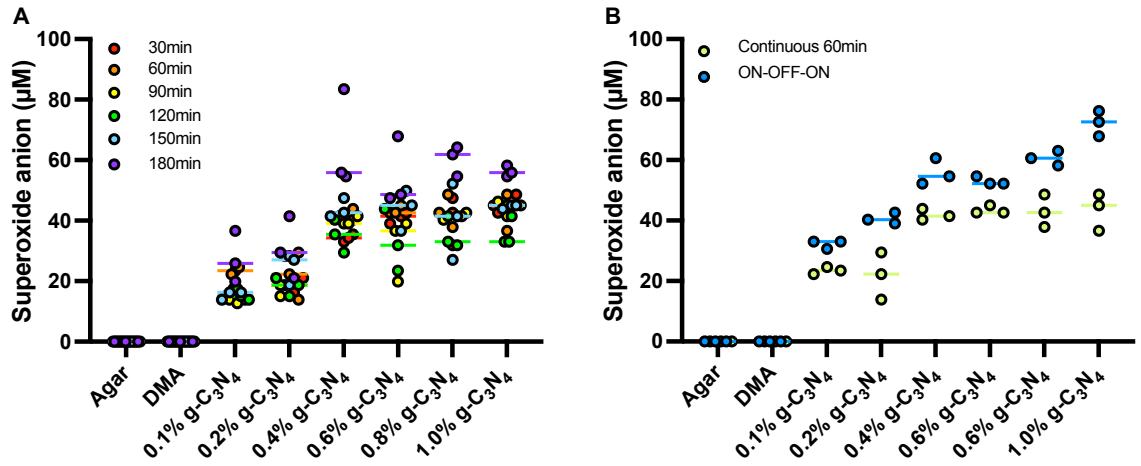

Fig. 4.6 Superoxide anion from g-C_3N_4 hydrogels. (A) Superoxide anion generated from all hydrogel discs with 10 mm in diameter and 2 mm thickness (Agar, DMA, 0.1% g-C_3N_4, 0.2% g-C_3N_4, 0.4% g-C_3N_4, 0.6% g-C_3N_4, 0.8% g-C_3N_4 and 1.0% g-C_3N_4) under 460 nm centered LED light irradiation for 30, 60, 90, 120, 150 and 180 minutes. (n=3) (B) Superoxide anion measurement from all hydrogel discs under continuous 60 minutes of irradiation and ON-OFF-ON mode with a 30-minute duration for one cycle. Data represent mean ± SD from three independent experiments (n = 3).

4.2.3 Quantification of hydrogen peroxide generated by g-C_3N_4 hydrogels

The hydrogen peroxide calibration curve was measured using the commercialised kit and standard 30% H_2O_2 solution. Briefly, the 30% H_2O_2 solution was diluted into 1-10 μM. The fluorescence signal was detected after reacting with an Amplex red solution in a ratio of 1:1. The calibration curve was calculated using the linear relationship between H_2O_2 concentration and their corresponding fluorescence signals, as shown in **Figure 4.7**.

Hydrogen peroxide released from 0.1% and 0.2% g-C_3N_4 hydrogel grew gradually as the irradiation period extended from 30 minutes to 180 minutes (**Figure 4.8A**), with the increment of hydrogen peroxide from 11 μM to 33 μM. When the doped concentration of g-C_3N_4 material increased to 0.4%, 0.6%, 0.8%, and 1.0%, hydrogen peroxide formed under 30 minutes of illumination rose from 14 μM in 0.2% g-C_3N_4 hydrogel to 25 μM.

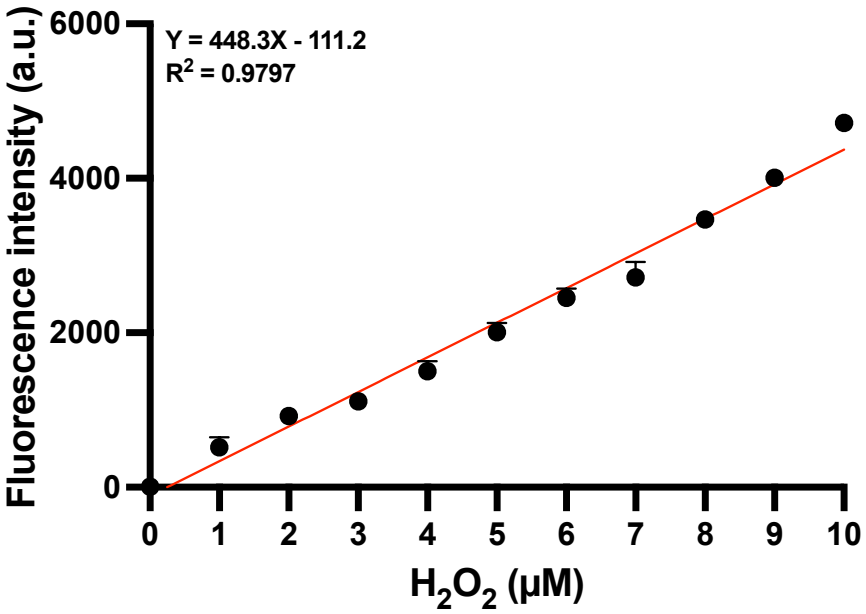

Fig. 4.7 Stanadard curve of hydrogen peroxide. Linear fitting equation: Y = 448.3X - 111.2, R^2 = 0.9797. Data represent mean ± SD from three independent experiments (n = 3).

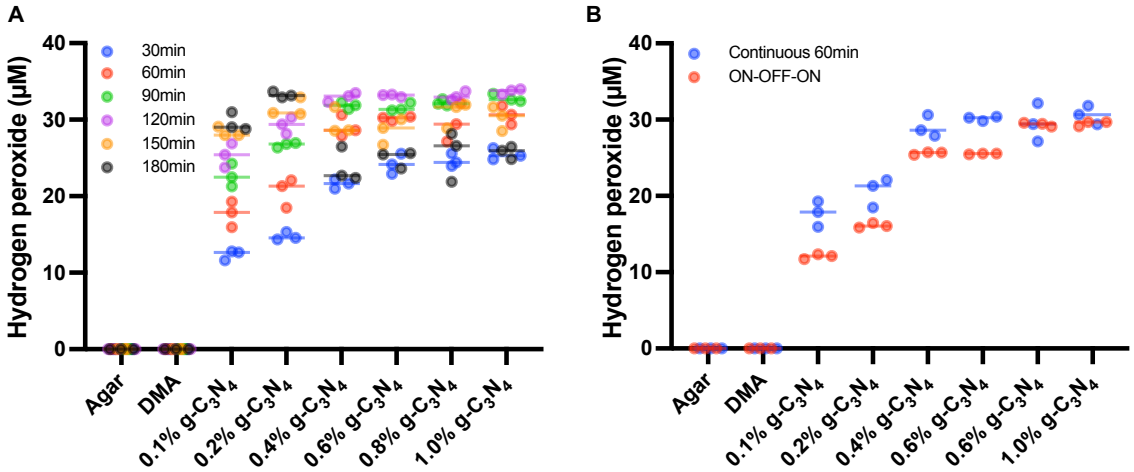

Fig. 4.8 Hydrogen peroxide from g-C_3N_4 hydrogels. (A) Hydrogen peroxide generated from all hydrogel discs with 10 mm in diameter and 2 mm thickness (Agar, DMA, 0.1%g-C_3N_4, 0.2% g-C_3N_4, 0.4% g-C_3N_4, 0.6% g-C_3N_4, 0.8% g-C_3N_4 and 1.0% g-C_3N_4) under 460 nm centered LED light irradiation for 30, 60, 90, 120, 150 and 180 minutes. (n=3) (B) Hydrogen peroxide measurement from all hydrogel discs under continuous 60 minutes of irradiation and ON-OFF-ON mode with a 30 minutes duration for one cycle. Data represent mean ± SD from three independent experiments (n = 3).

While the hydrogen peroxide increments in higher concentrations of g-C_3N_4 hydrogel

exhibited a lower rate, the maximum concentration of generated hydrogen peroxide in all g-C_3N_4 hydrogels was around 33 μM after 120 minutes of irradiation. When the irradiation time was prolonged to 150 and 180 minutes, the measured hydrogen peroxide concentration dropped to 28 μM and 23 μM on average, respectively. The rapid degradation rate could explain this decrease of hydrogen peroxide under prolonged irradiation; under the more extended irradiation period, hydrogen peroxide generation became slower due to the limited active sites on g-C_3N_4 material, whereas the decomposition was caused by both H_2O_2 reaction and light-induced degradation, thus, more extended time irradiation formed lower concentration of hydrogen peroxide from g-C_3N_4 hydrogel.

In the ON-OFF-ON mode test (**Figure 4.8B**), hydrogen peroxide generation displayed a different pattern from hydroxyl radical and superoxide anion, getting a lower concentration than the continuous irradiation; this could be due to the instability of hydrogen peroxide, leading to an extra degradation during the light off cycle. Therefore, hydrogen peroxide from the latter mode is close to the continuous mode but with a 3-5 μM decline.

4.2.4 Antibacterial activity of g-C_3N_4 hydrogel-generated ROS against *S. epidermidis* and *E. coli – DH 5α*

As the experiments carried out above, various reactive oxygen species (ROS), including hydroxyl radical, superoxide anion and hydrogen peroxide, could be released from all concentrations of g-C_3N_4 hydrogels under the LED light irradiation. The final aim of this hydrogel is expected to be applied to chronic open wounds. Thus, the interactions between the generated ROS and the bacteria and cells encountered become crucial. Firstly, the killing efficiency of separately cultured bacteria and mammalian cells caused by g-C_3N_4 hydrogels in all concentrations was evaluated under 10 and 60 minutes of irradiation.

Bacterial number calibration

Before the experimental implementation, the bacterial cell number was fixed to ensure that all obtained results were comparable. Generally, bacterial solutions were collected at the log phase and diluted into different concentrations with the optical density at 600 nm from 0.1 to 1.0. Then, these bacterial solutions were spread on an agar plate for culture. The bacterial cell number calibration curve was analysed from optical density, and the corresponding colonies form units counted from the agar plate, as shown in **Figure 4.9**.

The bacterial cell number was fixed in 1×10^8 cells/mL with $OD_{600} = 0.1$ in all following experiments. *S. epidermidis*, the most common strain in skin infection, was used as the gram-positive bacteria model, and *E. coli - DH 5α* was chosen as the gram-negative bacterial strain.

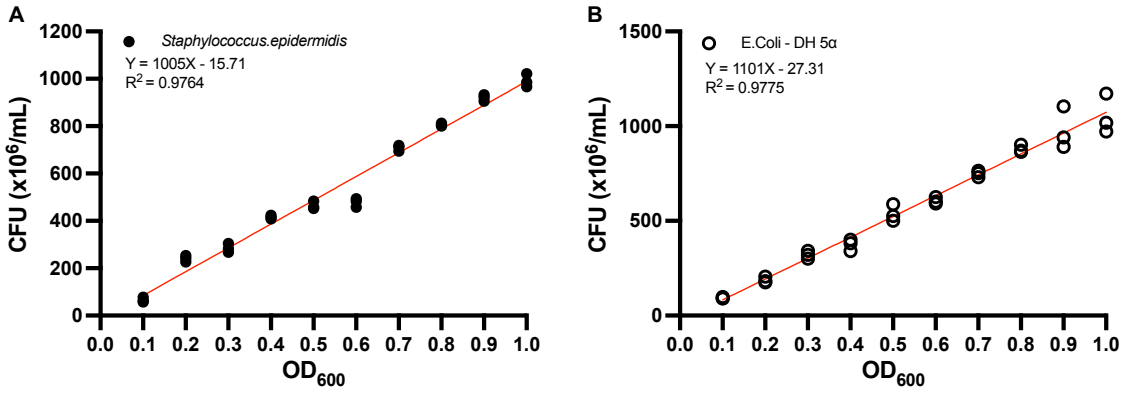

Fig. 4.9 Bacterial cell number calibration. (A) Calibration curve of *S. epidermidis*, linear fitting equation Y = 1005X - 15.71, R^2 = 0.9764. (n=3) (B) calibration curve of *E. coli - DH 5α*, linear fitting equation Y = 1101X - 27.31, R^2 = 0.9775. Data represent mean ± SD from three independent experiments (n = 3).

Standard bacterial samples with 0% to 100% live bacterial cells were prepared to confirm the slight viability change could be detected by a Live / Dead assay kit; the fluorescence signal was measured using a BIOTEK microplate reader and obtained data shown in **Figure 4.10A** for *S. epidermidis* and **Figure 4.10C** for *E. coli - DH 5α*, all bacterial solutions with 10% viability difference could be distinguished very well.

Thus, all g-C_3N_4 hydrogel disc concentrations were directly contacted with 1 mL of *S. epidermidis* and *E. coli - DH 5α* solution, 460 nm centred LED light was applied for 10 and 60 minutes, respectively. The killing percent of collected sample solutions was calculated using the following equation:

$$\text{Killing percent}(\%) = \frac{\text{Fluorescence intensity}_{\text{Dead}}}{\text{Fluorescence intensity}_{\text{Live}} + \text{Fluorescence intensity}_{\text{Dead}}} \times 100 \quad (4.5)$$

In **Figure 4.10B**, agar gel has no damage to *S. epidermidis* after 10 minutes and 60 minutes of irradiation; the killing from DMA hydrogel was due to its oxidative effect rather than ROS generation. After 10 minutes of irradiation, all g-C_3N_4 hydrogels presented around 10% antimicrobial efficiency to *S. epidermidis* and increased to 70% after 60 minutes; no significant difference was observed among all g-C_3N_4 hydrogels. Samples treated for 60 minutes were stained using a Live / Dead assay kit; fluorescence images were collected in **Figures 4.11, 4.12** and **4.13**; the live signal in the FITC channel was decreased rapidly while the signal for dead bacterial cells was evident.

In the *E. coli – DH 5α* group (**Figure 4.10D**), 10 minutes of irradiation caused 30% killing of bacterial cells, and this efficiency of bacterial eradication up to 65% after 60 minutes of irradiation; no noticeable difference was exhibited in g-C_3N_4 hydrogels with

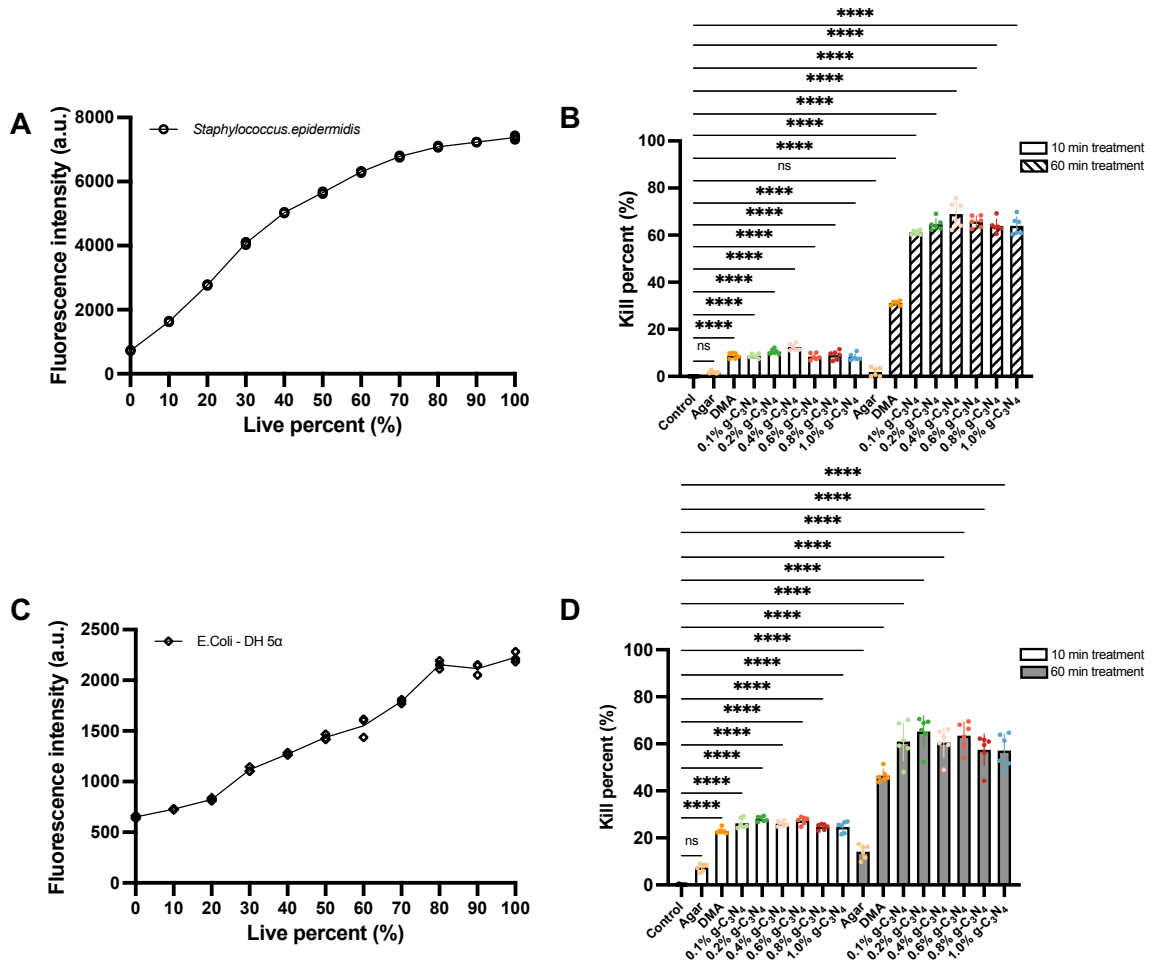

Fig. 4.10 Killing efficiency of *S. epidermidis* and *E. coli - DH 5α* caused by ROS from g-C_3N_4 hydrogels. (A) Live / Dead calibration curve of *S. epidermidis*. (B) Killing percent of *S. epidermidis* after irradiating by 460 nm LED for 10 minutes and 60 minutes. (n=6) (C) Live / Dead calibration curve of *E. coli - DH 5α*. (D) Killing percent of *E. coli - DH 5α* after irradiating by 460 nm LED for 10 minutes and 60 minutes. Data are presented as $mean \pm SD$ (n = 6). Statistical analysis was performed using one-way ANOVA followed by Dunnett's post hoc test. $P \leq 0.05$ was considered statistically significant (* $p \leq 0.05$, **$p \leq 0.01$, *** $p \leq 0.001$, **** $p \leq 0.0001$). Statistical analysis was conducted using GraphPad Prism 10.0.

various concentrations of g-C_3N_4 dopant. Fluorescence images displayed in **Figures 4.14, 4.15** and **4.16** are the *E. coli – DH 5α* samples irradiated with LED light for 60 minutes, same as *S. epidermidis*, comparing to the control and agar treated groups, g-C_3N_4 hydrogel treated group showed dead bacterial cell signal in TRITC channel, and the live cell signal was declined significantly.

Obtained data proved that the ROS generated from g-C_3N_4 hydrogels kills both gram-positive and gram-negative bacteria efficiently, and in these two shining periods, g-C_3N_4

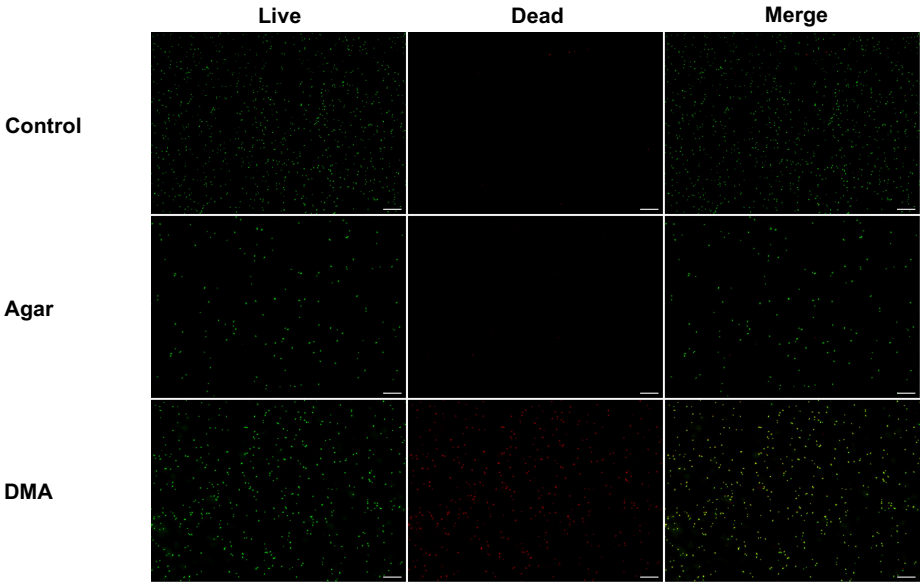

Fig. 4.11 Fluorescence images of *S. epidermidis* after treating with agar and DMA hydrogel for 60 minutes. The scale bar = 50 μm.

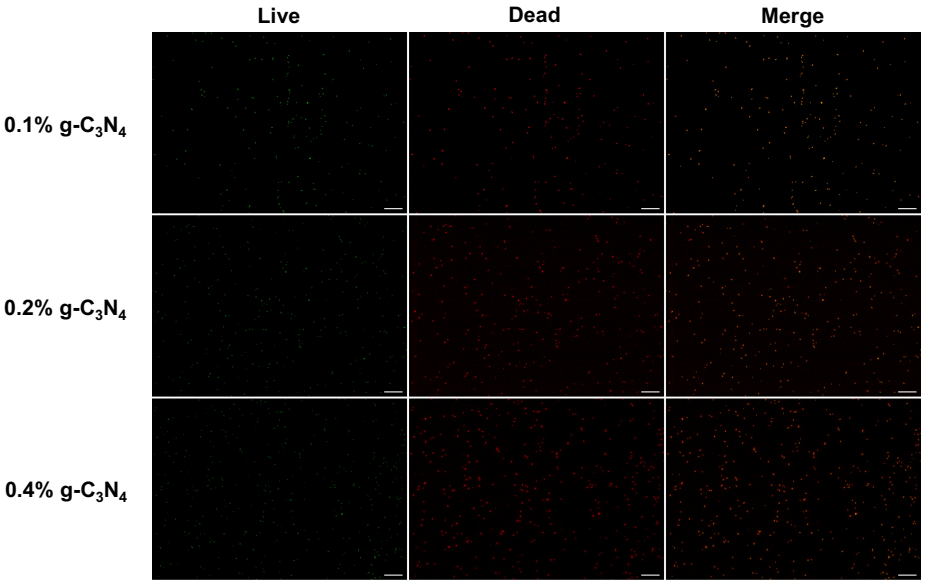

Fig. 4.12 Fluorescence images of *S. epidermidis* after treating with 0.1%, 0.2% and 0.4% g-C_3N_4 hydrogels for 60 minutes. The scale bar = 50 μm.

hydrogels with different concentrations of additive presented not much difference in killing percent, which is aligned with the results acquired in ROS quantify section 4.2.1 – section 4.2.3. Within 60 minutes of irradiation, the concentration of ROS released from all g-C_3N_4 hydrogels showed slight variation within 10 μM.

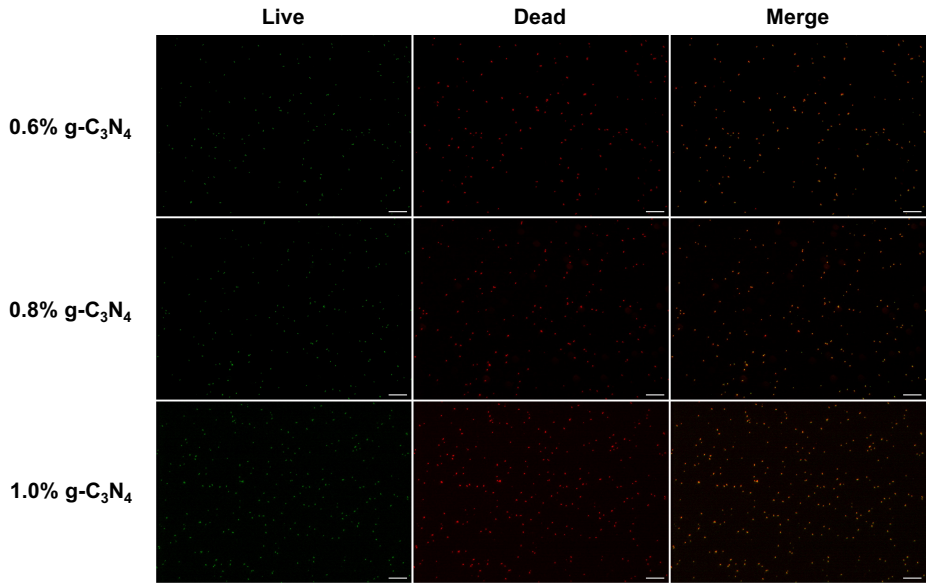

Fig. 4.13 Fluorescence images of *S. epidermidis* after treating with 0.6%, 0.8% and 1.0% g-C_3N_4 hydrogels for 60 minutes. The scale bar = 50 μm.

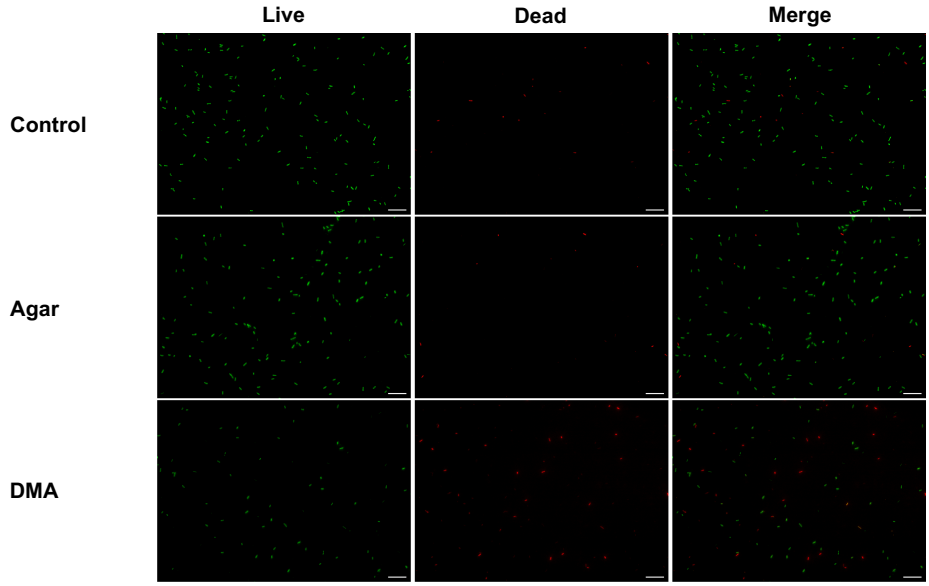

Fig. 4.14 Fluorescence images of *E. coli – DH 5*α after treating with agar and DMA hydrogel for 60 minutes. The scale bar = 50 μm.

4.2.5 Antibacterial efficiency of g-C_3N_4 hydrogel generated ROS against red fluorescent protein expressed *E. coli*

Figure 4.17 showed the results of antibacterial effects on *mCherry – E. coli* using different g-C_3N_4 hydrogels and the fluorescence images (**Figure 4.18**) of *mCherry – E. coli*

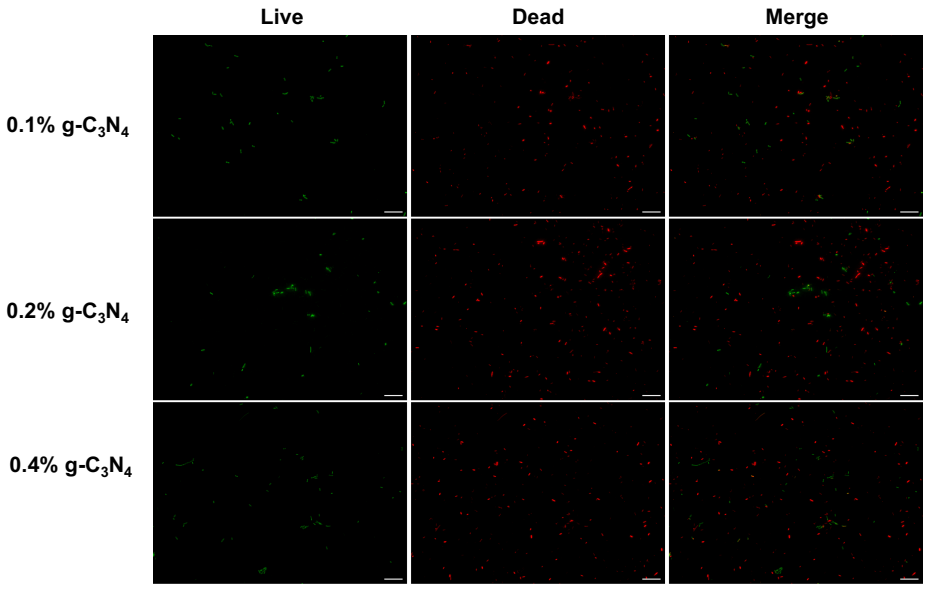

Fig. 4.15 Fluorescence images of *E. coli – DH 5α* after treating with 0.1%, 0.2% and 0.4% g-C_3N_4 hydrogels for 60 minutes. The scale bar = 50 μm.

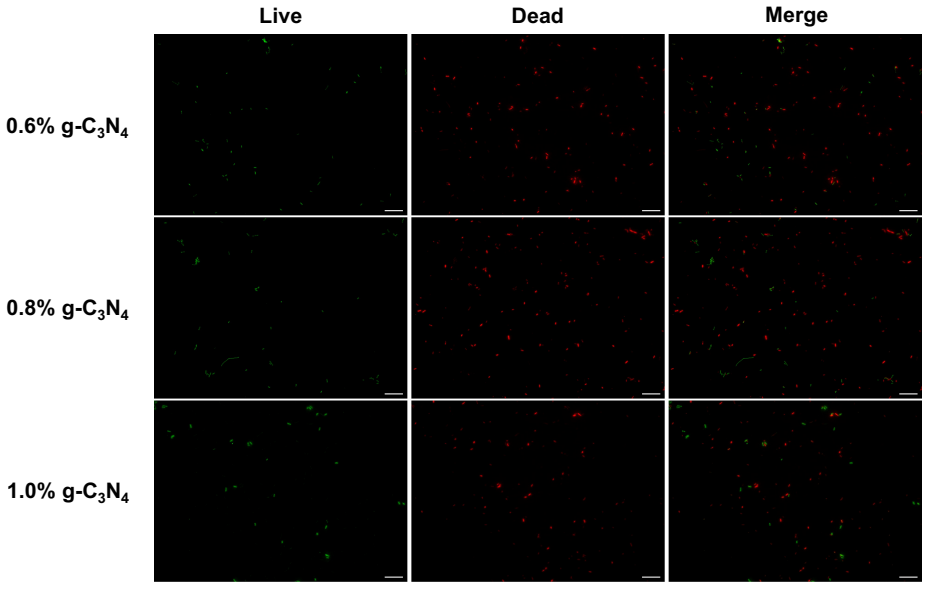

Fig. 4.16 Fluorescence images of *E. coli – DH 5α* after treating with 0.6%, 0.8% and 1.0% g-C_3N_4 hydrogels for 60 minutes. The scale bar = 50 μm.

killed by ROS were presented as the obviously diminished red fluorescence from expressed red fluorescent protein. Another evidence of the damaged *mCherry – E. coli* is that the bacteria gradually decomposed into several fragments instead of intact bacterial cell shape.

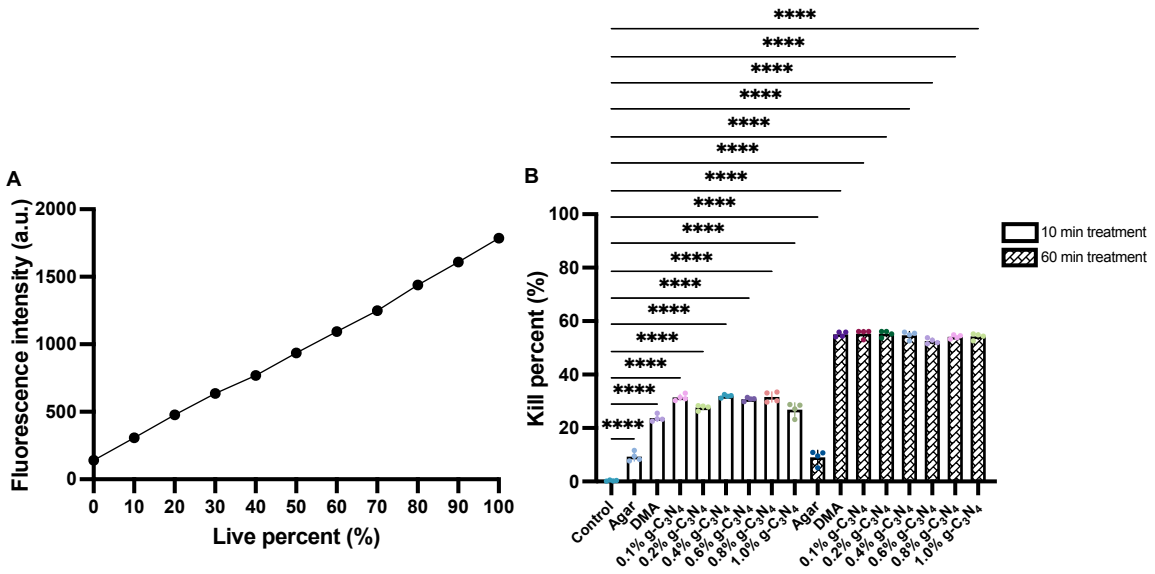

Fig. 4.17 Antibacterial effects of ROS generated by g-C_3N_4 hydrogels on *mCherry - E. coli*. (A) Live / Dead calibration curve of *mCherry - E. coli*. n=3. (B) Killing percent of mCherry - E. coli after irradiating by 460 nm LED for 10 minutes and 60 minutes. Data are presented as $mean \pm SD$ (n = 4). Statistical analysis was performed using one-way ANOVA followed by Dunnett's post hoc test. $P \leq 0.05$ was considered statistically significant (* $p \leq 0.05$, **$p \leq 0.01$, *** $p \leq 0.001$, **** $p \leq 0.0001$). Statistical analysis was conducted using GraphPad Prism 10.0.

In general, the obtained data showed similar variation to the *E. coli – DH 5α* sample, making it possible to be used as the component of the co-cultured group.

4.2.6 Interactions between ROS generated by g-C_3N_4 hydrogels and contacted fibroblast cells

As the chronic open wound is a complex environment occupied by both bacteria and mammalian cells, in this work, the interactions between fibroblast cells and ROS from g-C_3N_4 hydrogels were also investigated in detail. Standard fibroblast cell samples, including different numbers of live cells, showed steady fluorescence signal growth and certified the detectable viability change in mixed cell groups, as shown in **Figure 4.19A**. When 1×10^6 fibroblast cells made contact with g-C_3N_4 hydrogel under LED light irradiation for 10 minutes and 60 minutes, different from the data in bacteria groups, treated fibroblast cells showed no damage from ROS from g-C_3N_4 hydrogels. After 10 minutes and 60 minutes of irradiation (**Figure 4.19B**), fibroblast cells maintained over 85% viability; these gave us positive support for further selective killing exploration in bacteria and mammalian cell

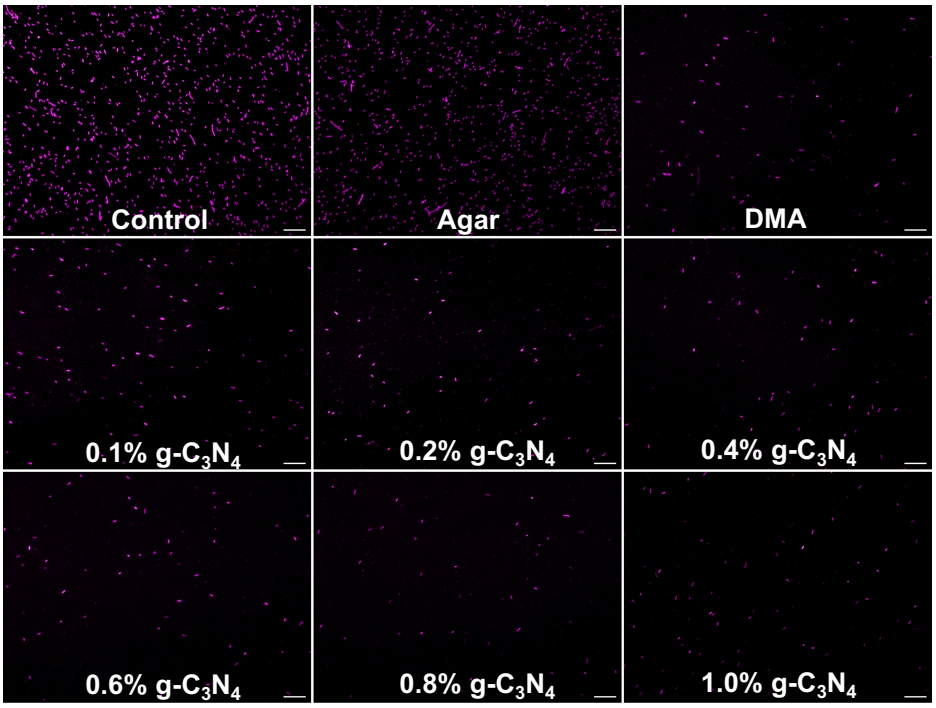

Fig. 4.18 Fluorescence images of *mCherry – E. coli* after treating with agar, DMA, 0.1%, 0.2%, 0.4%, 0.6%, 0.8% and 1.0% g-C_3N_4 hydrogels for 60 minutes. The scale bar = 50 μm.

co-cultured groups.

Corresponding Live / Dead fluorescence images of fibroblast cells treated with all hydrogels were also collected and shown in **Figure 4.20**, **Figure 4.21** and **Figure 4.22**. Live signals were labelled with Calcein-AM, which presented as green, and dead signals were labelled with Ethidium Homodimer-1 (EthD-1), which presented as red.

4.2.7 Quantification of intracellular hydroxyl radical using HPF probe

The reactive oxygen species considered in this work include hydroxyl radical, superoxide anion and hydrogen peroxide. According to their intrinsic properties and functions, the hydroxyl radical is one of the most reactive and invasive ROS species; it could react and damage all molecules in an effective radius indiscriminately, causing oxidative damage. Thus, it could take the primary responsibility of killing encountered bacteria. The quantification of hydroxyl radical in the last chapter can only implemented *ex vivo* using CBB solution as the indicator. To figure out the relationship between hydroxyl radical concentration and cell live status, the diffused hydroxyl radical needs to be further captured using a probe hydroxyphenyl fluorescein (HPF), which can work both in extra and intracellular environments to make the detected hydroxyl radical signal comparable. Standard hydroxyl radical solution from

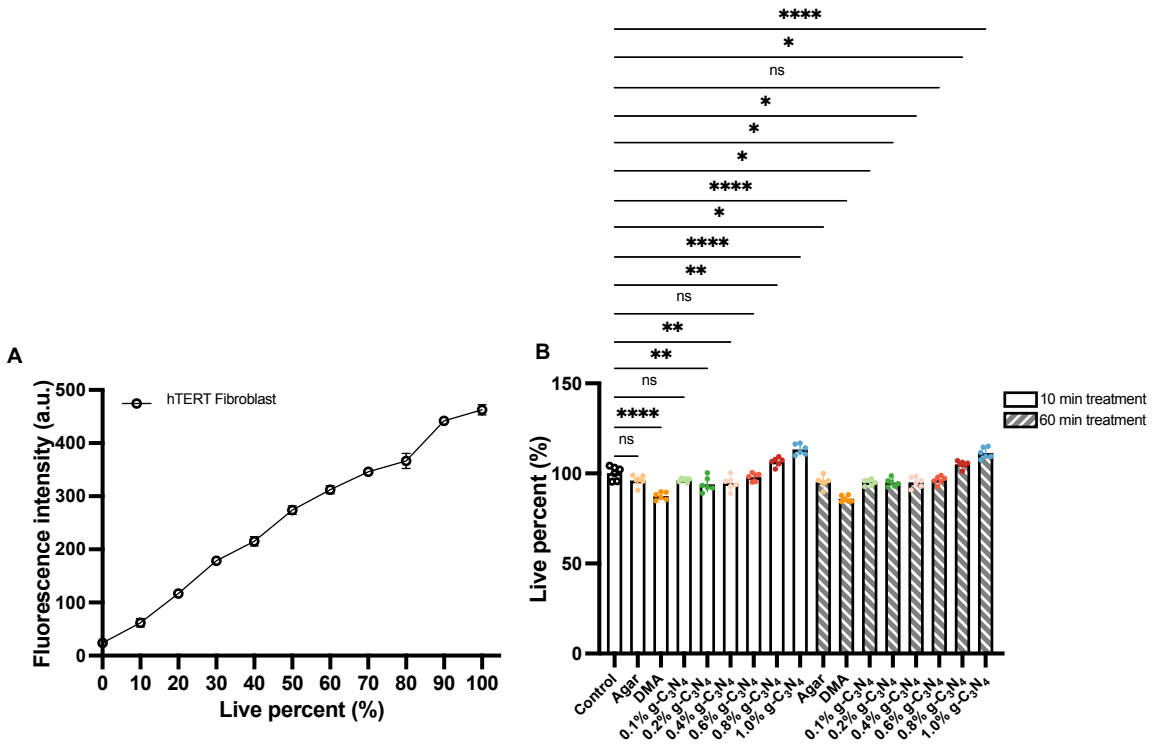

Fig. 4.19 Mammalian cell damage effects of ROS generated by g-C_3N_4 hydrogels on fibroblast cells. (A) Live / Dead calibration curve of fibroblast cells. (n=3) (B) Killing percent of fibroblast cells after irradiating by 460 nm LED for 10 minutes and 60 minutes. Data are presented as *mean* $\pm$ *SD* (n = 6). Statistical analysis was performed using one-way ANOVA followed by Dunnett's post hoc test. P $\leq$ 0.05 was considered statistically significant (* p $\leq$ 0.05, **p $\leq$ 0.01, *** p $\leq$ 0.001, **** p $\leq$ 0.0001). Statistical analysis was conducted using GraphPad Prism 10.0.

1-10 μM was detected using a hydroxyphenyl fluorescein (HPF) probe, shown in **Figure 4.23**.

4.2.8 Relationship between intracellular hydroxyl radical and viability in *S. epidermidis* bacteria after treating with 0.4% g-C_3N_4 hydrogel system

After the general test using g-C_3N_4 hydrogel with different contents of g-C_3N_4 materials, 0.4% g-C_3N_4 hydrogel was selected as the best-performing hydrogel for all following tests. This revealed ROS-caused bacterial killing and the relationship between intracellular hydroxyl radicals, accepted as the highly active killing factor in this work.

For the exhaustive understanding of hydroxyl radical-induced killing to *S. epidermidis*,

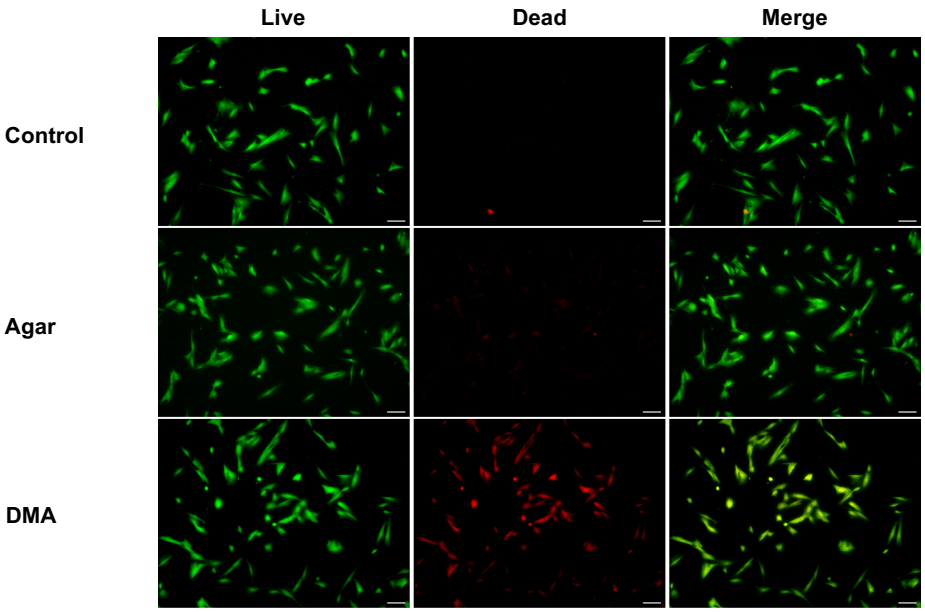

Fig. 4.20 Fluorescence images of fibroblast cells after treating with agar and DMA hydrogel for 60 minutes. The scale bar = 100 μm.

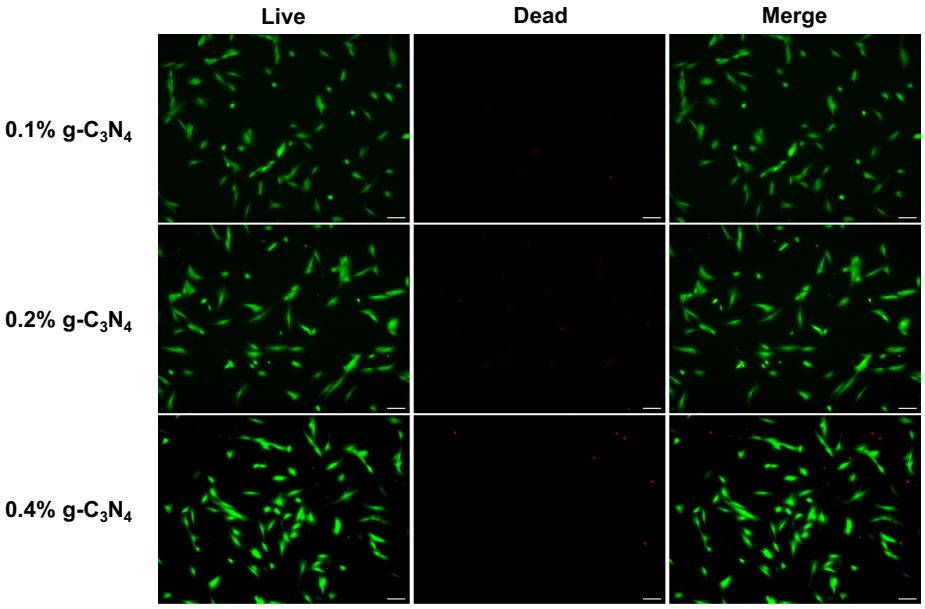

Fig. 4.21 Fluorescence images of fibroblast cells after treating with 0.1%, 0.2% and 0.4% g-C_3N_4 hydrogels for 60 minutes. The scale bar = 100 μm.

LED light was applied to 1×10^8 bacterial cells for a more extended treatment period with different time points, including 0, 1, 2, 4, 6, 8, 10, 30, 60, 120 and 180 minutes, variation of dead *S. epidermidis* cell percent and intracellular hydroxyl radical concentration were

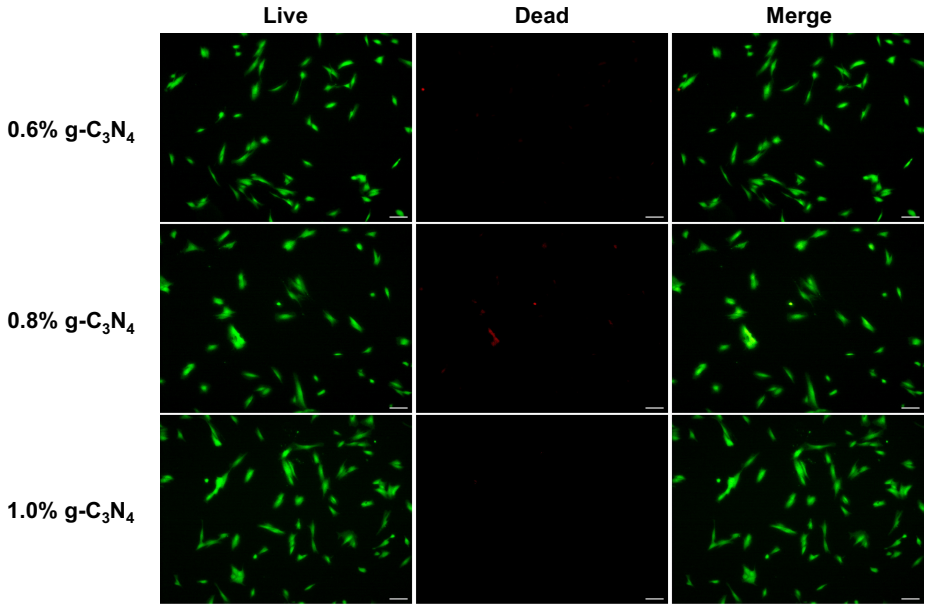

Fig. 4.22 Fluorescence images of fibroblast cells after treating with 0.6%, 0.8% and 1.0% g-C_3N_4 hydrogels for 60 minutes. The scale bar = 100 μm.

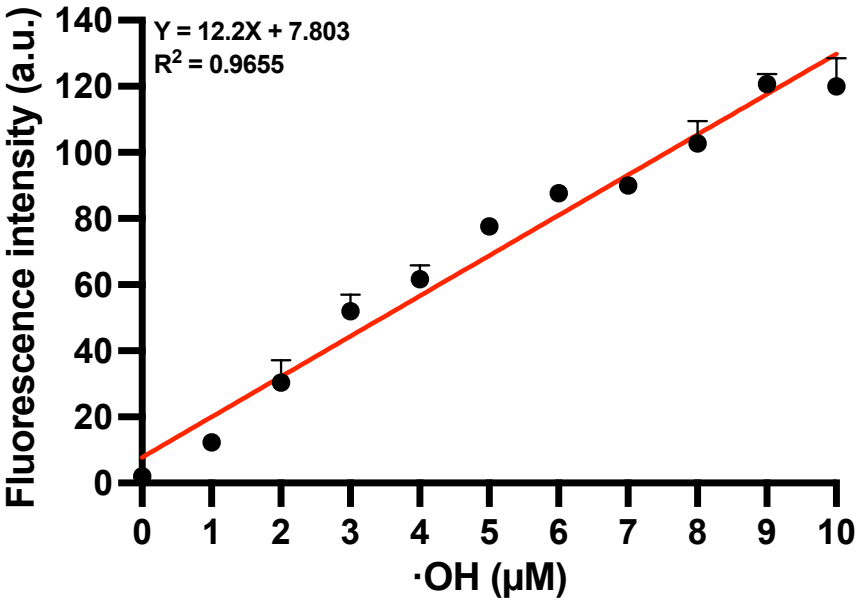

Fig. 4.23 Intracellular htdroxyl radical calibration using HPF as the indicator. Linear fitting equation: Y = 12.2X + 7.803, R^2 = 0.9655. Data represent mean ± SD from three independent experiments (n = 3).

measured, and fluorescence images for Live / Dead assay and hydroxyl radical signal were collected after 10 minutes, 30 minutes and 60 minutes of LED treatment (**Figure 4.24** and

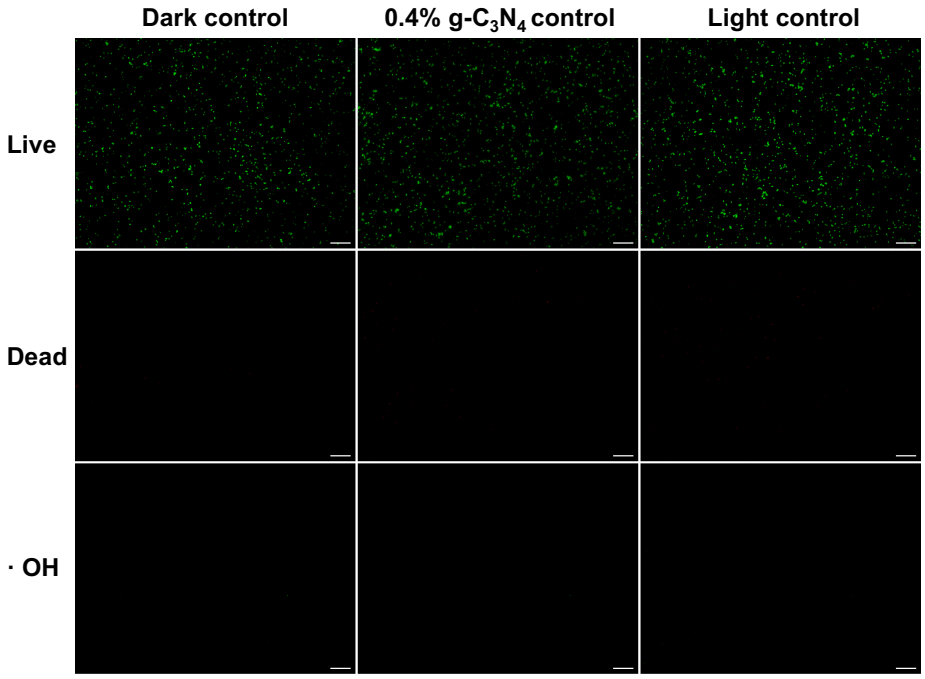

Fig. 4.24 Live / Dead and intracellular hydroxyl radical images of *S. epidermidis* treated with only 0.4% g-C_3N_4 hydrogel and only LED light irradiation for 60 minutes. The scale bar is 50 μm.

Figure 4.25). *S. epidermidis* damage was shown in **Figure 4.26A**; the first 10 minutes of treatment led to a small amount of bacterial cell killing, with 13% killing percent at 10 minutes. In the next 20 minutes, the percentage of killed bacteria rapidly grew to 55%, and 80% of *S. epidermidis* died after 2 hours of LED irradiation with 0.4% g-C_3N_4 hydrogel immersed. After 180 minutes of the test, 90% of the killing percent was realised, showing an excellent antibiotic property of 0.4% g-C_3N_4 hydrogel released ROS.

The hydroxyl radical diffused into bacterial cells was measured under the same test condition to find a clue between this killing performance and intracellular hydroxyl radical concentration. In the first 10 minutes, the hydroxyl radical signalled a gradual growth from 2 to 43 (**Figure 4.26B**), which means that the intracellular Hydroxyl radical concentration increases to 2.8 μM at 10 minutes. After this, the change of intracellular hydroxyl radical concentration is comparable to that of the tendency of dead percent displayed in **Figure 4.26C**, showing a sharp rise from 2.8 μM to 6.8 μM at 30 minutes (**Figure 4.26**), the highest concentration within 180 minutes of treatment. When irradiation time went longer, different from the killing percent, the measured intracellular hydroxyl radical concentration slightly decreased to 4 μM at 60 minutes and 2.3 μM at 180 minutes (**Figure 4.26C**). The bacterial structure was damaged due to the sustained diffused hydroxyl radical; the previous intact

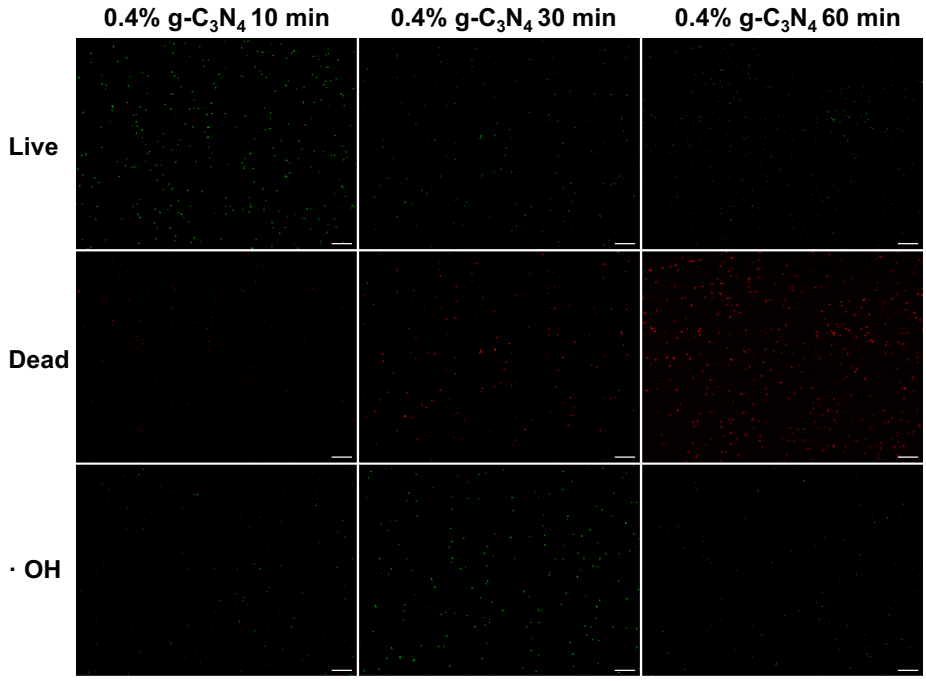

Fig. 4.25 Live / Dead and intracellular hydroxyl radical images of *S. epidermidis* treated with 0.4% g-C_3N_4 hydrogel and LED light irradiation for 10, 30 and 60 minutes. The scale bar is 50 μm.

structure was also broken; thereby, the intracellular hydroxyl radical probe could be leaked and lose signal. The highest detected hydroxyl radical in cells almost reached 45-fold (**Figure 4.26D**) compared to the control group. The 90% *S. epidermidis* was killed as a consequence of the hydroxyl radical generation and oxidation.

4.2.9 Relationship between intracellular hydroxyl radical and viability in *E. coli-DH 5α* bacteria after treating with 0.4% g-C_3N_4 hydrogel system

For gram-negative bacteria, the behaviour of *E. coli-DH 5α* was also monitored under the conditions: 1×10^8 bacterial cells were illuminated with a 460 nm-centred LED after 0.4% g-C_3N_4 hydrogel was immersed in. Treatment times were 0, 1, 2, 4, 6, 8, 10, 30, 60, 120, and 180 minutes. Both viability and intracellular hydroxyl radical concentration were measured. Obtained fluorescence images of Live / Dead and intracellular hydroxyl radical images are shown in **Figure 4.27** and **Figure 4.28**.

In the first 10 minutes, 30% of *E. coli-DH 5α* was killed(**Figure 4.29A**); this value is 18% higher than that in the *S. epidermidis* group. However, there was not a rapid increase

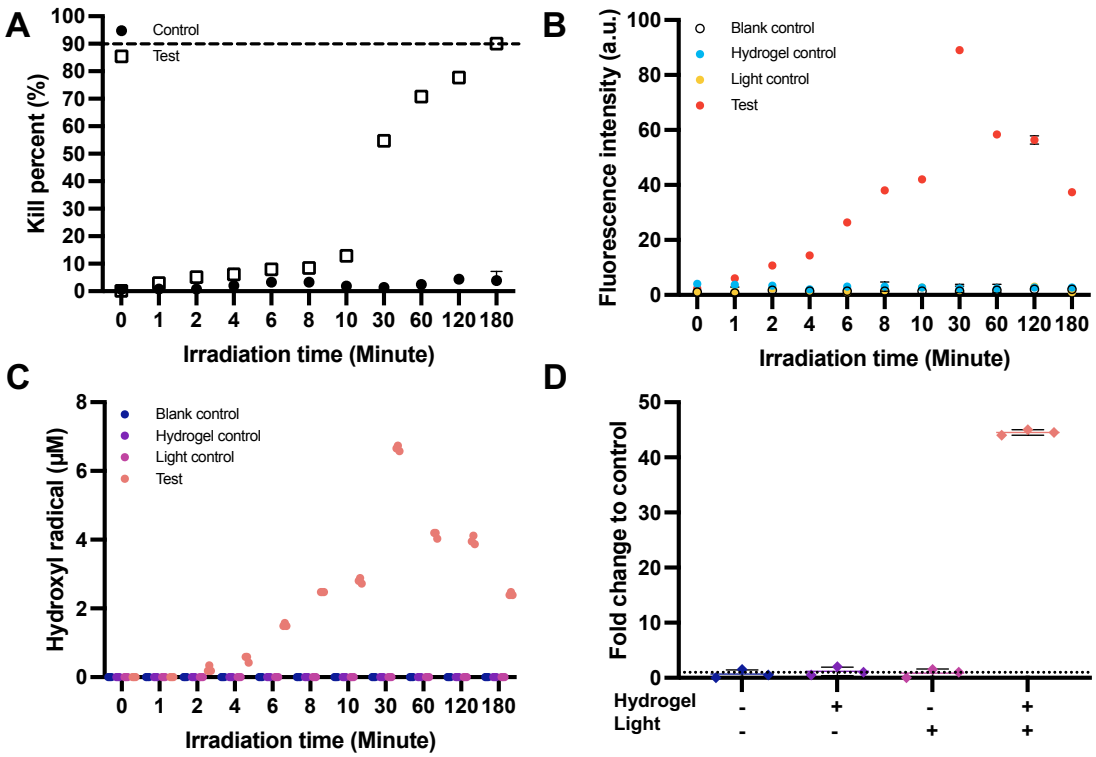

Fig. 4.26 Antibacterial effects and intracellular hydroxyl radical accumulation caused by ROS generated from 0.4% g-C_3N_4 hydrogels in the *S. epidermidis* group. 0.4% g-C_3N_4 hydrogel and visible light system induced (A) Antibacterial efficiency (B) Intracellular hydroxyl radical fluorescence signal (C) Intracellular hydroxyl radical concentration in *S. epidermidis* after 0, 1, 2, 4, 6, 8, 10, 30, 60, 120 and 180 minutes of irradiation. (D) Highest intracellular hydroxyl radical concentration change fold in *S. epidermidis* after 30 minutes of irradiation with 0.4% g-C_3N_4 hydrogel immersion. Data represent mean ± SD from three independent experiments (n = 3).

in the next 20 minutes; the killing percent of *E. Coli-DH 5α* showed a gradual increase, reaching 50% at 60 minutes, 60% killing percent at 120 minutes, and finally, almost 70% of *E. coli-DH 5α* was killed by the ROS from light irradiated 0.4% g-C_3N_4 hydrogel. The intracellular hydroxyl radical concentration in *E. coli-DH 5α* was shown in **Figure 4.29B** and **Figure 4.29C**; what can be seen in this figure is the continual growth of hydroxyl radical concentration, which reached 2.06 μM at 30 minutes and peaked at 60 minutes with 5.6 μM of intracellular hydroxyl radical. The maximum concentration of hydroxyl radicals in *E. coli-DH 5α* was 2.1 μM lower than that in *S. epidermidis*; it was 25-fold higher than the control group (**Figure 4.29D**). Compared to *S. epidermidis*, the intracellular hydroxyl radical variation in *E. coli-DH 5α* is moderate, taking longer to get the highest concentration, which is also lower than the value in *S. epidermidis*. This situation can be attributed to the

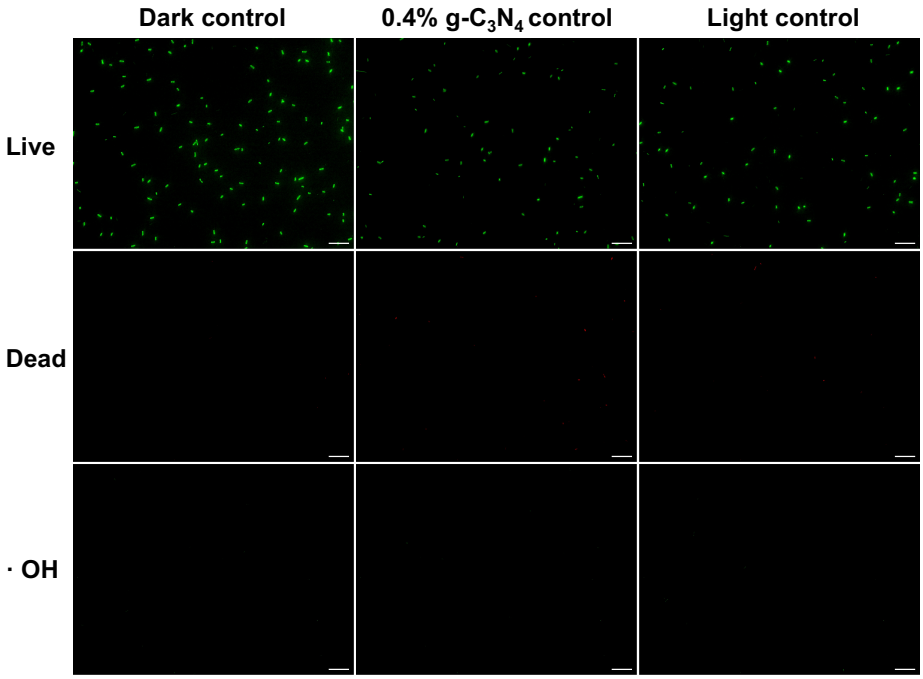

Fig. 4.27 Live / Dead and intracellular hydroxyl radical images of *E. coli-DH 5α* treated with only 0.4% g-C_3N_4 hydrogel and only LED light irradiation for 60 minutes. The scale bar is 50 μm.

membrane structure difference between gram-positive bacteria and gram-negative bacteria; a more complex membrane structure helps *E. coli-DH 5α* defend the invasion of hydroxyl radicals, alleviating the leading damage, thus causing a compromise killing percent, which is 66% at 180 minutes.

Given the later use of *mCherry -E. coli*, the same tests were also implemented against it; see the fluorescence images in **Figure 4.30**. The obtained data was plotted in **Figure 4.31**; the data tendency in *mCherry – E. coli* was almost the same as *E. coli-DH 5α*; 80% of bacteria were killed after 180 minutes of treatment (**Figure 4.31A**). The concentration of intracellular hydroxyl radical peaked at 60 minutes (**Figure 4.31B** and **Figure 4.31C**), the same as *E. coli-DH 5α*; the value is 3.78 μM, 18-fold increased than the control group (**Figure 4.31D**). It is acceptable for this slight discrepancy between *mCherry – E. coli* and *E. coli-DH 5α*, so the *mCherry – E. coli* was used in the later co-culture group to represent the behaviour of bacteria in the co-culture group.

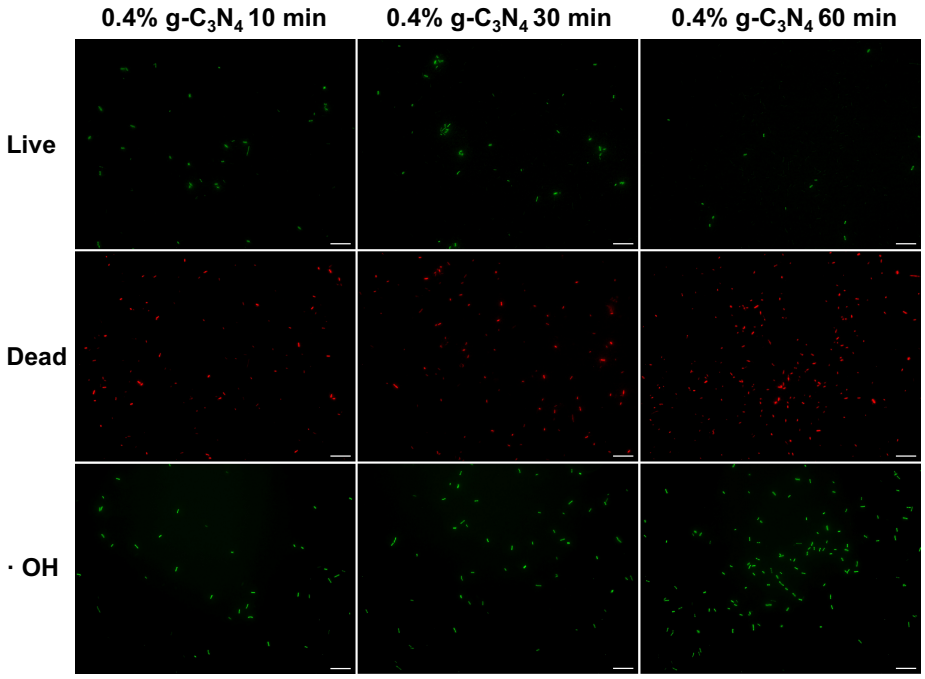

Fig. 4.28 Live / Dead and intracellular hydroxyl radical images of *E. coli-DH 5α* treated with 0.4% g-C_3N_4 hydrogel and LED light irradiation for 10, 30 and 60 minutes. The scale bar is 50 μm.

4.2.10 Relationship between intracellular hydroxyl radical and viability in fibroblast cells after treating with 0.4% g-C_3N_4 hydrogel system

After testing different bacteria, the ROS-induced killing pattern was explored in fibroblast cells. The obtained fluorescence images are presented in **Figures 4.32** and **4.33**. After different irradiation time points, the live status of treated fibroblast cells was measured. **Figure 4.34A** showed that the viability of fibroblast cells was all over 80%, presenting no significant difference compared to the other control groups.

The highest intracellular hydroxyl radical signal is 20 in fluorescenc signal intensity after 60 minutes of irradiation (**Figure 4.34B**), increasing 6.7-fold compared to the control group (**Figure 4.34C**), revealing that the diffused hydroxyl radical in the fibroblast cell is too low to damage. These results are consistent with the previous data, and further verification of its reliability was obtained.

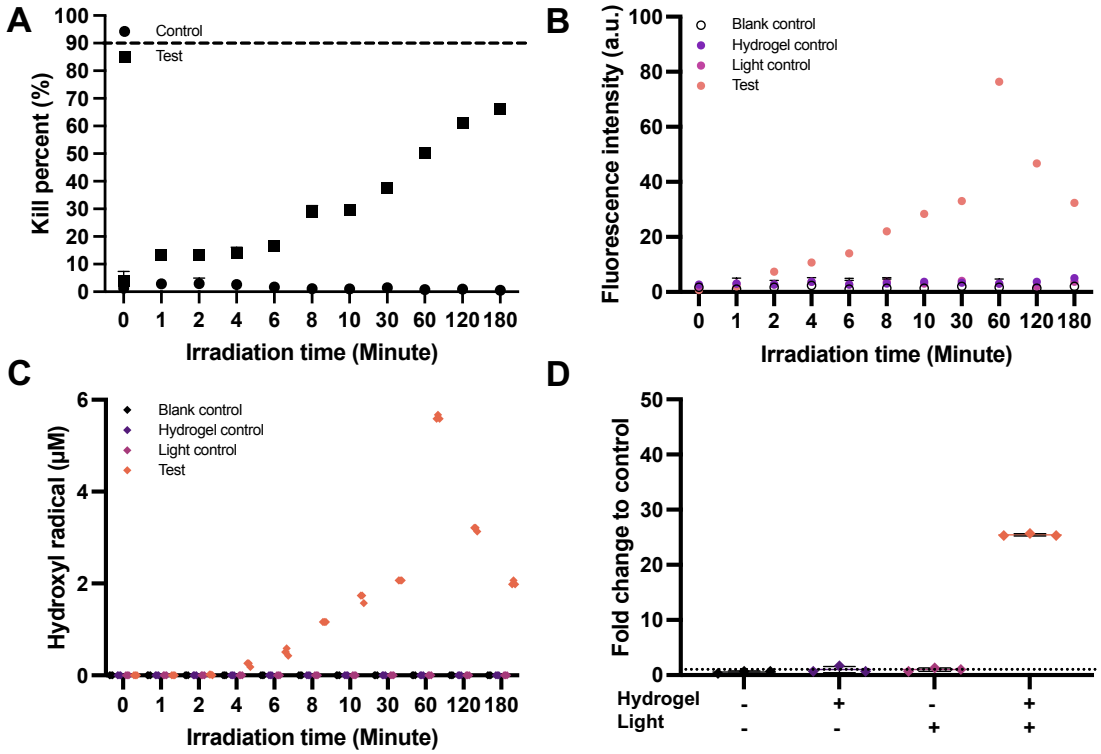

Fig. 4.29 Antibacterial effects and intracellular hydroxyl radical accumulation caused by ROS generated from 0.4% g-C_3N_4 hydrogels in the *E. coli-DH 5α* group. 0.4% g-C_3N_4 hydrogel and visible light system induced (A) Antibacterial efficiency (B) Intracellular hydroxyl radical fluorescence signal (C) Intracellular hydroxyl radical concentration in *E. coli-DH 5α* after 0, 1, 2, 4, 6, 8, 10, 30, 60, 120 and 180 minutes of irradiation. (n=3) (D) Highest intracellular hydroxyl radical concentration change fold in *E. coli-DH 5α* after 60 minutes of irradiation with 0.4% g-C_3N_4 hydrogel immersion. Data represent mean ± SD from three independent experiments (n = 3).

4.3 Discussion

In the work mentioned above, we studied the reactive oxygen species generation in g-C_3N_4 hydrogel under the 460 nm centred LED light, as the two-dimensional g-C_3N_4 material is one of the photocatalyst; that is also the reason why the doped g-C_3N_4 material could initiate the free radical based polymerisation after visible LED light irradiation. g-C_3N_4 exhibits a band gap energy as one of the semiconductor materials[158], following the energy band theory, when the semiconductor absorbs incident light with energy equal to or higher than its bandgap, electrons will be excited from the valence band (VB) to the conduction band (CB), and an equal number of holes left in the valence band (VB) (**Equation 4.6**). Then, these separated charge carriers in the excited states will migrate to the surface of

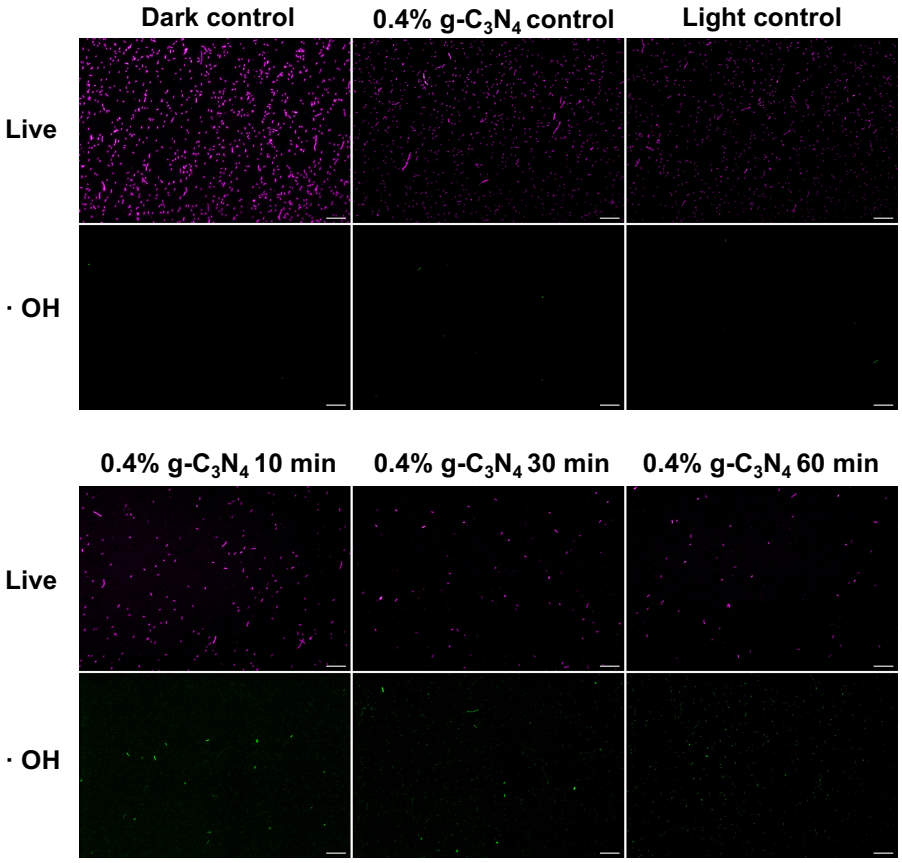

Fig. 4.30 Live / Dead and intracellular hydroxyl radical images of *mCherry - E. coli* treated with only 0.4% g-C_3N_4 hydrogel, only LED light irradiation and 0.4% g-C_3N_4 hydrogel and LED light irradiation for 10, 30 and 60 minutes. The scale bar is 50 μm.

g-C_3N_4 and be responsible for the photocatalytic conversion with the surrounding oxygen water molecules. Thus, high-activity molecules, such as superoxide anion ($O_2^{\cdot -}$), hydrogen peroxide (H_2O_2) and hydroxyl radical ($^{\cdot}OH$), would form through these processes.

$$\text{Photocatalyst} + h\nu \rightarrow e^- + h^+ \tag{4.6}$$

Based on this, specific reactive oxygen species, including hydroxyl radical ($^{\cdot}OH$), superoxide anion ($O_2^{\cdot -}$) and hydrogen peroxide (H_2O_2), were measured from g-C_3N_4 hydrogels after visible light irradiation.

To quantify the hydroxyl radical in all concentrations of g-C_3N_4 hydrogel, 1-10 μM of the standard sample was prepared using the Fenton reaction and the generated Hydroxyl radical concentrations were reflected by the absorbance value change of Coomassie Brilliant Blue (CBB) solution at 588 nm. As the intrinsic properties of hydroxyl radicals have extremely high reactivity and short lifespan, indirect capture methods are limited. Thus, the

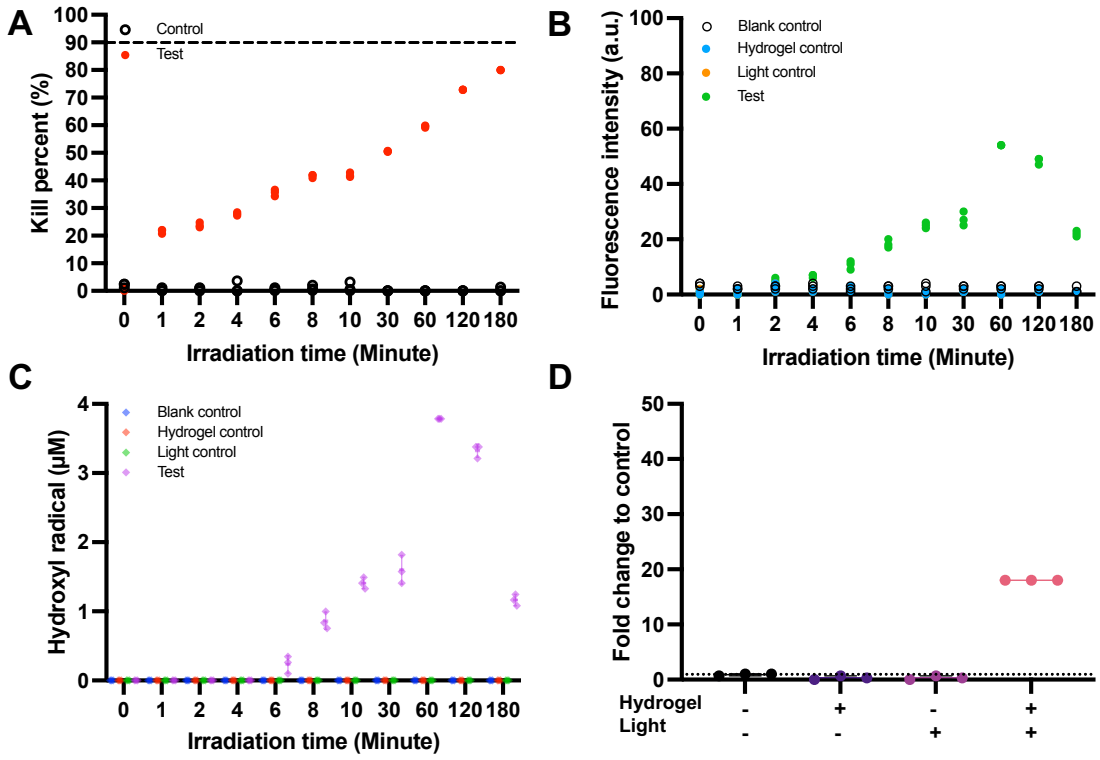

Fig. 4.31 Antibacterial effects and intracellular hydroxy radical accumulation induced by ROS generated from 0.4% g-C_3N_4 hydrogels in *mCherry - E. coli* group. 0.4% g-C_3N_4 hydrogel and visible light system induced (A) Antibacterial efficiency (B) Intracellular hydroxyl radical fluorescence signal (C) Intracellular hydroxyl radical concentration in *mCherry - E. coli* after 0, 1, 2, 4, 6, 8, 10, 30, 60, 120 and 180 minutes of irradiation. (n=3) (D) Highest intracellular hydroxyl radical concentration change fold in *mCherry - E. coli* after 60 minutes of irradiation with 0.4% g-C_3N_4 hydrogel immersion. Data represent mean ± SD from three independent experiments (n = 3).

spontaneous reduction caused degradation was accepted for the quantitative measurement in this work. According to the verification test, the absorption of CBB solution at 588 nm showed a noticeable change under different treatment conditions, indicating the sensitivity of the generated hydroxyl radical. Hydroxyl radical release was measured in all g-C_3N_4 hydrogels in two schemes: continuous irradiation for different periods and ON-OFF-ON mode with 30 minutes for one cycle. Under continuous irradiation, every g-C_3N_4 hydrogel with a specific concentration of g-C_3N_4 materials showed a gradually increase amount of Hydroxyl radical generation as the irradiation time extended, which means a longer period of irradiation-induced more photon energy to the doped g-C_3N_4 materials, more charge carriers were excited for the redox reaction. When the g-C_3N_4 hydrogel is doped with more g-C_3N_4 materials, providing more opportunity for electron-hole pairs formation and migration[162];

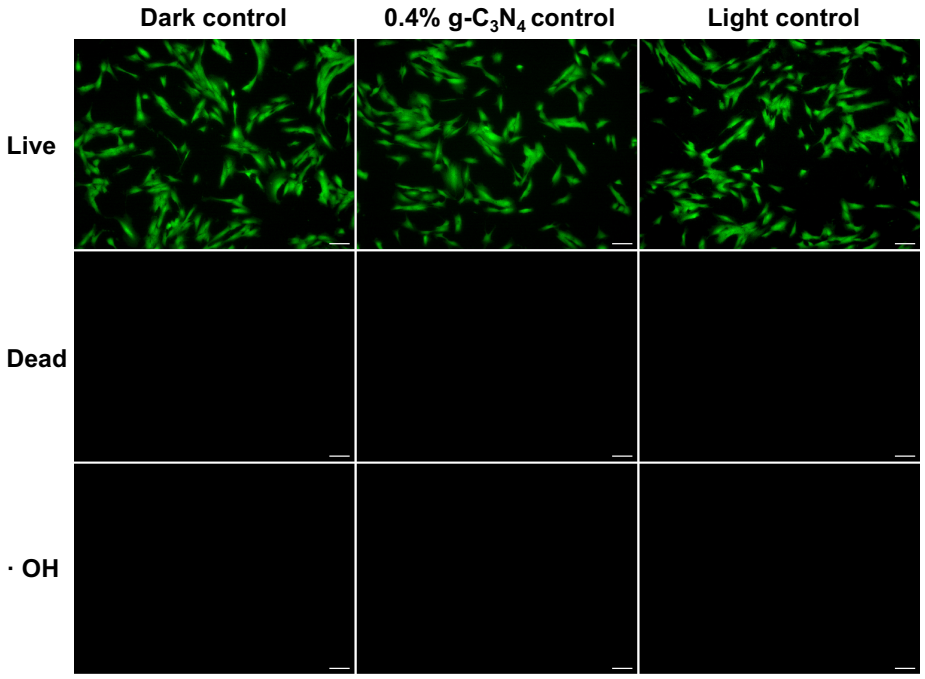

Fig. 4.32 Live / Dead and intracellular hydroxyl radical images of fibroblast cells treated with only 0.4% g-C_3N_4 hydrogel and only LED light irradiation for 60 minutes. The scale bar is 100 μm.

therefore, under the same time irradiation, released hydroxyl radical concentration also increases as the g-C_3N_4 materials amount increases in the g-C_3N_4 hydrogel system.

For the superoxide anion measurement, the same method was used with Nitrobule tetrazolium (NBT) as the colourimetric indicator; the measured superoxide anion concentration lay between 10 μM to 60 μM, obviously higher than the value of hydroxyl radical because the photocatalytic reactions, superoxide anion is the one-electron reduction product firstly formed by the charger carrier react with surrounding oxygen, as shown in **Equation 4.7**:

$$O_2 + e^- \rightarrow O_2^{\cdot -} \tag{4.7}$$

Then, the formed superoxide anion ($O_2^{\cdot -}$) further generates hydrogen peroxide as reactions shown below:

$$O_2^{\cdot -} + 2H^+ + e^- \rightarrow H_2O_2 \tag{4.8}$$

Alternatively, forming the hydrogen peroxide through disproportionation in aqueous medium (**Equation 4.9**):

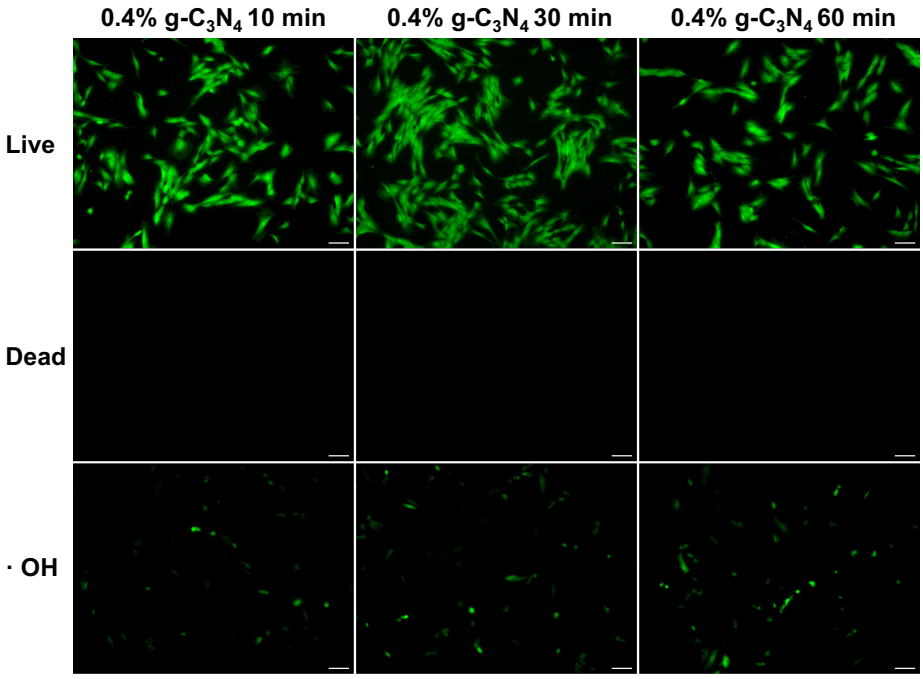

Fig. 4.33 Live / Dead and intracellular hydroxyl radical images of fibroblast cells treated with 0.4% g-C_3N_4 hydrogel and LED light irradiation for 10, 30 and 60 minutes. The scale bar is 100 μm.

$$O_2^{\cdot -} + O_2^{\cdot -} + 2H^+ \rightarrow H_2O_2 + O_2 \tag{4.9}$$

Obtained hydrogen peroxide from all g-C_3N_4 hydrogels in different irradiation periods ranged from 10 μM to 35 μM, which is similar to the concentration of hydroxyl radical, as the hydroxyl radical is one of the products from hydrogen peroxide (**Equation 4.10**)

$$H_2O_2 + e^- \rightarrow {}^{\cdot}OH + OH^- \tag{4.10}$$

One interesting thing observed in the hydroxyl radical measurement is that the DMA hydrogel degrades the CBB solution after irradiation because of the strong oxidative effect in its polymerisation system, which could be further supported by superoxide anion and hydrogen peroxide data. However, in our g-C_3N_4 hydrogel system, the g-C_3N_4 material was used as the initiator, neutralising the intense oxidative damage very well and providing excellent biocompatibility. ON-OFF-ON irradiation mode was implemented to investigate the sustainable release of ROS in g-C_3N_4 hydrogel through this photocatalytic mechanism;

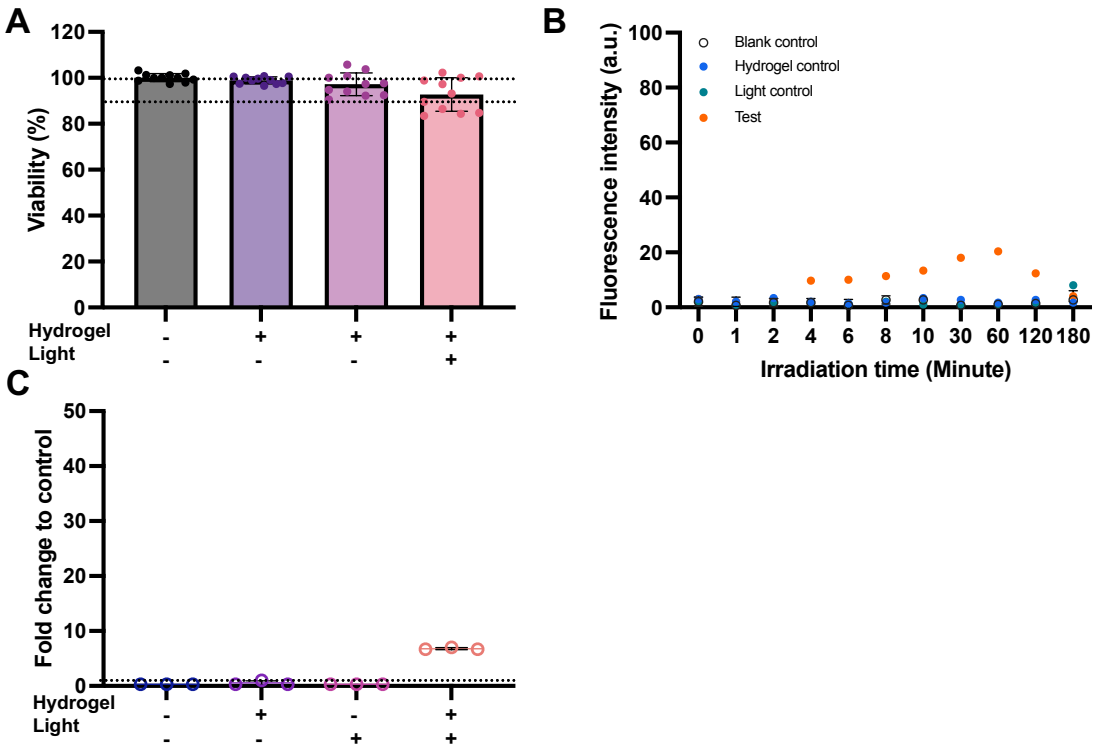

Fig. 4.34 Mammalian cell damage effects and intracellular hydroxyl radical accumulation induced by ROS generated from 0.4% g-C_3N_4 hydrogels in fibroblast cell. 0.4% g-C_3N_4 hydrogel and visible light system induced (A) Viability Data represent mean ± SD from independent experiments (n = 11). (B) Intracellular hydroxyl radical fluorescence signal in fibroblast cells after 0, 1, 2, 4, 6, 8, 10, 30, 60, 120 and 180 minutes of irradiation. (n=3) (C) Highest intracellular hydroxyl radical concentration change fold in fibroblast cells after 60 minutes of irradiation with 0.4% g-C_3N_4 hydrogel immersion. Data represent mean ± SD from three independent experiments (n = 3).

obtained data suggested that g-C_3N_4 hydrogels could continuously form reactive oxygen species in the light-off cycle; this makes it more competitive as a wound healing bandage material.

After detailed confirmation of reactive oxygen species generation in g-C_3N_4 hydrogel under visible light illumination, the Live / Dead assays were implemented against gram-positive, gram-negative, and fibroblast cells. All prepared g-C_3N_4 hydrogels presented a practical bacterial killing effect in gram-positive bacteria and gram-negative bacteria, but no apparent fibroblast cell damage was observed. Based on this information and previous ROS generation and polymerisation data, 0.4% g-C_3N_4 was selected for the further detailed exploration sample.

Extended irradiation with different interested time points was applied to the 0.4% g-

C_3N_4 hydrogel-interpreted bacteria and mammalian cell systems to fully understand the ROS-caused bacterial killing pattern in different cells. Live / Dead assay, fluorescence images and intracellular hydroxyl radical concentration were monitored in parallel experiments. Our results showed that the ROS-caused killing efficiency in gram-positive bacteria was higher than the value in gram-negative bacteria; combing with the intracellular hydroxyl radical concentration variation, intracellular hydroxyl radical in gram-positive bacteria reached highest concentration after 30 minutes of irradiation of immersed 0.4% g-C_3N_4 hydrogel, and maximum concentration of hydroxyl radical appeared in gram-negative bacteria 30 minutes later than that in gram-positive bacteria, showing around 2.1 μM lower than the value in gram-positive bacteria as well. Meanwhile, the killing efficiency in gram-positive bacteria reached 90% after 180 minutes of irradiation, and a sharp increase in killing occurred after 30 minutes of irradiation, which resulted from the maximum hydroxyl radical accumulation in bacterial cells at 30 minutes. Moreover, the tendency in gram-negative bacteria differed; killing efficiency increased gradually, with a final killing percentage at around 70%. Intracellular hydroxyl radical concentration measured in gram-positive bacteria and gram-negative bacteria samples also showed a significant difference; in the gram-positive bacterial group, the highest intracellular hydroxyl radical concentration enhanced 45-fold compared to the negative control group and only 25-fold of intracellular hydroxyl radical concentration increased in gram-negative bacteria.

Their membrane structure disparity can explain this killing difference caused by ROS between gram-positive and gram-negative bacteria[204]; the existing structural discrepancy plays a crucial role in how bacteria encounter attack and respond to different reactive oxygen species, leading to varying degrees of susceptibility. Gram-positive bacterial only have one layer of membrane, which mainly consists of a thicker peptidoglycan layer around 20 – 80 nm; this relatively porous structure presents higher permeability, allowing ROS to diffuse through quickly, getting into contact with inside components such as lipids and DNA, leading to rapid cell lysis and death. As we considered the hydroxyl radical as the primary attack factor in this work, it possesses high activity but is limited by diffuse distance; however, as the simple structure of gram-positive bacteria, more severe damage will be caused once the hydroxyl radical is attached and penetrated.

Lower killing efficiency in gram-negative bacteria could be attributed to several factors. Compared to the gram-positive bacteria, gram-negative bacteria have two membrane layers. The outer membrane comprises lipopolysaccharides (LPS), which consume encountered ROS effectively, acting as an extra protective layer for gram-negative bacteria[205]. Besides this, the hydrophobic character of the constructed outer membrane could also be against the invasion of hydroxyl radicals due to its hydrophilic affinity. Moreover, the periplasmic

space between the outer and inner cytoplasmic membranes extends the distance between outside and intracellular, decreasing the risk of hydroxyl radical diffusion. All these effective depletions and physical defence against hydroxyl radicals protect gram-negative bacteria from being killed very well. We further confirmed no significant damage in fibroblast cells, because fibroblast cells[206] have more complex intracellular structures than bacterial cells and possess more comprehensive antioxidative mechanisms. Previous attachment test reveals that bacteria tended to attach on the surface of 0.4% g-C_3N_4 hydrogel, and these closely attached bacteria consume most of the highly active hydroxyl radical; the rest of the species existed in an average physiological concentration; they mainly act as the signalling factor in redox biological processes.

As a promising material for chronic wound healing bandage, our developed g-C_3N_4 hydrogel embedded the semiconductor material into the hydrogel system and obtained the ideal hydrogel with the same optical properties as its two-dimensional material but eliminated its potential toxicity and avoided the necessity for inducing another extra material into the open wound site. Under the physiological concentration, ROS commonly stay low and react with specific targets for highly organised cellular proceedings. In contrast, when this tight control of ROS concentration is broken, it means in an oxidative stress environment, the formed concentration difference of ROS would break the maintained steady state of the target. The essential redox balance in the microenvironment is an opportunity for this controllable photocatalytic reaction generated reactive oxygen species to defend the invasion pathogen as well, in the bacteria mammalian cells co-occupied chronic wound site, to clear bacteria and restore the environment through a method of relatively breaking the internal physiological homeostasis then reconstruct by using the moderate ROS as signalling transduction factor, effectively avoiding extra drug-induced resistance. As all biological processes are regulated in a dose-dependent manner, our quantified ROS generation made it more predictable and reliable.

4.4 Conclusion

In this chapter, the reactive oxygen species (ROS), including hydroxyl radical, superoxide anion and hydrogen peroxide, generated from all g-C_3N_4 hydrogels were quantified in detail. The calibration curve of hydroxyl radical was obtained using the Fenton reaction, and the Coomassie brilliant Blue (CBB) solution was used as the indicator. Under the irradiation of visible light for different periods, the hydroxyl radical generated from all g-C_3N_4 hydrogels is between 8 – 32.6 μM. Superoxide anion was calibrated by the standard curve from the xanthine/xanthine oxidase reaction, Nitrobule tetrazolium (NBT) was used as the

probe, and g-C_3N_4 hydrogel generated superoxide anion ranged from 19 μM to 83 μM with different irradiation periods. Hydrogen peroxide was measured using the Amplex red assay kit, and the calibrated hydrogel peroxide from g-C_3N_4 hydrogels under different irradiation periods ranged from 10 μM to 33 μM.

To select the best-performance g-C_3N_4 hydrogel, *S. epidermidis*, *E. coli-DH 5α*, *mCherry-E. coli-DH 5α* and fibroblast cells were treated with all g-C_3N_4 hydrogels with 60 minutes of visible light irradiation; the Live/Dead staining and fluorescence images were conducted, combined with the preparation conditions, 0.4% g-C_3N_4 hydrogel was chosen for the following experiments.

When the ROS generation concentration was quantified with all g-C_3N_4 hydrogels under different irradiation periods, the hydroxyl radical was selected, as it is the main source of damage. After this, the relationship between viability and intracellular hydroxyl radical concentration was explored in bacteria and mammalian cell groups, all of which were treated using 0.4% g-C_3N_4 hydrogel under different times of irradiation. The obtained results showed that the gram-positive bacteria are much more easily diffused and inactivated by hydroxyl radical from g-C_3N_4 hydrogel than gram-negative bacteria. However, the fibroblast cells presented much less intracellular hydroxyl radical concentration after the same treatment, implying the different oxidative defence situations among gram-positive bacteria, gram-negative bacteria and mammalian cells.

The work in this chapter confirmed that the visible light illuminated g-C_3N_4 hydrogel could quantitatively form various reactive oxygen species following the subsequent photocatalytic process. 0.4% g-C_3N_4 hydrogel released reactive oxygen species that could kill different bacteria to different extents and showed no severe harm to fibroblast cells. Monitored intracellular hydroxyl radicals also exhibited a similar tendency to kill efficiency in different cell groups, indicating the consistency of results. This work reveals a promising hydrogel system to effectively treat the complex chronic wound environment in novel drug-free methods for the future development of antibacterial strategies for wound healing.

Chapter 5

Selective Antibacterial Action of ROS Generated by g-C_3N_4 Hydrogels

5.1 Introduction

As the largest organ, the intact skin barrier protects underlying biological tissue from invasion by exogenous and pathogenic microorganisms. A wound is formed when the skin barrier gets injured; without the shielding of the barrier skin[76]the exposed wound bed and vulnerable biological tissue are susceptible to contamination, leading to infection. Regular or acute wound repair follows well-organised and overlapping phases, including haemostasis, inflammation, re-epithelialisation and remodelling. The immunocompromised conditions could cause these events to be dysfunctional and lead to chronic wounds; these nonhealing chronic wounds pose a dramatic threat to the whole globe due to the aging population and increased obesity, diabetes and systemic disease. Understanding the complexity of the chronic wound environment and its underlying mechanisms is essential for improving the healing process and developing appropriate therapeutic methods. From a cellular perspective, wound healing requires the devotion and coordination of various host cells, including keratinocytes, fibroblasts and immune cells. However, the invasive and colonised microorganisms could hinder the healing progression across the healing stages by dysregulating the mammalian cell function and resulting in systematic infection. Thus, it is crucial to selectively kill bacteria over mammalian cells in the infected chronic wound site.

In addition, chronic wounds are commonly polymicrobial, and the colonised bacteria in chronic wounds usually alter the microenvironment to impair wound healing; some of them can form a biofilm, which is the structured bacterial communities enclosed by extracellular polymeric substance (EPS) that protect the colonised bacterial resident. More than 80%

of chronic wounds are covered by biofilms[119], considered one of the severe obstructions during wound healing. Thus, improving wound healing involves appropriately inactivating bacteria over mammalian cells while regulating and reshaping the coordinating sequence of cell signalling events.

We have previously studied the reactive oxygen species generation in our developed g-C_3N_4 hydrogel, and the controllable release of ROS was confirmed in g-C_3N_4 hydrogel after visible light irradiation. The ROS molecules formed effectively inactivate the bacteria in both Gram-positive and Gram-negative conditions but show no apparent damage to the fibroblast cells. However, the potential of selective damage was detected in the separately cultured bacterial group and fibroblast group. Here, to further confirm the selective antibacterial effect of ROS against bacteria on mammalian cells in a wound-similar environment, a simple bacteria mammalian cell co-culture group was constructed to mimic the chronic wound site situation, 0.4% g-C_3N_4 hydrogel was applied to the co-culture group in a controllable format. First, the evolution of bacteria accumulation and fibroblast cell viability in a coculture model was studied to determine the robustness of the basement of the coculture mode. Based on this, the viability of bacteria and fibroblast cells was evaluated after direct contact with 0.4% g-C_3N_4 hydrogel after different irradiation times. The performance of biofilm eradication and the essential functions of mammalian cells were also determined in detail.

5.2 Results

5.2.1 Accumulation of RFP-expressed bacteria in the co-culture group

The bacteria and mammalian cell co-culture model was constructed with RFP–*E. coli* (*mCherry–E. coli*) and fibroblast cells to mimic the chronic wound environment. As our aim in this part is to check whether the bacteria in the co-culture group will be killed and leave the mammalian cell to live well, the accumulation status of RFP–*E. coli* was monitored throughout different co-culture periods. After 2, 4, 6, 8, 12 and 24 hours, co-cultured samples were stained with CellMask TM Actin Tracking Stains and NucRed for the skeleton and nucleus of fibroblast cells, respectively.

Fluorescence images were collected, as shown in **Figure 5.1A**, and then the number of RFP–*E. coli* accumulated around the fibroblast cells at specific time points was analyzed using colocalization analysis. In **Figure 5.1B**, different from the images of 2 hours, 4 hours, and 6 hours, when the co-culture period increases to 8 hours, it is evident that the RFP-*E. coli* cells gradually become close to the fibroblast cells, attaching to the fibroblast cells, moving

from the periphery towards the center nucleus.

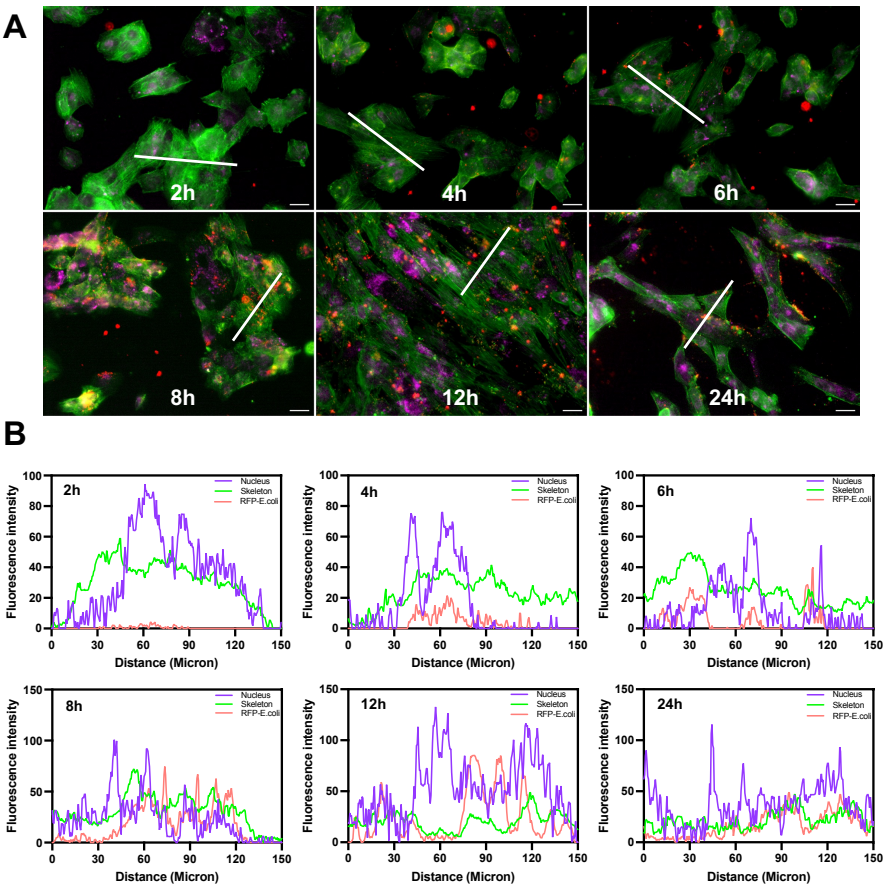

Fig. 5.1 RFP-*E. coli* accumulation status in co-cultured group. (A) Fluorescence images of co-cultured group after 2, 4, 6, 8, 12 and 24 hours of co-culture. The scale bar is 50 μm. (B) Co-localization analysis of images in figure A.

The data from the co-localization analysis suggested that almost no red fluorescent protein signal was observed along with the cell skeleton signal after 2 hours of co-incubation, and the signals gradually increased after 4 -6 hours of co-culture. 12- and 24-hour co-culture led to a high co-localise between fibroblast cell signal and accumulated RFP-*E. coli* signal and captured fluorescence images showed the same condition. Slightly less RFP-*E. coli* bacterial cell number in the fluorescence images (**Figure 5.1A**) resulted from the washing step in fluorescence sample preparation because, after 24 hours of co-culture, earlier biofilm was formed, which is easily destroyed by repeated washing, flushing more RFP-*E. coli* cells away.

5.2.2 Viability of fibroblast cells in the co-cultured group

Another vital factor in this co-cultured model is the viability of fibroblast cells. To selectively kill bacteria over mammalian cells, the live status of the co-group needs to be confirmed first to avoid any possible misinterpretation for the next step of work. Thus, the fibroblast cells in the co-cultured group were stained with a Live / Dead assay kit after 2, 4, 6, 8, 12 and 24 hours of co-culture, and then fluorescence images and fluorescence signal from the live channel were measured as well. No unmistakable dead signal of fibroblast was observed in both fluorescence images and fluorescence intensity across all co-cultured periods (**Figure 5.2A** and **Figure 5.2B**). Meanwhile, a red fluorescent protein signal was also detected; data shown in **Figure 5.2C** presented the same variation as data in the co-localisation analysis. The obtained red fluorescent protein signal grew steady as the incubation period extended, and a noticeable drop was observed in the 24-hour sample. No significant damage was exhibited; 8 hours of co-culture were used as the co-incubating period for all following co-cultured work.

5.2.3 Selectively inactivation in bacteria over mammalian cells by ROS generated from g-C_3N_4 hydrogel in the co-cultured group

To find the evidence for the hypothesis that hydroxyl radical from 460 nm catered LED light irradiated 0.4% g-C_3N_4 is capable of killing bacteria over mammalian cells, even in the co-cultured group. They verified the co-culture group with RFP-*E. coli* and fibroblast cells were treated using 0.4% g-C_3N_4 under different irradiation times, viability of fibroblast cells and RFP-*E. coli* was monitored using both microplate data reading and fluorescence microscopic images.

As the data shown in **Figure 5.3A**, after the first 10 minutes of treatment, 20% of RFP-*E. coli* cells were damaged, and the kill percent of fibroblast cells was about 6%. From the view of intracellular hydroxyl radical concentration change, the detected hydroxyl radical signal in the co-cultured group after 10 minutes was 111 in fluorescence intensity (**Figure 5.3B**), corresponding to 8.46 μM of hydroxyl radical inside. Fibroblast cell killing percent in the co-cultured group was kept lower than 10% within 180 minutes of treatment, while the RFP-*E. coli* was killed 30% after 60 minutes, 50% after 120 minutes and 70% after 180 minutes of treatment, showing similar development in the single group treatment.

Regarding intracellular hydroxyl radical concentration in the co-cultured group, the highest concentration reached at 30 minutes, the same as *S. epidermidis* but earlier than the *E. coli - DH 5α* group due to the contributions from two species. At 30 minutes, the fluorescence intensity of hydroxyl radical in the co-group was 225 with 18 μM in exact

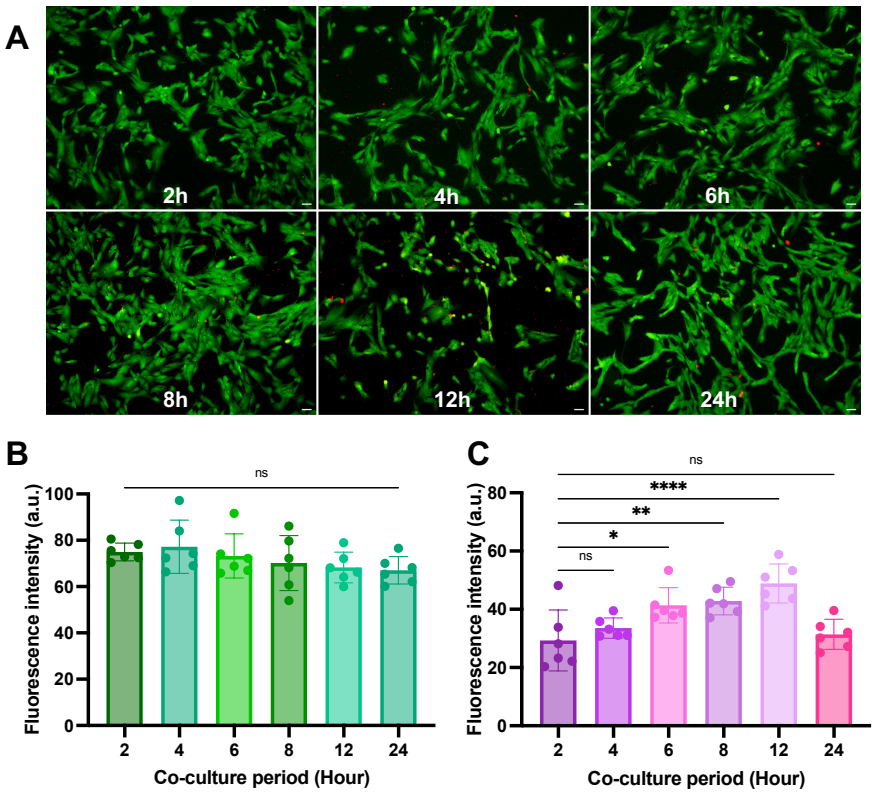

Fig. 5.2 Viability of fibroblast cells in the co-cultured group. (A) Fluorescence images of fibroblast cells in co-cultured group. Scale bar is 50 μm. (B) Live signal of fibroblast cells in co-cultured group, (n=6) (C) Red fluorescent protein signal from RFP-*E. coli* in the co-culture group, (n=6). Data are presented as $mean \pm SD$ (n = 6). Statistical analysis was performed using one-way ANOVA followed by Dunnett's post hoc test. $P \leq 0.05$ was considered statistically significant (* $p \leq 0.05$, **$p \leq 0.01$, *** $p \leq 0.001$, **** $p \leq 0.0001$). Statistical analysis was conducted using GraphPad Prism 10.0.

intracellular hydroxyl radical concentration. The detected hydroxyl radical signal dropped gradually as irradiation time lasted (**Figure 5.3C**). Fluorescence images of Live / Dead staining and intracellular ROS were collected after 10 and 60 minutes of irradiation (**Figure 5.4** and **Figure 5.5**), showing the same results as plotted data in **Figure 5.3**. Live signal of RFP-*E. coli* was diminished gradually without disturbing fibroblast cells, and the hydroxyl radical signal could be seen slightly.

5.2.4 Biofilm eradication

One significant factor contributing to the complex microenvironment in chronic wounds is that they are easily occupied by bacterial strains that hinder wound healing. Some of

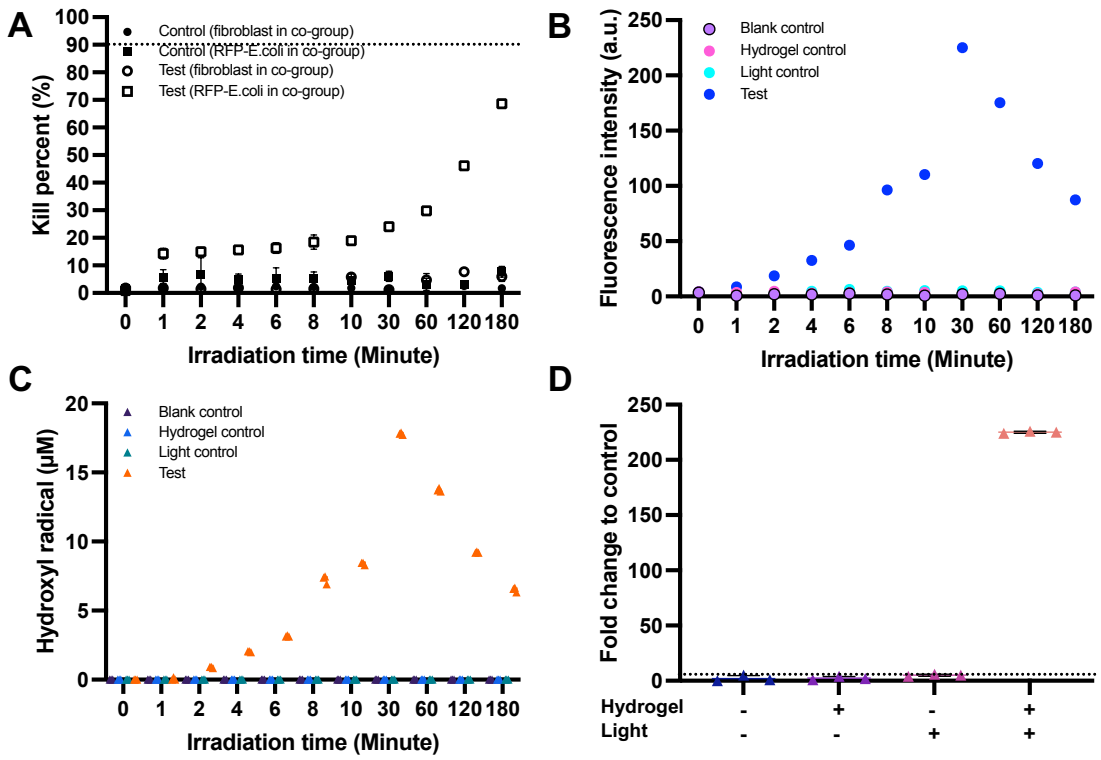

Fig. 5.3 Selectively killing and intracellular hydroxyl radical concentration caused by ROS from 0.4% g-C_3N_4 hydrogel in RFP-*E. coli* and fibroblast cells co-cultured group. 0.4% g-C_3N_4 hydrogel caused (A) selectively Killing efficiency (B) intracellular hydroxyl radical fluorescence signal (C) intracellular hydroxyl radical concentration in co-cultured group after 0, 1, 2, 4, 6, 8, 10, 30, 60, 120 and 180 minutes of irradiation. (n=3) (D) Highest intracellular hydroxyl radical concentration change fold in co-cultured group after 30 minutes of irradiation with 0.4% g-C_3N_4 hydrogel immersion. Data represent mean ± SD from three independent experiments (n = 3).

these strains can form biofilm, a sophisticated microenvironment consisting of bacteria and polysaccharides, proteins, lipids and nucleic acids. The biofilms are commonly persistent, difficult to destroy, and may lead to severe infectious diseases. Thus, in this work, the performance of ROS released from g-C_3N_4 hydrogel against the compact biofilm was also studied. Biofilms were formed using *S. epidermidis* and *E. coli - DH 5α* after 24 hours of culture. 0.4% g-C_3N_4 hydrogel was applied onto the formed biofilm for 30 minutes and 60 minutes of treatment; a quantified assessment was carried out using crystal violet staining and confocal laser scanning to evaluate the efficiency of biofilm eradication. *S. epidermidis* elimination effect was shown in **Figure 5.6**; after 30 minutes of irradiation, 80% of biofilm was destroyed and reached 93.8% after 60 minutes of irradiation (**Figure 5.6A**). In the CLSM images, almost no intact biofilm structure remains after 60 minutes of treatment (**Figure**

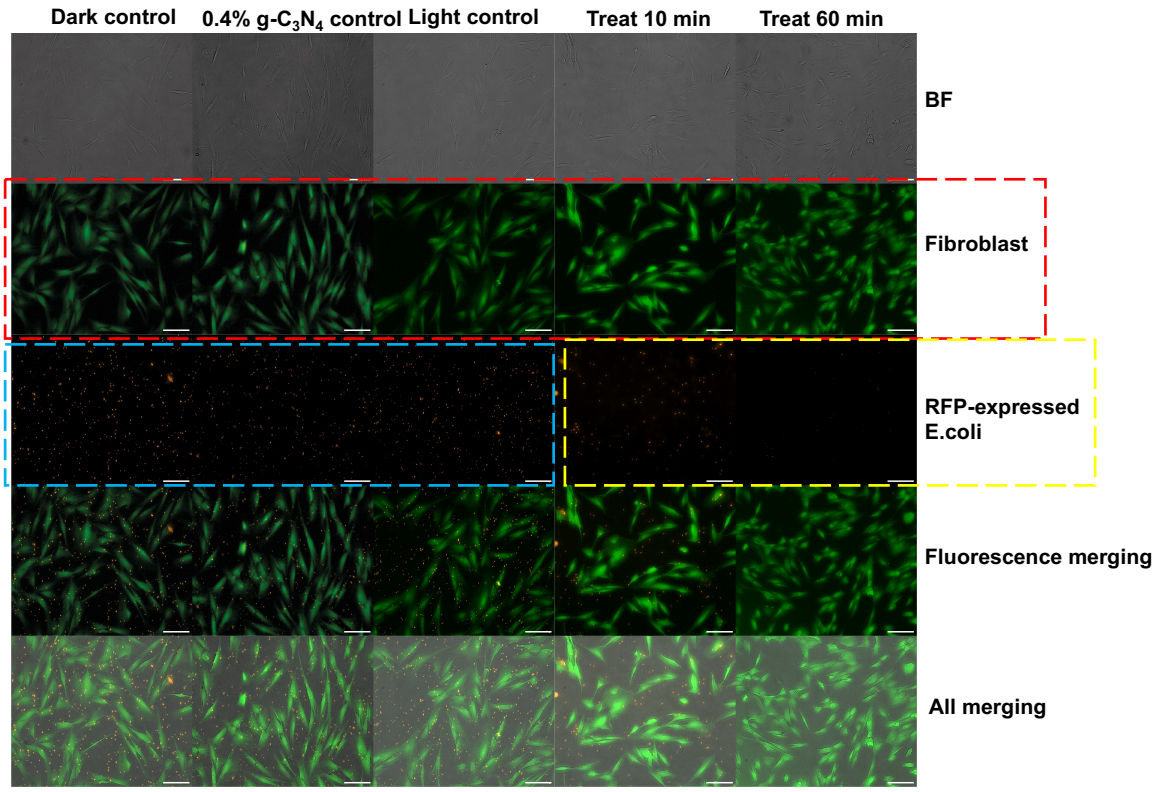

Fig. 5.4 Live / Dead fluorescence images of co-cultured group after the treatment with 0.4% g-C_3N_4 hydrogel and LED light irradiation. **Dark control**, only co-cultured group with no treatment; **0.4% g-C_3N_4 hydrogel control**, the co-cultured group covered by 0.4% g-C_3N_4 hydrogel for 60 minutes without light irradiation; **Light control**, the co-cultured group irradiated using visible light for 60 minutes without 0.4% g-C_3N_4 hydrogel; **Treat 10 minutes**, the co-cultured group covered with 0.4% g-C_3N_4 hydrogel and irradiated using visible light for 10 minutes; **Treat 60 minutes**, the co-cultured group covered with 0.4% g-C_3N_4 hydrogel and irradiated using visible light for 60 minutes; **Row BF** is the bright field images of co-cultured group; **Row Fibroblast** is the Live/Dead staining images of fibroblast cells in the co-cultured group after the different treatments, green is the live fibroblast cells, red is the dead fibroblast cells; **Row RFP-expressed *E. coli*** is the Live/Dead images of RFP-expressed *E. coli* in the co-cultured group after the different treatments, orange is the fluorescence signal of RFP-expressed *E. coli*, which is decreased and disappeared as viability of RFP-expressed *E. coli* decreased and dead; **Row fluorescence merging** is the merge of the Live/Dead fluorescence images of fibroblast cells and RFP-expressed *E. coli* in the co-cultured group; **Row all merging** is the merge of fluorescence merging images with bright field images. Green is the live fibroblast cells, red is the dead fibroblast cells; and orange is the fluorescence signal from RFP. The scale bar is 100 μm.

5.6B), aligned with the crystal violet staining data. Another interesting point observed is that the only light-irradiated control sample showed slight degradation, possibly because the *S.*

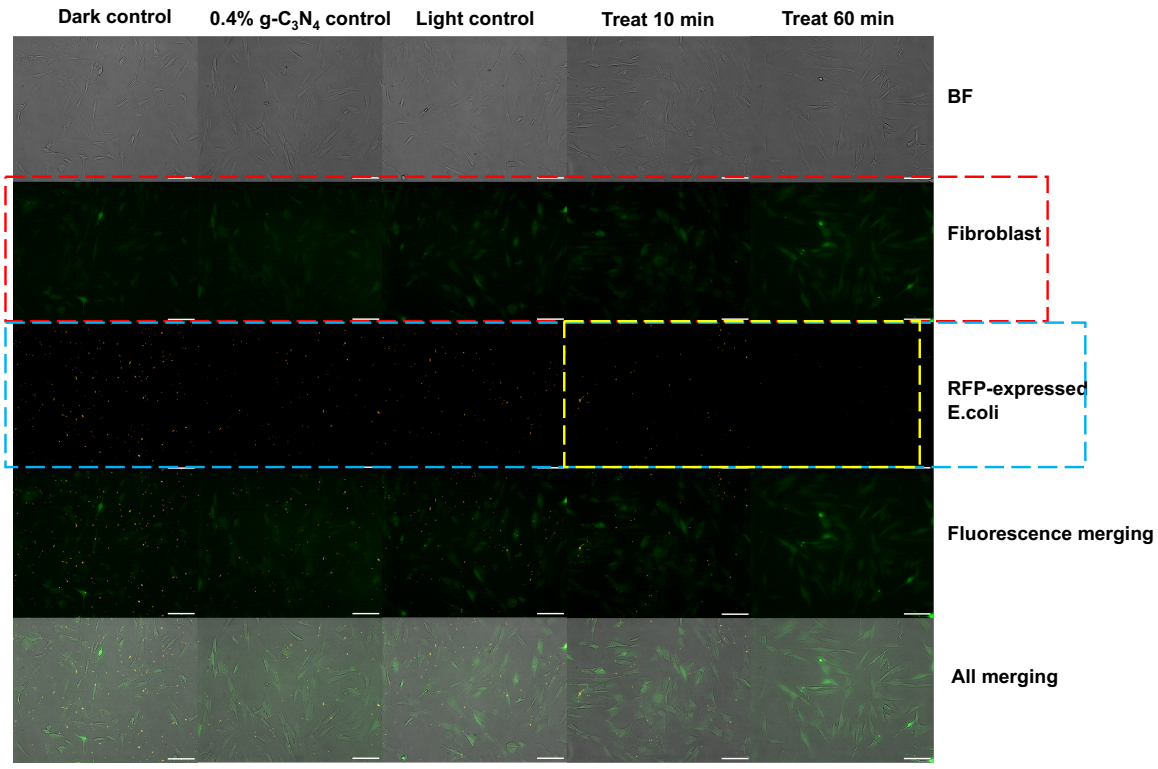

Fig. 5.5 Intracellular hydroxyl radical in co-cultured group after treatment of 0.4% g-C_3N_4 hydrogel and LED light irradiation. **Dark control**, only co-cultured group with no treatment; **0.4% g-C_3N_4 hydrogel control**, the co-cultured group covered by 0.4% g-C_3N_4 hydrogel for 60 minutes without light irradiation; **Light control**, the co-cultured group irradiated using visible light for 60 minutes without 0.4% g-C_3N_4 hydrogel; **Treat 10 minutes**, the co-cultured group covered with 0.4% g-C_3N_4 hydrogel and irradiated using visible light for 10 minutes; **Treat 60 minutes**, the co-cultured group covered with 0.4% g-C_3N_4 hydrogel and irradiated using visible light for 60 minutes; **Row BF** is the bright field images of co-cultured group; **Row Fibroblast** is the intracellular hydroxyl radical images of fibroblast cells in the co-cultured group after the different treatments, green is the fluorescence signal of intracellular hydroxyl radical; **Row RFP-expressed *E. coli*** is the intracellular hydroxyl radical images of RFP-expressed *E. coli* in the co-cultured group after the different treatments, orange is the fluorescence signal of RFP-expressed *E. coli*, which is decreased and disappeared as the intracellular hydroxyl radical increase in bacterial cell, because of the bacterial cell membrane broken, here, no obvious hydroxyl radical signal observed is also affected by the size difference and signal intensity difference between bacteria and fibroblast cells; **Row fluorescence merging** is the merge of intracellular hydroxyl radical in fibroblast cells and RFP-expressed *E. coli*; **Row all merging** is the merge of fluorescence merging images with bright field images. Green is the intracellular hydroxyl radical signal; orange is the fluorescence signal from RFP. The scale bar is 100 μm.

epidermidis is much easier to break.

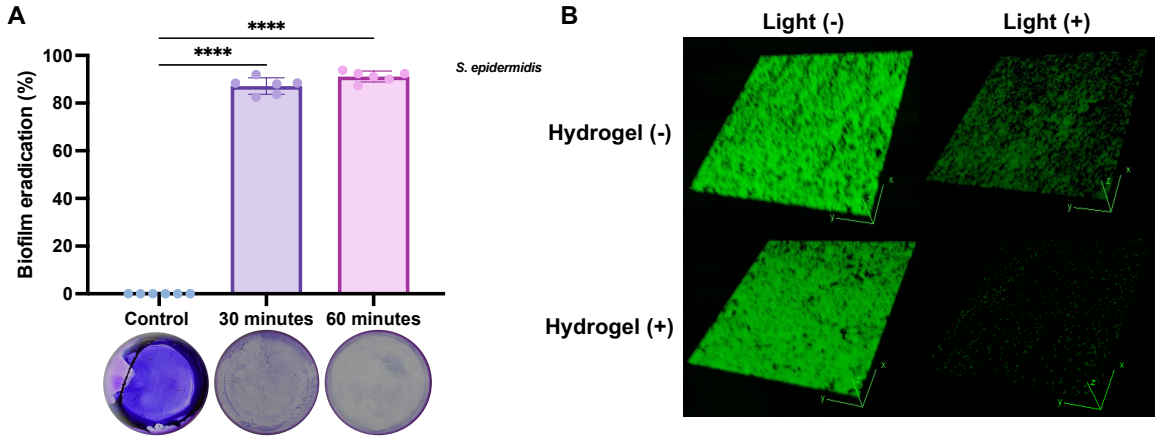

Fig. 5.6 *S. epidermidis* formed biofilm eradication. (A) Crystal violet stainning test and (B) Confocal Laser Scanning microscopic images of *S. epidermidis* formed biofilm after treated by 0.4% g-C_3N_4 hydrogel and LED light irradiation. Purple is the biofilm stained with Crystal violet solution. Green is the bacteria in biofilm stained with SYTO-9 dye. Data are presented as $mean \pm SD$ (n = 6). Statistical analysis was performed using one-way ANOVA followed by Dunnett's post hoc test to compare each treatment group with the control. $P \leq 0.05$ was considered statistically significant (ns = not significant, * $p \leq 0.05$, ** $p \leq 0.01$, *** $p \leq 0.001$, **** $p \leq 0.0001$). Statistical analysis was conducted using GraphPad Prism 10.0.

In the *E. coli - DH 5α* test, the biofilm eradication rate was also over 88% after 30 minutes and 92% after 60 minutes of treatment (**Figure 5.7A**). The obtained confocal scanning images show an effective biofilm intactness decomposition. The data collected in this part confidently support that the ROS from 0.4% g-C_3N_4 hydrogel eradicate compact biofilm very well; it is beneficial for chronic wound environment management.

5.2.5 Effects of 0.4% g-C_3N_4 hydrogel treatment on mammalian cell functions

To obtain robust results for our selectively killing work, we investigated in detail the live status and essential functions of fibroblast cells in this co-culture group after treatment.

Measurement of migration in fibroblast cell

Firstly, the migration capability of fibroblast cells was evaluated after 10 minutes, 30 minutes and 60 minutes of treatment; fluorescence images were collected after 12 hours, 24 hours and 3 days of continuous culture (**Figure 5.8A**), and the wound healing rate was analysed for every specific time. 12 hours of data was shown in **Figure 5.8B** 10 and 30

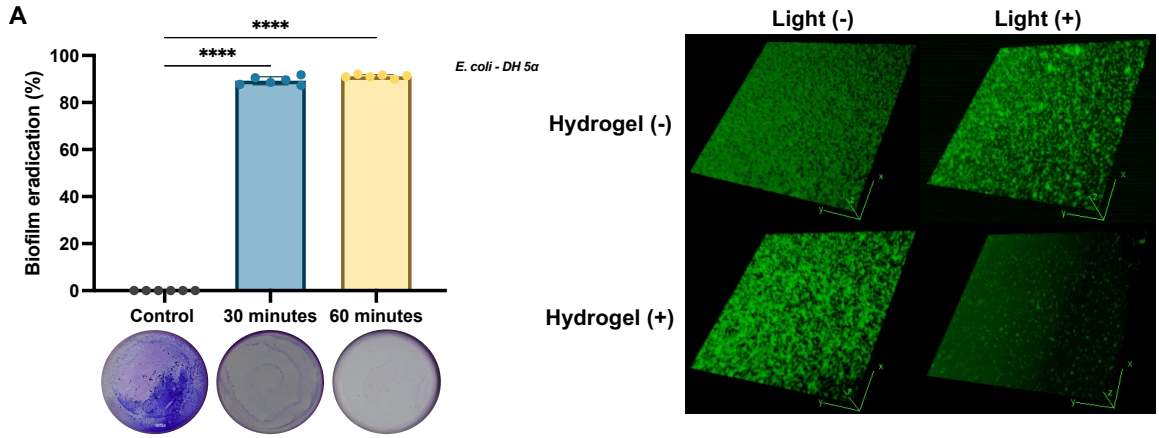

Fig. 5.7 *E. coli - DH 5α* formed biofilm eradication. (A) Crystal violet stainning test and (B) Confocal Laser Scanning microscopic images of *E. coli - DH 5α* formed biofilm after treated by 0.4% g-C_3N_4 hydrogel and LED light irradiation. Purple is the biofilm stained with Crystal violet solution. Green is the bacteria in biofilm stained with SYTO-9 dye. Data are presented as $mean \pm SD$ (n = 6). Statistical analysis was performed using one-way ANOVA followed by Dunnett's post hoc test to compare each treatment group with the control. $P \leq 0.05$ was considered statistically significant (ns = not significant, * $p \leq 0.05$, ** $p \leq 0.01$, *** $p \leq 0.001$, **** $p \leq 0.0001$). Statistical analysis was conducted using GraphPad Prism 10.0.

minutes irradiation samples presented 11% and 14% gap closing, slower than the control group with a 19% closure rate. 60 minutes treated sample migrated 17% after 12 hours of culture, showing no significant difference from the control group. After 24 hours of culture, there is no obvious statistical difference between the control, 10-minute, and 30-minute treated samples, with around 30% healing. 60 minutes irradiated sample presented the highest closure rate with 42% (**Figure 5.8C**). 3 days later (**Figure 5.8D**), the gap was nearly closed, and all treated groups showed an 80% closure rate, the same as the control group. Therefore, the migration behaviour of treated fibroblast cells proved that hardly impairment was induced by LED irradiated 0.4% g-C_3N_4 hydrogel, which means the released ROS did not affect the proliferation and migration capability of fibroblast cells.

Assessment of morphology change in fibroblast cells

Then, the morphology of fibroblast cells was checked after treatment. The area of fibroblast cells was located at 2000 μm^2 on average (**Figure 5.9B**). Obtained data suggested that cell attachment status remained unaffected by either 0.4% g-C_3N_4 covering and ROS released after LED irradiation (p-value ≥ 0.05). The area analysis data is consistent with previous samples that only covered g-C_3N_4, which means that the fibroblast cells can maintain

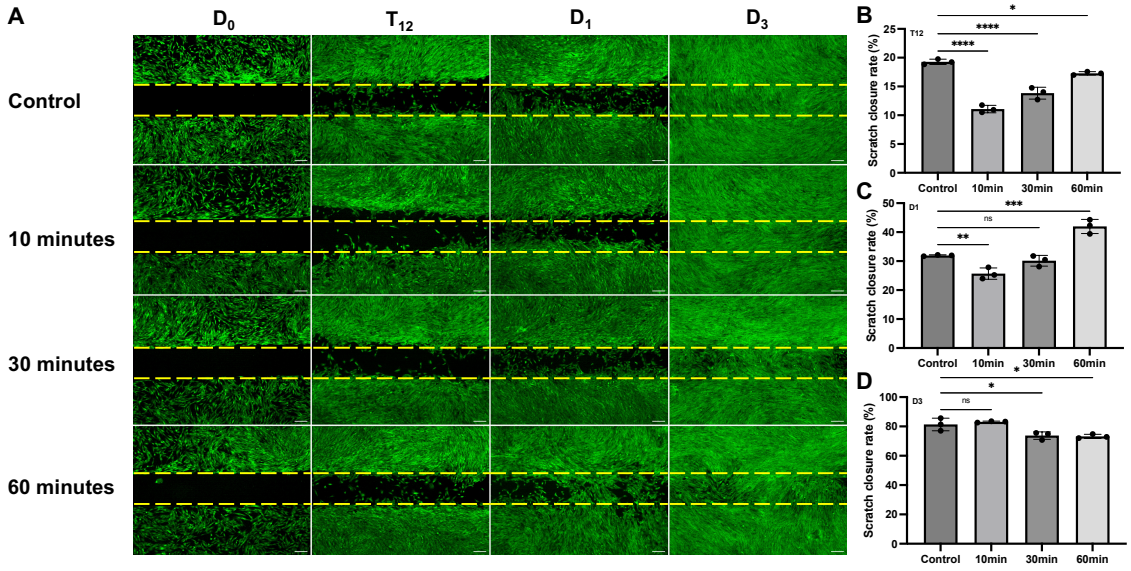

Fig. 5.8 Fibroblast cells migration capability after treated with 0.4% g-C_3N_4 hydrogel and LED light irradiation. (A) Fluorescence images of 0.4% g-C_3N_4 hydrogel and LED light treated fibroblast cell migration after 12 hours, 1 day and 3 days, scale bar is 100 μm. Scratch closure rate of treated fibroblast cells after (B) 12 hours, (C) 1 day and (D) 3 days. D_0 is the gap formed originally; T_12 is the gap after co-incubating without and with covered hydrogels for 12 hours; D_1 is the gap after co-incubating without and with covered hydrogels for 1 day (24 hours); D_3 is the gap after co-incubating without and with covered hydrogels for 3 days (72 hours). Data are presented as $mean \pm SD$ (n = 3). Statistical analysis was performed using one-way ANOVA followed by Dunnett's post hoc test to compare each treatment group with the control. $P \leq 0.05$ was considered statistically significant (ns = not significant, * $p \leq 0.05$, ** $p \leq 0.01$, *** $p \leq 0.001$, **** $p \leq 0.0001$). Statistical analysis was conducted using GraphPad Prism 10.0.

good attachment and stretch under the selective killing treatment condition. The aspect ratio data was in the range of 2 – 5; this data represented how elongated or stretched the cells are, calculated using the formula below:

$$\text{Aspect ratio} = \frac{\text{Length of the cell}}{\text{Width of the cell}} \tag{5.1}$$

When the aspect ratio is close to 1, the cell is shaped more circularly, indicating impaired cell attachment. If the aspect ratio is greater than 1, like the data in **Figure 5.9C**, the cell is spindle-shaped, a typical status for healthy fibroblast cells. Combing with the roundness data defined as:

$$\text{Roundness} = \frac{4 \times \text{Area}}{\pi \times (\text{Perimeter})^2} \tag{5.2}$$

In **Figure 5.9D**, the roundness of fibroblast cells after treatment was lower than 0.5, and no statistical difference was observed between the roundness of the fibroblast cells irradiated from different time points compared to the culture without 0.4% g-C_3N_4 hydrogel immersion or LED irradiation. This low roundness of all treated fibroblast cells suggested a more stretched and elongated shape, revealing no alteration in its functional state under selective killing conditions.

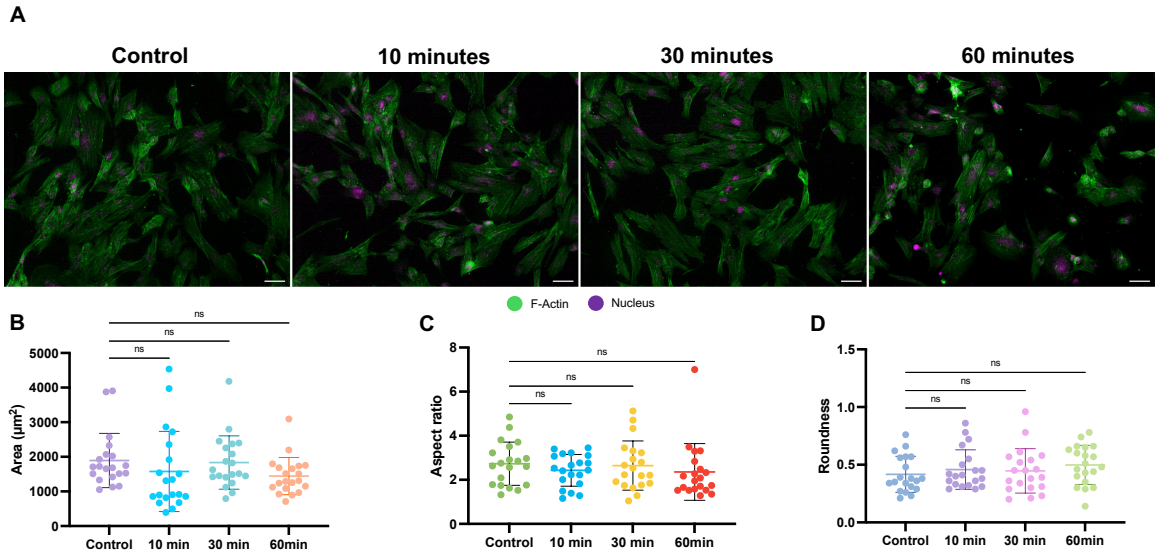

Fig. 5.9 Fibroblast cells morphology change after 0.4% g-C_3N_4 hydrogel and LED light irradiation treatment. (A) Fluorescence images of fibroblast cells after 0.4% g-C_3N_4 hydrogel and LED light irradiation treatment. The scale bar is 50 μm. Analysis of (B) area (C) aspect ratio and (D) roundness of fibroblast cells after treatment. Green is the skeleton of fibroblast cells stained with CellMaskTM Actin Tracking Stains and the purple is the cell nucleus stained with NucRed. Data are presented as $mean \pm SD$ (n = 35). Statistical analysis was performed using one-way ANOVA followed by Dunnett's post hoc test to compare each treatment group with the control. $P \leq 0.05$ was considered statistically significant (ns = not significant, * $p \leq 0.05$, ** $p \leq 0.01$, *** $p \leq 0.001$, **** $p \leq 0.0001$). Statistical analysis was conducted using GraphPad Prism 10.0.

Assessment of tube formation in HUVECs

Human umbilical vein endothelial cells (HUVECs) are also vital for chronic wound healing, playing a crucial role in angiogenesis. In chronic wounds, impaired angiogenesis is a critical issue that hinders organised healing. Thus, the angiogenesis function of HUVECs was also evaluated under the same conditions as that of selective killing. Fluorescence images and characterisation data were collected to discover the effect from either 0.4% g-C_3N_4 hydrogel

contact or ROS diffusion after LED irradiation. In **Figure 5.10B**, extremities from all groups were analysed using the collected fluorescence images (**Figure 5.10A**). An extremity or

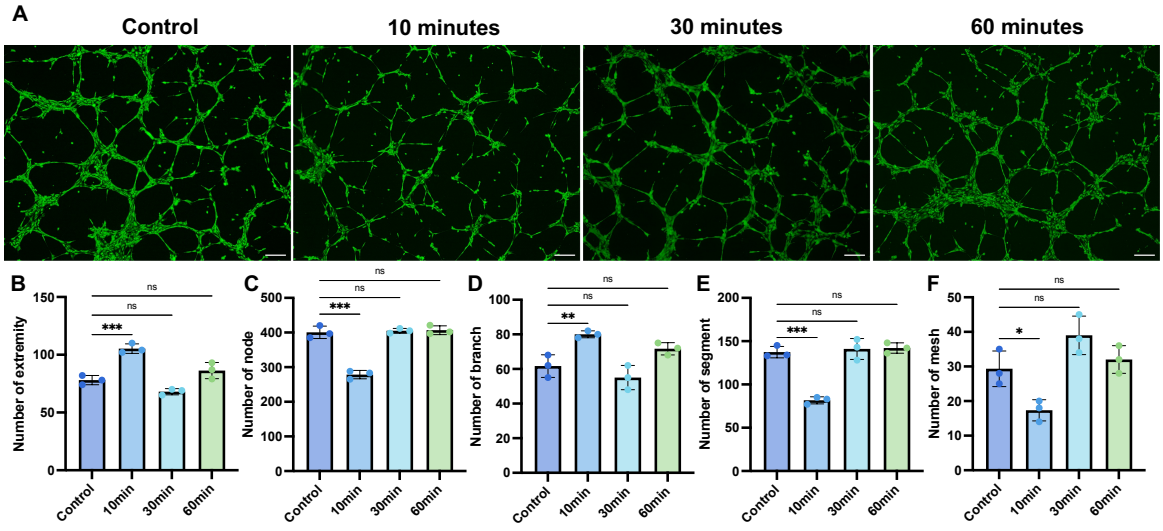

Fig. 5.10 Angiogenesis capability of HUVECs after 0.4% g-C_3N_4 hydrogel and LED light irradiation treatment. (A) Fluorescence images of HUVECs after treatment, scale bar is 200 μm. Analysis of (B) extremity (C) node (D) branch (E) segment and (F) mesh number in figure A. The HUVECs were seed on matrigel then treated with and without 0.4% g-C_3N_4 hydrogel and visible light irradiation, then all samples were put back to cell culture incubator for 6-hour of incubation, after this, the tube formation was assessment to evaluate the effect of ROS from 0.4% g-C_3N_4 hydrogel to HUVECs function. Phase-contrast images were analyzed using ImageJ with the AngioTool plugin to quantify number of extremity, node, branch, segment, and number of mesh. Images were converted to grayscale, thresholded, and skeletonized before analysis. Data are presented as *mean* $\pm$ *SD* (n = 3). Statistical analysis was performed using one-way ANOVA followed by Dunnett's post hoc test to compare each treatment group with the control. $P \leq 0.05$ was considered statistically significant (ns = not significant, * $p \leq 0.05$, ** $p \leq 0.01$, *** $p \leq 0.001$, **** $p \leq 0.0001$). Statistical analysis was conducted using GraphPad Prism 10.0.

endpoint in the angiogenesis sample refers to the terminal end of a tubule in the network. In **Figure 5.10B**, the 10-minute treated sample had an increased number of extremities than the other groups, which means a lower connection formed after 10 minutes of irradiation with 0.4% g-C_3N_4 hydrogel covered, generating an immature network during the angiogenesis process. Node is defined as a point where two or more tubules intersect or branch out, representing regions where endothelial cells are actively forming connections, which is a key indicator of formed network complexity. In the count of nodes from fluorescence images (**Figure 5.10C**), the 10-minute treated sample generated a lower number of nodes, implying a lower degree of branching and interconnection, which aligns with the extremity number

counting. No obvious difference was observed in the 30-minute and 60-minute irradiated samples compared to the control group without intervention, indicating a better angiogenic potential. Brach is the extension of a tubule that starts from a node or junction and extends outward to connect with other nodes or form a new extremity. The number of branches indicates the extent of vascular development; **Figure 5.10D** displayed a significant difference between the 10-minute treatment sample androl group, revealing a positive angiogenic response caused by early ROS stimulation. Segment and mesh numbers were counted in **Figure 5.10E** and **Figure 5.10F**, except for the lower maturity shown in 10-minute samples; 30-minute and 60-minute irradiated samples presented a well-developed capillary-like network, which means an unaffected angiogenesis performance.

5.2.6 Target site of ROS generated from 0.4% g-C_3N_4 hydrogel system

Reactive oxygen species (ROS), a group of highly active molecules, have cytotoxicity against bacterial and mammalian cells. When the co-cultured group containing bacteria and mammalian cells is exposed to released ROS from 0.4% g-C_3N_4, the damage efficiency should be technically close. Thus, this section investigated the possible reason for the selective killing properties observed in our work.

Membrane integrity measurement

ROS is considered the ROS-killing mechanism. It can directly attack the lipid bilayer of bacterial or mammalian cell membranes, causing lipid peroxidation. ROS can lead to membrane disruption, increasing permeability, and cell lysis. Gram-negative and gram-positive bacteria have different membrane structures, which could explain their different killing efficiency.

This work assessed the killing efficiency with potential membrane-permeabilising effects using fluorescence probes N-phenyl-1-naphthylamine (NPN) and propidium iodide (PI). NPN is one of the hydrophobic dyes with very low fluorescent emission when dissolved in only water; the fluorescence signal steeply increases when NPN binds with nonpolar molecules. The outer membrane of gram-negative bacteria prevents NPN from binding to the inside hydrophobic tail of phospholipids; this allows us to detect the intactness of the outer membrane, as the fluorescence intensity of NPN will increase sharply when outer membrane rupture occurs. PI is a red-fluorescent nucleic acid stain that tends to bind to DNA and RNA by intercalating the bases. This binding leads to a 20 to 30-fold enhancement of PI fluorescence intensity. This membrane-impermeable stain can only label bacteria with a damaged inner membrane.

Based on this, the membrane integrity of two different bacteria was evaluated after treatment with 0.4% g-C_3N_4 hydrogel and LED light. Outer membrane intactness was only detected in gram-negative bacteria, *E. coli – DH 5α* using NPN as a probe; the positive group was treated with polymyxin B, which is a typical antibiotic that disrupts the outer membrane of gram-negative bacteria, allowing the binding of NPN to the tail of inside phospholipids, obtained data was plotted in **Figure 5.11**.

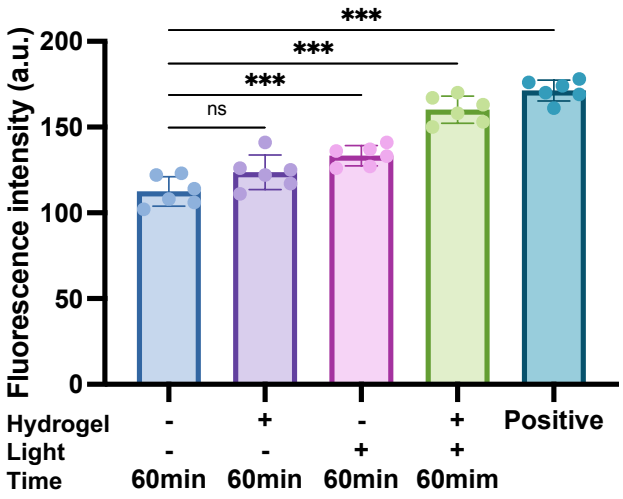

Fig. 5.11 Outer membrane intactness of *E. coli - DH 5α* after 0.4% g-C_3N_4 hydrogel and LED light irradiation, control groups: negative, only 0.4% g-C_3N_4 hydrogel, only LED light irradiation, positive control treated with polymyxin B. Data are presented as *mean* $\pm$ *SD* (n = 6). Statistical analysis was performed using one-way ANOVA followed by Dunnett's post hoc test to compare each treatment group with the control. $P \leq 0.05$ was considered statistically significant (ns = not significant, * $p \leq 0.05$, ** $p \leq 0.01$, *** $p \leq 0.001$, **** $p \leq 0.0001$). Statistical analysis was conducted using GraphPad Prism 10.0.

0.4% g-C_3N_4 hydrogel showed no impair to the intactness of outer membrane, fluorescence signal from LED light treated sample increased slightly compared to the negative control group, because the light irradiation could induce oxidative process in bacteria. When the sample was treated with 0.4% g-C_3N_4 hydrogel and LED light irradiation for 60 minutes, a significant difference was observed compared to the negative control group, indicating the effective break of the outer membrane with the 1.42-fold signal enhancement of NPN binding. For further exploration, inner membrane integrity was detected using PI as the fluorescence probe. Here, the positive group was treated with 0.1% Triton X-100, a non-ionic surfactant; the bacterial inner membrane disruption results from its amphipathic nature, leading to a permeability increase of inner membrane and PI probes binding to DNA. **Figure 5.12A**, the tested group of *S. epidermidis* showed strong damage by ROS released from 0.4% g-C_3N_4

hydrogel, causing the effect to be close to the positive control group. Regarding *E. coli – DH 5α* (**Figure 5.12B**), the measured PI signal showed a statistical difference between the ROS-treated group and the negative control. Still, it was much lower than the positive control group. These obtained data suggested that gram-positive bacteria with only one outer membrane consisting of peptidoglycan could be oxidised easily, leading to further content leakage and lysis. In the gram-negative bacteria, the existing outer membrane provides protection to some extent; ROS released from 0.4% g-C_3N_4 hydrogel was consumed; thus, the inner membrane could avoid severe disruption.

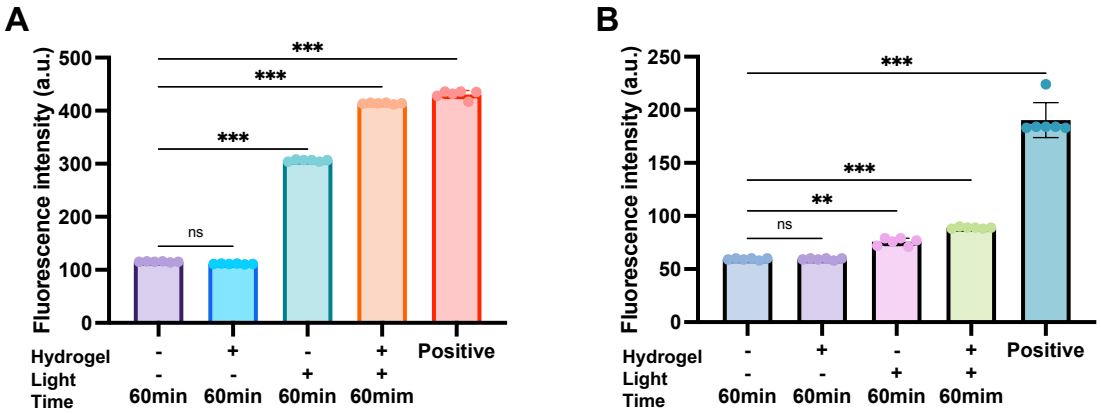

Fig. 5.12 Inner membrane intactness of (A) *S. epidermidis* and (B) *E. coli - DH 5α* after 0.4% g-C_3N_4 hydrogel and LED light irradiation, control groups: negative, only 0.4% g-C_3N_4 hydrogel, only LED light irradiation, positive control treated with 0.1% Triton X-100. Data are presented as $mean \pm SD$ (n = 6). Statistical analysis was performed using one-way ANOVA followed by Dunnett's post hoc test to compare each treatment group with the control. $P \leq 0.05$ was considered statistically significant (ns = not significant, * $p \leq 0.05$, ** $p \leq 0.01$, *** $p \leq 0.001$, **** $p \leq 0.0001$). Statistical analysis was conducted using GraphPad Prism 10.0.

Protein damage measurement

In addition, damage to proteins inserted on bacterial membranes was also studied here; the activity of β-galactosidase from the *S. epidermidis* group (**Figure 5.13A**) is considerably lower than that of the *E. coli – DH 5α* group (**Figure 5.13B**), revealing that the two-layer structure of gram-negative bacteria can effectively protect their structural integrity and the gram-positive bacteria with simple membrane structure is much more relying on their proteins to neutralizing the oxidation from ROS.

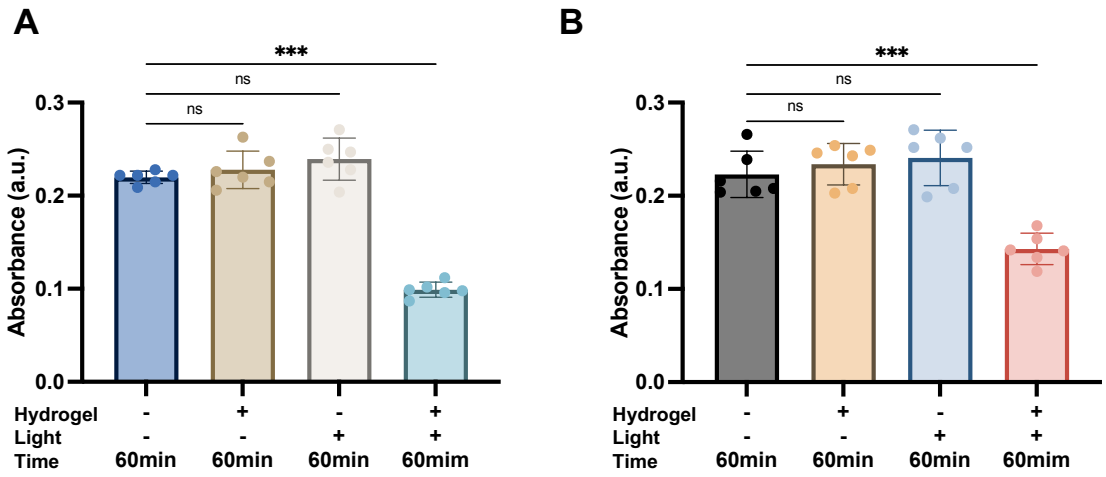

Fig. 5.13 Protein damage measurement of (A) *S. epidermidis* and (B) *E. coli – DH 5α*. Data are presented as *mean* ± *SD* (n = 6). Statistical analysis was performed using one-way ANOVA followed by Dunnett's post hoc test to compare each treatment group with the control. $P \leq 0.05$ was considered statistically significant (ns = not significant, * $p \leq 0.05$, ** $p \leq 0.01$, *** $p \leq 0.001$, **** $p \leq 0.0001$). Statistical analysis was conducted using GraphPad Prism 10.0.

5.2.7 Oxidative stress measurement

Compared to previous light-based biomedical devices, most of them rely on Ultraviolet (UV) light; simple visible LED light was implemented in this work. Therefore, light-induced auto-oxidative could be different; forming reactive oxygen species (ROS) from only light irradiation can also lead to extra oxidation of molecules such as lipids, proteins and nucleic acids. Different light source performances might support our robust selective killing results in bacterial and mammalian cells co-cultured groups. Fibroblast cells were irradiated using UV and our visible LED light in two different schemes to reveal the auto-oxidative effect caused by different light sources, and the genotoxicity of fibroblast cells was evaluated using γH2Ax immunofluorescence (**Figure 5.14**). Statistically significant increases in the signal of γH2Ax were measured in irradiated fibroblast cells for all types of exposure compared to control cells (**Figure 5.15**).

Under UV light irradiation, the fluorescence intensity of γH2Ax in fibroblast cells increased 21.8-fold for acute exposure and 40.7-fold for chronic exposure. However, the data obtained from our visible LED light showed no noticeable difference in acute and chronic exposure (p-value ≥ 0.99), suggesting this LED light led to negligible oxidative stress. Thus, the killing effect resulted mainly from the ROS from 0.4% g-C_3N_4 hydrogel, making the selective killing more controllable.

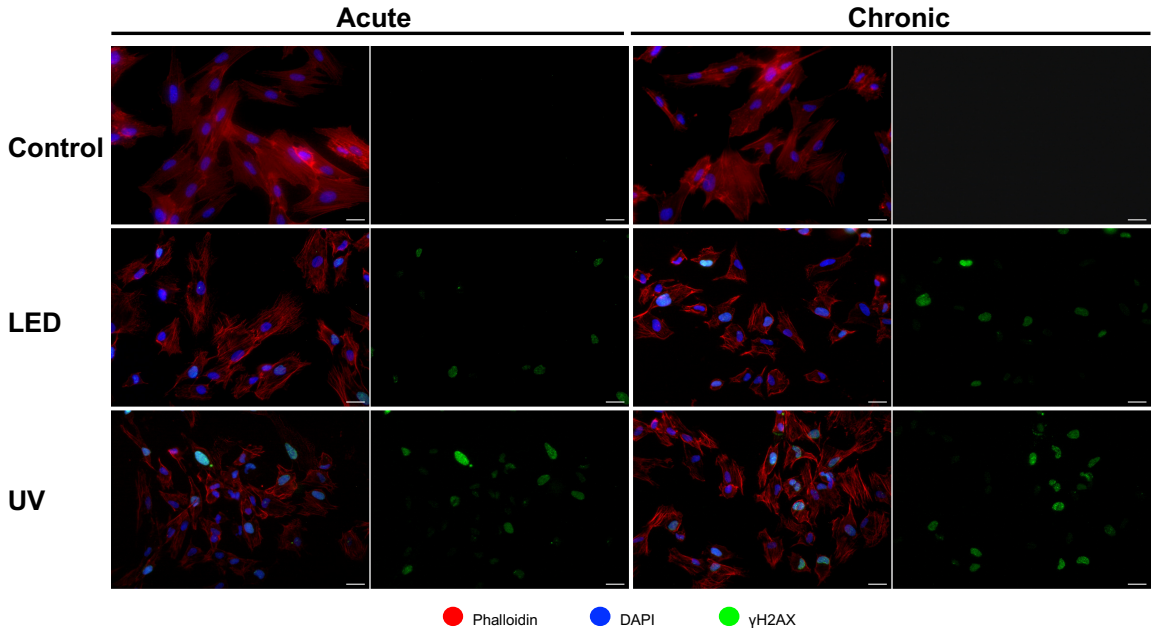

Fig. 5.14 Immunofluorescence stain of fibroblast cells after irradiating with LED and UV light in both acute and chronic exposure. The scale bar is 20 μm.

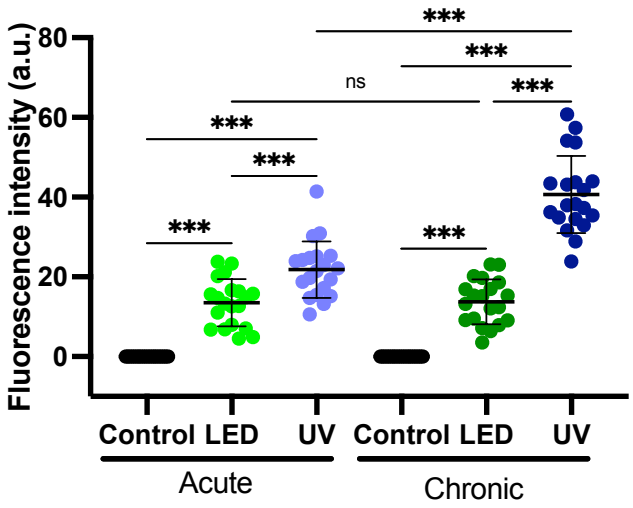

Fig. 5.15 Analysis of immunofluorescence images after irradiating with LED and UV light in both acute and chronic exposure. Data are presented as *mean* $\pm$ *SD* (n = 20). Statistical analysis was performed using one-way ANOVA followed by Turkey's post hoc test to compare all groups. P $\leq$ 0.05 was considered statistically significant (ns = not significant, * p $\leq$ 0.05, ** p $\leq$ 0.01, *** p $\leq$ 0.001, **** p $\leq$ 0.0001). Statistical analysis was conducted using GraphPad Prism 10.0.

5.3 Discussion

ROS release from our developed g-C_3N_4 hydrogel was confirmed previously, and effective bacterial killing was also observed in different methods. However, the chronic wound environment is a complex biological situation encompassing functional mammalian cells and bacterial residents. The damage caused by ROS formed from 0.4% g-C_3N_4 hydrogel to the bacteria and fibroblast cells in the single cultured group may altered in the co-culture group, in which the fibroblast cells stay close with the co-cultured bacteria, and both of them encounter with ROS molecule equally. In contrast to normal wound healing, proliferation, angiogenesis, and stem cell activation for further extracellular matrix remodelling have all been impaired in chronic wounds[78]. At the same time, long-term inflammation has also been persistent and damaging. These nonhealing chronic wounds allow polymicrobial occupation and entry to the underlying biological tissue to colonise and grow. Interactions of symbiotic microorganisms with supportive skin cells in the normal wound healing process could be helpful for the immune response. However, pathogenic bacteria play a substantial role in the delayed healing of wounds[116]. Thus, analysing the co-group composed environment in an impaired chronic wound is indispensable for identifying a novel treatment strategy for chronic wound healing improvement. First, the basic information of the co-culture group was investigated from bacteria accumulation and viability change of fibroblast cells. *mCherry-E. coli* was used as the bacteria, and the fibroblast cell was accepted as the mammalian cell to study the specific details through data and image collection. Bacteria and fibroblast cells were co-cultured for 2, 4, 6, 8, 12 and 24 hours to study the *mCherry-E. coli* occupation status in the previously seeded fibroblast cell group. *mCherry-E. coli* number increased as the co-culture period increased, showing the gradual attachment and colonisation of bacteria in the fibroblast cell. The longer the co-culture, the more bacteria were shown in the view with the accumulation tendency from the outline of cells towards the nucleus. The co-localisation analysis also proved the same results (**Figure 5.1**). The viability of fibroblast cells was also assessed to provide a reliable baseline for our selectively killing test; with the bacterial number increase, no obvious cell damage was detected(**Figure 5.2**). Thus, this constructed co-culture group provided a model to explore the possible effect after the 0.4% g-C_3N_4 hydrogel released ROS interacting with the co-cultured group.

Most developed chronic wound treatment strategies have faced significant challenges in clinical application, such as manipulating the therapeutic approach to find a reliable strategy that ensures the bacteria is killed rather than mammalian cells. A previous attempt was implemented using nanoenzyme-generated surface-bond ROS to selectively kill[207]. However, the synthesis process of nanoenzymes is complicated, and extra exogenous material was introduced into the biological system, which is not good for long-term physical conditions. In this

work, the selective killing effect was confirmed in the bacteria and fibroblast cells co-cultured group when exposed to the 0.4% g-C_3N_4 hydrogel formed ROS molecules(**Figure 5.3**); up to 180 minutes of irradiation, gradually increased bacterial killing was observed. Fibroblast cell impairment was kept lower than 10% at the same time(**Figure 5.3A**). Intracellular hydroxyl radical concentration, which should be the main damage factor within the three specific ROS molecules we investigated, shows a similar tendency as in the single culture *S. epidermidis* group when the co-cultured group with *mCherry-E. coli*. A Rapid maximum hydroxyl radical concentration accumulation was observed due to a large number of cells in the co-cultured group (**Figure 5.3B**). As a biocompatible hydrogel, 0.4% g-C_3N_4 released ROS kept in a mammalian cell tolerated range, while the most effective hydroxyl radical is highly limited by the diffuse distance when the bacterial cells in co-group showed greater affinity preference than mammalian cells, the primary damage was caused in bacterial cells. Compared to bacteria, fibroblast cells have more complex intracellular structures and various antioxidant defence mechanisms; after the consumption caused by bacteria penetration, the rest of the ROS species would potentially act as the signalling transduction factor in fibroblast cells rather than damaged molecules. We developed a method that can selectively kill bacteria over mammalian cells non-invasively, even in a co-existed environment, which is typically suited for chronic wound environment management.

Breaking the compact biofilm in the wound site is the beginning of wound healing initiation. Thus, wound healing materials are expected to be effective in biofilm damage. Our developed g-C_3N_4 hydrogel eradicates the formed biofilm very well, further broadening the application. In addition, this biofilm-breaking process would consume a lot of highly active ROS molecules, alleviating the possible damage to underlying mammalian cells and further confirming the excellent performance as a chronic wound healing bandage material (**Figure 5.6** and **Figure 5.7**).

Wound healing is an intricate process requiring several cells to work sequentially, contributing to different cellular events, including proliferation, migration and vascular formation. Thus, functions in different cell types were investigated under the previous treatment condition. Normal fibroblast cell morphology with stretched fibres and healthy nuclei can maintain structural integrity. The well-organised structure allows them to behave well for proliferation and adhere to the extracellular matrix for damaged tissue reconstruction[208]. Moreover, the typical morphology of fibroblast cells is essential for collagen formation and the strength of newly formed tissues. (**Figure 5.9**) As a critical cell in tissue repair, fibroblast cells are responsible for migrating to the wound site and producing collagen, providing the basic structure for newly formed healing tissue. Our test proved that this treatment does not harm the migration capability of fibroblast cells, which is more robust evidence for this selectively

killing work (**Figure 5.8**). Angiogenesis is a crucial process for the vascular system remodelling. The well-behaved endothelial cells in angiogenesis are involved in growth factor release for further tissue repair, cell migration, and proliferation. The appropriate diffusion of ROS promotes tube formation in the treatment of HUVECs, which is essential for the formation of new connective tissue and the reconstruction of blood vessels. (**Figure 5.10**) All mammalian cell function measurements provide strong support for this material.

As the obtained results demonstrated, in our constructed co-cultured model, 0.4% g-C_3N_4 hydrogel generated ROS can selectively kill bacteria over mammalian cells and participate in essential mammalian cells work well; it can be explained as the formed ROS are primarily consumed by firstly encountered bacterial cells, stopping an oxidative stress accumulation in mammalian cells. Moreover, different bacterial strains also presented different tolerance to the ROS attack; results about membrane (**Figure 5.11** and **Figure 5.12**) and protein (F**igure 5.13**) damage measurements explained that the gram-positive bacteria quickly lose their structural integrity and sacrifice the protein to defend against the attack from ROS molecules, which is aligned with our observation in Chapter 4.

Different from most previous studies, this work was based on low-power visible light, making wearable bandages feasible. The light source is one of the limitations of photo-activated biomedical applications; most of them rely on laser power or UV light, which hinders the utilisation as a point-of-care device due to their lab-based properties and possible damage to the skin[209]. Excessive ROS accumulation in biological tissue could lead to oxidative stress, leading to delay or impairment of wound healing; light source could be one of the essential factors to induce unnecessary ROS formation. Phosphorylation of H2Ax at Ser 139 (γH2Ax) was used to express the light source-induced genomic damage(**Figure 5.14**); data obtained from immunofluorescence presented slightly double-stranded DNA breaks after our visible light irradiation (**Figure 5.15**), which is different under the UV light irradiation. On the other hand, this negligible oxidative stress caused by the light source in our system was also beneficial for precise ROS regulation, which is important for the selective killing process, as biological events are highly dependent on the applied dosage.

5.4 Conclusion

In this chapter, a bacteria/mammalian cell cocultured group was constructed to verify the selective killing in a similar environment as a chronic wound. First, the coculture conditions were clarified, and an 8-hour coculture period was used to obtain a comparable cell number in both bacteria and fibroblast cells in the co-group. The viability of bacteria and fibroblast cells was also measured, reassuring the coculture group was in good condition. After that, this

co-group was treated using 0.4% g-C_3N_4 hydrogel under different periods of light irradiation, Live/Dead staining and intracellular hydroxyl radical label was implemented in parallel set experimental groups to explore the details of hydroxyl radical-induced selectively killing in this cocultured group. Obtained results proved that in the cocultured group, bacteria presented a faster intracellular hydroxyl radical accumulation than fibroblast. The selective killing of bacteria over mammalian cells was also achieved due to this hydroxyl radical concentration difference. Fluorescence images were collected both in the Live/Dead test and intracellular hydroxyl radical diffusion test group, showing the same tendency as plotted data.

The biofilm eradication efficiency was evaluated both with crystal violet staining and confocal image scanning after 30 minutes and 60 minutes of treatment with 0.4% g-C_3N_4 hydrogel and visible light irradiation, 80% biofilm was destroyed in gram-positive bacteria and gram-negative bacteria, showing great biofilm degradation efficiency.

Considering the bacteria and mammalian cell co-occupy situation in the chronic wound environment, previous treatment approaches were limited by the inevitable damage to healthy mammalian cells and few work realized the selectivity killings using only hydrogel[207, 210, 211]. Here, the mammalian cell functions were also evaluated under the same treatment conditions. Results from fibroblast cell morphology and migration showed no obvious impairment, and the tube formation ability of HUVECs also presented no significant statistical difference after 30 minutes and 60 minutes of treatment. Providing the evidence for avoiding damage to surrounding mammalian cells. The membrane intactness and protein activity tests support the killing efficiency difference in gram-positive and gram-negative bacteria. The negligible oxidative stress caused by LED light source is also helpful to the ROS dosage control in the whole g-C_3N_4 hydrogel system. Generally, the developed g-C_3N_4 hydrogel system presented excellent selectively killing properties in the co-cultured E. coli and fibroblast cells group. In contrast, all the necessary mammalian cell functions work well. The visible light-activated g-C_3N_4 hydrogel system was effective in bacterial inactivation over mammalian cells in the co-cultured group and showed excellent biofilm eradication performance. Applied light source leads to no side effects and is suited for wearable device development. This work verified a feasible hydrogel system to realise the selective killing of bacteria in the complex chronic wound environment, providing a promising material that realises a drug-free and redox homeostasis regulation cooperated method to manage chronic wounds.

Chapter 6

Summary and Outlook

6.1 Innovations and limitations

- A visible light-triggered hydrogel platform was developed using a free-radical polymerized g-C_3N_4 material, *N, N*-dimethylacrylamide (DMA) and *N, N'*-methylene-bisacrylamide (MBA), this new hydrogel system is light-responsible and biocompatible, and is the first time used in chronic wound management.
- Reactive oxygen species (ROS) are generated under visible light irradiation using the -C_3N_4 hydrogel only, and the released ROS were quantified in detail in this work, helping with the ROS dosage optimisation.
- The possible relationship between intracellular hydroxyl radical concentration and bacteria/mammalian cell viability is evaluated on a timely scale in detail.
- Selectively killing bacteria without damaging surrounding mammalian cells through ROS dosage control is achieved for the first time using a simple hydrogel system in a bacteria/mammalian cell cocultured model.
- The possible limitation or improvement of this work is that the visible light source is now a lab-based version, for the wearable device development demands, a minimised visible light patch should be fabricated to meet the requirements of the device.

6.2 Overall Discussions

The rapid growth of antimicrobial resistance (AMR) is recognised as an urgent threat to global health. Previous antimicrobial approaches, including biological molecules, or-

ganic molecules and metallic materials, usually deactivate bacteria through one or several mechanisms; however, these methods also adversely disrupt the live status of surrounding mammalian cells, challenging and compromising chronic wound site management, making it difficult to kill the bacteria without damaging of surrounding mammalian cells. Hydrogel-based smart bandages have become useful in research and translational fields to further nonhealing wound management. The development of wound bandages with the potential to monitor and analyse the wound healing process in real-time, give the appropriate intervention, and collect and report the overall signals of individuals have made the smart wound bandage emerge as a promising solution for remote and long-term wound care management. The tendency of cutting-edge wound bandage development is to mimic the native skin functions to provide a suitable microenvironment and therapy to accelerate the healing process. Hydrogel has been used for chronic wound treatment since 1989, and its physiochemical properties have been continuously improved by researchers to satisfy the open wound environment. Moreover, compared to other bandage materials, such as films and foams, the unique three-dimensional network structure of hydrogels makes them more similar to native ECM structures to support cellular functions; thus, most natural hydrogels, such as chitosan, hyaluronan, and alginate have attracted more attention. However, chronic wounds are complex environments that are suspicious of infection; this promotes the development of the combination of hydrogel with other functional molecules, such as growth factors, nanomaterials, and antibiotics, to meet the purpose of therapy.

The overall aim of this project was to develop a promising hydrogel for the fabrication of chronic wound healing bandages that can be adequately managed and intervened in the open wound site. The work presented in this thesis provides a g-C_3N_4 material doped polymerisation system, the g-C_3N_4 was used as a photoinitiator for the polymerization reaction to obtain the g-C_3N_4 hydrogel under visible light irradiation. The doped g-C_3N_4 material alleviates the strong oxidative effect and forms a biocompatible hydrogel that is suitable for biomedical devices, retaining the optical properties of g-C_3N_4 material allow this hydrogel to generate reactive oxygen species (ROS). We have also evaluated this light-responsibility property with different amounts of g-C_3N_4 material addition, and all prepared g-C_3N_4 hydrogels were illuminated with visible light to explore ROS generation in detail.

We then showed that portable LED light can be used as a source to activate the g-C_3N_4 hydrogels, and ROS can also be formed by a precisely controlled method, which makes it possible for antimicrobial purposes and immune microenvironment reshaping. Based on this, the relationship between viability and intracellular hydroxyl radical concentration of bacteria and mammalian cells was monitored in different time scales, shining a light on the potential to discriminate kill bacteria over mammalian cells. To further confirm and solve the challenge

that remains in chronic wound healing, this work proved the ability of the g-C_3N_4 hydrogel system to kill bacteria over mammalian cells in a co-cultured model selectively. This appropriately provided a system that can specifically manage the chronic wound environment and provide a new solution to alleviate the burden of antibiotic-induced antimicrobial resistance, realising a possible approach to cover and cure the nonhealing wounds with a multifunctional endogenous biomolecule, avoiding extra drug or macromolecule introduction.

Generally, all the superior properties of g-C_3N_4 hydrogel proved in this work, such as easy preparation, visible-light response and great biocompatibility, make it perfect for wearable wound healing bandage material. Reactive oxygen species (ROS) are controlled to act as high-activity chemical molecules and 'second messengers' in biological processes. In a microenvironment containing mammalian cells and bacteria, this g-C_3N_4 hydrogel system can achieve a well-controlled selective kill of bacteria over mammalian cells through their biological structure differences and affinity for the g-C_3N_4 hydrogel surface. The biological processes are usually dose dependent. Thus, this precisely controlled ROS provide a promising solution to complex environment management, avoiding the concerns of introduced drug uptake, efflux and efficiency target recognition. This g-C_3N_4 hydrogel platform uncovers a new pathway to manage chronic wound and develop the next-generation healthcare device.

6.3 Key findings

1. g-C_3N_4 can work well in the polymerisation system, providing the extra light-responsive capability for the formed hydrogel and modifying the oxidative effect of involved chemical components, making excellent biocompatible hydrogel possible.

2. As a semiconductor material, g-C_3N_4 can keep its physiochemical properties to generate reactive oxygen species under visible light irradiation, and the generation rate can be controlled precisely.

3. This controllable released reactive oxygen species can selectively kill bacteria without damaging healthy mammalian cells through the well-controlled ROS generation, which makes this g-C_3N_4 perfect for chronic wound care.

6.4 Outlook for future work

ROS extensively affects cellular processes such as cell cycle progression, apoptosis, quiescence, and differentiation. This evidence gives us insight into that ROS also acts as a signalling mediator that could influence stem cell fate through various metabolic regulations.

Thus, investigations involving ROS regulation on stem cell differentiation and maintenance of self-renewal capability could contribute to the *in vitro* stem cell culture system, embryonic stem cell development, and fate control for the following therapeutic applications.

Several studies[212, 213] already found some clues for this; one of the pieces of evidence is that embryonic stem cells (ESCs) differentiation towards cardiac lineage is dependent on H_2O_2 mediated signalling induced by NOX4 upregulation. Apart from this, differentiation of mesenchymal stem cells (MSCs) towards adipocytes and neuron-like cells has also been proved to be affected by NOX4-mediated H_2O_2 and other mitochondrial ROS[214, 215]. Increasing research results also implicate a considerable effect from ROS on MSCs differentiation into mesodermal lineage, including adipocytes, osteocytes, chondrocytes and myocytes; several pathways that affect the transcription machinery significant to MSCs differentiation are involved, such as Wnt, Hedgehog, and FOXO signalling cascades[216, 217].

ROS has been considered a negative factor for cell function and metabolic processes for many years, it has gradually been noticed in various critical physiological processes[16]. However, most of the research is limited by ROS generation control and measurement methods; it still needs to be determined which species are implicated in the specific metabolic process. Thus, there is still a huge research gap on ROS-mediated stem cell development, including 1) How to manipulate the ROS-mediated metabolism to control the stem cell fate and differentiation into various lineages. 2) The role of different ROS species in specific pathways. 3) What is their optimal concentration? 4) Is it possible for exogenous ROS to act the same as endogenous ones? Further detailed exploration might reveal a promising area for stem cell-based therapy. Combined with the work in this thesis, the following sections of future work may be considered to advance the hydrogel system.

The g-C_3N_4 hydrogels in this thesis were studied with the basic physiochemical properties and primary function as a wound care bandage material; however, further characterisations in mechanical properties may be beneficial for the wound tissue contraction evaluation, which is also essential for the wound healing process initiation. Several animal studies have revealed that the reduced contractibility of diabetic wounds is one of the significant reasons for impaired diabetic wound healing[218, 219]. Thus, mechanical modulation can be one of the effective methods to promote open wound closure and then activate the timely responses of stem cells.

For the aim of the development of an integrated device for diabetic wound healing, an ideal smart bandage platform should combine with both sensing and stimulation components for autonomous, closed-loop wound management[220, 11, 221]. Besides, it may be helpful to integrate with microstructures to improve the in situ vital signal detection and analysis.

The role of reactive oxygen species (ROS) has been challenging in clinical transla-

tion because their multifunctional properties and involved complex processes[222]; based on this specific situation, there is a potential for future work to be carried out on the detailed exploration of interactions of specific concentration ROS species with stem cells fate regulation[223], discovering the possibility of g-C_3N_4 hydrogel-based platform to tune the host immune response in immunotherapy[224], even improving the survival ratio of transplanted stem cells to realise a synergistic method with both cell-therapy and chemotherapy.

References

[1] Melanie Rodrigues, Nina Kosaric, Clark A. Bonham, and Geoffrey C. Gurtner. Wound healing: A cellular perspective. *Physiological Reviews*, 99(1):665–706, 2019. doi: 10.1152/physrev.00067.2017. URL https://doi.org/10.1152/physrev.00067.2017. PMID: 30475656.

[2] Canran Wang, Ehsan Shirzaei Sani, and Wei Gao. Wearable bioelectronics for chronic wound management. *Advanced Functional Materials*, 32(17):2111022, 2022. doi: https://doi.org/10.1002/adfm.202111022. URL https://onlinelibrary.wiley.com/doi/abs/10.1002/adfm.202111022.

[3] Carey-Ann D. Burnham, Jennifer Leeds, Patrice Nordmann, Justin O'Grady, and Jean Patel. Diagnosing antimicrobial resistance. *NATURE REVIEWS MICROBIOLOGY*, 15(11):697–703, NOV 2017. ISSN 1740-1526. doi: 10.1038/nrmicro.2017.103.

[4] Helmut Sies, Ryan J. Mailloux, and Ursula Jakob. Fundamentals of redox regulation in biology. *NATURE REVIEWS MOLECULAR CELL BIOLOGY*, 25(9):701–719, SEP 2024. ISSN 1471-0072. doi: 10.1038/s41580-024-00730-2.

[5] Dunya Tomic, Jonathan E. Shaw, and Dianna J. Magliano. The burden and risks of emerging complications of diabetes mellitus. *NATURE REVIEWS ENDOCRINOLOGY*, 18(9):525–539, SEP 2022. ISSN 1759-5029. doi: 10.1038/s41574-022-00690-7.

[6] David G. Armstrong, Tze-Woei Tan, Andrew J. M. Boulton, and Sicco A. Bus. Diabetic foot ulcers a review. *JAMA-JOURNAL OF THE AMERICAN MEDICAL ASSOCIATION*, 330(1):62–75, JUL 3 2023. ISSN 0098-7484. doi: 10.1001/jama.2023.10578.

[7] Rebecca H. Ritchie and E. Dale Abel. Basic mechanisms of diabetic heart disease. *CIRCULATION RESEARCH*, 126(11):1501–1525, MAY 22 2020. ISSN 0009-7330. doi: 10.1161/CIRCRESAHA.120.315913.

[8] Oscar A. Pena and Paul Martin. Cellular and molecular mechanisms of skin wound healing. *NATURE REVIEWS MOLECULAR CELL BIOLOGY*, 25(8):599–616, AUG 2024. ISSN 1471-0072. doi: 10.1038/s41580-024-00715-1.

[9] Lucilia P. da Silva, Rui L. Reis, Vitor M. Correlo, and Alexandra P. Marques. Hydrogel-based strategies to advance therapies for chronic skin wounds. In ML Yamush, editor, *ANNUAL REVIEW OF BIOMEDICAL ENGINEERING, VOL 21*, volume 21 of *Annual Review of Biomedical Engineering*, pages 145–169. 2019. doi: 10.1146/annurev-bioeng-060418-052422.

[10] Karin Sauer, Paul Stoodley, Darla M. Goeres, Luanne Hall-Stoodley, Mette Burmolle, Philip S. Stewart, and Thomas Bjarnsholt. The biofilm life cycle: expanding the conceptual model of biofilm formation. *NATURE REVIEWS MICROBIOLOGY*, 20 (10):608–620, OCT 2022. ISSN 1740-1526. doi: 10.1038/s41579-022-00767-0.

[11] Canran Wang, Ehsan Shirzaei Sani, and Wei Gao. Wearable bioelectronics for chronic wound management. *ADVANCED FUNCTIONAL MATERIALS*, 32(17), APR 2022. ISSN 1616-301X. doi: 10.1002/adfm.202111022.

[12] Yong Wang, Xinchen Wang, and Markus Antonietti. Polymeric graphitic carbon nitride as a heterogeneous organocatalyst: From photochemistry to multipurpose catalysis to sustainable chemistry. *Angewandte Chemie International Edition*, 51(1): 68–89, 2012. doi: https://doi.org/10.1002/anie.201101182. URL https://onlinelibrary.wiley.com/doi/abs/10.1002/anie.201101182.

[13] Qian Cao, Baris Kumru, Markus Antonietti, and Bernhard V. K. J. Schmidt. Graphitic carbon nitride and polymers: a mutual combination for advanced properties. *MATERIALS HORIZONS*, 7(3):762–786, MAR 1 2020. ISSN 2051-6347. doi: 10.1039/c9mh01497g.

[14] Pablo Hernansanz-Agustín and José Antonio Enríquez. Generation of reactive oxygen species by mitochondria. *Antioxidants*, 10(3), 2021. ISSN 2076-3921. doi: 10.3390/antiox10030415. URL https://www.mdpi.com/2076-3921/10/3/415.

[15] Tsung-Hsien Chen, Hsiang-Chen Wang, Chia-Jung Chang, and Shih-Yu Lee. Mitochondrial glutathione in cellular redox homeostasis and disease manifestation. *International Journal of Molecular Sciences*, 25(2), 2024. ISSN 1422-0067. doi: 10.3390/ijms25021314. URL https://www.mdpi.com/1422-0067/25/2/1314.

[16] World Health Organization. *Global report on diabetes*. World Health Organization, 2016.

[17] Alberto Cordero, David Sirera, Jose Mendez-Gallego, and Ignacio Echeverria. Report effect of diabetes mellitus on global longitudinal strain. *AMERICAN JOURNAL OF CARDIOLOGY*, 223:120–122, JUL 15 2024. ISSN 0002-9149. doi: 10.1016/j.amjcard.2024.04.017.

[18] Angelica Artasensi, Alessandro Pedretti, Giulio Vistoli, and Laura Fumagalli. Type 2 diabetes mellitus: A review of multi-target drugs. *Molecules*, 25(8), 2020. ISSN 1420-3049. doi: 10.3390/molecules25081987. URL https://www.mdpi.com/1420-3049/25/8/1987.

[19] Bing-Fang Hwang, Made Ary Sarasmita, and Ming-Chieh Li. Global, regional, and national burden of diabetes from 1990 to 2021, with projections of prevalence to 2050: a systematic analysis for the global burden of disease study 2021 (vol 402, pg 203, 2023). *LANCET*, 402(10408):1132, SEP 30 2023. ISSN 0140-6736. doi: 10.1016/S0140-6736(23)02044-5.

[20] Kanyin Liane Ong, Lauryn K Stafford, Susan A McLaughlin, Edward J Boyko, Stein Emil Vollset, Amanda E Smith, Bronte E Dalton, Joe Duprey, Jessica A Cruz, Hailey Hagins, Paulina A Lindstedt, Amirali Aali, Yohannes Habtegiorgis Abate,

Melsew Dagne Abate, Dianna J Magliano, Christopher J L Murray, Simon I Hay, and Theo Vos. Global, regional, and national burden of diabetes from 1990 to 2021, with projections of prevalence to 2050: a systematic analysis for the global burden of disease study 2021. *The Lancet*, 402(10397):203–234, 2023. ISSN 0140-6736. doi: https://doi.org/10.1016/S0140-6736(23)01301-6. URL https://www.sciencedirect.com/science/article/pii/S0140673623013016.

[21] N. Holman, N. G. Forouhi, E. Goyder, and S. H. Wild. The association of public health observatories (apho) diabetes prevalence model: estimates of total diabetes prevalence for england, 2010-2030. *DIABETIC MEDICINE*, 28(5):575–582, MAY 2011. ISSN 0742-3071. doi: 10.1111/j.1464-5491.2010.03216.x.

[22] N. G. Forouhi, D. Merrick, E. Goyder, B. A. Ferguson, J. Abbas, K. Lachowycz, and S. H. Wild. Diabetes prevalence in england, 2001—estimates from an epidemiological model. *Diabetic Medicine*, 23(2):189–197, 2006. doi: https://doi.org/10.1111/j.1464-5491.2005.01787.x. URL https://onlinelibrary.wiley.com/doi/abs/10.1111/j.1464-5491.2005.01787.x.

[23] N. Holman, N. G. Forouhi, E. Goyder, and S. H. Wild. The association of public health observatories (apho) diabetes prevalence model: estimates of total diabetes prevalence for england, 2010–2030. *Diabetic Medicine*, 28(5):575–582, 2011. doi: https://doi.org/10.1111/j.1464-5491.2010.03216.x. URL https://onlinelibrary.wiley.com/doi/abs/10.1111/j.1464-5491.2010.03216.x.

[24] Juergen Harreiter and Michael Roden. Diabetes mellitus: definition, classification, diagnosis, screening and prevention (update 2023). *WIENER KLINISCHE WOCHENSCHRIFT*, 135(SUPPL 1, 1, SI):7–17, JAN 2023. ISSN 0043-5325. doi: 10.1007/s00508-022-02122-y.

[25] Jinli Liu, Zhen-Hu Ren, Hua Qiang, Jine Wu, Mingwang Shen, Lei Zhang, and Jun Lyu. Trends in the incidence of diabetes mellitus: results from the global burden of disease study 2017 and implications for diabetes mellitus prevention. *BMC PUBLIC HEALTH*, 20(1), SEP 17 2020. doi: 10.1186/s12889-020-09502-x.

[26] FR Kaufman. Type 1 diabetes mellitus. *PEDIATRICS IN REVIEW*, 24(9):291–299, SEP 2003. ISSN 0191-9601. doi: 10.1542/pir.24-9-291.

[27] Kristi M. Cowell. Type 2 diabetes mellitus. *PEDIATRICS IN REVIEW*, 29(8):289–292, AUG 2008. ISSN 0191-9601. doi: 10.1542/pir.29-8-289.

[28] H. David McIntyre, Patrick Catalano, Cuilin Zhang, Gernot Desoye, Elisabeth R. Mathiesen, and Peter Damm. Gestational diabetes mellitus. *NATURE REVIEWS DISEASE PRIMERS*, 5, JUL 11 2019. ISSN 2056-676X. doi: 10.1038/s41572-019-0098-8.

[29] Nuha ElSayed, Grazia R. Aleppo, Vanita R. Aroda, Raveendhara M. Bannuru, Florence Brown, Dennis S. Bruemmer, Billy E. Collins, Marisa Hilliard, Diana L. Isaacs, Eric Johnson, Scott Kahan, Kamlesh Khunti, Jose K. Leon, Sarah Lyons, Mary Lou Perry, Priya E. Prahalad, Richard Pratley, Jane Jeffrie C. Seley, Robert A. Stanton, Robert Gabbay, and American Diabet Assoc. 2. classification and diagnosis of diabetes: Standards of care in diabetes-2023 (vol 46, pg s19, 2023). *DIABETES CARE*, 46(5): 1106, MAY 2023. ISSN 0149-5992. doi: 10.2337/dc23-er05.

[30] Dennis F. Bandyk. The diabetic foot: Pathophysiology, evaluation, and treatment. *SEMINARS IN VASCULAR SURGERY*, 31(2-4):43–48, JUN-DEC 2018. ISSN 0895-7967. doi: 10.1053/j.semvascsurg.2019.02.001.

[31] Julian F Guest, Graham W Fuller, and Peter Vowden. Diabetic foot ulcer management in clinical practice in the uk: costs and outcomes. *International Wound Journal*, 15(1): 43–52, 2018. doi: https://doi.org/10.1111/iwj.12816. URL https://onlinelibrary.wiley.com/doi/abs/10.1111/iwj.12816.

[32] Frank L. Bowling, S. Tawqeer Rashid, and Andrew J. M. Boulton. Preventing and treating foot complications associated with diabetes mellitus. *NATURE REVIEWS ENDOCRINOLOGY*, 11(10):606–616, OCT 2015. ISSN 1759-5029. doi: 10.1038/nrendo.2015.130.

[33] Sujit Kumar Das, Pinki Roy, Prabhishek Singh, Manoj Diwakar, Vijendra Singh, Ankur Maurya, Sandeep Kumar, Seifedine Kadry, and Jungeun Kim. Diabetic foot ulcer identification: A review. *DIAGNOSTICS*, 13(12), JUN 2023. doi: 10.3390/diagnostics13121998.

[34] David G. Armstrong, Andrew J. M. Boulton, and Sicco A. Bus. Diabetic foot ulcers and their recurrence. *NEW ENGLAND JOURNAL OF MEDICINE*, 376(24):2367–2375, JUN 15 2017. ISSN 0028-4793. doi: 10.1056/NEJMra1615439.

[35] RE PECORARO, GE REIBER, and EM BURGESS. Pathways to diabetic limb amputation - basis for prevention. *DIABETES CARE*, 13(5):513–521, MAY 1990. ISSN 0149-5992. doi: 10.2337/diacare.13.5.513.

[36] Varun Parkash Singh, Anjana Bali, Nirmal Singh, and Amteshwar Singh Jaggi. Advanced glycation end products and diabetic complications. *KOREAN JOURNAL OF PHYSIOLOGY & PHARMACOLOGY*, 18(1):1–14, FEB 2014. ISSN 1226-4512. doi: 10.4196/kjpp.2014.18.1.1.

[37] H SHAMOON, H DUFFY, N FLEISCHER, S ENGEL, P SAENGER, M STRELZYN, M LITWAK, J WYLIEROSETT, A FARKASH, D GEIGER, H ENGEL, P FLEISCHMAN, O CROFFORD, M DAVIS, L RAND, and C SIEBERT. The effect of intensive treatment of diabetes on the development and progression of long-term complications in insulin-dependent diabetes-mellitus. *NEW ENGLAND JOURNAL OF MEDICINE*, 329(14):977–986, SEP 30 1993. ISSN 0028-4793. doi: 10.1056/NEJM199307293290502.

[38] Rodica Pop-Busui, Jiang Lu, Maria Mori Brooks, Stewart Albert, Andrew D. Althouse, Jorge Escobedo, Jenifer Green, Pasquale Palumbo, Bruce A. Perkins, Fred Whitehouse, Teresa L. Z. Jones, and BARI 2D Study Grp. Impact of glycemic control strategies on the progression of diabetic peripheral neuropathy in the bypass angioplasty revascularization investigation 2 diabetes (bari 2d) cohort. *DIABETES CARE*, 36(10):3208–3215, OCT 2013. ISSN 0149-5992. doi: 10.2337/dc13-0012.

[39] M. Ndosi, A. Wright-Hughes, S. Brown, M. Backhouse, B. A. Lipsky, M. Bhogal, C. Reynolds, P. Vowden, E. B. Jude, J. Nixon, and E. A. Nelson. Prognosis of the infected diabetic foot ulcer: a 12-month prospective observational study. *DIABETIC MEDICINE*, 35(1):78–88, JAN 2018. ISSN 0742-3071. doi: 10.1111/dme.13537.

[40] Grant H. Skrepnek, Joseph L. Mills, Sr., and David G. Armstrong. A diabetic emergency one million feet long: Disparities and burdens of illness among diabetic foot ulcer cases within emergency departments in the united states, 2006-2010. *PLOS ONE*, 10(8), AUG 6 2015. ISSN 1932-6203. doi: 10.1371/journal.pone.0134914.

[41] Benjamin A. Lipsky, Eric Senneville, Zulfiqarali G. Abbas, Javier Aragon-Sanchez, Mathew Diggle, John M. Embil, Shigeo Kono, Lawrence A. Lavery, Matthew Malone, Suzanne A. van Asten, Vilma Urbancic-Rovan, Edgar J. G. Peters, and Int Working Grp Diab Foot. Guidelines on the diagnosis and treatment of foot infection in persons with diabetes (iwgdf 2019 update). *DIABETES-METABOLISM RESEARCH AND REVIEWS*, 36(1), MAR 2020. ISSN 1520-7552. doi: 10.1002/dmrr.3280.

[42] Katherine McDermott, Michael Fang, Andrew J. M. Boulton, Elizabeth Selvin, and Caitlin W. Hicks. Etiology, epidemiology, and disparities in the burden of diabetic foot ulcers. *DIABETES CARE*, 46(1):209–221, JAN 2023. ISSN 0149-5992. doi: 10.2337/dci22-0043.

[43] Nicolas W. Cortes-Penfield, David G. Armstrong, Meghan B. Brennan, Maya Fayfman, Jonathan H. Ryder, Tze-Woei Tan, and Marcos C. Schechter. Evaluation and management of diabetes-related foot infections. *CLINICAL INFECTIOUS DISEASES*, 2023 JUN 12 2023. ISSN 1058-4838. doi: 10.1093/cid/ciad255.

[44] Nia J. Jones and Keith Harding. 2015 international working group on the diabetic foot guidance on the prevention and management of foot problems in diabetes. *INTERNATIONAL WOUND JOURNAL*, 12(4):373–374, AUG 2015. ISSN 1742-4801. doi: 10.1111/iwj.12475.

[45] Suzan Tabur, Mehmet Ali Eren, Yakup Celik, Omer Faruk Dag, Tevfik Sabuncu, Zeynel Abidin Sayiner, and Esen Savas. The major predictors of amputation and length of stay in diabetic patients with acute foot ulceration. *WIENER KLINISCHE WOCHENSCHRIFT*, 127(1-2):45–50, JAN 2015. ISSN 0043-5325. doi: 10.1007/s00508-014-0630-5.

[46] SO Oyibo, EB Jude, I Tarawneh, HC Nguyen, LB Harkless, and AJM Boulton. A comparison of two diabetic foot ulcer classification systems - the wagner and the university of texas wound classification systems. *DIABETES CARE*, 24(1):84–88, JAN 2001. ISSN 0149-5992. doi: 10.2337/diacare.24.1.84.

[47] Joseph L. Mills, Sr., Michael S. Conte, David G. Armstrong, Frank B. Pomposelli, Andres Schanzer, Anton N. Sidawy, George Andros, and Soc Vasc Surg Lower Extremity. The society for vascular surgery lower extremity threatened limb classification system: Risk stratification based on wound, ischemia, and foot infection (wifi). *JOURNAL OF VASCULAR SURGERY*, 59(1):220+, JAN 2014. ISSN 0741-5214. doi: 10.1016/j.jvs.2013.08.003.

[48] Nick S. van Reijen, Kevin Ponchant, Dirk T. Ubbink, and Mark J. W. Koelemay. Editor's choice - the prognostic value of the wifi classification in patients with chronic limb threatening ischaemia: A systematic review and meta-analysis. *EUROPEAN JOURNAL OF VASCULAR AND ENDOVASCULAR SURGERY*, 58(3):362–371, SEP 2019. ISSN 1078-5884. doi: 10.1016/j.ejvs.2019.03.040.

[49] David Dayya, Owen J. O'Neill, Tania B. Huedo-Medina, Nusrat Habib, Joanna Moore, and Kartik Iyer. Debridement of diabetic foot ulcers. *ADVANCES IN WOUND CARE*, 11(12):666–686, DEC 1 2022. ISSN 2162-1918. doi: 10.1089/wound.2021.0016.

[50] Stephanie C. Wu, Vickie R. Driver, James S. Wrobel, and David G. Armstrong. Foot ulcers in the diabetic patient, prevention and treatment. *VASCULAR HEALTH AND RISK MANAGEMENT*, 3(1):65–76, MAR 15 2007. ISSN 1176-6344.

[51] Perry Elliott, Bert Andersson, Eloisa Arbustini, Zofia Bilinska, Franco Cecchi, Philippe Charron, Olivier Dubourg, Uwe Ku R. Hl, Bernhard Maisch, William J. McKenna, Lorenzo Monserrat, Sabine Pankuweit, Claudio Rapezzi, Petar Seferovic, Luigi Tavazzi, and Andre Keren. Classification of the cardiomyopathies: a position statement from the european society of cardiology working group on myocardial and pericardial diseases. *EUROPEAN HEART JOURNAL*, 29(2):270–276, JAN 2008. ISSN 0195-668X. doi: 10.1093/eurheartj/ehm342.

[52] S RUBLER, YZ YUCEOGLU, T KUMRAL, A GRISHMAN, AW BRANWOOD, and J DLUGASH. New type of cardiomyopathy associated with diabetic glomerulosclerosis. *AMERICAN JOURNAL OF CARDIOLOGY*, 30(6):595–&, 1972. ISSN 0002-9149. doi: 10.1016/0002-9149(72)90595-4.

[53] Laura Ernande and Genevieve Derumeaux. Diabetic cardiomyopathy: Myth or reality? *ARCHIVES OF CARDIOVASCULAR DISEASES*, 105(4):218–225, APR 2012. ISSN 1875-2136. doi: 10.1016/j.acvd.2011.11.007.

[54] Piotr Ponikowski, Adriaan A. Voors, Stefan D. Anker, Hector Bueno, John G. F. Cleland, Andrew J. S. Coats, Volkmar Falk, Jose Ramon Gonzalez-Juanatey, Veli-Pekka Harjola, Ewa A. Jankowska, Mariell Jessup, Cecilia Linde, Petros Nihoyannopoulos, John T. Parissis, Burkert Pieske, Jillian P. Riley, Giuseppe M. C. Rosano, Luis M. Ruilope, Frank Ruschitzka, Frans H. Rutten, Peter van der Meer, Gerasimos Filippatos, John J. V. McMurray, Victor Aboyans, Stephan Achenbach, Stefan Agewall, Nawwar Al-Attar, John James Atherton, Johann Bauersachs, A. John Camm, Scipione Carerj, Claudio Ceconi, Antonio Coca, Perry Elliott, Cetin Erol, Justin Ezekowitz, Covadonga Fernandez-Golfin, Donna Fitzsimons, and Marco Guazzi. 2016 esc guidelines for the diagnosis and treatment of acute and chronic heart failure: The task force for the diagnosis and treatment of acute and chronic heart failure of the european society of cardiology (esc). developed with the special contribution of the heart failure association (hfa) of the esc. *EUROPEAN JOURNAL OF HEART FAILURE*, 18(8):891–975, AUG 2016. ISSN 1388-9842. doi: 10.1002/ejhf.592.

[55] Osama Abo Alrob, Sowndramalingam Sankaralingam, Cary Ma, Cory S. Wagg, Natasha Fillmore, Jagdip S. Jaswal, Michael N. Sack, Richard Lehner, Mahesh P. Gupta, Evangelos D. Michelakis, Raj S. Padwal, David E. Johnstone, Arya M. Sharma, and Gary D. Lopaschuk. Obesity-induced lysine acetylation increases cardiac fatty acid oxidation and impairs insulin signalling. *CARDIOVASCULAR RESEARCH*, 103 (4):485–497, SEP 1 2014. ISSN 0008-6363. doi: 10.1093/cvr/cvu156.

[56] Michinari Nakamura, Tong Liu, Seema Husain, Peiyong Zhai, Junco S. Warren, Chiao-Po Hsu, Takahisa Matsuda, Christopher J. Phiel, James E. Cox, Bin Tian, Hong Li, and Junichi Sadoshima. Glycogen synthase kinase-3 promotes fatty acid uptake and

lipotoxic cardiomyopathy. *CELL METABOLISM*, 29(5):1119+, MAY 7 2019. ISSN 1550-4131. doi: 10.1016/j.cmet.2019.01.005.

[57] Dharendra Thapa, Bingxian Xie, Manling Zhang, Michael W. Stoner, Janet R. Manninf, Brydie R. Huckestein, Lia R. Edmunds, Steven J. Mullett, Charles F. McTiernan, Stacy G. Wendell, Michael J. Jurczak, and Lain Scott. Adropin treatment restores cardiac glucose oxidation in pre-diabetic obese mice. *JOURNAL OF MOLECULAR AND CELLULAR CARDIOLOGY*, 129:174–178, APR 2019. ISSN 0022-2828. doi: 10.1016/j.yjmcc.2019.02.012.

[58] WC Stanley, FA Recchia, and GD Lopaschuk. Myocardial substrate metabolism in the normal and failing heart. *PHYSIOLOGICAL REVIEWS*, 85(3):1093–1129, JUL 2005. ISSN 0031-9333. doi: 10.1152/physrev.00006.2004.

[59] RJ BING, A SIEGEL, I UNGAR, and M GILBERT. Metabolism of the human heart .2. studies on fat, ketone and amino acid metabolism. *AMERICAN JOURNAL OF MEDICINE*, 16(4):504–515, 1954. ISSN 0002-9343. doi: 10.1016/0002-9343(54)90365-4.

[60] Aubert. The failing heart relies on ketone bodies as a fuel (vol 133, pg 698, 2016). *CIRCULATION*, 138(15):E422, OCT 9 2018. ISSN 0009-7322. doi: 10.1161/CIR.0000000000000621.

[61] Gary D. Lopaschuk, Qutuba G. Karwi, Kim L. Ho, Simran Pherwani, and Ezra B. Ketema. Ketone metabolism in the failing heart. *BIOCHIMICA ET BIOPHYSICA ACTA-MOLECULAR AND CELL BIOLOGY OF LIPIDS*, 1865(12), DEC 2020. ISSN 1388-1981. doi: 10.1016/j.bbalip.2020.158813.

[62] Gary D. Lopaschuk, Qutuba G. Karwi, Rong Tian, Adam R. Wende, and E. Dale Abel. Cardiac energy metabolism in heart failure. *CIRCULATION RESEARCH*, 128(10):1487–1513, MAY 14 2021. ISSN 0009-7330. doi: 10.1161/CIRCRESAHA.121.318241.

[63] LH OPIE, KR MANSFORD, and P OWEN. Effects of increased heart work on glycolysis and adenine nucleotides in perfused heart of normal and diabetic rats. *BIOCHEMICAL JOURNAL*, 124(3):475+, 1971. ISSN 0264-6021. doi: 10.1042/bj1240475.

[64] JA WISNESKI, EW GERTZ, RA NEESE, and M MAYR. Myocardial-metabolism of free fatty-acids - studies with c-14-labeled substrates in humans. *JOURNAL OF CLINICAL INVESTIGATION*, 79(2):359–366, FEB 1987. ISSN 0021-9738. doi: 10.1172/JCI112820.

[65] Daniel J. Fazakerley, Scott P. Lawrence, Vladimir A. Lizunov, Samuel W. Cushman, and Geoffrey D. Holman. A common trafficking route for glut4 in cardiomyocytes in response to insulin, contraction and energy-status signalling. *JOURNAL OF CELL SCIENCE*, 122(5):727–734, MAR 1 2009. ISSN 0021-9533. doi: 10.1242/jcs.041178.

[66] S PETERSEN, M BAHR, and J ECKEL. Insulin-dependent regulation of glut4 gene-expression in ventricular cardiomyocytes - evidence for a direct effect on glut4 transcription. *BIOCHEMICAL AND BIOPHYSICAL RESEARCH COMMUNICATIONS*, 213(2):533–540, AUG 15 1995. ISSN 0006-291X. doi: 10.1006/bbrc.1995.2164.

[67] C Becker, L Sevilla, E Tomàs, M Palacin, A Zorzano, and Y Fischer. The endosomal compartment is an insulin-sensitive recruitment site for glut4 and glut1 glucose transporters in cardiac myocytes. *ENDOCRINOLOGY*, 142(12):5267–5276, DEC 2001. ISSN 0013-7227. doi: 10.1210/en.142.12.5267.

[68] Y Fischer, J Thomas, L Sevilla, P Munoz, C Becker, G Holman, IJ Kozka, M Palacin, X Testar, H Kammermeier, and A Zorzano. Insulin-induced recruitment of glucose transporter 4 (glut4) and glut1 in isolated rat cardiac myocytes - evidence of the existence of different intracellular glut4 vesicle populations. *JOURNAL OF BIOLOGICAL CHEMISTRY*, 272(11):7085–7092, MAR 14 1997. ISSN 0021-9258. doi: 10.1074/jbc.272.11.7085.

[69] Xinghui Li, Yandi Wu, Jingjing Zhao, Haiping Wang, Jing Tan, Ming Yang, Yuanlong Li, Shijie Deng, Saifei Gao, Hui Li, Zhenyu Yang, Fengmin Yang, Jianxing Ma, Jianding Cheng, and Weibin Cai. Distinct cardiac energy metabolism and oxidative stress adaptations between obese and non-obese type 2 diabetes mellitus. *THERANOSTICS*, 10(6):2675–2695, 2020. ISSN 1838-7640. doi: 10.7150/thno.40735.

[70] Zhongwei Yin, Yanru Zhao, Mengying He, Huaping Li, Jiahui Fan, Xiang Nie, Mengwen Yan, Chen Chen, and Dao Wen Wang. Mir-30c/pgc-1 protects against diabetic cardiomyopathy via ppar. *CARDIOVASCULAR DIABETOLOGY*, 18, JAN 11 2019. doi: 10.1186/s12933-019-0811-7.

[71] Kunal Sikder, Sanket Kumar Shukla, Neel Patel, Harpreet Singh, and Khadija Rafiq. High fat diet upregulates fatty acid oxidation and ketogenesis via intervention of ppar-. *CELLULAR PHYSIOLOGY AND BIOCHEMISTRY*, 48(3):1317–1331, 2018. ISSN 1015-8987. doi: 10.1159/000492091.

[72] Ina Katrine Nitschke Pettersen, Deusdedit Tusubira, Hanan Ashrafi, Sissel Elisabeth Dyrstad, Lena Hansen, Xiao-Zheng Liu, Linn Iren Hodneland Nilsson, Nils Gunnar Lovsletten, Kjetil Berge, Hege Wergedahl, Bodil Bjorndal, Oystein Fluge, Ove Bruland, Arild Christian Rustan, Nils Halberg, Gro Vatne Rosland, Rolf Kristian Berge, and Karl Johan Tronstad. Upregulated pdk4 expression is a sensitive marker of increased fatty acid oxidation. *MITOCHONDRION*, 49:97–110, NOV 2019. ISSN 1567-7249. doi: 10.1016/j.mito.2019.07.009.

[73] Adam R. Wende, John C. Schell, Chae-Myeong Ha, Mark E. Pepin, Oleh Khalimonchuk, Hansjoerg Schwertz, Renata O. Pereira, Manoja K. Brahma, Joseph Tuinei, Ariel Contreras-Ferrat, Li Wang, Chase A. Andrizzi, Curtis D. Olsen, Wayne E. Bradley, Louis J. Dell'Italia, Wolfgang H. Dillmann, Sheldon E. Litwin, and E. Dale Abel. Maintaining myocardial glucose utilization in diabetic cardiomyopathy accelerates mitochondrial dysfunction. *DIABETES*, 69(10):2094–2111, OCT 2020. ISSN 0012-1797. doi: 10.2337/db19-1057.

[74] Mark Rinnerthaler, Johannes Bischof, Maria Karolin Streubel, Andrea Trost, and Klaus Richter. Oxidative stress in aging human skin. *BIOMOLECULES*, 5(2):545–589, JUN 2015. doi: 10.3390/biom5020545.

[75] Richard Wong, Stefan Geyer, Wolfgang Weninger, Jean-Claude Guimberteau, and Jason K. Wong. The dynamic anatomy and patterning of skin. *EXPERIMENTAL DERMATOLOGY*, 25(2):92–98, FEB 2016. ISSN 0906-6705. doi: 10.1111/exd.12832.

[76] Richard L. Gallo. Human skin is the largest epithelial surface for interaction with microbes. *JOURNAL OF INVESTIGATIVE DERMATOLOGY*, 137(6):1213–1214, JUN 2017. ISSN 0022-202X. doi: 10.1016/j.jid.2016.11.045.

[77] Geoffrey C. Gurtner, Sabine Werner, Yann Barrandon, and Michael T. Longaker. Wound repair and regeneration. *NATURE*, 453(7193):314–321, MAY 15 2008. ISSN 0028-0836. doi: 10.1038/nature07039.

[78] WK Stadelmann, AG Digenis, and GR Tobin. Physiology and healing dynamics of chronic cutaneous wounds. *AMERICAN JOURNAL OF SURGERY*, 176(2A, S): 26S–38S, AUG 1998. ISSN 0002-9610. doi: 10.1016/S0002-9610(98)00183-4.

[79] RF Diegelmann and MC Evans. Wound healing: An overview of acute, fibrotic and delayed healing. *FRONTIERS IN BIOSCIENCE-LANDMARK*, 9:283–289, JAN 2004. ISSN 1093-9946. doi: 10.2741/1184.

[80] G Broughton, JE Janis, and CE Attinger. A brief history of wound care. *PLASTIC AND RECONSTRUCTIVE SURGERY*, 117(7, S):6S–11S, JUN 2006. ISSN 0032-1052. doi: 10.1097/01.prs.0000225429.76355.dd.

[81] Joshua S. Boateng, Kerr H. Matthews, Howard N. E. Stevens, and Gillian M. Eccleston. Wound healing dressings and drug delivery systems: A review. *JOURNAL OF PHARMACEUTICAL SCIENCES*, 97(8):2892–2923, AUG 2008. ISSN 0022-3549. doi: 10.1002/jps.21210.

[82] T. Velnar, T. Bailey, and V. Smrkoli. The wound healing process: an overview of the cellular and molecular mechanisms. *JOURNAL OF INTERNATIONAL MEDICAL RESEARCH*, 37(5):1528–1542, SEP-OCT 2009. ISSN 0300-0605. doi: 10.1177/147323000903700531.

[83] Bruce Furie and Barbara C. Furie. Mechanisms of disease: Mechanisms of thrombus formation. *NEW ENGLAND JOURNAL OF MEDICINE*, 359(9):938–949, AUG 28 2008. ISSN 0028-4793. doi: 10.1056/NEJMra0801082.

[84] JG POOL and P GATLIN. Normal hemostatic mechanisms - review. *AMERICAN JOURNAL OF MEDICAL TECHNOLOGY*, 43(8):776–780, 1977. ISSN 0002-9335.

[85] ABG Lansdown. Calcium: a potential central regulator in wound healing in the skin. *WOUND REPAIR AND REGENERATION*, 10(5):271–285, SEP-OCT 2002. ISSN 1067-1927. doi: 10.1046/j.1524-475X.2002.10502.x.

[86] Albert van der Vliet and Yvonne M. W. Janssen-Heininger. Hydrogen peroxide as a damage signal in tissue injury and inflammation: Murderer, mediator, or messenger? *JOURNAL OF CELLULAR BIOCHEMISTRY*, 115(3):427–435, MAR 2014. ISSN 0730-2312. doi: 10.1002/jcb.24683.

[87] L. Ferrero-Miliani, O. H. Nielsen, P. S. Andersen, and S. E. Girardin. Chronic inflammation:: importance of nod2 and nalp3 in interleukin-1 generation. *CLINICAL AND EXPERIMENTAL IMMUNOLOGY*, 147(2):227–235, FEB 2007. ISSN 0009-9104. doi: 10.1111/j.1365-2249.2006.03261.x.

[88] Carl Nathan and Aihao Ding. Nonresolving inflammation. *CELL*, 140(6):871–882, MAR 19 2010. ISSN 0092-8674. doi: 10.1016/j.cell.2010.02.029.

[89] Guillaume Charras and Erik Sahai. Physical influences of the extracellular environment on cell migration. *NATURE REVIEWS MOLECULAR CELL BIOLOGY*, 15(12):813–824, DEC 2014. ISSN 1471-0072. doi: 10.1038/nrm3897.

[90] T Asahara, T Murohara, A Sullivan, M Silver, R vanderZee, T Li, B Witzenbichler, G Schatteman, and JM Isner. Isolation of putative progenitor endothelial cells for angiogenesis. *SCIENCE*, 275(5302):964–967, FEB 14 1997. ISSN 0036-8075. doi: 10.1126/science.275.5302.964.

[91] Hanna M. Eilken and Ralf H. Adams. Dynamics of endothelial cell behavior in sprouting angiogenesis. *CURRENT OPINION IN CELL BIOLOGY*, 22(5):617–625, OCT 2010. ISSN 0955-0674. doi: 10.1016/j.ceb.2010.08.010.

[92] Richard J. Bodnar. Chemokine regulation of angiogenesis during wound healing. *ADVANCES IN WOUND CARE*, 4(11):641–650, NOV 1 2015. ISSN 2162-1918. doi: 10.1089/wound.2014.0594.

[93] MG Tonnesen, XD Feng, and RAF Clark. Angiogenesis in wound healing. *JOURNAL OF INVESTIGATIVE DERMATOLOGY SYMPOSIUM PROCEEDINGS*, 5(1):40–46, DEC 2000. ISSN 1087-0024. doi: 10.1046/j.1087-0024.2000.00014.x. 48th Annual Montagna Symposium on the Biology of Skin, SNOWMASS, COLORADO, AUG 07-11, 1999.

[94] Annika Armulik, Guillem Genove, and Christer Betsholtz. Pericytes: Developmental, physiological, and pathological perspectives, problems, and promises. *DEVELOPMENTAL CELL*, 21(2):193–215, AUG 16 2011. ISSN 1534-5807. doi: 10.1016/j.devcel.2011.07.001.

[95] Catherine N. Hall, Clare Reynell, Bodil Gesslein, Nicola B. Hamilton, Anusha Mishra, Brad A. Sutherland, Fergus M. O'Farrell, Alastair M. Buchan, Martin Lauritzen, and David Attwell. Capillary pericytes regulate cerebral blood flow in health and disease. *NATURE*, 508(7494):55+, APR 3 2014. ISSN 0028-0836. doi: 10.1038/nature13165.

[96] S Song, AJ Ewald, W Stallcup, Z Werb, and G Bergers. Pdgfr⁺ perivascular progenitor cells in tumours regulate pericyte differentiation and vascular survival. *NATURE CELL BIOLOGY*, 7(9):870–U16, SEP 2005. ISSN 1465-7392. doi: 10.1038/ncb1288.

[97] Ilaria Spadoni, Elena Zagato, Alice Bertocchi, Roberta Paolinelli, Edina Hot, Antonio Di Sabatino, Flavio Caprioli, Luca Bottiglieri, Amanda Oldani, Giuseppe Viale, Giuseppe Penna, Elisabetta Dejana, and Maria Rescigno. A gut-vascular barrier controls the systemic dissemination of bacteria. *SCIENCE*, 350(6262):830–834, NOV 13 2015. ISSN 0036-8075. doi: 10.1126/science.aad0135.

[98] CR Cogle, DA Wainman, ML Jorgensen, SM Guthrie, RN Mames, and EW Scott. Adult human hematopoietic cells provide functional hemangioblast activity. *BLOOD*, 103(1):133–135, JAN 1 2004. ISSN 0006-4971. doi: 10.1182/blood-2003-06-2101.

[99] MB Grant, WS May, S Caballero, GAJ Brown, SM Guthrie, RN Mames, BJ Byrne, T Vaught, PE Spoerri, AB Peck, and EW Scott. Adult hematopoietic stem cells provide functional hemangioblast activity during retinal neovascularization. *NATURE MEDICINE*, 8(6):607–612, JUN 2002. ISSN 1078-8956. doi: 10.1038/nm0602-607.

[100] Ian A. Darby and Tim D. Hewitson. Fibroblast differentiation in wound healing and fibrosis. In KW Jeon, editor, *INTERNATIONAL REVIEW OF CYTOLOGY - A SURVEY OF CELL BIOLOGY, VOL 257*, volume 257 of *INTERNATIONAL REVIEW OF CYTOLOGY-A SURVEY OF CELL BIOLOGY*, pages 143+. 2007. ISBN 978-0-12-373701-4. doi: 10.1016/S0074-7696(07)57004-X.

[101] KM FRIES, T BLIEDEN, RJ LOONEY, GD SEMPOWSKI, MR SILVERA, RA WILLIS, and RP PHIPPS. Evidence of fibroblast heterogeneity and the role of fibroblast subpopulations in fibrosis. *CLINICAL IMMUNOLOGY AND IMMUNOPATHOLOGY*, 72(3):283–292, SEP 1994. ISSN 0090-1229. doi: 10.1006/clin.1994.1144.

[102] Prabhat K. Singhal, Slim Sassi, Lan Lan, Patrick Au, Stefan C. Halvorsen, Dai Fukumura, Rakesh K. Jain, and Brian Seed. Mouse embryonic fibroblasts exhibit extensive developmental and phenotypic diversity. *PROCEEDINGS OF THE NATIONAL ACADEMY OF SCIENCES OF THE UNITED STATES OF AMERICA*, 113 (1):122–127, JAN 5 2016. ISSN 0027-8424. doi: 10.1073/pnas.1522401112.

[103] Gregory S. Schultz, Jeffrey M. Davidson, Robert S. Kirsner, Paul Bornstein, and Ira M. Herman. Dynamic reciprocity in the wound microenvironment. *WOUND REPAIR AND REGENERATION*, 19(2):134–148, MAR-APR 2011. ISSN 1067-1927. doi: 10.1111/j.1524-475X.2011.00673.x.

[104] JJ Tomasek, G Gabbiani, B Hinz, C Chaponnier, and RA Brown. Myofibroblasts and mechano-regulation of connective tissue remodelling. *NATURE REVIEWS MOLECULAR CELL BIOLOGY*, 3(5):349–363, MAY 2002. ISSN 1471-0072. doi: 10.1038/nrm809.

[105] James J. Tomasek, Carol J. Haaksma, Robert J. Schwartz, and Eric W. Howard. Whole animal knockout of smooth muscle alpha-actin does not alter excisional wound healing or the fibroblast-to-myofibroblast transition. *WOUND REPAIR AND REGENERATION*, 21(1):166–176, JAN-FEB 2013. ISSN 1067-1927. doi: 10.1111/wrr.12001.

[106] U Ozerdem, K Alitalo, P Salven, and A Li. Contribution of bone marrow-derived pericyte precursor cells to corneal vasculogenesis. *INVESTIGATIVE OPHTHALMOLOGY & VISUAL SCIENCE*, 46(10):3502–3506, OCT 2005. ISSN 0146-0404. doi: 10.1167/iovs.05-0309.

[107] I Rajantie, M Ilmonen, A Alminaite, U Ozerdem, K Alitalo, and P Salven. Adult bone marrow-derived cells recruited during angiogenesis comprise precursors for periendothelial vascular mural cells. *BLOOD*, 104(7):2084–2086, OCT 1 2004. ISSN 0006-4971. doi: 10.1182/blood-2004-01-0336.

[108] T Takahashi, C Kalka, H Masuda, D Chen, M Silver, M Kearney, M Magner, JM Isner, and T Asahara. Ischemia- and cytokine-induced mobilization of bone marrow-derived

endothelial progenitor cells for neovascularization. *NATURE MEDICINE*, 5(4):434–438, APR 1999. ISSN 1078-8956. doi: 10.1038/7434.

[109] Robert Nunan, Keith G. Harding, and Paul Martin. Clinical challenges of chronic wounds: searching for an optimal animal model to recapitulate their complexity. *DISEASE MODELS & MECHANISMS*, 7(11):1205–1213, NOV 2014. ISSN 1754-8403. doi: 10.1242/dmm.016782.

[110] RF Diegelmann and MC Evans. Wound healing: An overview of acute, fibrotic and delayed healing. *FRONTIERS IN BIOSCIENCE-LANDMARK*, 9:283–289, JAN 2004. ISSN 1093-9946. doi: 10.2741/1184.

[111] T Mustoe. Understanding chronic wounds: a unifying hypothesis on their pathogenesis and implications for therapy. *AMERICAN JOURNAL OF SURGERY*, 187(5A, S): 65S–70S, MAY 2004. ISSN 0002-9610. doi: 10.1016/S0002-9610(03)00306-4. Symposium on Clinical Wound Healing of the Diabetic Foot Ulcer, New York, NY, DEC 14, 2001.

[112] MC Robson, DL Steed, and MG Franz. Wound healing: Biologic features and approaches to maximize healing trajectories - in brief. *CURRENT PROBLEMS IN SURGERY*, 38(2):65–140, FEB 2001. ISSN 0011-3840.

[113] Nathalie Thieblemont, Helen L. Wright, Steven W. Edwards, and Veronique Witko-Sarsat. Human neutrophils in auto-immunity. *SEMINARS IN IMMUNOLOGY*, 28(2): 159–173, APR 2016. ISSN 1044-5323. doi: 10.1016/j.smim.2016.03.004.

[114] Maggie J. Westby, Gill Norman, Rachel E. B. Watson, Nicky A. Cullum, and Jo C. Dumville. Protease activity as a prognostic factor for wound healing in complex wounds. *WOUND REPAIR AND REGENERATION*, 28(5):631–644, SEP 2020. ISSN 1067-1927. doi: 10.1111/wrr.12835.

[115] S Werner and R Grose. Regulation of wound healing by growth factors and cytokines. *PHYSIOLOGICAL REVIEWS*, 83(3):835–870, JUL 2003. ISSN 0031-9333. doi: 10.1152/physrev.2003.83.3.835.

[116] S. Guo and L. A. DiPietro. Factors affecting wound healing. *JOURNAL OF DENTAL RESEARCH*, 89(3):219–229, MAR 2010. ISSN 0022-0345. doi: 10.1177/0022034509359125.

[117] Sabine A. Eming, Paul Martin, and Marjana Tomic-Canic. Wound repair and regeneration: Mechanisms, signaling, and translation. *SCIENCE TRANSLATIONAL MEDICINE*, 6(265), DEC 3 2014. ISSN 1946-6234. doi: 10.1126/scitranslmed.3009337.

[118] Thomas Bjarnsholt, Klaus Kirketerp-Møller, Peter Østrup Jensen, Kit G. Madsen, Richard Phipps, Karen Krogfelt, Niels Høiby, and Michael Givskov. Why chronic wounds will not heal: a novel hypothesis. *Wound Repair and Regeneration*, 16(1): 2–10, 2008. doi: https://doi.org/10.1111/j.1524-475X.2007.00283.x. URL https://onlinelibrary.wiley.com/doi/abs/10.1111/j.1524-475X.2007.00283.x.

[119] Garth A. James, Ellen Swogger, Randall Wolcott, Elinor deLancey Pulcini, Patrick Secor, Jennifer Sestrich, John W. Costerton, and Philip S. Stewart. Biofilms in chronic wounds. *Wound Repair and Regeneration*, 16(1):37–44, 2008. doi: https://doi.org/10.1111/j.1524-475X.2007.00321.x. URL https://onlinelibrary.wiley.com/doi/abs/10.1111/j.1524-475X.2007.00321.x.

[120] Yasuhiko Irie, Bradley R. Borlee, Jennifer R. O'Connor, Preston J. Hill, Caroline S. Harwood, Daniel J. Wozniak, and Matthew R. Parsek. Self-produced exopolysaccharide is a signal that stimulates biofilm formation in pseudomonas aeruginosa. *Proceedings of the National Academy of Sciences*, 109(50):20632–20636, 2012. doi: 10.1073/pnas.1217993109. URL https://www.pnas.org/doi/abs/10.1073/pnas.1217993109.

[121] Ida C. Thaarup and Thomas Bjarnsholt. Current in vitro biofilm-infected chronic wound models for developing new treatment possibilities. *Advances in Wound Care*, 10(2):91–102, 2021. doi: 10.1089/wound.2020.1176. URL https://doi.org/10.1089/wound.2020.1176. PMID: 32496982.

[122] Claus Sternberg, Thomas Bjarnsholt, and Mark Shirtliff. Methods for dynamic investigations of surface-attached in vitro bacterial and fungal biofilms. In G Donelli, editor, *MICROBIAL BIOFILMS: METHODS AND PROTOCOLS*, volume 1147 of *Methods in Molecular Biology*, pages 3–22. 2014. ISBN 978-1-4939-0467-9; 978-1-4939-0466-2. doi: 10.1007/978-1-4939-0467-9_1.

[123] Nira Rabin, Yue Zheng, Clement Opoku-Temeng, Yixuan Du, Eric Bonsu, and Herman O. Sintim. Biofilm formation mechanisms and targets for developing antibiofilm agents (vol 7, pg 493, 2015). *FUTURE MEDICINAL CHEMISTRY*, 7(10):1362, 2015. ISSN 1756-8919.

[124] RM Donlan. Biofilms and device-associated infections. *EMERGING INFECTIOUS DISEASES*, 7(2):277–281, MAR-APR 2001. ISSN 1080-6040. doi: 10.3201/eid0702.010226. 4th Decennial International Conference on Nosocomial and Healthcare-Associated Infections in Conjunction with the 10th Annual Meeting of SHEA, ATLANTA, GA, MAR 05-09, 2000.

[125] Lantian Zhou, Yue Zhang, Yongze Ge, Xuan Zhu, and Jianyi Pan. Regulatory mechanisms and promising applications of quorum sensing-inhibiting agents in control of bacterial biofilm formation. *FRONTIERS IN MICROBIOLOGY*, 11, OCT 15 2020. ISSN 1664-302X. doi: 10.3389/fmicb.2020.589640.

[126] Andrew A. Bridges and Bonnie L. Bassler. The intragenus and interspecies quorum-sensing autoinducers exert distinct control over vibrio cholerae biofilm formation and dispersal. *PLOS BIOLOGY*, 17(11), NOV 2019. ISSN 1544-9173. doi: 10.1371/journal.pbio.3000429.

[127] Timothy J. Foster. Surface proteins ofstaphylococcus epidermidis. *FRONTIERS IN MICROBIOLOGY*, 11, JUL 29 2020. ISSN 1664-302X. doi: 10.3389/fmicb.2020.01829.

[128] Nira Rabin, Yue Zheng, Clement Opoku-Temeng, Yixuan Du, Eric Bonsu, and Herman O. Sintim. Biofilm formation mechanisms and targets for developing antibiofilm

agents. *FUTURE MEDICINAL CHEMISTRY*, 7(4):493–512, 2015. ISSN 1756-8919. doi: 10.4155/FMC.15.6.

[129] Anna Krasowska and Karel Sigler. How microorganisms use hydrophobicity and what does this mean for human needs? *FRONTIERS IN CELLULAR AND INFECTION MICROBIOLOGY*, 4, AUG 2014. ISSN 2235-2988. doi: 10.3389/fcimb.2014.00112.

[130] Caroline Dowett and Elizabeth Ayello. Time principles of chronic wound bed preparation and treatment. *British Journal of Nursing*, 13(Sup3):S16–S23, 2004. doi: 10.12968/bjon.2004.13.Sup3.15546. URL https://doi.org/10.12968/bjon.2004.13.Sup3.15546. PMID: 15365480.

[131] Putna Sai Korrapati, K. Karthikeyan, Aishwarya Satish, Venkat Raghavan Krishnaswamy, Jayarama Reddy Venugopal, and Seeram Ramakrishna. Recent advancements in nanotechnological strategies in selection, design and delivery of biomolecules for skin regeneration. *MATERIALS SCIENCE & ENGINEERING C-MATERIALS FOR BIOLOGICAL APPLICATIONS*, 67:747–765, OCT 1 2016. ISSN 0928-4931. doi: 10.1016/j.msec.2016.05.074.

[132] Shirin Nour, Nafiseh Baheiraei, Rana Imani, Mohammad Khodaei, Akram Alizadeh, Navid Rabiee, and S. Mohammad Moazzeni. A review of accelerated wound healing approaches: biomaterial- assisted tissue remodeling. *JOURNAL OF MATERIALS SCIENCE-MATERIALS IN MEDICINE*, 30(10), OCT 2019. ISSN 0957-4530. doi: 10.1007/s10856-019-6319-6.

[133] Meilang Xue, Ruilong Zhao, Haiyan Lin, and Christopher Jackson. Delivery systems of current biologicals for the treatment of chronic cutaneous wounds and severe burns. *ADVANCED DRUG DELIVERY REVIEWS*, 129(1):219–241, APR 2018. ISSN 0169-409X. doi: 10.1016/j.addr.2018.03.002.

[134] Bryan K. Sun, Zurab Siprashvili, and Paul A. Khavari. Advances in skin grafting and treatment of cutaneous wounds. *SCIENCE*, 346(6212):941–945, NOV 21 2014. ISSN 0036-8075. doi: 10.1126/science.1253836.

[135] Muholan Kanapathy, Nadine Hachach-Haram, Nicola Bystrzonowski, John T. Connelly, Edel A. O'Toole, David L. Becker, Afshin Mosahebi, and Toby Richards. Epidermal grafting for wound healing: a review on the harvesting systems, the ultrastructure of the graft and the mechanism of wound healing. *INTERNATIONAL WOUND JOURNAL*, 14(1):16–23, FEB 2017. ISSN 1742-4801. doi: 10.1111/iwj.12686.

[136] Robert J. Morin and Nancy L. Tomaselli. Interactive dressings and topical agents. *CLINICS IN PLASTIC SURGERY*, 34(4):643+, OCT 2007. ISSN 0094-1298. doi: 10.1016/j.cps.2007.07.004.

[137] S Wittaya-areekul and C Prahsarn. Development and in vitro evaluation of chitosan-polysaccharides composite wound dressings. *INTERNATIONAL JOURNAL OF PHARMACEUTICS*, 313(1-2):123–128, APR 26 2006. ISSN 0378-5173. doi: 10.1016/j.ijpharm.2006.01.027.

[138] Joshua S. Boateng, Kerr H. Matthews, Howard N. E. Stevens, and Gillian M. Eccleston. Wound healing dressings and drug delivery systems: A review. *JOURNAL OF PHARMACEUTICAL SCIENCES*, 97(8):2892–2923, AUG 2008. ISSN 0022-3549. doi: 10.1002/jps.21210.

[139] Margaret A. Fonder, Gerald S. Lazarus, David A. Cowan, Barbara Aronson-Cook, Angela R. Kohli, and Adam J. Mamelak. Treating the chronic wound: A practical approach to the care of nonhealing wounds and wound care dressings. *JOURNAL OF THE AMERICAN ACADEMY OF DERMATOLOGY*, 58(2):185–206, FEB 2008. ISSN 0190-9622. doi: 10.1016/j.jaad.2007.08.048.

[140] Stephen D Milne, Ihab Seoudi, Hanadi Al Hamad, Talal K Talal, Anzila A Anoop, Niloofar Allahverdi, Zain Zakaria, Robert Menzies, and Patricia Connolly. A wearable wound moisture sensor as an indicator for wound dressing change: an observational study of wound moisture and status. *International Wound Journal*, 13(6):1309–1314, 2016. doi: https://doi.org/10.1111/iwj.12521. URL https://onlinelibrary.wiley.com/doi/abs/10.1111/iwj.12521.

[141] M. Mulder. The selection of wound care products for wound bed preparation : wound bed preparation. *Wound Healing Southern Africa*, 2(2):76–78, 2009. doi: 10.10520/EJC82750. URL https://journals.co.za/doi/abs/10.10520/EJC82750.

[142] JR Hilton, DT Williams, B Beuker, DR Miller, and KG Harding. Wound dressings in diabetic foot disease. *CLINICAL INFECTIOUS DISEASES*, 39(2):S100–S103, AUG 1 2004. ISSN 1058-4838. doi: 10.1086/383270. 5th Annual Almelo Diabetic Foot Symposium, Almelo, NETHERLANDS, 2001.

[143] WJ Jeffcoate, P Price, and KG Harding. Wound heating and treatments for people with diabetic foot ulcers. *DIABETES-METABOLISM RESEARCH AND REVIEWS*, 20(1):S78–S89, MAY-JUN 2004. ISSN 1520-7552. doi: 10.1002/dmrr.476. 4th International Symposium on the Diabetic Foot, Noordwijkerhout, NETHERLANDS, MAY 22-24, 2003.

[144] KG Harding, V Jones, and P Price. Topical treatment: which dressing to choose. *DIABETES-METABOLISM RESEARCH AND REVIEWS*, 16(1):S47–S50, SEP-OCT 2000. ISSN 1520-7552. doi: 10.1002/1520-7560(200009/10)16:1+<::AID-DMRR133>3.0.CO;2-Q. 3rd International Symposium on the Diabetic Foot, NOORDWIJKERHOUT, NETHERLANDS, MAY 05-08, 1999.

[145] Suzanne O'Callaghan, Paul Galvin, Conor O'Mahony, Zena Moore, and Rosemarie Derwin. 'smart' wound dressings for advanced wound care: a review. *JOURNAL OF WOUND CARE*, 29(7):394–406, JUL 2020. ISSN 0969-0700. doi: 10.12968/jowc.2020.29.7.394.

[146] Christine Anne Murphy, Leanne Atkin, Terry Swanson, Masahiro Tachi, Yih Kai Tan, Melina Vega de Céniga, Dot Weir, Randall D. Wolcott, Júlia ernohorská, Guido Ciprandi, Joachim Dissemond, Garth A James, Jennifer Hurlow, José Luis Lázaro Martínez, Beata Mrozikiewicz-Rakowska, and Pauline Wilson. Defying hard-to-heal wounds with an early antibiofilm intervention strategy: wound hygiene. *Journal of wound care*, 29 Sup3b:S1–S26, 2020. URL https://api.semanticscholar.org/CorpusID:212679653.

[147] Hayley B. Schultz, Roshan B. Vasani, Amy M. Holmes, Michael S. Roberts, and Nicolas H. Voelcker. Stimulus-responsive antibiotic releasing systems for the treatment of wound infections. *ACS APPLIED BIO MATERIALS*, 2(2):704–716, FEB 18 2019. ISSN 2576-6422. doi: 10.1021/acsabm.8b00577.

[148] Innovations and emerging technologies in wound care. In A Gefen, editor, *INNOVATIONS AND EMERGING TECHNOLOGIES IN WOUND CARE*, pages 1–388. 2020. ISBN 978-0-12-815029-0; 978-0-12-815028-3.

[149] Ganary Dabiri, Elizabeth Damstetter, and Tania Phillips. Choosing a wound dressing based on common wound characteristics. *ADVANCES IN WOUND CARE*, 5(1):32–41, JAN 1 2016. ISSN 2162-1918. doi: 10.1089/wound.2014.0586.

[150] Ziqi Liu, Junqing Liu, Tiancheng Sun, Deke Zeng, Chengduan Yang, Hao Wang, Cheng Yang, Jun Guo, Qianni Wu, Hui-Jiuan Chen, and Xi Xie. Integrated multiplex sensing bandage for in situ monitoring of early infected wounds. *ACS SENSORS*, 6 (8):3112–3124, AUG 27 2021. ISSN 2379-3694. doi: 10.1021/acssensors.1c01279.

[151] Yuji Gao, Dat T. Nguyen, Trifanny Yeo, Su Bin Lim, Wei Xian Tan, Leigh Edward Madden, Lin Jin, Ji Yong Kenan Long, Fazila Abu Bakar Aloweni, Yi Jia Angela Liew, Mandy Li Ling Tan, Shin Yuh Ang, Sivagame D. O. Maniya, Ibrahim Abdelwahab, Kian Ping Loh, Chia-Hung Chen, David Laurence Becker, David Leavesley, John S. Ho, and Chwee Teck Lim. A flexible multiplexed immunosensor for point-of-care in situ wound monitoring. *SCIENCE ADVANCES*, 7(21), MAY 2021. ISSN 2375-2548. doi: 10.1126/sciadv.abg9614.

[152] Tianhong Dai, Masamitsu Tanaka, Ying-Ying Huang, and Michael R. Hamblin. Chitosan preparations for wounds and burns: antimicrobial and wound-healing effects. *EXPERT REVIEW OF ANTI-INFECTIVE THERAPY*, 9(7):857–879, JUL 2011. ISSN 1478-7210. doi: 10.1586/ERI.11.59.

[153] Gang Xu, Yanli Lu, Chen Cheng, Xin Li, Jie Xu, Zhaoyang Liu, Jinglong Liu, Guang Liu, Zhenghan Shi, Zetao Chen, Fenni Zhang, Yixuan Jia, Danfeng Xu, Wei Yuan, Zheng Cui, Sze Shin Low, and Qingjun Liu. Battery-free and wireless smart wound dressing for wound infection monitoring and electrically controlled on-demand drug delivery. *Advanced Functional Materials*, 31(26):2100852, 2021. doi: https://doi.org/10.1002/adfm.202100852. URL https://onlinelibrary.wiley.com/doi/abs/10.1002/adfm.202100852.

[154] Qian Pang, Dong Lou, Shijian Li, Guangming Wang, Bianbian Qiao, Shurong Dong, Lie Ma, Changyou Gao, and Zhaohui Wu. Smart flexible electronics-integrated wound dressing for real-time monitoring and on-demand treatment of infected wounds. *Advanced Science*, 7(6):1902673, 2020. doi: https://doi.org/10.1002/advs.201902673. URL https://onlinelibrary.wiley.com/doi/abs/10.1002/advs.201902673.

[155] Qian Wang, Takashi Hisatomi, Qingxin Jia, Hiromasa Tokudome, Miao Zhong, Chizhong Wang, Zhenhua Pan, Tsuyoshi Takata, Mamiko Nakabayashi, Naoya Shibata, Yanbo Li, Ian D. Sharp, Akihiko Kudo, Taro Yamada, and Kazunari Domen. Scalable water splitting on particulate photocatalyst sheets with a solar-to-hydrogen energy conversion efficiency exceeding 1%. *NATURE MATERIALS*, 15(6):611+, JUN 2016. ISSN 1476-1122. doi: 10.1038/NMAT4589.

[156] K Maeda, K Teramura, DL Lu, T Takata, N Saito, Y Inoue, and K Domen. Photocatalyst releasing hydrogen from water - enhancing catalytic performance holds promise for hydrogen production by water splitting in sunlight. *NATURE*, 440(7082):295, MAR 16 2006. ISSN 0028-0836. doi: 10.1038/440295a.

[157] Jingrun Ran, Jun Zhang, Jiaguo Yu, Mietek Jaroniec, and Shi Zhang Qiao. Earth-abundant cocatalysts for semiconductor-based photocatalytic water splitting. *CHEMICAL SOCIETY REVIEWS*, 43(22):7787–7812, NOV 21 2014. ISSN 0306-0012. doi: 10.1039/c3cs60425j.

[158] Xinchen Wang, Kazuhiko Maeda, Arne Thomas, Kazuhiro Takanabe, Gang Xin, Johan M. Carlsson, Kazunari Domen, and Markus Antonietti. A metal-free polymeric photocatalyst for hydrogen production from water under visible light. *NATURE MATERIALS*, 8(1):76–80, JAN 2009. ISSN 1476-1122. doi: 10.1038/NMAT2317.

[159] DM Teter and RJ Hemley. Low-compressibility carbon nitrides. *SCIENCE*, 271(5245): 53–55, JAN 5 1996. ISSN 0036-8075. doi: 10.1126/science.271.5245.53.

[160] Yang Zhao, Jing Zhang, and Liangti Qu. Graphitic carbon nitride/graphene hybrids as new active materials for energy conversion and storage. *CHEMNANOMAT*, 1(5): 298–318, SEP 2015. ISSN 2199-692X. doi: 10.1002/cnma.201500060.

[161] A. Zambon, J. M. Mouesca, C. Gheorghiu, P. A. Bayle, J. Pecaut, M. Claeys-Bruno, S. Gambarelli, and L. Dubois. s-heptazine oligomers: promising structural models for graphitic carbon nitride. *CHEMICAL SCIENCE*, 7(2):945–950, 2016. ISSN 2041-6520. doi: 10.1039/c5sc02992a.

[162] Prashant V. Kamat. Manipulation of charge transfer across semiconductor interface. a criterion that cannot be ignored in photocatalyst design. *JOURNAL OF PHYSICAL CHEMISTRY LETTERS*, 3(5):663–672, MAR 1 2012. ISSN 1948-7185. doi: 10.1021/jz201629p.

[163] Sanjaya D. Perera, Ruperto G. Mariano, Khiem Vu, Nijem Nour, Oliver Seitz, Yves Chabal, and Kenneth J. Balkus, Jr. Hydrothermal synthesis of graphene-tio₂ nanotube composites with enhanced photocatalytic activity. *ACS CATALYSIS*, 2(6):949–956, JUN 2012. ISSN 2155-5435. doi: 10.1021/cs200621c.

[164] Junwei Fu, Jiaguo Yu, Chuanjia Jiang, and Bei Cheng. g-c3n4-based heterostructured photocatalysts. *Advanced Energy Materials*, 8(3):1701503, 2018. doi: https://doi.org/10.1002/aenm.201701503. URL https://onlinelibrary.wiley.com/doi/abs/10.1002/aenm.201701503.

[165] Wenbo Sheng, Wei Li, Deming Tan, Panpan Zhang, En Zhang, Evgeniya Sheremet, Bernhard V. K. J. Schmidt, Xinliang Feng, Raul D. Rodriguez, Rainer Jordan, and Ihsan Amin. Polymer brushes on graphitic carbon nitride for patterning and as a sers active sensing layer via incorporated nanoparticles. *ACS APPLIED MATERIALS & INTERFACES*, 12(8):9797–9805, FEB 26 2020. ISSN 1944-8244. doi: 10.1021/acsami.9b21984.

[166] Baris Kumru, Jesus Barrio, Jianrui Zhang, Markus Antonietti, Menny Shalom, and Bernhard V. K. J. Schmidt. Robust carbon nitride-based thermoset coatings for surface modification and photochemistry. *ACS APPLIED MATERIALS & INTERFACES*, 11 (9):9462–9469, MAR 6 2019. ISSN 1944-8244. doi: 10.1021/acsami.8b21670.

[167] Daniel Cruz, Jose Garcia Cerrillo, Baris Kumru, Ning Li, Jose Dario Perea, Bernhard V. K. J. Schmidt, Iver Lauermann, Christoph J. Brabec, and Markus Antonietti. Influence of thiazole-modified carbon nitride nanosheets with feasible electronic properties on inverted perovskite solar cells. *JOURNAL OF THE AMERICAN CHEMICAL SOCIETY*, 141(31):12322–12328, AUG 7 2019. ISSN 0002-7863. doi: 10.1021/jacs.9b03639.

[168] Xiao Chu, Kang Li, Hongyu Guo, Huibin Zheng, Suzanne Shuda, Xiaolan Wang, Junying Zhang, Wei Chen, and Yu Zhang. Exploration of graphitic-c₃n₄ quantum dots for microwave-induced photodynamic therapy. *ACS BIOMATERIALS SCIENCE & ENGINEERING*, 3(8, SI):1836–1844, AUG 2017. ISSN 2373-9878. doi: 10.1021/acsbiomaterials.7b00110.

[169] Di Sun, Zhongyang Zhang, Mengya Chen, Yanping Zhang, Jordi Amagat, Shifei Kang, Yuanyi Zheng, Bing Hu, and Menglin Chen. Co-immobilization of ce6 sono/photosensitizer and protonated graphitic carbon nitride on pcl/gelation fibrous scaffolds for combined sono-photodynamic cancer therapy. *ACS APPLIED MATERIALS & INTERFACES*, 12(36):40728–40739, SEP 9 2020. ISSN 1944-8244. doi: 10.1021/acsami.0c08446.

[170] Clare L. Hawkins and Michael J. Davies. Detection, identification, and quantification of oxidative protein modifications. *JOURNAL OF BIOLOGICAL CHEMISTRY*, 294 (51):19683–19708, DEC 20 2019. doi: 10.1074/jbc.REV119.006217.

[171] Helmut Sies and Dean P. Jones. Reactive oxygen species (ros) as pleiotropic physiological signalling agents. *NATURE REVIEWS MOLECULAR CELL BIOLOGY*, 21(7): 363–383, JUL 2020. ISSN 1471-0072. doi: 10.1038/s41580-020-0230-3.

[172] DC BORG. Free radicals in biology and medicine. *RADIATION RESEARCH*, 47(1): 296–&, 1971. ISSN 0033-7587.

[173] James A. Imlay. Cellular defenses against superoxide and hydrogen peroxide. *ANNUAL REVIEW OF BIOCHEMISTRY*, 77:755–776, 2008. ISSN 0066-4154. doi: 10.1146/annurev.biochem.77.061606.161055.

[174] B CHANCE, H SIES, and A BOVERIS. Hydroperoxide metabolism in mammalian organs. *PHYSIOLOGICAL REVIEWS*, 59(3):527–605, 1979. ISSN 0031-9333. doi: 10.1152/physrev.1979.59.3.527.

[175] Saba Parvez, Marcus J. C. Long, Jesse R. Poganik, and Yimon Aye. Redox signaling by reactive electrophiles and oxidants. *CHEMICAL REVIEWS*, 118(18):8798–8888, SEP 26 2018. ISSN 0009-2665. doi: 10.1021/acs.chemrev.7b00698.

[176] Claudia Lennicke and Helena M. Cocheme. Redox metabolism: Ros as specific molecular regulators of cell signaling and function. *MOLECULAR CELL*, 81(18): 3691–3707, SEP 16 2021. ISSN 1097-2765. doi: 10.1016/j.molcel.2021.08.018.

[177] Helmut Sies, Vsevolod V. Belousov, Navdeep S. Chandel, Michael J. Davies, Dean P. Jones, Giovanni E. Mann, Michael P. Murphy, Masayuki Yamamoto, and Christine Winterbourn. Defining roles of specific reactive oxygen species (ros) in cell biology and physiology. *NATURE REVIEWS MOLECULAR CELL BIOLOGY*, 23(7):499–515, JUL 2022. ISSN 1471-0072. doi: 10.1038/s41580-022-00456-z.

[178] Karen Bedard and Karl-Heinz Krause. The nox family of ros-generating nadph oxidases: Physiology and pathophysiology. *PHYSIOLOGICAL REVIEWS*, 87(1): 245–313, JAN 2007. ISSN 0031-9333. doi: 10.1152/physrev.00044.2005.

[179] Alessia Parascandolo and Mikko O. Laukkanen. Carcinogenesis and reactive oxygen species signaling: Interaction of the nadph oxidase nox1-5 and superoxide dismutase 1-3 signal transduction pathways. *ANTIOXIDANTS & REDOX SIGNALING*, 30(3): 443–486, JAN 20 2019. ISSN 1523-0864. doi: 10.1089/ars.2017.7268.

[180] Michael P. Murphy. How mitochondria produce reactive oxygen species. *BIOCHEMICAL JOURNAL*, 417(1):1–13, JAN 1 2009. ISSN 0264-6021. doi: 10.1042/BJ20081386.

[181] YA Suh, RS Arnold, B Lassegue, J Shi, XX Xu, D Sorescu, AB Chung, KK Griendling, and JD Lambeth. Cell transformation by the superoxide-generating oxidase mox1. *NATURE*, 401(6748):79–82, SEP 2 1999. ISSN 0028-0836. doi: 10.1038/43459.

[182] Karl-Heinz Krause. Aging: A revisited theory based on free radicals generated by nox family nadph oxidases. *EXPERIMENTAL GERONTOLOGY*, 42(4):256–262, APR 2007. ISSN 0531-5565. doi: 10.1016/j.exger.2006.10.011.

[183] JD Lambeth. Nox enzymes and the biology of reactive oxygen. *NATURE REVIEWS IMMUNOLOGY*, 4(3):181–189, MAR 2004. ISSN 1474-1733. doi: 10.1038/nri1312.

[184] H. Susana Marinho, Carla Real, Luisa Cyrne, Helena Soares, and Fernando Antunes. Hydrogen peroxide sensing, signaling and regulation of transcription factors. *REDOX BIOLOGY*, 2:535–562, 2014. ISSN 2213-2317. doi: 10.1016/j.redox.2014.02.006.

[185] Martin D. Brand. Mitochondrial generation of superoxide and hydrogen peroxide as the source of mitochondrial redox signaling. *FREE RADICAL BIOLOGY AND MEDICINE*, 100:14–31, NOV 2016. ISSN 0891-5849. doi: 10.1016/j.freeradbiomed.2016.04.001.

[186] Ashlee Higdon, Anne R. Diers, Joo Yeun Oh, Aimee Landar, and Victor M. Darley-Usmar. Cell signalling by reactive lipid species: new concepts and molecular mechanisms. *BIOCHEMICAL JOURNAL*, 442(3):453–464, MAR 15 2012. ISSN 0264-6021. doi: 10.1042/BJ20111752.

[187] Alvin Eng Kiat Loo, Rongjian Ho, and Barry Halliwell. Mechanism of hydrogen peroxide-induced keratinocyte migration in a scratch-wound model. *Free radical biology & medicine*, 51 4:884–92, 2011. URL https://api.semanticscholar.org/CorpusID:5086113.

[188] Shivali Gupta, Monisha Dhiman, Jian jun Wen, and Nisha Jain Garg. *ROS Signalling of inflammatory cytokines during trypanosoma cruzi infection*, pages 153–170. Advances in Parasitology. Academic Press, 2011. doi: 10.1016/B978-0-12-385895-5.00007-4. Funding Information: The work in NJG's laboratory has been supported in part by grants from the American Heart Association, John Sealy Memorial Endowment Fund for Biomedical Research, American Health Assistance Foundation, and National Institutes of Health. S. G. is an awardee of a Postdoctoral Fellowship from the Sealy Center of Vaccine Development.

[189] J. David Lambeth. Nox enzymes, ros, and chronic disease: An example of antagonistic pleiotropy. *FREE RADICAL BIOLOGY AND MEDICINE*, 43(3):332–347, AUG 1 2007. ISSN 0891-5849. doi: 10.1016/j.freeradbiomed.2007.03.027.

[190] WL Shen, PJ Gao, ZQ Che, KD Ji, M Yin, C Yan, BC Berk, and DL Zhu. Nad(p)h oxidase-derived reactive oxygen species regulate angiotensin-ii induced adventitial fibroblast phenotypic differentiation. *BIOCHEMICAL AND BIOPHYSICAL RESEARCH COMMUNICATIONS*, 339(1):337–343, JAN 6 2006. ISSN 0006-291X. doi: 10.1016/j.bbrc.2005.10.207.

[191] Xingang Liu, Meng Wang, Lei Cao, Jiahao Zhuang, Dandan Wang, Min Wu, and Bin Liu. Living artificial skin: Photosensitizer and cell sandwiched bacterial cellulose for chronic wound healing. *Advanced Materials*, 36(26):2403355, 2024. doi: https://doi.org/10.1002/adma.202403355. URL https://advanced.onlinelibrary.wiley.com/doi/abs/10.1002/adma.202403355.

[192] Umama Binte Irshad, Zareen Akhtar, Götz Bucher, Alexey Y. Ganin, Humaira Masood Siddiqi, and Bernhard V. K. J. Schmidt. Adsorption and photocatalytic properties of tris(4-aminophenyl)amine-based polyimide/graphitic carbon nitride composites for organic dye removal. *ACS Applied Polymer Materials*, 2024. doi: 10.1021/acsapm.4c00019. URL http://dx.doi.org/10.1021/acsapm.4c00019.

[193] George Han and Roger Ceilley. Chronic wound healing: A review of current management and treatments. *ADVANCES IN THERAPY*, 34(3):599–610, MAR 2017. ISSN 0741-238X. doi: 10.1007/s12325-017-0478-y.

[194] Mojtaba Farahani and Abbas Shafiee. Wound healing: From passive to smart dressings. *ADVANCED HEALTHCARE MATERIALS*, 10(16), AUG 2021. ISSN 2192-2640. doi: 10.1002/adhm.202100477.

[195] Abhinanda Kar, Nadim Ahamad, Mahima Dewani, Lisha Awasthi, Runali Patil, and Rinti Banerjee. Wearable and implantable devices for drug delivery: Applications and challenges. *BIOMATERIALS*, 283, APR 2022. ISSN 0142-9612. doi: 10.1016/j.biomaterials.2022.121435.

[196] Parinaz Nezhad-Mokhtari, Marjan Ghorbani, Leila Roshangar, and Jafar Soleimani Rad. Chemical gelling of hydrogels-based biological macromolecules for tissue engineering: Photo- and enzymatic-crosslinking methods. *INTERNATIONAL JOURNAL OF BIOLOGICAL MACROMOLECULES*, 139:760–772, OCT 15 2019. ISSN 0141-8130. doi: 10.1016/j.ijbiomac.2019.08.047.

[197] Baris Kumru, Valerio Molinari, Menny Shalom, Markus Antonietti, and Bernhard V. K. J. Schmidt. Tough high modulus hydrogels derived from carbon-nitride via an ethylene glycol co-solvent route. *SOFT MATTER*, 14(14):2655–2664, APR 14 2018. ISSN 1744-683X. doi: 10.1039/c8sm00232k.

[198] Baris Kumru, Menny Shalom, Markus Antonietti, and Bernhard V. K. J. Schmidt. Reinforced hydrogels via carbon nitride initiated polymerization. *MACROMOLECULES*, 50(5):1862–1869, MAR 14 2017. ISSN 0024-9297. doi: 10.1021/acs.macromol.6b02691.

[199] Wee-Jun Ong, Lling-Lling Tan, Yun Hau Ng, Siek-Ting Yong, and Siang-Piao Chai. Graphitic carbon nitride (g-c3n4)-based photocatalysts for artificial photosynthesis and environmental remediation: are we a step closer to achieving sustainability? *Chemical reviews*, 116(12):7159–7329, 2016.

[200] Damia Mawad, Penny J. Martens, Ross A. Odell, and Laura A. Poole-Warren. The effect of redox polymerisation on degradation and cell responses to poly (vinyl alcohol) hydrogels. *Biomaterials*, 28(6):947–955, 2007. ISSN 0142-9612. doi: https://doi.org/10.1016/j.biomaterials.2006.10.007. URL https://www.sciencedirect.com/science/article/pii/S0142961206008982.

[201] Miriam Khodeir, Bruno Ernould, Jérémy Brassinne, Sina Ghiassinejad, He Jia, Sayed Antoun, Christian Friebe, Ulrich S. Schubert, Zdravko Kochovski, Yan Lu, Evelyne Van Ruymbeke, and Jean-François Gohy. Synthesis and characterisation of redox hydrogels based on stable nitroxide radicals. *Soft Matter*, 15:6418–6426, 2019. doi: 10.1039/C9SM00905A. URL http://dx.doi.org/10.1039/C9SM00905A.

[202] Max C. Darnell, Jeong-Yun Sun, Manav Mehta, Christopher Johnson, Praveen R. Arany, Zhigang Suo, and David J. Mooney. Performance and biocompatibility of extremely tough alginate/polyacrylamide hydrogels. *Biomaterials*, 34(33):8042–8048, 2013. ISSN 0142-9612. doi: https://doi.org/10.1016/j.biomaterials.2013.06.061. URL https://www.sciencedirect.com/science/article/pii/S014296121300776X.

[203] Zhongwei Zhao. Hydroxyl radical generations form the physiologically relevant fenton-like reactions. *FREE RADICAL BIOLOGY AND MEDICINE*, 208:510–515, NOV 1 2023. ISSN 0891-5849. doi: 10.1016/j.freeradbiomed.2023.09.013.

[204] Jiawei Sun, Steven T. Rutherford, Thomas J. Silhavy, and Kerwyn Casey Huang. Physical properties of the bacterial outer membrane. *NATURE REVIEWS MICROBIOLOGY*, 20(4):236–248, APR 2022. ISSN 1740-1526. doi: 10.1038/s41579-021-00638-0.

[205] Trevor Lithgow, Christopher J. Stubenrauch, and Michael P. H. Stumpf. Surveying membrane landscapes: a new look at the bacterial cell surface. *NATURE REVIEWS MICROBIOLOGY*, 21(8):502–518, AUG 2023. ISSN 1740-1526. doi: 10.1038/s41579-023-00862-w.

[206] Maksim Plikus, V, Xiaojie Wang, Sarthak Sinha, Elvira Forte, Sean M. Thompson, Erica L. Herzog, Ryan R. Driskell, Nadia Rosenthal, Jeff Biernaskie, and Valerie Horsley. Fibroblasts: Origins, definitions, and functions in health and disease. *CELL*, 184(15):3852–3872, JUL 22 2021. ISSN 0092-8674. doi: 10.1016/j.cell.2021.06.024.

[207] Feng Gao, Tianyi Shao, Yunpeng Yu, Yujie Xiong, and Lihua Yang. Surface-bound reactive oxygen species generating nanozymes for selective antibacterial action. *NATURE COMMUNICATIONS*, 12(1), FEB 2 2021. doi: 10.1038/s41467-021-20965-3.

[208] Nafise Amiri, Andrew P. Golin, Reza B. Jalili, and Aziz Ghahary. Roles of cutaneous cell-cell communication in wound healing outcome: An emphasis on keratinocyte-fibroblast crosstalk. *EXPERIMENTAL DERMATOLOGY*, 31(4):475–484, APR 2022. ISSN 0906-6705. doi: 10.1111/exd.14516.

[209] Maria Zhivagui, Areebah Hoda, Noelia Valenzuela, Yi-Yu Yeh, Jason Dai, Yudou He, Shuvro P. Nandi, Burcak Otlu, Bennett Van Houten, and Ludmil B. Alexandrov. Dna damage and somatic mutations in mammalian cells after irradiation with a nail polish dryer. *NATURE COMMUNICATIONS*, 14(1), JAN 17 2023. doi: 10.1038/s41467-023-35876-8.

[210] Hao Liu, Zhixuan Yu, Ling Liu, and Shaojun Dong. Cell wall binding strategies based on cu3sbs3 nanoparticles for selective bacterial elimination and promotion of infected wound healing. *ACS Applied Materials & Interfaces*, 16(26):33038–33052, 2024. doi: 10.1021/acsami.4c04726. URL https://doi.org/10.1021/acsami.4c04726. PMID: 38961578.

[211] Yunjiang Jiang, Wan Zheng, Keith Tran, Elizabeth Kamilar, Jitender Bariwal, Hairong Ma, and Hongjun Liang. Hydrophilic nanoparticles that kill bacteria while sparing mammalian cells reveal the antibiotic role of nanostructures. *Nature Communications*, 13(1):197, 2022.

[212] Nan Wang, Kun Xie, Siwei Huo, Jing Zhao, Shangli Zhang, and Junying Miao. Suppressing phosphatidylcholine-specific phospholipase c and elevating ros level, nadph oxidase activity and rb level induced neuronal differentiation in mesenchymal stem cells. *JOURNAL OF CELLULAR BIOCHEMISTRY*, 100(6):1548–1557, APR 15 2007. ISSN 0730-2312. doi: 10.1002/jcb.21139.

[213] Qingzhong Xiao, Zhenling Luo, Anna Elena Pepe, Andriani Margariti, Lingfang Zeng, and Qingbo Xu. Embryonic stem cell differentiation into smooth muscle cells is mediated by nox4-produced h₂o₂. *AMERICAN JOURNAL OF PHYSIOLOGY-CELL PHYSIOLOGY*, 296(4):C711–C723, APR 2009. ISSN 0363-6143. doi: 10.1152/ajpcell.00442.2008.

[214] Kathryn V. Tormos, Elena Anso, Robert B. Hamanaka, James Eisenhart, Joy Joseph, Balaraman Kalyanaraman, and Navdeep S. Chandel. Mitochondrial complex iii ros regulate adipocyte differentiation. *CELL METABOLISM*, 14(4):537–544, OCT 5 2011. ISSN 1550-4131. doi: 10.1016/j.cmet.2011.08.007.

[215] Yasunari Kanda, Takashi Hinata, Sang Won Kang, and Yasuhiro Watanabe. Reactive oxygen species mediate adipocyte differentiation in mesenchymal stem cells. *LIFE SCIENCES*, 89(7-8):250–258, AUG 15 2011. ISSN 0024-3205. doi: 10.1016/j.lfs.2011.06.007.

[216] Jixiang Zhang, Xiaoli Wang, Vikash Vikash, Qing Ye, Dandan Wu, Yulan Liu, and Weiguo Dong. Ros and ros-mediated cellular signaling. *OXIDATIVE MEDICINE AND CELLULAR LONGEVITY*, 2016, 2016. ISSN 1942-0900. doi: 10.1155/2016/4350965.

[217] Jianfeng Xu, Juying Qian, Xinxing Xie, Li Lin, Yunzeng Zou, Mingqiang Fu, Zheyong Huang, Guoping Zhang, Yangang Su, and Junbo Ge. High density lipoprotein protects mesenchymal stem cells from oxidative stress-induced apoptosis via activation of the pi3k/akt pathway and suppression of reactive oxygen species. *INTERNATIONAL JOURNAL OF MOLECULAR SCIENCES*, 13(12):17104–17120, DEC 2012. doi: 10.3390/ijms131217104.

[218] S. O. Blacklow, J. Li, B. R. Freedman, M. Zeidi, C. Chen, and D. J. Mooney. Bioinspired mechanically active adhesive dressings to accelerate wound closure. *SCIENCE ADVANCES*, 5(7), JUL 2019. ISSN 2375-2548. doi: 10.1126/sciadv.aaw3963.

[219] Georgios Theocharidis, Hyunwoo Yuk, Heejung Roh, Liu Wang, Ikram Mezghani, Jingjing Wu, Antonios Kafanas, Mauricio Contreras, Brandon Sumpio, Zhuqing Li, Enya Wang, Lihong Chen, Chuan Fei Guo, Navin Jayaswal, Xanthi-Leda Katopodi, Nikolaos Kalavros, Christoph S. Nabzdyk, Ioannis S. Vlachos, Aristidis Veves, and Xuanhe Zhao. A strain-programmed patch for the healing of diabetic wounds. *NATURE BIOMEDICAL ENGINEERING*, 6(10):1118+, OCT 2022. ISSN 2157-846X. doi: 10.1038/s41551-022-00905-2.

[220] Yuanwen Jiang, Artem A. Trotsyuk, Simiao Niu, Dominic Henn, Kellen Chen, Chien-Chung Shih, Madelyn R. Larson, Alana M. Mermin-Bunnell, Smiti Mittal, Jian-Cheng Lai, Aref Saberi, Ethan Beard, Serena Jing, Donglai Zhong, Sydney R. Steele, Kefan Sun, Tanish Jain, Eric Zhao, Christopher R. Neimeth, Willian G. Viana, Jing Tang, Dharshan Sivaraj, Jagannath Padmanabhan, Melanie Rodrigues, David P. Perrault, Arhana Chattopadhyay, Zeshaan N. Maan, Melissa C. Leeolou, Clark A. Bonham, Sun Hyung Kwon, Hudson C. Kussie, Katharina S. Fischer, Gurupranav Gurusankar, Kui Liang, Kailiang Zhang, Ronjon Nag, Michael P. Snyder, Michael Januszyk, Geoffrey C. Gurtner, and Zhenan Bao. Wireless, closed-loop, smart bandage with integrated sensors and stimulators for advanced wound care and accelerated healing. *NATURE BIOTECHNOLOGY*, 41(5):652+, MAY 2023. ISSN 1087-0156. doi: 10.1038/s41587-022-01528-3.

[221] Canran Wang, Ehsan Shirzaei Sani, and Wei Gao. Wearable bioelectronics for chronic wound management. *ADVANCED FUNCTIONAL MATERIALS*, 32(17), APR 2022. ISSN 1616-301X. doi: 10.1002/adfm.202111022.

[222] Hiroyuki Kawagishi and Toren Finkel. Ros and disease: finding the right balance. *NATURE MEDICINE*, 20(7):711–713, JUL 2014. ISSN 1078-8956. doi: 10.1038/nm.3625.

[223] Juhyun Oh, Yang David Lee, and Amy J. Wagers. Stem cell aging: mechanisms, regulators and therapeutic opportunities. *NATURE MEDICINE*, 20(8):870–880, AUG 2014. ISSN 1078-8956. doi: 10.1038/nm.3651.

[224] Xinyan Li, Jingjing Gao, Chengcheng Wu, Chaoyu Wang, Ruoshi Zhang, Jia He, Ziting Judy Xia, Nitin Joshi, Jeffrey M. Karp, and Rui Kuai. Precise modulation and use of reactive oxygen species for immunotherapy. *Science Advances*, 10(20): eadl0479, 2024. doi: 10.1126/sciadv.adl0479. URL https://www.science.org/doi/abs/10.1126/sciadv.adl0479.